UNIVERSITY OF SOUTAMPTON
FACULTY OF SCIENCE
DEPARTMENT OF PHYSICS

OPTICAL SIGNAL PROCESSING USING PHOTOREFRACTIVE CRYSTALS

by Ghazanfar Hussain

A thesis submitted for the degree of Doctor of Philosophy

August 1992

UNIVERSITY OF SOUTHAMPTON

ABSTRACT

FACULTY OF SCIENCE

PHYSICS

Doctor of Philosophy

OPTICAL SIGNAL PROCESSING USING PHOTOREFRACTIVE CRYSTALS

by Ghazanfar Hussain

I describe in this thesis various techniques of optical signal processing using photorefractive BSO and $BaTiO_3$ crystals. Operations of contrast manipulation, motion detection and parallel optical logic operations are demonstrated. Dynamic instabilities have also been investigated in photorefractive $BaTiO_3$, in the mutually pumped geometry.

Contrast manipulation of optical images has been performed via degenerate four wave mixing in BSO and $BaTiO_3$ crystals. In BSO the technique adopted has the apparent drawback of intensity reduction, due to low reflectivities achieved, while using $BaTiO_3$, selective **enhancement** is achieved for specific Fourier components. An improved versatile technique of polarization encoding of the object Fourier transform has also been implemented with, and without the inclusion of photorefractive crystals. Applications of this technique for phase contrast imaging, and observation in the field of aerodynamics, and Fourier transform synthesis, has been proposed and demonstrated.

Optical motion detection using the differential response time of multiplexed gratings in photorefractive BSO has been demonstrated. The operation of velocity filtering has also been demonstrated using complementary gratings in a BSO crystal, in which specific features are only detected at particular speeds. All sixteen basic parallel optical logic operations have been demonstrated using polarization encoding in a phase conjugate Michelson interferometer with a crystal of BSO as a phase conjugate mirror. Finally dynamic instabilities in $BaTiO_3$ in the 'Bird-wing' mutually-pumped configuration have also been investigated, and a phenomenological model is developed.

Additionally various improvements and refinements have been proposed which will make these techniques more flexible and versatile.

In the name of Allah, Most Gracious, Most Merciful

Read! in the name Of thy Lord and Cherisher, Who created

Created human being, out of A (mere) clot Of congealed blood

Proclaim! And thy Lord Is Most Bountiful

He Who taught (The use of), the Pen

Taught human beings that Which they knew not

AL-ALAQ (1-5)

to *Abba Jee* and *Amee Jee*

and to my *wife*, but I don't know yet who she will be,

and who I have been looking for, for so long

CONTENTS

Acknowledgements

I would like to express my gratitude to Dr. Robert W. Eason, for his support, encouragement and enthusiastic supervision throughout this research work, and thesis writing up period. I am also grateful to Dr. Robert W. Eason for sponsoring me and encouraging me to attend several conferences. I am thankful to the Government of Pakistan for their postgraduate scholarship and also to the Overseas Research Studentship Award for two consecutive years.

I am grateful to my colleagues Sarah Clapham, Steve James (also for the development of his phenomenological model described in Chapter 8), Stuart MacCormack, Katharine Youden, Graeme Ross and many others in the ORC.

Finally my parents, brothers and sisters, nephews and niece whose patience and encouragement were much appreciated throughout this research work.

Introduction

This thesis describes the techniques of optical signal processing using photorefractive BSO and $BaTiO_3$ crystals in different geometries. Techniques of contrast manipulation of optical images are described in Chapters 2, 3, and 4, Chapters 5 and 6 describe techniques of motion detection and Chapters 7 and 8 deals with parallel optical logic operations and dynamic instabilities respectively.

Chapter 2 deals with the experimental investigation of the controlled contrast enhancement operation and contrast inversion of periodic objects. These operations are achieved via degenerate four wave mixing and an erasing beam. Results of contrast manipulation of a binary object have also been reported via multiplexed degenerate four wave mixing, which illustrates that DC and higher order features can be enhanced independently of each other.

In Chapter 3 we present a scheme of controllable spatial filtering via two beam coupling in $BaTiO_3$ between a reference beam and the optical Fourier transform of the input image. The nature of the spatial filtering is determined by the intensity dependent gain of each component of the Fourier transform. By adjusting the intensity ratios to an appropriate level, the operations of contrast enhancement, feature extraction and defect enhancement have been demonstrated.

A new approach for contrast manipulation of optical images is reported in Chapter 4, which exploits the polarization encoding of a Fourier transform. This chapter is sub divided into three sections where polarization encoding of the Fourier transform is applied in three different ways to achieve contrast manipulation. Section 4.2.1, describes a technique of contrast manipulation which is based upon the analysis of a polarization encoded Fourier transform of the object distribution. Experimental results are presented for contrast manipulation of amplitude, as well as phase objects. Applications of this technique are also described for phase contrast microscopy and observation of wind tunnel aerodynamics. This technique obviates the requirement of different phase filters for positive and negative contrast and also for fixed values of these filters formerly required for different levels of contrast.

In Section 4.2.2 the application of this technique in combination with degenerate four wave mixing in a photorefrative BSO crystal is used for contrast manipulation of optical images. Experimental results of contrast manipulation of binary as well as grey level objects are described. In Section 4.2.3 we describe selective amplification of the polarization encoded Fourier transform orders via two beam coupling in $BaTiO_3$. Experimental results are presented which show significant gain, however the presence of fanning noise can sometimes lead to distorted or poor quality output images.

Chapter 5, deals with differentiation of time varying optical images to detect motion. This technique exploits the spatial frequency dependent response time of grating formation in photorefractive BSO for each arm of a phase conjugate Michelson interferometer arrangement. Therefore the response time can be changed by changing the angle between the interfering beams, in this multiplexed arrangement.

Chapter 6, describes a technique for velocity filtering and feature extraction of time varying optical images. This operation is achieved via recording of complementary gratings with a relative shift of 180° in photorefractive BSO via degenerate four wave mixing configuration. For suitable experimental parameters, such as grating response time, input intensity, almost complete subtraction is achieved in the phase conjugate output. When there is any movement in the object plane a bright output image is observed depending on the experimental variables of feature size and velocity. We also present results for motion detection of features of various dimensions at a range of speeds in both x and y directions via Fourier plane observation.

Chapter 7 deals with two dimensional optical Boolean logic gates which are the basic elements of digital optical processors. Multiple signal beams interfere with a single reference beam to record multiplexed gratings. A self-pumped $BaTiO_3$ crystal provides a counter propagating common readout beam for all the gratings. The whole set up is in the form of a phase conjugate Michelson interferometer. The technique depends upon changing the polarizations of the two phase conjugate beams with some relative phase shift between them. Therefore the output logic

operation achieved depends on their relative polarizations and phases. The phase conjugate Michelson interferometer set up works in two modes, of polarization preserving and non-preserving modes. When the interferometer works in polarization preserving mode, complete subtraction is achieved, however in non-polarization preserving mode a variable operation is achieved.

Chapter 8 briefly reviews the family of mutually pumped phase conjugators (MPPC). The fluctuations in the phase conjugate output from the Bird-wing phase conjugator are investigated experimentally. A phenomenological model, developed by another member of the group Dr. Steve James, is presented which is based upon observations of beam patterns within the crystal during a typical oscillation cycle.

CHAPTER 1

THE PHOTOREFRACTIVE EFFECT AND ITS APPLICATIONS IN OPTICAL SIGNAL PROCESSING

1.1 Optical Phase Conjugation

Optical phase conjugation (OPC) is a nonlinear process which generates the phase conjugate replica of an input signal beam, and as such, this device may be called a phase conjugate mirror (PCM), [1.1 - 1.6]. When an input beam of light is incident upon a PCM, the **reflected** beam will precisely trace back its original path, the wavefront of which assumes the same shape throughout space, but propagates in the reverse direction at every point. As shown in Figure 1.1 (a), an input beam is incident with an arbitrary wave vector k_{in} on a conventional mirror. On reflection the angle between the incident and reflected beams is double the incident angle as expected. However the situation with a PCM is entirely different, where the reflected beam wavevector $k_{out} = -k_{in}$, is reversed, therefore allowing the output to retrace its original path.

Consider an incident wave E(r,t) of the form: [1.1-1.7],

$$E(r,t) = \frac{A(r)}{2}\exp[i(\omega t - kz)] + \frac{A^*(r)}{2}\exp[-i(\omega t - kz)] \quad (1.1)$$

Where the complex amplitude A(r) can describe any spatial information imposed upon E. ω is the optical frequency, and k is the propagation wavevector. Wavefront reversal is obtained by complex conjugating the spatial part of the input wave in (1.1) above i.e.,

$$E_{PC}(r,t) = \frac{A^*(r)}{2}\exp[i(\omega t + kz)] + \frac{A(r)}{2}\exp[-i(\omega t + kz)] \quad (1.2)$$

This process is illustrated in Figure 1.1 (b), where an input beam is incident on the mirror, and after phase conjugation, returns precisely back along the same outward path.

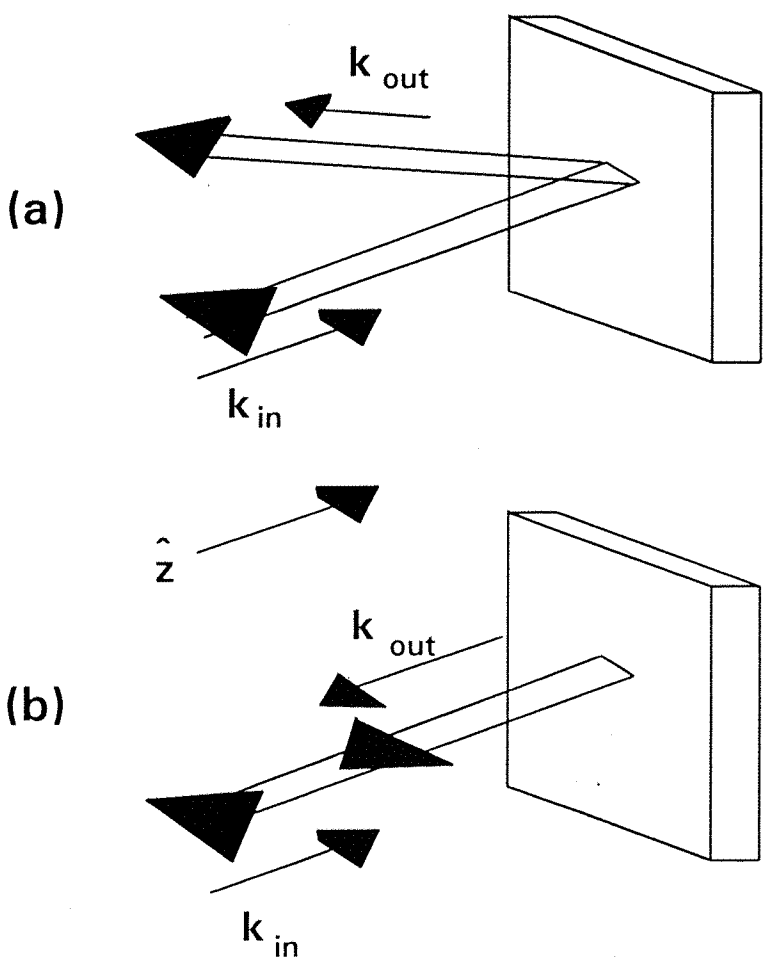

Figure 1.1 Shows the reflection characteristics from (a) conventional mirror and (b) from a phase conjugate mirror.

1.2 Applications of Optical Phase Conjugation

1.2.1 Spatial Applications

Here we briefly discuss various applications of OPC which exploit the spatial nature of the nonlinear optical interaction. These applications may be subdivided into two categories namely real time adaptive optics and image processing [1.2].

1.2.1.1 Real Time Adaptive Optics

Much of the interest in using a PCM is due to the compensation that occurs for distortions that are generated as a result of turbulence, vibration, temperature, or imperfect optical elements, and in the generation, transmission and processing of coherent images. Phase aberrations can be compensated by letting the wavefront retrace its path through the aberrating medium, i.e., wavefront reversal via reflection from a PCM as illustrated via Figure 1.2 (a) and (b). In Figure 1.2, 1 is the input beam, 2 is the aberrated beam, 3 is the reflected beam from conventional and phase conjugate mirror, while 4 is the output beam. The reflection from a conventional mirror shows clearly the drawback of aberration.

Consider an example of an image transmitted through a long multimode optical fibre, where the image will be scrambled after travelling a sufficiently long distance. The reason is that the image travels in many spatial modes each of which (in the geometrical analogy) corresponds to a given ray that travels in a zigzag path down the fibre. Since all the modes travel different paths they therefore reach the end of the fibre out of step with each other. This phase distortion can be eliminated from the output of the optical fibre by using the phase reversal properties of a PCM. The unscrambled image is achieved after back propagation through either the initial waveguide or in principle, another similar fibre link with equal modal dispersion.

Next let us consider the problem of maintaining diffraction limited output from a laser onto a given target. Figure 1.3 illustrates a typical application of adaptive optics via OPC for a target. When the target is illuminated, some of the light scattered from it is captured by the aperture of a lens. This light then travels through

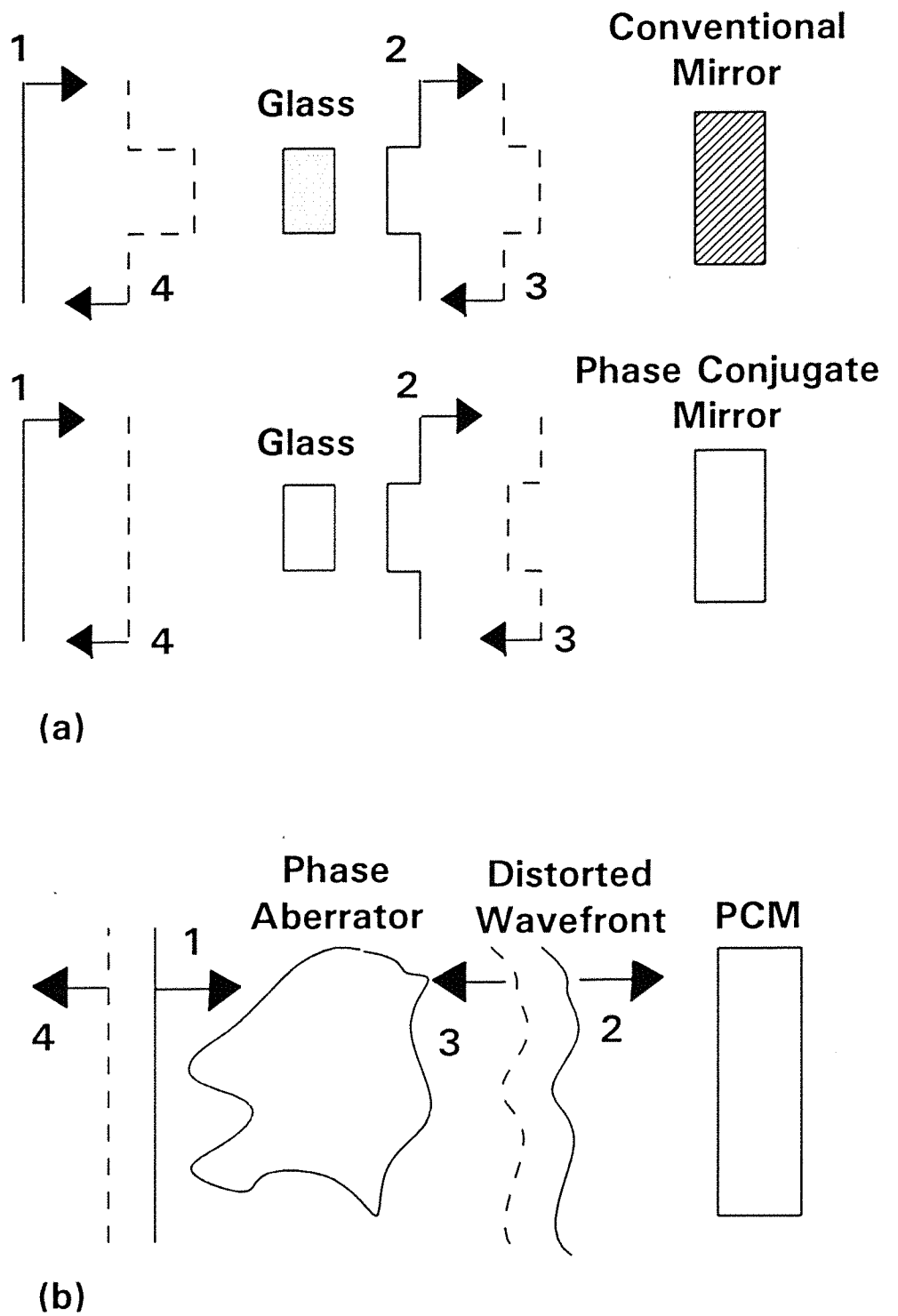

Figure 1.2 Shows the compensation for the aberration via a phase conjugate mirror.

an amplifier and is reflected from a PCM and retraces the same route towards the target. Any possible phase aberrations introduced during the initial pass will be compensated in the return path because of the phase compensation property of the PCM. When we compare this to the use of a conventional mirror instead of a PCM, we see the serious drawbacks.

OPC can also be used to transfer a two dimensional pattern from one plane in space to another via lensless imaging. The performance of conventional photolithographic techniques is typically affected by phase aberrations, diffraction, and the physical contact between mask and photoresist. The photolithographic arrangement is shown in Figure 1.4, which uses a PCM to eliminate the problem of aberrations [1.8].

1.2.1.2 Image processing

So far various techniques of OPC via four wave mixing have been demonstrated and will be discussed in more detail in Section 1.11 of this chapter.

1.2.2 Temporal Domain Applications

It has been suggested that a PCM can also be used to compensate for pulse broadening effects in optical fibre cables. The temporal broadening occurs because the various frequency components of a pulse travelling in such a dispersive medium experience slightly different phase velocities. Therefore, when a train of pulses propagates through a single mode optical fibre of a certain length, the sequence of pulses will be temporally broadened. This temporal broadening can be cured using a PCM at a midpoint of such an optical fibre provided the proceeding half of the fibre has the same optical properties. Due to the frequency flipping nature of the PCM the faster propagating frequency components undergo a shift in frequency with respect to those arriving at correspondingly later times. This frequency reordering results in a pulse whose initial frequency components propagate more slowly while their faster counterparts will catch up with them after subsequent propagation through the second half of the fibre link.

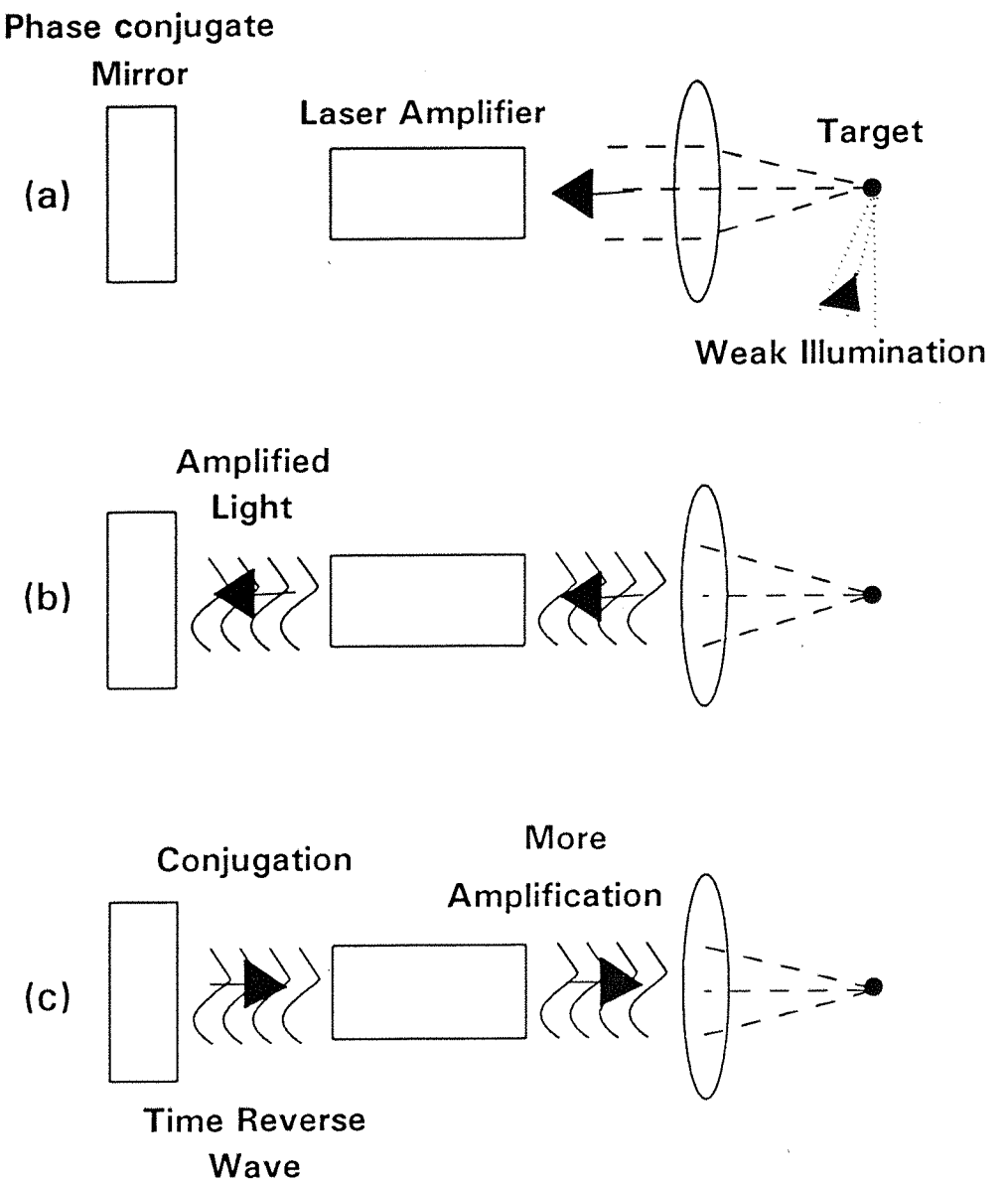

Figure 1.3 Illustrates a potential application of optical phase conjugation for target illumination.

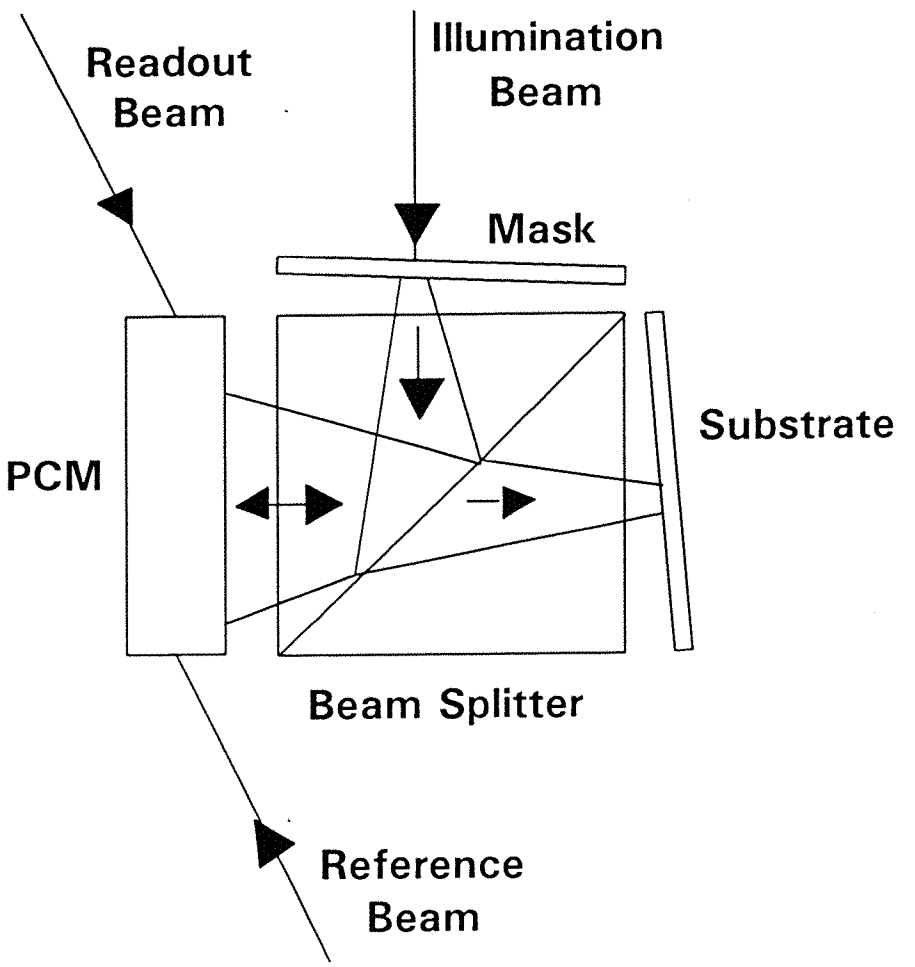

Figure 1.4 Shows a lensless imaging system for photolithography using a phase conjugate mirror.

1.3 The Photorefractive Effect

When a photorefractive material is illuminated by a fringe pattern, photoexcited carriers migrate from bright regions to dark regions. These charges originate from impurities or defect sites in the photorefractive crystal [1.7, 1.9, 1.10]. The photorefractive effect consists of a sequence of events as illustrated in Figure 1.5. The spatial intensity pattern I(x) redistributes charges to form a charge density pattern $\rho(x)$. The separation between the charge carriers due to the intensity pattern, sets up a space charge field corresponding to the charge density $\rho(x)$. The space charge field $E_{sc}(x)$ causes a change in refractive index of the material via the Pockels effect. The induced refractive index pattern $\Delta n(x)$ is spatially shifted therefore with respect to the incident light pattern I(x).

Since the photorefractive effect occurs due to the light induced charge separation inside the material. The photorefractive nonlinearity can saturate at a large, steady state value even at a very low light intensity. However the photorefractive nonlinearity will be decreased if the light intensity is so weak that the photoconductivity is less than or comparable to the dark conductivity and the temporal response of the photorefractive effect increases as the intensity of the optical beams increases. This temporal response of the photorefractive effect has been observed to increase linearly or sub-linearly with optical intensity, depending on the material [1.7].

Assuming that there is no uniform electric field in the crystal, the interference pattern of the two optical plane waves varies periodically in space according to

$$I(x) = I_o [1 + M\cos(k_g x)] \qquad (1.3)$$

Where $M = 2(I_1 \cdot I_2)^{1/2} / I_o$, and $I_o = I_1 + I_2$ is the total light intensity and k_g is the grating wavevector. The free charges generated in the crystal by absorption of light diffuse from regions of higher intensity into regions of lower intensity, resulting in a steady state charge density pattern $\rho(x)$. This final charge pattern represents a balance between the diffusion of charges in the nonuniform light intensity and the tendency of the resulting space charge field $E_{sc}(x)$ to restore the charge to its initial uniform distribution. The resulting space charge field $E_{sc}(x)$ can be expressed as

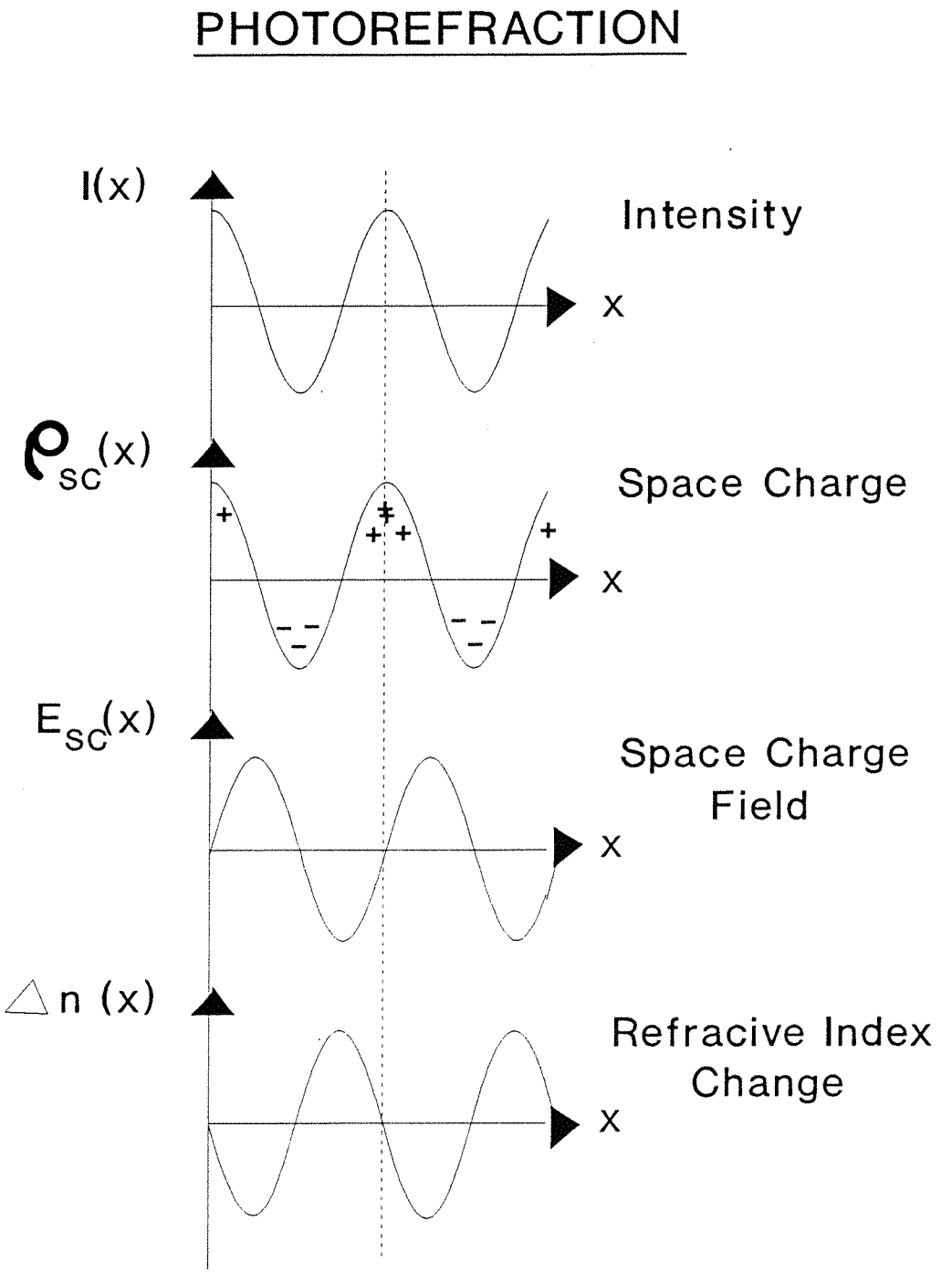

Figure 1.5 Illustrate the build-up process of a phase grating in a photorefractive medium.

$$\rho(x) = \frac{\epsilon}{4\pi} \nabla . E_{sc}(x) \qquad (1.4)$$

The space charge field $E_{sc}(x)$ in the crystal generates a refractive index variation pattern $\Delta n(x)$ by the linear electrooptic effect

$$\Delta n(x) = -r_{eff} \frac{n^3}{2} E_{sc}(x) \qquad (1.5)$$

where r_{eff} is the effective electrooptic coefficient.

1.4 Band Transport Model

The build up of a light induced space charge field within the photorefractive crystal can be described by the band transport model which may be explained by a set of material equations formulated by Kukhtarev et al [1.11]. We consider for simplicity a single charge carrier species, in this case electrons, so the continuity equation for the mobile electrons in the conduction band is given by

$$\frac{\partial n}{\partial t} - \frac{\partial N_D^+}{\partial t} = \frac{1}{q} \nabla . J \qquad (1.6)$$

where n = free electron number density

t = time

N_D^+ = ionized donor density

q = electron charge

J = electron current density

The continuity equation of immobile ionized donors can be expressed by

$$\frac{\partial N_D^+}{\partial t} = (N_D - N_D^+)(sI + \beta) - \gamma_R N_D^+ n \qquad (1.7)$$

Where N_D is the total density of donors, s is the photoexcitation constant, I is the light intensity, β is probability rate of thermal excitation and γ_R is the recombination constant.

It is assumed that the donors remain localised while the photo- and thermal

excitation of electrons causes promotion from a donor level to the conduction band. After remaining there for a finite time the electron will recombine with an already ionized donor (acceptor). The generation rate is assumed to be linearly proportional to the number of occupied donors, the probability that a conduction band state is unoccupied and the probability rate of ionization. Similarly the recombination rate is linearly proportional to the number of free electrons and the probability that a trap is empty. Accordingly, Gauss's law in this case can be re-expressed as

$$\nabla . (\epsilon E) = q(N_D^+ - N_A - n) \qquad (1.8)$$

where ϵ is permittivity. However in electrostatic condition we express

$$\nabla x E = 0 \qquad (1.9)$$

Equation (1.9) corresponds to quasi-steady state approximation ($\partial B/\partial t$). The term $sI(N_D - N_D^+) + \beta(N_D - N_D^+)$ in Equation (1.7), describes the rate of generation of mobile conduction band electrons by photoexcitation and thermal generation. The generation of photocarriers depends upon the number of unionized donors, intensity and photoexcitation cross-section, while the thermal generation rate of mobile electrons will occur uniformly throughout the crystal independently of the incident light intensity.

1.4.1 Linear generation and recombination

For the linear generation and recombination regime the space charge field under the drift and diffusion case can be expressed as

$$E_{sc} = \frac{E_o\sqrt{1-m^2}}{1+m\cos(k_g x)} - \frac{E_D m \sin(k_g x)}{1+m\cos(k_g x)} \qquad (1.10)$$

where E_o is any applied field, and E_D is the diffusion field which can be expressed as

$$E_D = \frac{K_B T}{q} k_g \qquad (1.11)$$

where K_B is Boltzmann's constant, T is the absolute temperature, q is the electronic charge, and m is the reduced modulation ratio due to the thermal generation of carriers, which can be expressed by

$$m=\frac{M}{1+\frac{\beta}{sI_o}} \qquad (1.12)$$

1.5 Important Properties of Photorefractive Materials

1.5.1 Photorefractive Sensitivity

Photorefractive sensitivity of a material tells us how efficiently input optical energy is used to change the refractive index, per unit of absorbed energy, per unit volume and can be expressed as [1.7, 1.9]

$$S=\frac{\Delta n}{\alpha I_o t} \qquad (1.13)$$

where Δn is the change in refractive index, and α is absorption coefficient and t is the response time of the crystal.

1.5.2 Steady State Index Change

The steady state index change is the maximum possible change in refractive index reached after illumination for a time that is long compared to the response time of the material and is given by

$$\Delta n_{ss}=\frac{1}{2}n^3 r_{eff} m E_{sc} \qquad (1.14)$$

where n is the refractive index of the crystal, r_{eff} is effective electrooptic coefficient and E_{sc} is the space charge field in steady state and are material dependent quantities. E_{sc} has three limits:

(i) $E_{sc} \approx E_D$ for the diffusion only case, where E_D is less than E_q, which is the maximum space charge field. This holds for materials with moderate values of dielectric constant such as BSO, BGO etc, with the grating period greater than 0.5 μm for typical trap densities of about 10^{16} cm^{-3}. In materials with large dielectric constants however such as $BaTiO_3$, $KNbO_3$, SBN, $E_D < E_q$ occurs for Λ_g = 1.5 to 5 μm with similar trap densities.

(ii) When drift (displacement of charges under externally applied), and diffusion are both present such that $E_q > E_o > E_D$ than E_{sc} is proportional to E_o. The steady state index, in this case, depends on the material quantity r_{eff}.

(iii) E_o or $E_D > E_q$ in which case $E_{sc} = E_q$ and the steady state index will have a material dependence on N_A.

1.5.3 Response Time

In photorefractive crystals the induced change in refractive index requires a time which depends on the efficiency of the charge generation and transport process as well as on experimental arrangement such as light intensity and grating fringe spacing. The response time of a photorefractive material is of considerable importance because, it is the single most useful figure by which the optical implementation of various processes may be compared with their electronic counterparts. In the case of short recombination times, the response time approaches the dielectric relaxation time,

$$\tau_{di} = \left[\frac{\epsilon \gamma_R}{4\pi e \mu s}\right]\left[\frac{N_A}{N_D - N_A}\right]\frac{1}{I_o} \qquad (1.15)$$

where ϵ is the dielectric constant and s is the photoionization cross section which can be varied by the choice of the wavelength of the incident laser light.

1.6 The Linear Electrooptic Effect

The behaviour of a propagating wave in an anisotropic medium can be determined from the index ellipsoid surface [1.4]. The index ellipsoid, for any given direction allows the indices of the two mutually orthogonal ordinary and extraordinary rays to be evaluated. The equation of the index ellipsoid can be expressed as

$$\left(\frac{1}{n^2}\right)_1 x^2 + \left(\frac{1}{n^2}\right)_2 y^2 + \left(\frac{1}{n^2}\right)_3 z^2 + 2\left(\frac{1}{n^2}\right)_4 yz + 2\left(\frac{1}{n^2}\right)_5 xz + 2\left(\frac{1}{n^2}\right)_6 xy = 1 \qquad (1.16)$$

Diagonalizing the above equation gives

$$\frac{x^2}{n_x^2} + \frac{y^2}{n_y^2} + \frac{z^2}{n_z^2} = 1 \qquad (1.17)$$

Where x, y, and z are the new principle dielectric constant axes. For a uniaxial crystal $n_x = n_y \neq n_z$. The application of an electric field changes the refractive index via the equation

$$\Delta\left(\frac{1}{n^2}\right)_i = \sum r_{ij} E_j \qquad (1.18)$$

Where j represents 1 = x, 2 = y, 3 = z. The 6 x 3 matrix with elements r_{ij} is called the electrooptic tensor. The form of the electrooptic tensor dictates which, if any, of the coefficients are zero, and also the relation between non-zero elements.

1.7 Optical Properties of BSO

Photorefractive BSO belongs to the sillenite class of crystals and is an electrooptic and photoconductive material of the cubic system. The crystal is strongly optically active, ($\rho_o = 45°\ mm^{-1}$ at $\lambda = 514.5$ nm) and different polarization states are typically observed for the incident beam, diffracted beam and scattered light [1.12]. Due to this property, coherently scattered noise can be suppressed by a properly oriented analyzer at the output image plane which improves the signal to noise ratio.

It has been observed that the photorefractive sensitivity of BSO crystals can be increased by up to 16 fold for long wavelengths (633 nm). This is achieved by heating the BSO crystal up to 300° C and it is thought that this effect is due to the temperature dependence of the photoionization cross section in BSO. The electron recombination time is independent of wavelength in the spectral region 633 to 456 nm which leaves the photoionization cross section as the parameter that introduces the temperature dependence of the photorefractive sensitivity [1.13].

Photo and dark conductivities are n and p type respectively. The small dark conductivity is equivalent to long storage times, useful for many applications. The trap number density responsible for saturation effects is typically $10^{16}\ cm^{-3}$. Other relevant material parameters for BSO are background refractive index, n = 2.54, dielectric constant $\epsilon = 56$, electrooptic coefficient $r_{41} = 5$ pm/V, donor number

density N = 10^{19} cm^{-3}, recombination coefficient γ_r = 2 x 10^{-11} cm^3/s and mobility μ = 0.03 cm^2/Vs [1.9].

BSO crystals are commonly used in two different crystallographic orientations for optical data processing applications, as shown in Figure 1.6 [1.7, 1.14]. The first configuration is suitable for coupling or energy exchange and therefore mainly used for two wave mixing arrangements. An electric field (photoinduced or applied), along the <001> direction induces in the x direction a change in refractive index

$$\Delta n_x = \frac{1}{2} n_o^3 r_{41} E_{sc} \qquad (1.19)$$

Therefore when the readout beam is vertically polarized along the x-direction, maximum diffraction efficiency is obtained with a diffracted beam also with the same polarization (ignoring optical activity). In the second configuration, when the electric field is applied along the <110> direction two new principle electrooptic axes are induced with refractive index modulation given by

$$\Delta n_{x'} = \frac{1}{2} n_o^3 r_{41} E_{sc} \qquad (1.20)$$

$$\Delta n_{y'} = -\frac{1}{2} n_o^3 r_{41} E_{sc} \qquad (1.21)$$

When reading a grating in this configuration with a vertical beam polarization, the diffracted beam is rotated through 90°. In this configuration the total index modulation seen by the reading beam is

$$\Delta n = n_o^3 r_{41} E_{sc} \qquad (1.22)$$

Therefore the diffraction efficiency is 4 times higher than in the other configuration.

1.8 Photorefractive Properties of $BaTiO_3$

$BaTiO_3$ is one of the first ferroelectric materials to be discovered and recognized as photorefractive. The photorefractive effect was first observed and reported by Townsend and laMacchia in 1970 [1.15]. However during the seventies, the photorefractive effect received little attention, and no significant applications

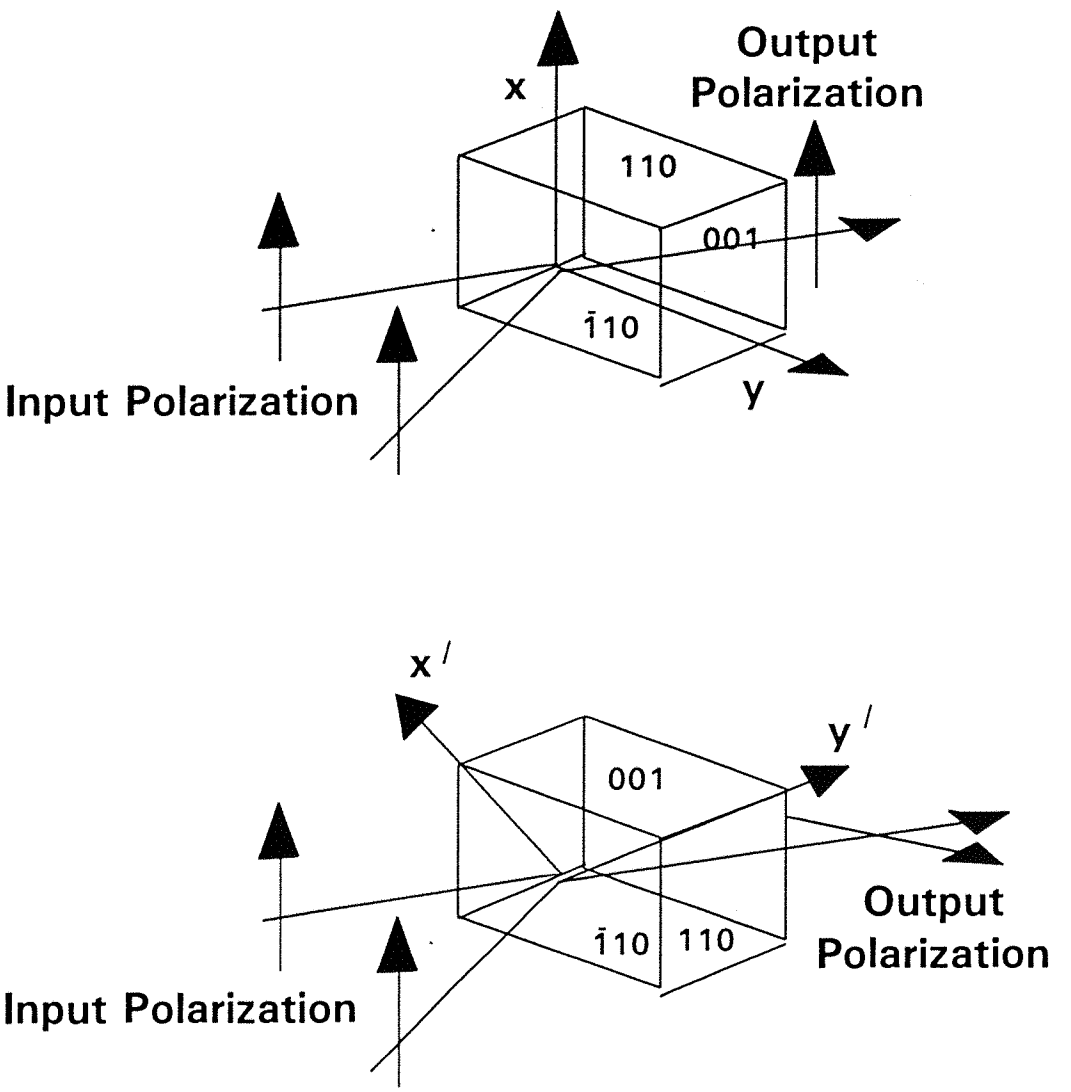

Figure 1.6 Shows two commonly used crystallographic orientations for optical data processing applications to optimize (a) energy transfer and (b) diffraction efficiency.

emerged. In 1980 Feinberg et al [1.16], started work on $BaTiO_3$ since at this time considerable progress has been achieved toward the better understanding of the important properties of this material. The particular advantage of $BaTiO_3$ is its large value of electrooptic coefficient which leads to its ready application in two beam coupling gain, and four wave mixing experiments.

At room temperature, the stable crystal structure of $BaTiO_3$ is tetragonal, however at $\approx 9^{\circ}$ C a transition to an orthorhombic phase occurs [1.17]. At this stage cracking may develop if the crystal is cooled too fast through this phase transition. In the tetragonal phase two types of domains exist. One of the class of domains has its spontaneous polarization at 90°, while the other domains are antiparallel (180°). In a multidomain crystal effects such as electrooptic behaviour are averaged out to zero. Therefore to achieve significant electrooptic effect the crystal must be made single domain via mechanical or electrical poling procedures.

Photorefractive effects in $BaTiO_3$ may be due to two types of defects in the crystal structure, namely vacancies and impurities. Impurities, which will always occur, are in the range of 10-100 ppm. The three major groups of impurities which exist in $BaTiO_3$ are; (i) Calcium and Strontium, (ii) Aluminium and Silicon, (iii) transition metals. Calcium and Strontium belong to the same family of the periodic table as Barium and always occur with Barium in nature. It is difficult to separate them from Ba and are also isovalent with it, therefore do not participate in the photorefractive effect.

1.9 Two Beam Coupling and Beam Fanning

The interference pattern of two beams in a photorefractive crystal results in a recording of a real time volume phase grating as shown in Figure 1.7. The index grating is spatially phase shifted with respect to the intensity interference pattern by ϕ. Materials in which the transport mechanism is diffusion dominated have $\phi = 90^{\circ}$. The diffracted portion of beam R i.e., R/ and S will interfere constructively due to 0° relative phase. Similarly S/ and R interfere destructively because of the 180° relative phase shift between the two. Two beam coupling in photorefractive media is used therefore to achieve optical signal amplification and a range of other signal

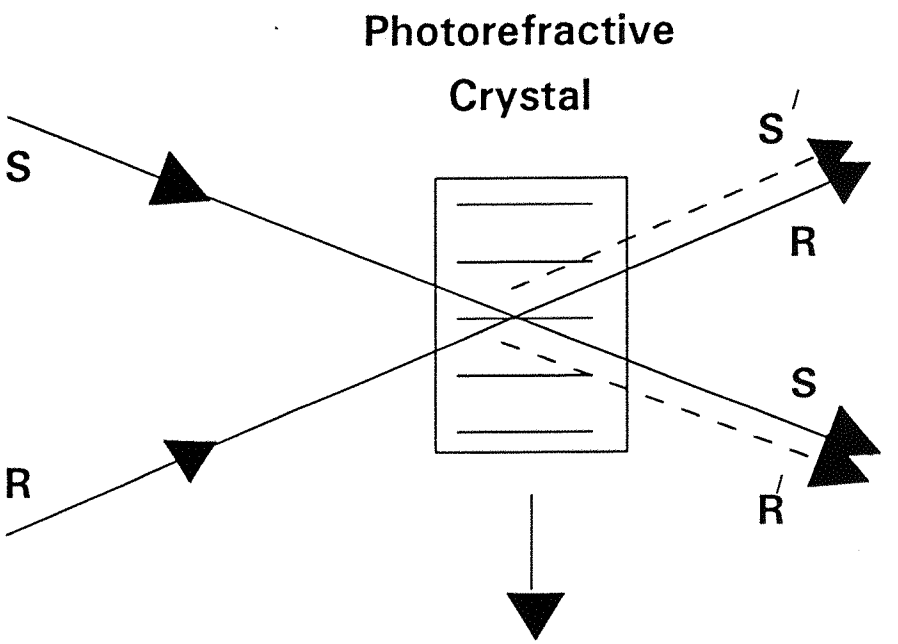

Figure 1.7 Shows the recording of photorefractive grating via two wave mixing.

processing applications which will be discussed in subsequent chapters.

When a beam of light passes through a photorefractive medium such as a $BaTiO_3$ crystal, beam fanning or asymmetric light scattering takes place. Beam fanning is described as the selective amplification of scattered light in a photorefractive crystal. Beam fanning was first observed by Feinberg [1.18], who proposed a self-defocusing model for the effect in which the Gaussian shape of the beam causes the fanning. However an alternative and more realistic approach is that the beam fanning originates from the light scattered from defect sites in the crystal, which then experiences amplification by the two beam coupling process. Figure 1.8 illustrates the beam fanning mechanism where the dark circles represent defect centres which scatter the input beam. Preferential amplification of the scattered light in the direction of the $+c$ axis occurs, while light scattered in the opposite direction will be deamplified. The two beam coupling gain of the scattered light will depend on the exact angle between various scattered light components and the input beam, which passes straight through the crystal without undergoing scattering. The net consequence is a sequential scattering, or **fanning**, which causes a progressive bending of the path of the incident light.

The process of beam fanning has been used in a number of applications such as optical limiting in which the incident light beam undergoes fanning, leaving a small proportion of incident light to be transmitted [1.19]. Other applications of fanning only include self-pumped phase conjugators via external mirrors [1.7] as well as the cat PCM [1.20]. However beam fanning also poses problems, especially under conditions of high gain, when noise will also experience equally high gain, and a degraded image may result.

This problem has been addressed via rotating the crystal at a speed which (ideally) will wash out the noise gratings [1.21]. This phenomenon is based on a slower build up time constant for the noise gratings, relative to any injected signal grating.

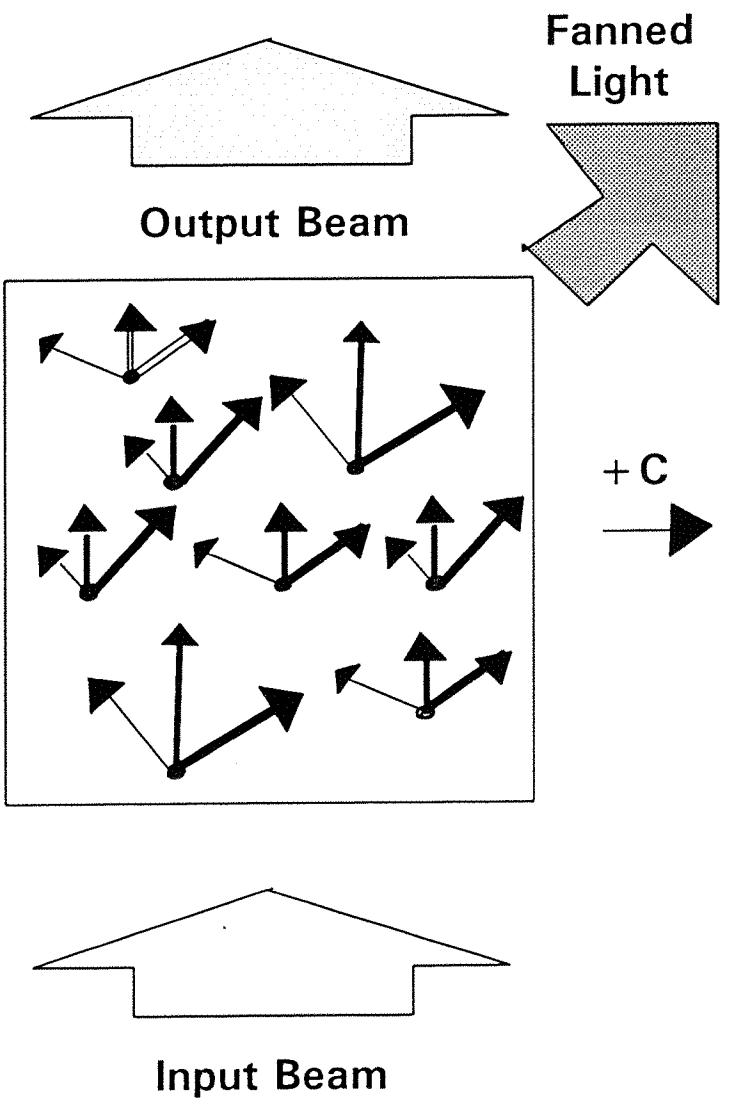

Figure 1.8 Shows beam fanning mechanism from defect centres which scatter the input beam.

1.10 Self Pumped Phase Conjugate Mirror

Photorefrative materials provide the possibility of recording and readout of a real time hologram which leads to a phase conjugate replica of, for example, a complicated image bearing beam. In a PCM, alignment of the pump beams as well as their relative intensities play a crucial role in the fidelity of the phase conjugate replica.

There is another way to achieve phase conjugate imaging, known as self-pumped phase conjugation [1.20]. In a self-pumped PCM the pump waves are generated from the incident beam itself. As described above, this occurs when an incident e-polarized beam enters the crystal and undergoes self-defocussing, or fanning in the plane formed by the incident beam and the crystal c-axis, creating a fan of light that will illuminate the back faces of the crystal. The edge, as illustrated in Figure 1.9, acts as a two dimensional corner-cube reflector and by two internal reflections, directs the fan of light back toward the incident beam.

In practice, due to complicated and not well understood processes, the fan of light self-concentrates into several narrow beams, each of which contains counter propagating beams. Each pair of counter propagating beams may interfere with the incident beam, to create a phase conjugate signal beam. These self-generated pump waves may be of arbitrarily complex configurations inside the crystal, but always self-optimize, to produce a high quality phase conjugate output. Therefore SPPC in $BaTiO_3$ requires only one beam to generate its own phase conjugate replica, and is an experimentally easy, and versatile technique that is often used.

1.11 Wave Mixing and its applications for Image Processing

Degenerate four wave mixing (DFWM), is one of the basic schemes used with photorefractive materials for optical signal processing. This scheme unlike conventional holography which is performed in two sequential stages of recording and then reading as shown in Figure 1.10 (a) and (b), consists of simultaneous interaction of all three input beams in the photorefractive material as shown in Figure 1.10 (c), (d). Figure 1.10 (c) and (d) shows hologram recording and readout in transmission and reflection geometries respectively. The effect of the nonlinear

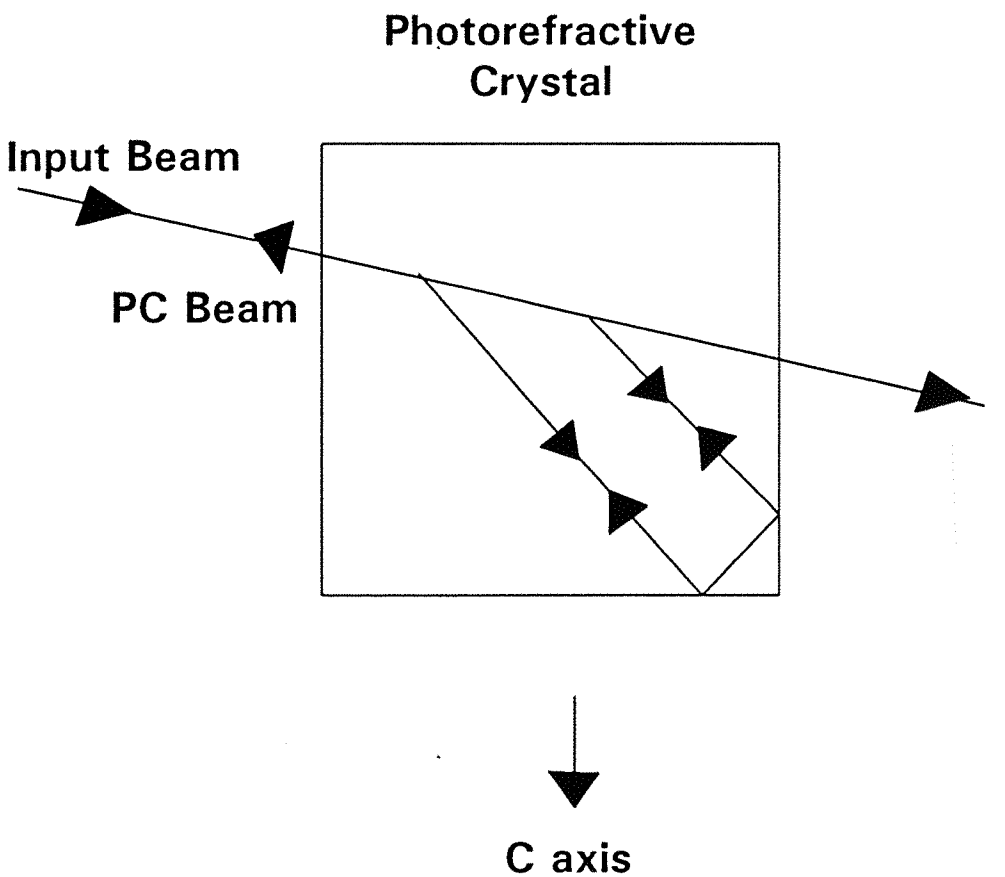

Figure 1.9 Shows a self-pumped phase conjugate mirror geometry.

interaction gives rise to an output E_4 which is proportional to the amplitude phase conjugate of the original input field E_1 and can be expressed as

$$E_4 \propto E_1^* E_2 E_3 \tag{1.23}$$

Where * represents complex conjugation. When an input beam passes through a phase aberrator, before it interferes with the reference beam inside the crystal, phase distortions are introduced. The phase conjugate output however will have inverted, or conjugated phase fronts which propagate counter to those of the input direction, and therefore all these undesirable phase distortions will be cancelled out after the second return pass.

By introducing a lens arrangement, Fourier transformation of an input object can be easily achieved inside the photorefractive crystal [see Appendix A], to interact with the reference beam. By adjusting the intensity of the interfering beams a number of spatial filtering operations can be performed.

DFWM in photorefractive crystals is also used to achieve a range of interesting applications for image processing, and may roughly be divided into two types of operations, namely linear and nonlinear. In the linear regime, the intensity of the pump beams is much higher than that of the object beam. However in the nonlinear regime the object beam intensity is higher than that of the pump beams. In the linear regime, operations of convolution and correlation have been realized by taking into account the field multiplicative property of DFWM, which provide a flexible method of real time parallel processing for such operations as shown in Figure 1.11 [1.22,1.23]. Similarly operation of matrix multiplication has been reported using DFWM [1.24].

The operation of edge enhancement is the result of the larger intensity of the image bearing beam when compared to the lower intensities of the reference and readout beams. In this case, both the weaker and the higher intensity parts of the image are ineffective in writing a high efficiency grating. However, at places such as an intensity edge, the intensities of the image and the reference beams are equal, and hence the most efficient grating is recorded here, and therefore an edge enhanced image is achieved at the output [1.25]. Similarly in the Fourier transform

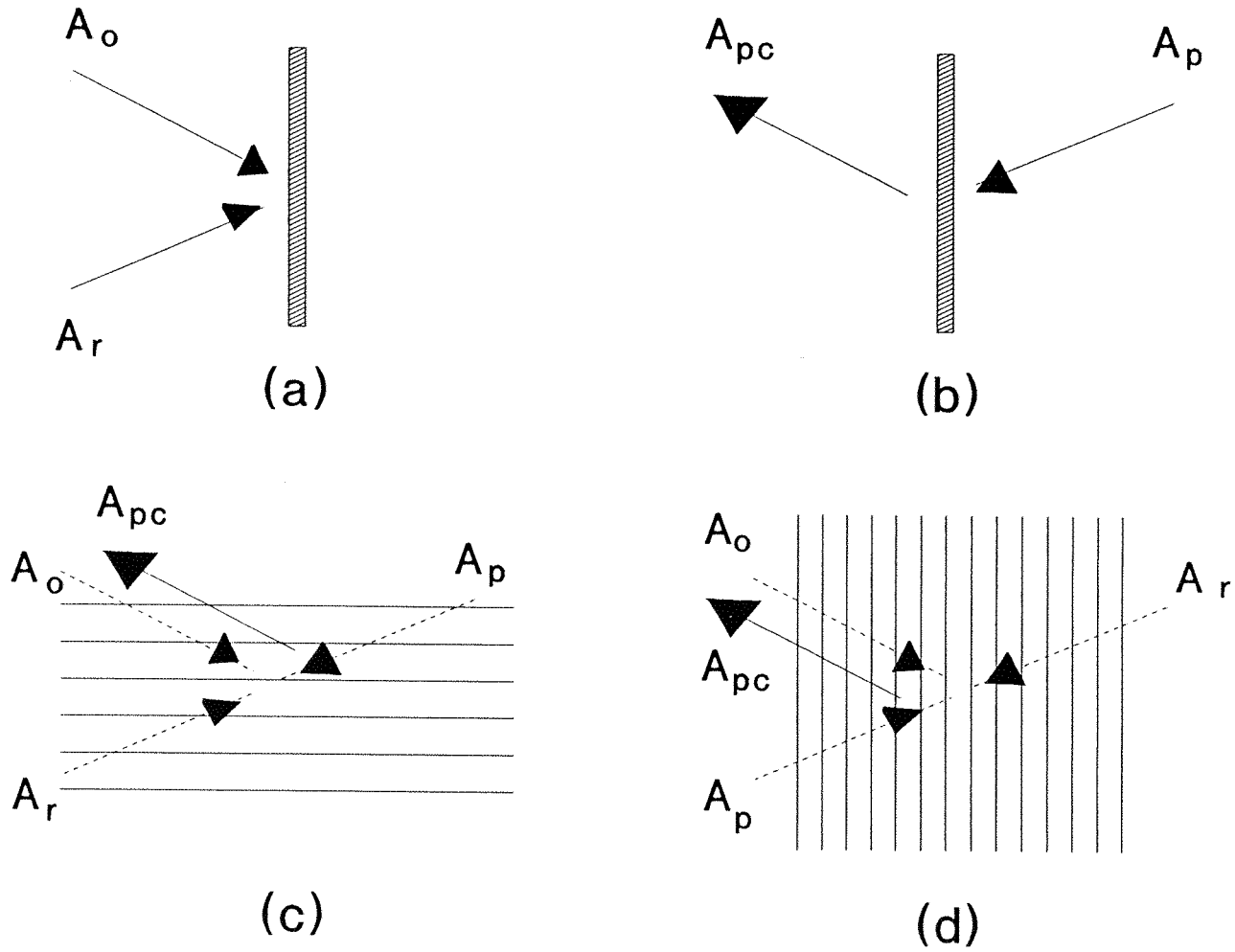

Figure 1.10 Shows hologram recording and readout via conventional and real time holography.

regime, lower intensity higher orders record higher efficiency gratings while higher intensity lower orders record gratings having lower diffraction efficiency gratings [1.26]. The same principle has been used to enhance defect structures in periodic objects. These defects correspond to the low intensity continuous orders in the Fourier plane, against the background of separate periodic orders from the periodic object. Therefore gratings that corresponds to defects give maximum diffraction efficiency [1.27]. However the operation of edge enhancement can also be achieved via erasing of some of the lower orders by an additional erasing beam [1.28].

The time reversal property of PCM in photorefractive crystals, combined with angular multiplexing of several holograms [1.29], makes it possible to construct a phase conjugate interferometer with a single crystal of BSO or $BaTiO_3$ as shown in Figure 1.12. The practical importance of phase conjugate Michelson interferometers (PCMI), is that the two outputs are replicas of the input across the entire wavefront and their subtraction can be achieved at the output of the beam-splitter BS without any fringes or any particular alignment problems which are common limitations in conventional Michelson interferometers. Operations of subtraction , addition, and a set of logic operations have been demonstrated using this technique [1.30-1.32]. Additionally using the differential response time of multiplexed holograms in these materials in a PCMI configuration, operations of optical novelty filtering and motion detection have been demonstrated [1.33, 1.34] and will be discussed in Chapter 5.

Optical subtraction has also been achieved using complementary gratings in a four wave mixing configuration (FWM), where the required phase shift of 180° between the two images is achieved via introducing such a phase difference in the reference beam to record the complementary gratings. When such gratings are read, subtraction is achieved at the output [1.35, 1.36]. Image addition and subtraction has been demonstrated via complementary gratings in a BSO crystal in which one of the gratings is a permanent one while the other is recorded in real time [1.37]. Using this principle of complementary gratings we have demonstrated velocity filtering operations in moving objects [1.38], and this will be discussed in Chapter 6

Finally two-wave mixing also leads to a range of interesting applications in the field of image processing. Due to the large gain in photorefractive

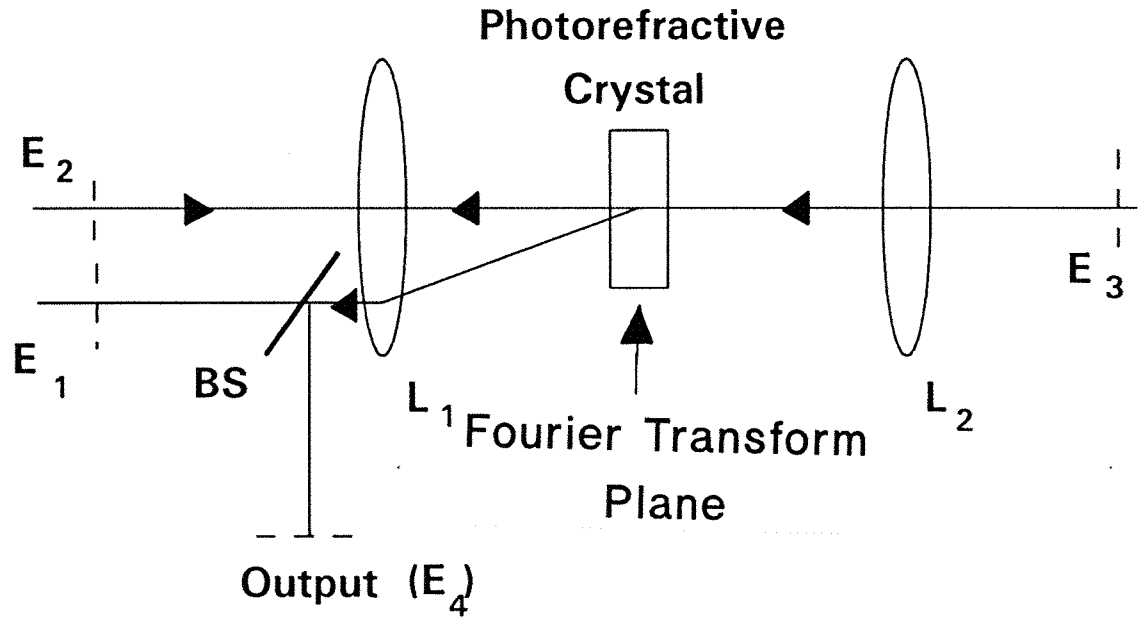

Figure 1.11 Schematic shows the four wave mixing geometry in a photorefractive material for convolution and correlation.

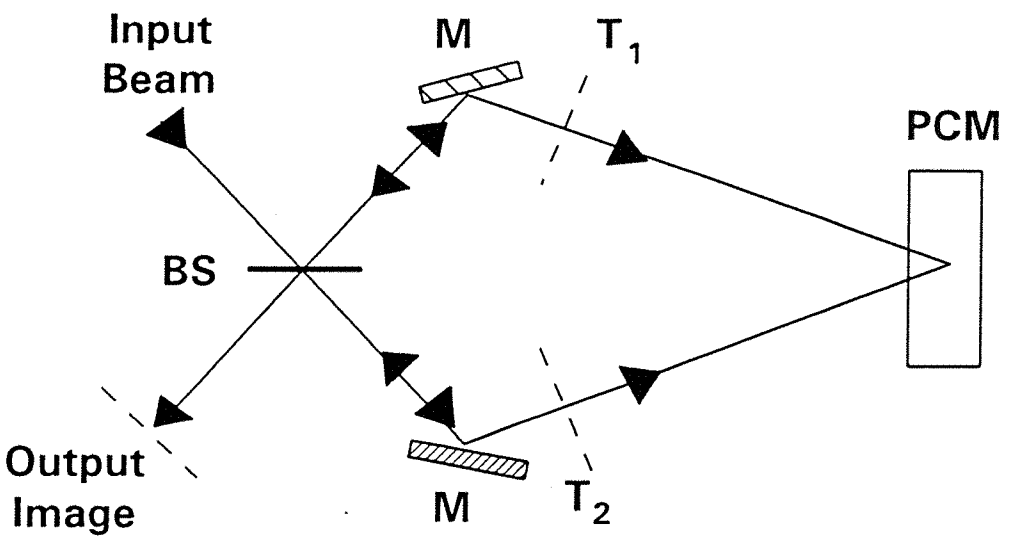

Figure 1.12 Real time image subtraction arrangement using phase conjugate Michelson interferometer.

crystals, it is possible to amplify a low intensity signal beam containing spatial information. The arrangement for two beam mixing is shown in the schematic diagram of Figure 1.7, and is typically used for amplification in $BaTiO_3$ in the diffusion regime [1.39-1.41]. However this is not the case with materials such as BSO (or BGO) which leads to very low beam coupling due to the low steady state index modulation via diffusion. To achieve significant gain a phase shift of 90° under drift conditions is required and this can be achieved by moving the interference fringes at an optimum speed. Image amplification has been achieved via this technique in BSO [1.42].

Two beam coupling has also been used for spatial filtering operations to amplify certain Fourier orders, for contrast manipulation in $BaTiO_3$ [1.43], and is discussed in Chapter 3. A selective amplification of certain Fourier orders has also been demonstrated via recording the hologram for particular orders only and leaving others as they are [1.44]. The other useful applications of two beam coupling (TBC) lie in the field of motion detection where the response time of the two wave mixing process in photorefractive materials is used to detect moving features in the object plane [1.45-1.48].

Optical phase conjugation between two mutually incoherent beams has also been realized via a range of geometries for the incident beams [1.49-1.53]. This technique will be further reviewed in Chapter 8, and has been used to achieve image subtraction and similar other operations.

REFERENCES

1.1 D. M. Pepper, "Applications of optical phase conjugation", Sci. Am., **254**, 56 (1986).

1.2 D. M. Pepper, "Nonlinear optical phase conjugation", Opt. Eng. **21**, 156 (1982).

1.3 A. Yariv, "Phase conjugate optics and real-time holography", IEEE J. Quant. Elect. **QE-14**, 650 (1978).

1.4 A. Yariv, "Optical Electronics", **3rd ed**, Holt-Saunders International Edition, Japan (1985).

1.5 J. O. White, A. Yariv, "Spatial information processing and distortion correction via four-wave mixing", Opt. Eng. **21**, 224, (1982).

1.6 C. R. Giuliano, "Applications of optical phase conjugation", Phys. Today, 27, April 1981.

1.7 P. Gunter, J. P. Huignard (Eds.), Topics in Applied Physics Vol 61, "Photorefractive Materials and Their Applications II", Springer-Verlag, Berlin (1989).

1.8 M. D. Levinson, K. M. Johnson, V. C. Hanchett and K. Chiang, "Projection photolithography by wave-front conjugation", J. Opt. Soc. Am. **71**, 737, (1981).

1.9 G. C. Valley, M. B. Klein, "Optimal properties of photorefractive materials for optical data processing", Opt. Eng., **22**, 704 (1983).

1.10 T. J. Hall, R. Jaura, L. M. Connors and P. D. Foote, "The photorefractive effect - A review", Prog. Quant. Electr.", **10**, 77-146 (1985).

1.11 N. V. Kukhtarev, V. B. Markov, S. G. Odulov, M. S. Soskin and V. L.

Vinetskii, "Holographic storage in Electrooptic crystals. 1. Steady state", Ferroelectrics, **22**, 949-960 (1979).

1.12 J. P. Herriau, J. P. Huignard and P. Aubourg, "Some polarization properties of volume holograms in $Bi_{12}SiO_{20}$ crystal", Appl. Opt. **17**, 1851 (1978).

1.13 M. A. Powell and C. R. Petts, "Temperature enhancement of the photorefractive sensitivity of BSO and BGO", Opt. Lett., **11**, 36 (1986).

1.14 A. Marrakchi and J. P. Huignard, "Diffraction efficiency and energy transfer in two-wave mixing experiments with $Bi_{12}SiO_{20}$ crystals", Appl. Phys. **24**, 131 (1981).

1.15 R. L. Townsend, J. T. LaMacchia, "Optically induced refractive index charges in $BaTiO_3$", J. Appl. Phys. 41, 5188 (1970).

1.16 J. Feinberg, D. Heiman, A. R. Tanguay, Jr. R. W. Hellwarth, "Photorefractive effect and light-induced charge migration in barium titanate", J. Appl. Phys. 51, 1297 (1980).

1.17 M. B. Klein and R. N. Schwartz, "Photorefractive effect in $BaTiO_3$: microscopic origins", J. Opt. Soc. Am. B, **3**, 293 (1986).

1.18 J. Feinberg, "Asymmetric self-defocusing of an optical beam from the photorefractive effect", J. Opt. Soc. Am., **72**, 46 (1982).

1.19 M. Cronin-Golomb, "Optical limiters using photorefractive nonlinearities", J. Appl. Phy., **57**, 4906 (1985).

1.20 J. Feinberg, "Self-pumped, continuous-wave phase conjugator using internal reflection", Opt. Lett. **7**, 486 (1982).

1.21 H. Rajbenbach, A. Delboulbe and J. P. Huignard, "Noise suppression in

photorefractive image amplifiers", Opt. Lett. **14**, 1275 (1989).

1.22 J. O. White and A. Yariv, "Real-time image processing via four-wave mixing in a photorefractive medium", Appl. Phys. Lett. **37**, 5 (1980).

1.23 C. R. Petts, M. W. McCall and L. C. Laycock, "Optical correlation in $Bi_{12}SiO_{20}$ at 632.8 nm", Elect. Lett. **20**, 32 (1984).

1.24 P. Yeh and A. E. T. Chiou, "Optical matrix-vector multiplication through four - wave mixing in photorefractive media", Opt. Lett. **12**, 138 (1987).

1.25 J. P. Huignard and J. P. Herriau, "Real-time coherent object edge reconstruction with $Bi_{12}SiO_{20}$ crystals", Appl. Opt. **17**, 2671 (1978).

1.26 J. Feinberg, "Real-time edge enhancement using the photorefractive effect", Opt. Lett. **5**, 331 (1980).

1.27 E. Ochoa, J. W. Goodman, L. Hesselink, "Real-time enhancement of defects in a periodic mask using photorefractive $Bi_{12}SiO_{20}$", Opt. Lett. **10**, 430 (1985).

1.28 N. A. Vainos and R. W. Eason, "Real time edge enhancement by active spatial filtering via five wave mixing in photorefractive BSO", Opt. Commun. **59**, 167 (1986).

1.29 N. A. Vainos and R. W. Eason, "Spatially multiplexed phase conjugate imaging and processing in photorefractive BSO", Opt. Commun. **62**, 311 (1987).

1.30 S. K. Kwong, G. A. Rakuljic and A. Yariv, "Real time image subtraction and exclusive OR operation using a self-pumped phase conjugate mirror", Appl. Phys. Lett. **48**, 201 (1986).

1.31 A. E. Chiou and P. Yeh, "Parallel image subtraction using a phase-conjugate Michelson interferometer", Opt. lett. **11**, 306 (1986).

1.32 N. A. Vainos, J. A. Khoury and R. W. Eason, "Real-time parallel optical logic in photorefractive bismuth silicon oxide", Opt. Lett. **13**, 503 (1988).

1.33 D. Z. Anderson and D. M. Lininger, "Optical tracking novelty filter", Opt. Lett. **12**, 123 (1987).

1.34 D. T. H. Liu and L. Chen, " Resolution of a target-tracking optical filter", Opt. Eng. **30**, 571 (1991).

1.35 J. P. Huignard, J. P. Herriau and F. Micheron, "Selective erasure and processing in volume holograms superimposed in photosensitive ferroelectrics", Ferroelectrics, **11**, 393 (1976).

1.36 Y. H. Ja, "Real-time image subtraction in Four-wave mixing with photorefractive $Bi_{12}GeO_{20}$ crystal", Opt. Commun. **42**, 377 (1982).

1.37 N. A. Vainos, S. L. Clapham and R. W. Eason, "Applications of multiplexed real time and permanent holographic recording in photorefractive BSO", Appl. Opt. **28**, 4386 (1989).

1.38 G. Hussain and R. W. Eason, "Velocity filtering using complementary gratings in photorefractive BSO", Opt. Commun. **86**, 106 (1991).

1.39 F. Laeri and T. Tschudi, "Coherent CW image amplifier and oscillator using two-wave interaction in a $BaTiO_3$ crystal", Opt. Commun. **47**, 387 (1983).

1.40 D. Rak, I. Ledoux and J. P. Huignard, "Two-wave mixing and energy transfer in $BaTiO_3$ application to laser beamsteering", Opt. Commun. **49**, 302 (1984).

1.41 Y. Fainman, E. Klancnik and S. H. Lee, "Optimal coherent image amplification by two-wave coupling in photorefractive $BaTiO_3$", Opt. Eng. **25**, 228 (1986).

1.42 J. P. Huignard, H. Rajbenbach, P. Refregier and L. Solymar, "Wave mixing in photorefractive bismuth silicon oxide crystals and its applications", Opt. Eng. **24**, 586 (1985).

1.43 J. A. Khoury, G. Hussain and R. W. Eason, "Contrast manipulation and controllable spatial filtering via photorefractive two-beam coupling", Opt. Commun. **70**, 272 (1989).

1.44 T. Y. Chang, J. H. Hong and P. Yeh, "Spatial amplification: an image-processing technique using the selective amplification of spatial frequencies", Opt. Lett. **15**, 743 (1990).

1.45 C. Soutar, C. M. Cartwright, W. A. Gillespie and Z. Q. Wang, "Tracking novelty filter using transient enhancement of gratings in photorefractive BSO", Opt. Commun. **86**, 255 (1991).

1.46 N. S. K. Kwong, Y. Tamita and A. Yariv, "Optical tracking filter using transient energy coupling", J. Opt. Soc. Am. B. **5**, 1788 (1988).

1.47 R. S. Cudney, R. M. Pierce and J. Feinberg, "The transient detection microscope", Nature, **332**, 424 (1988).

1.48 M. Cronin-Golumb, A. M. Biernacki, C. Lin and H. Kong, "Photorefractive time differentiation of coherent optical images", Opt. Lett. **12**, 1029 (1987).

1.49 S. Weiss, S. Sternklar and B. Fischer, "Double phase-conjugate mirror: analysis, demonstration and applications", Opt. Lett. **12**, 114 (1987).

1.50 M. D. Ewbank, R. A. Vazquez, R. R. Neurgaonkar, " Mutually pumped phase conjugation in photorefractive Strontium Barium Niobate: theory and experiment", J. Opt. Soc. Am. B, **7**, 2306 (1990).

1.51 M. D. Ewbank, "Mechanism for photorefractive phase conjugation using incoherent beams", Opt. Lett. **13**, 47 (1988).

1.52 D. Wang, Z. Zhang, Y. Zhu, S. Zang and P. Ye, " Observations on the coupling channel of two mutually incoherent beams without internal reflection in $BaTiO_3$", Opt. Commun. **73**, 495 (1989).

1.53 A. M. C. Smout and R. W. Eason, "Analysis of mutually incoherent beam coupling in $BaTiO_3$", Opt. Lett, **12**, 498 (1987).

CHAPTER 2

CONTRAST MANIPULATION VIA FOUR AND FIVE WAVE MIXING IN PHOTOREFRACTIVE BSO

2.1 Introduction

When an object is illuminated with a collimated beam of coherent light in the front focal plane of a lens, a Fraunhofer diffraction pattern of the object distribution function is achieved at the back focal plane of the same lens. The Fraunhofer diffraction pattern is actually the Fourier transform of the object light distribution. By taking the inverse transform of this Fourier transform, by placing another lens at a distance of one focal length, an image of this object can be achieved at the back focal plane of the second lens. The process of Fourier transformation of a two dimensional light distribution is one of the most important aspects of coherent optical processing. The optical Fourier transform can be manipulated simply by placing apertures, masks or optical filters in the Fourier transform plane, which may lead to operations such as contrast manipulation of the output image. Such a process of manipulation of the spatial frequency spectrum of the object is known as spatial filtering. The optical Fourier transform performs the data compression and classification of the different features of the object distribution in the form of spatial frequencies and their relative orientation. Therefore a single point in the Fourier transform plane may contain a global description of the object plane. Similarly a set of spatial frequencies in the Fourier plane may describe a group of features in the object plane.

So far various techniques of spatial filtering have been used to manipulate the optical Fourier transform of the input object using spatial filters. We can group such spatial filters into two classes; the first one describes amplitude filters, which multiply the object Fourier transform by a positive real number and therefore can attenuate either completely or partially the desired Fourier orders. The other class of spatial filters are termed complex filters, which are used to multiply the object spectrum by a complex function. Complex spatial filters are used to modify both the amplitude

and the phase of the input transform. This additional flexibility is used for performing convolution and correlation [2.1].

Various techniques of spatial filtering have been demonstrated using amplitude filters in the Fourier plane [2.2, 2.3], where certain of the lower Fourier orders have been stopped to achieve edge enhancement. The operation of contrast enhancement is also achieved using a Fourier transform amplitude filter whose transmission characteristics are varied as an inverse Gaussian function. Lower spatial frequencies therefore are strongly absorbed while higher frequencies are preferentially transmitted and the intermediate frequencies are subject to an inverse Gaussian suppression, leading to an image with contrast enhancement at the output [2.4].

Using such conventional techniques for fabrication of Fourier masks, we can faithfully achieve such spatial filtering operations. However these masks are permanent and cannot be changed in real time, to achieve any variable spatial filtering operations. Therefore when we require different filtering operations on the Fourier transform, we need different masks whose fabrication is a time consuming task. To overcome this problem we need to have some kind of spatial filtering process which can be changed in real time to achieve a range of spatial filtering operations. We present in this chapter such a technique which is based on the photorefractive effect, and uses the DFWM geometry in a BSO crystal.

During the past decade, DFWM has been used as one of the standard configurations for photorefractive materials in optical data processing applications. A number of linear and nonlinear optical image processing operations can be performed by DFWM. The operations that have been performed in the linear regime where the intensity of the pump beams is much higher than that of the object beam, include correlation [2.5], convolution [2.6], and matrix multiplication [2.7]. Operations such as division [2.8], contrast inversion [2.9], edge enhancement [2.10, 2.11], and enhancement of defects in periodic objects [2.12], involve nonlinear behaviour in which the object beam intensity is high compared with the pump beam intensities. So far, edge enhancement has been performed by two different techniques i.e., via degenerate four wave mixing and five wave mixing in photorefractive crystals.

The operation of edge enhancement using DFWM can be explained by considering the diffraction efficiency [2.12] of volume phase holograms as given by the analysis of Kogelnik. The diffraction efficiency of such a hologram depends on the modulation ratio which is itself determined by the object to reference beam intensity ratio. When the object beam intensity is less than that of the reference beam, the diffraction efficiency will be proportional to the object beam intensity. Whereas, when the object beam intensity is higher than that of the reference beam the diffraction efficiency will be inversely proportional to the object beam intensity. Maximum diffraction efficiency is obtained when the intensities of both the beams are the same. In the operation of edge enhancement via DFWM (in one of the techniques) higher spatial frequencies that correspond to sharp features in the object, satisfy this third condition while the lower frequencies are not efficiently conjugated. The second technique of edge enhancement relies on the basic FWM arrangement together with an additional erasing beam that is directed at the DC and low spatial orders [2.13]. A resultant erasure of the DC and adjacent lower frequency components allows the preferential reconstruction of higher orders only, which correspond to the edges. In this chapter we present an experimental investigation of the controlled contrast enhancement operation and contrast inversion of periodic objects. These operations are achieved by using a modified version of the above mentioned techniques of edge enhancement.

2.2 Contrast Enhancement

An object whose contrast is poor due to a high level of background illumination can be represented as

$$f(x,y)=A+g(x,y) \tag{2.1}$$

where **A** is the amplitude of the uniform background illumination and g(x,y) corresponds to the spatial information of the object. Using a simple positive spherical lens to perform Fourier transformation, the intensity distribution of such an object in the Fourier plane can be expressed as

$$F[f(x,y)] = \frac{1}{\lambda f^*}[A\delta(0) + G(\nu_x, \nu_y)] \tag{2.2}$$

Where $G(\nu_x, \nu_y)$ is the Fourier transform of g(x,y), λ is the wavelength of the light used and $\delta(0)$ is a delta function which exists for the DC component only, and f^* is the focal length of the transforming lens. Such an object can be treated classically to improve the contrast by absorbing part of the DC component by putting an obstacle in the Fourier plane [2.14], a technique that has been used also for improving the contrast of phase objects [2.15].

However, this operation can also be performed by five wave mixing in photorefractive crystals as shown in Figure 2.1. The Fourier transform of an object interferes with a reference beam to write a hologram in the photorefractive medium, a BSO crystal in our case. After erasing the DC component of the recorded hologram by a focused beam, it is read by a readout beam, which is counter propagating with respect to the reference beam. The index of modulation during this process is subjected to manipulation and is given by the relation

$$m(\nu_x, \nu_y) = \frac{\frac{2}{\lambda f} R^{\frac{1}{2}} [A\delta(0) + G(\nu_x, \nu_y)]}{RS + 1 + R(\lambda f)^{-2} [A\delta(0) + G(\nu_x, \nu_y)]^2 + E\delta^2(0)} \tag{2.3}$$

$$R = \frac{I_o}{I_r}, S = \frac{I_p}{I_o}, E = \frac{I_e}{I_r}$$

and I_o, I_r, and I_p are the intensities of the object beam and counter propagating beams respectively, while I_e is an erasing beam.

Equation (2.3), expresses the result that the index of modulation can be modified by controlling the parameters R, S, and E above. These parameters therefore, play an important role in manipulating the contrast of an object i.e., increasing the intensity of the object beam or erasing the DC component, results in the reduction of the index of modulation. Contrast enhancement may be performed to an optimum limit by erasing preferentially the background DC component; any further erasure will cause edge enhancement. The amplitude distribution can be reconstructed in the

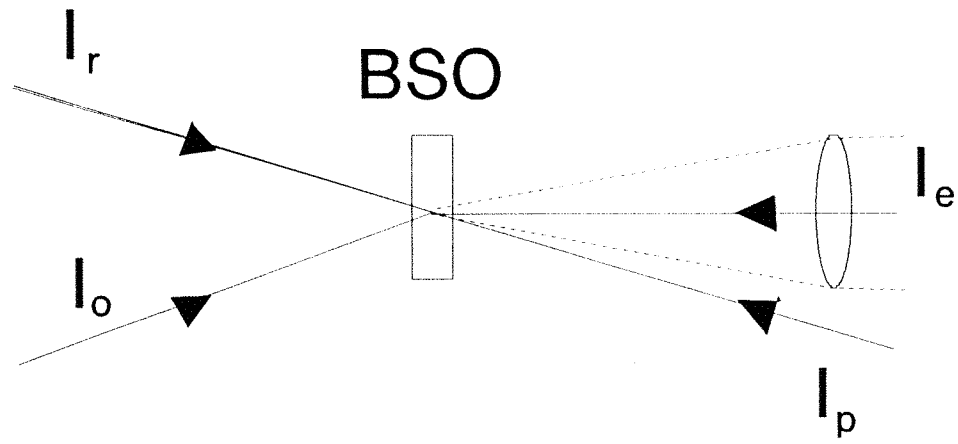

Figure 2.1 Schematic diagram showing arrangement for active spatial filtering.

image plane by the inverse transform of the manipulated Fourier transform of the object. When the intensity ratio between various orders of the object Fourier plane and reference beam is smaller, the reflectivity of these orders will be proportional to their intensities. Therefore an object can be reconstructed faithfully from its Fourier transform hologram by erasing part of the DC order.

Passive contrast enhancement also occurs in the limiting case when E=0 i.e., no erasing beam is present. By changing the parameters R and S, it is possible to control the reflectivity of various components in the Fourier plane to enhance certain features in the object. Assuming the case, for example, of increasing the intensity of the image (I_o), while keeping the intensity of the reference (I_r) and readout (I_p) beams constant, the DC component in the image spectrum will also increase in intensity. A resultant decrease of the index of modulation will occur due to this DC component. Bearing this in mind it can be said that higher orders with lower intensities will be enhanced more than lower orders with higher intensities. This is the case for passive contrast enhancement.

2.3 Contrast Reversal of Periodic Objects

Contrast reversal of images has been performed by a number of techniques such as grating modification [2.16], and negation [2.17], where an image is subtracted from a uniformly illuminated plane wave resulting in inversion of the black and white parts, and division which depends on the diffraction efficiency of four wave mixing in BSO.

Inversion of a periodic object is an important operation in optical image processing. The Fourier transform of such an object consists of discrete spatial frequency components and the distance between them depends inversely on the period of repetition in the periodic object. Contrast reversal of periodic objects has been demonstrated by Kolodziejczyk [2.18] by suppression of the DC component in the Fourier transform plane. It is found that the success of such contrast reversal depends on the ratio of black to white areas and can be expressed by a parameter α which is the ratio of the area of the white part of the unit cell to the total area of the cell. The contrast of such a periodic object can be reversed if the white area in

the object is larger than that of the black area. It is possible to reverse the contrast of a periodic object with a suitable degree of illumination i.e., $\alpha > 1/2$, by focusing an erasing beam on the DC component. Due to the presence of discrete components in the Fourier transform of a periodic object, it is easy to erase the DC component without erasing the lower frequency components. The output will have the intensity distribution

$$I(x',y') = \begin{matrix} (1-\alpha)^2 & \textit{For the white part} \\ \alpha^2 & \textit{For the black part} \end{matrix} \qquad (2.4)$$

In the limiting case when E=0, contrast reversal can still be achieved; when a Fourier transform hologram is written in the crystal, and by adjusting the parameters **R** and **S**, a certain point is reached where the ratio between the intensities of the DC component and interfering reference beam is very large. Under such conditions the DC component will experience reduced reflectivity and reversal of contrast occurs. However the disadvantage of this technique is that the lower frequency components may also have less reflectivity so the quality of inversion may be affected.

2.4 Contrast manipulation via Multiplexed DFWM

The technique described above for passive contrast manipulation has its own drawbacks when applied to contrast enhancement of images. There is an obvious trade off between improving the contrast and reducing the object brightness due to the increasing intensity ratios of the DC component with the corresponding reference beam. When the DC component is reproduced faithfully, higher orders may not have their maximum diffraction efficiencies. However, using an erasing beam for the DC component, contrast enhancement can always be achieved, but still at the cost of overall brightness.

Therefore to improve this situation where both DC and higher orders have their optimum diffraction efficiencies, without suffering erasure or changing the intensity of the object beam (or using a de-focused Fourier transform in the BSO crystal), we propose and demonstrate a new technique. This technique can be implemented for contrast enhancement without erasing any part of the Fourier transform while enhancing the required features to an optimum level by controlling the beam

intensities of the reference beams.

The new scheme relies on two multiplexed DFWM interactions in a single crystal of BSO with a single object beam as shown in Figure 2.2. The object Fourier transform is focused into the crystal and a plane reference beam I_{r1} interferes with it and records a real time hologram, and a counter propagating plane beam I_{p1} reads this grating, as is the case with the previously described technique. Contrast manipulation with this single DFWM has already also been discussed, and demonstrated with its limitations. To overcome these limitations we record another real time grating for the DC order alone. This can be achieved by allowing a focused reference beam to interfere with the DC term only of the Fourier transform. To read this grating a counter propagating focused probe beam is required. For ideal results the reference beam and probe beam should be phase conjugates of each other. The diffraction efficiency of the two gratings can now be adjusted by controlling the indices of modulation in the two individual DFWM interactions and can be expressed via the following equations

$$m(\nu_o,\nu_o)=\frac{\frac{2}{\lambda f}(I_{r2}I_o)^{\frac{1}{2}}A\delta(0)}{I_{p2}+I_{r2}+I_oA\delta(0)} \qquad \textbf{2.5 (a)}$$

for DC order while for higher orders

$$m(\nu_x,\nu_y)=\frac{\frac{2}{\lambda f}(I_{r1}I_o)^{\frac{1}{2}}G(\nu_x,\nu_y)}{I_{p1}+I_{r1}+I_{p2}+I_{r2}+I_oG(\nu_x,\nu_y)} \qquad \textbf{2.5 (b)}$$

From Equations 2.5(a) and 2.5(b) it is clear that the index of modulation can be modified by controlling the intensities of the reference beams, probe beams of the individual DFWM arrangement, and also of the object beam. However we only consider here varying the intensities of the reference beams. Therefore contrast of the input object can be manipulated with greater flexibility as compared to the first technique. The diffraction efficiency of the higher orders can be adjusted independently of the DC component, by controlling the reference and probe beams of $DFWM_1$. As mentioned in [2.12] the maximum diffraction efficiency is achieved when the intensity ratio of signal to reference beam is unity. Therefore we can adjust

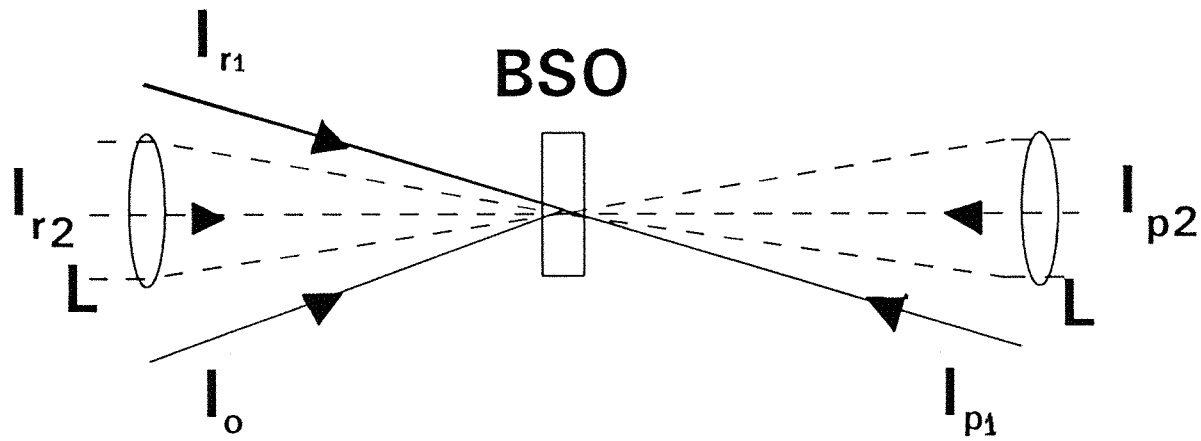

Figure 2.2 Schematic diagram showing the arrangement of multiplexed DFWM for contrast manipulation of images.

the beam intensity ratios of the higher orders to the reference beam without any complication for the diffraction efficiency for the DC in $DFWM_1$. An optimum diffraction efficiency can be achieved therefore for a range of higher orders by adjusting their intensities. This process alone gives rise to edge enhanced images of the input object. Similarly by adjusting the beam intensity ratio of the DC to the reference beam to a desired value in $DFWM_2$ we can achieved the operation of contrast manipulation at the output.

2.5 Experimental and Results

2.5.1 Contrast Enhancement via DFWM

The experimental arrangement for contrast enhancement and contrast inversion described in Sections 2.2 and 2.3 is shown in Figure 2.3. An Argon ion laser operating at 488 nm was spatially filtered and expanded to a diameter of ≈10 mm and divided by a beam splitter BS_1 into two beams. The transmitted beam is subdivided by a second beam splitter BS_2 into a reference beam I_r and a signal beam I_o having intensities of 24 mW and 22 mW respectively. The two beams interfere in the BSO crystal to write a volume phase hologram. To read this hologram, a beam I_p, counter propagating with respect to I_r, is used with an intensity of 15 mW. An erasing beam incident at an angle with respect to I_p, is directed onto the DC order of the Fourier transform inside the crystal and its intensity is controlled by a variable neutral density filter. The angle between the beams I_o and I_r outside the crystal was 30°, and lenses L_1 and L_2 had focal lengths of 100 mm.

It was difficult, but not impossible, to reconstruct a replica of the object from its Fourier transform hologram by erasing the DC component, and we achieved predominantly edge enhanced results. We were forced to change, therefore the corresponding distance between the crystal and lens to 85 mm to de-focus the Fourier transform inside the crystal; the distance between the lens and object was 200 mm. This scheme is shown in Figure 2.4, where the size of the DC component of the image and that of the erasing beam should ideally be the same. In this way the ratio between the DC component and the reference beam can also be reduced and the level of the DC order is controllable in the image. However it is possible to erase

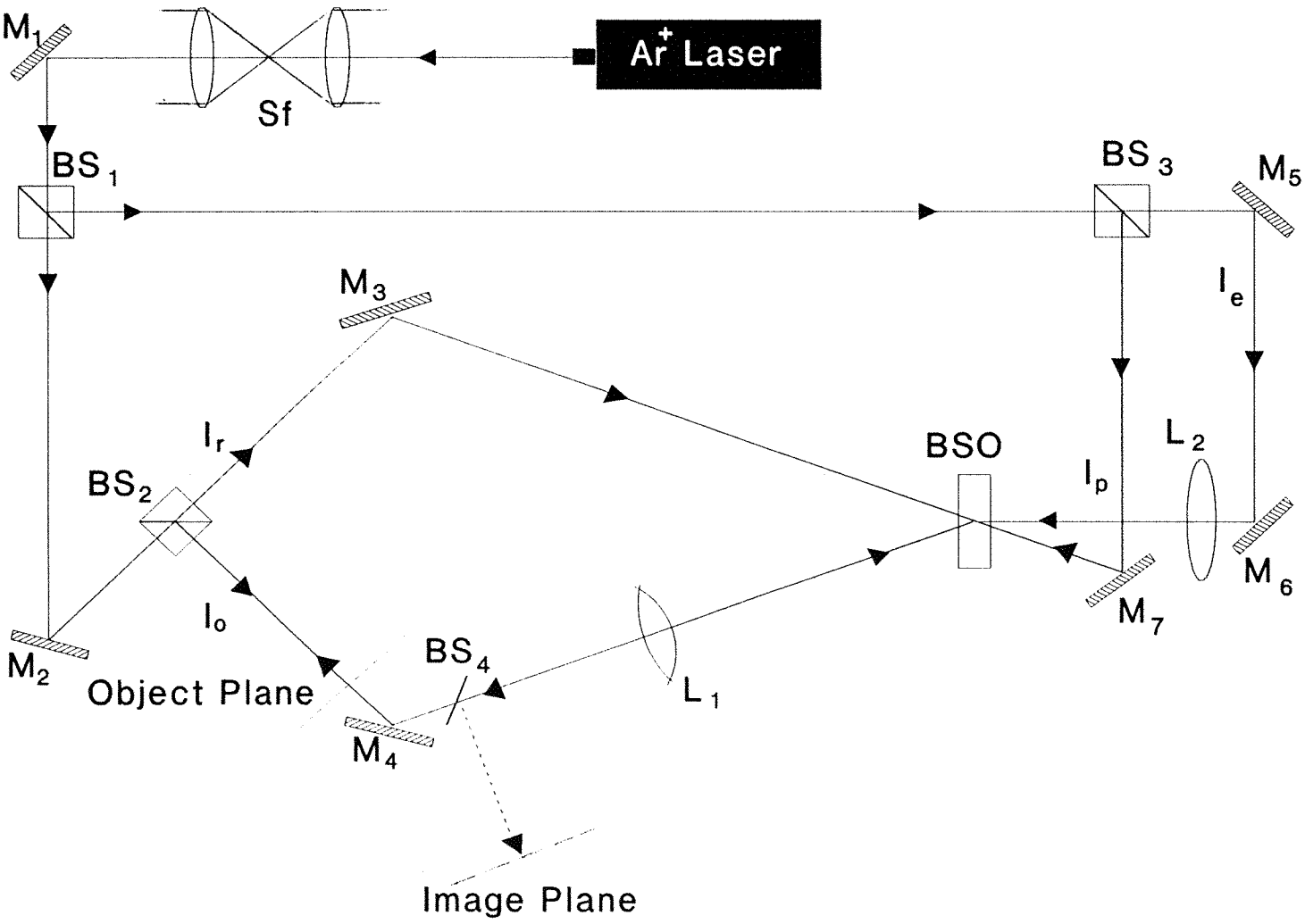

Figure 2.3 The experimental configuration for active spatial filtering via modification of the DC order.

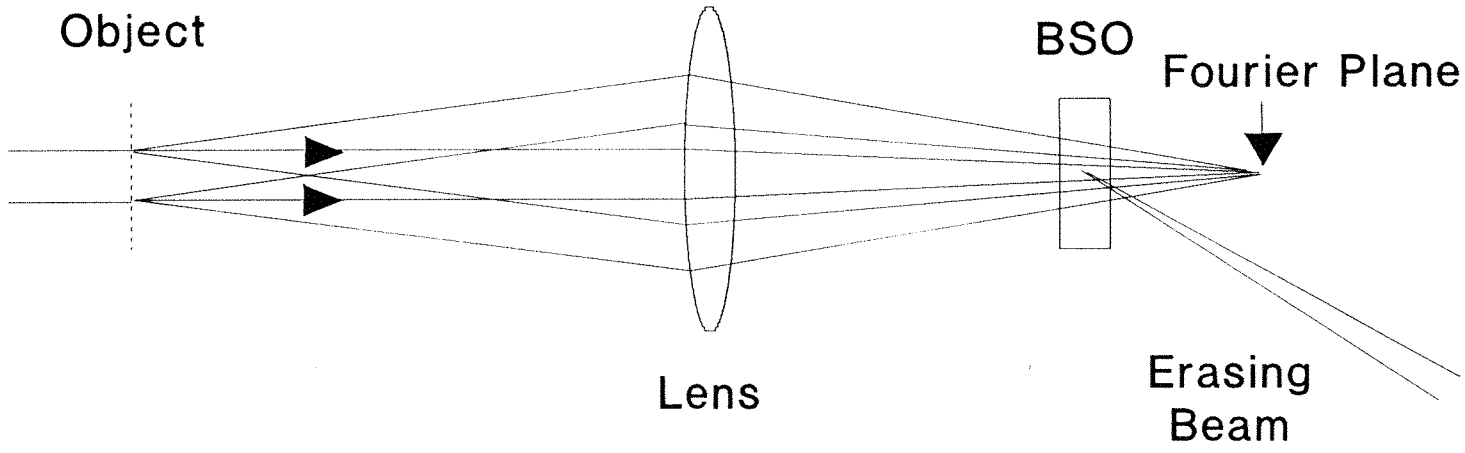

Figure 2.4 Slight de-focusing of the Fourier transform plane from the crystal. The erasing beam is focused to about the same size as the DC order.

adjacent orders unintentionally in the Fourier plane. No voltage is applied across the crystal here which might induce unintentional high band pass filtering [2.19]. Figure 2.5 shows the arrangement in which an object is focused in one direction only.

Figure 2.6 shows the results of contrast enhancement for an object of maximum dimensions of 1 mm and minimum dimensions of 0.1 mm. Figure 2.6 (a) shows the result of reconstruction from direct imaging of the object into the crystal. Figure 2.6 (b) illustrates the result of reconstruction from its quasi-Fourier transform after partial suppression of the DC order. Figure 2.6 (c) and (d) show the results of progressive contrast enhancement via partial erasure of the DC component. It is clear that with the improvement in contrast, edge enhancement effects are less prominent because the object dimensions are smaller. This follows from the fact that the Fourier transform of a smaller object is more widely extended with smaller amplitudes in Fourier space, compared with a large object whose Fourier transform is contracted and has larger amplitude. Therefore suppression of the DC order in the Fourier plane will not introduce appreciable edge enhancement in smaller objects.

Figure 2.7 shows the photographs of an object during different stages of contrast enhancement. Figure 2.7 (a) is the image reconstruction from 1:1 imaging after slight improvement passively. Figure 2.7(b) shows the image reconstructed after slight improvement in the contrast from its quasi-Fourier transform hologram, Figure 2.7 (c) and (d) illustrate the image which results after progressive suppression of the DC component. These results show the apparent increase in the contrast, albeit at the expense of undesirable edge enhancement and a reduction in image brightness.

Figure 2.8 shows contrast manipulation which has occurred in certain parts of the image. The object was focused by a cylindrical lens of focal length 200 mm in the x-direction only, while in the y-direction no focusing occurred as shown in Figure 2.5. The DC order therefore in the focal plane is in the form of a line, part of which is erased by an erasing beam focused by a spherical lens. It is clear that the resolution in the x-direction suffers here. This occurs due to the loss of certain orders due to the small size of crystal and longer focal length of the lens.

Figure 2.9 shows inversion of contrast of a periodic object with $\alpha = 7/8$; the

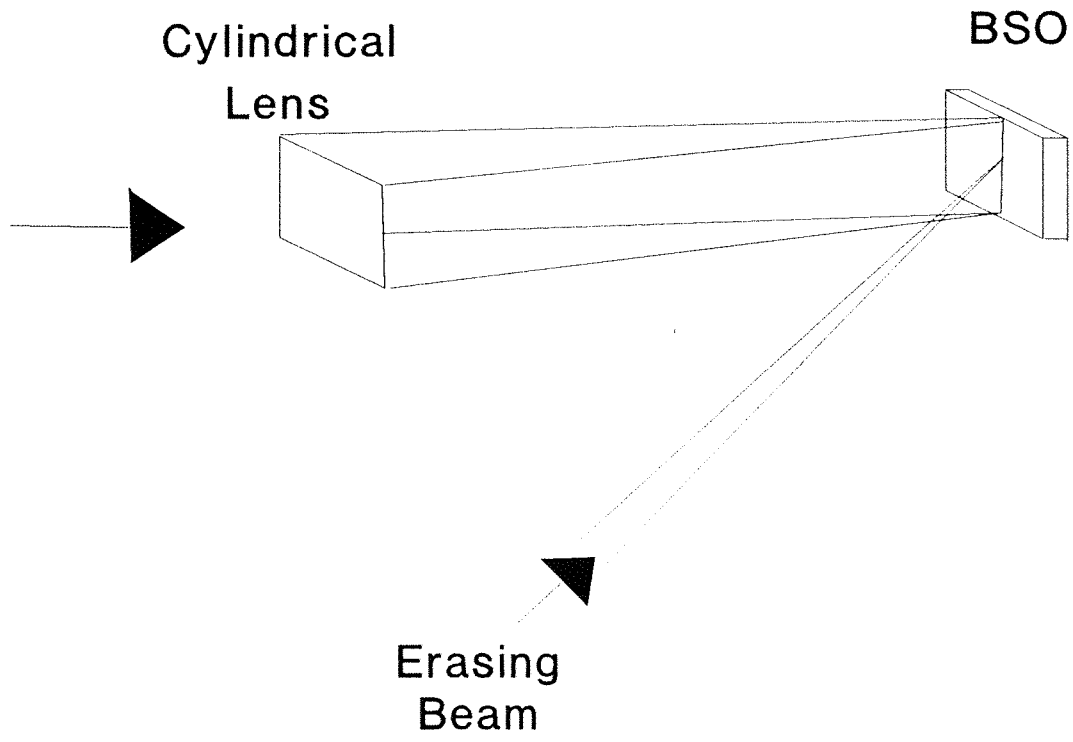

Figure 2.5 An object which is focused in one direction, while no focusing effect occurs in the other direction.

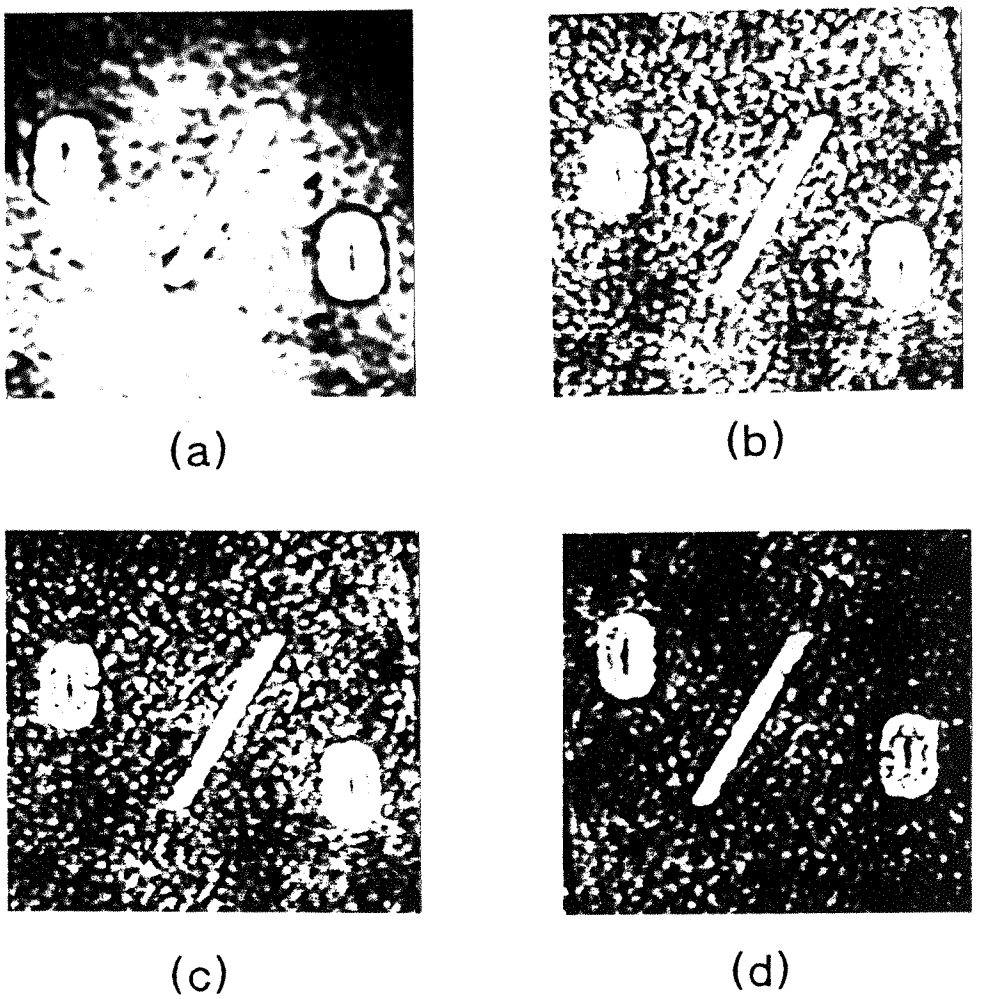

Figure 2.6 An object showing progressive increase in contrast. (a) is reconstructed from the image of the object on the crystal while (b) from its quasi-Fourier transform. (c) and (d) show a progressive suppression of the DC order.

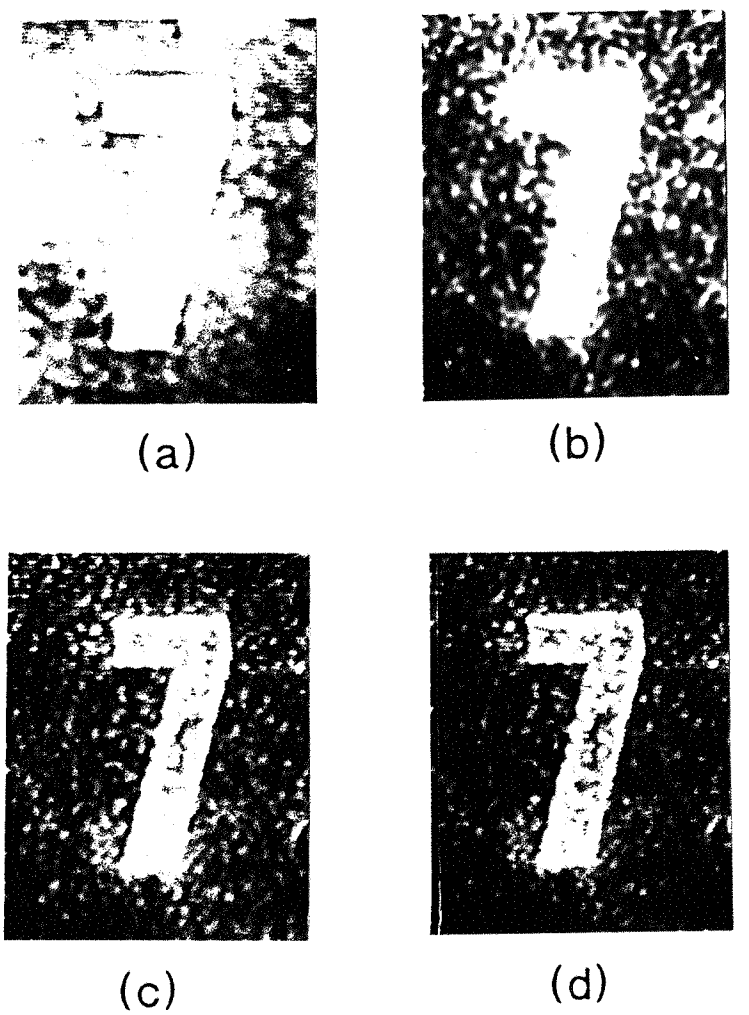

Figure 2.7 An object with relatively larger dimensions than shown in Figure 2.6, during different stages of its contrast enhancement towards progressive suppression of the DC.

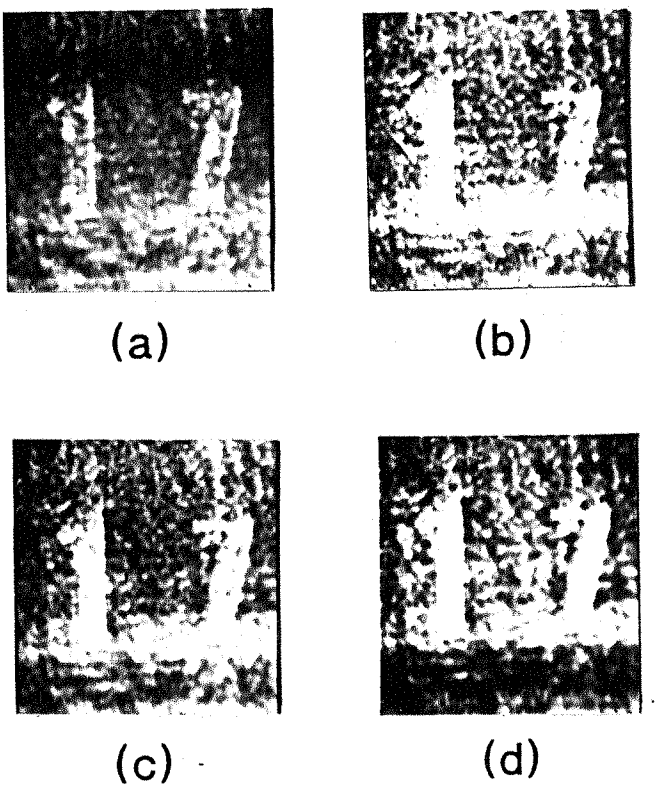

Figure 2.8 Contrast manipulation achieved by using the arrangement shown in Figure 2.5.

object dimensions were 4 mm x 4 mm. Figure 2.9 (a) is the image to be inverted, Figure 2.9 (b) is the inversion of contrast that is achieved by passive suppression of the DC component.

2.5.2 Contrast Manipulation Via Multiplexed DFWM

The experimental arrangement of the multiplexed DFWM used for contrast manipulation is shown in Figure 2.10. An Ar^+ laser was used operating at 514.5 nm. The laser input was spatially filtered, expanded to ≈8 mm diameter and divided by a beam-splitter BS_1 into two beams. Subsequently the transmitted beam is again divided into a reflected (reference) beam I_{r2} and a transmitted beam by a beam-splitter BS_2. BS_3 divides the incoming beams into a reference beam I_{r1} and an object beam I_o. A BSO crystal was used as a phase conjugate mirror. BS_5 divides the incoming beam into two probe beams I_{p1} and I_{p2}. The intensities of reference beams I_{r1} and I_{r2} were 13 mW and 30 mW respectively and intensity of the object beam was 6 mW. However, the intensities of the two reference beams were controlled by the respective neutral density filters. The intensities of the two probe beams I_{p1} and I_{p2} were set at 15 mW and 10 mW respectively and also controlled by neutral density filters. The reference beam I_{r2} and probe beam I_{p2} were focused down into the crystal by lenses L_1 and L_2. The angle between object beam and reference beam I_{r1} was 45° outside the crystal while the angle between the object beam and the second reference beam I_{r2} was 35°.

Figure 2.11 shows the photograph of a resolution test chart which was placed in the object plane. Figure 2.12 shows the experimental results of contrast manipulation obtained by the multiplexed DFWM arrangement. Photograph 2.12 (a) show the contrast manipulation of the resolution test chart, when the plane reference beam I_{r1} was blocked and no grating was recorded for the Fourier transform of the object. However the reference beam I_{r2} was allowed to record the grating for the DC order only, which is then readout to give mainly the background features. Photograph (b) shows the results when both the beams I_{r1} and I_{r2} were allowed to record the Fourier transform for DC and higher orders. Photograph (c) shows the results when the intensities of beams I_{r1} and I_{r2} are adjusted in a way that both DC and higher orders are faithfully diffracted from their corresponding gratings.

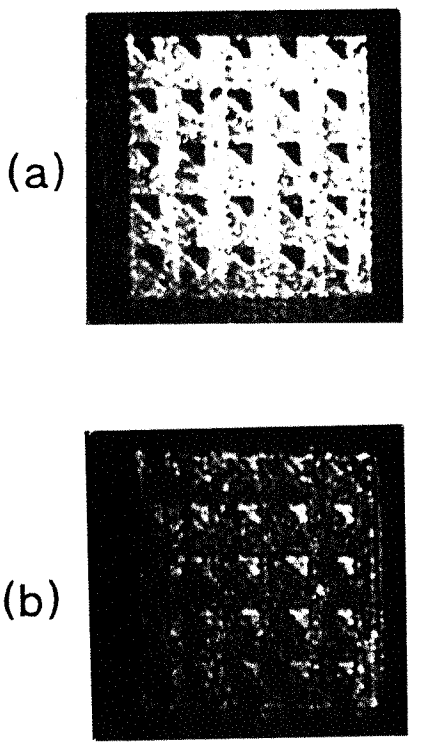

Figure 2.9 Illustration of contrast inversion; original periodic object (a) and its inverted contrast replica (b).

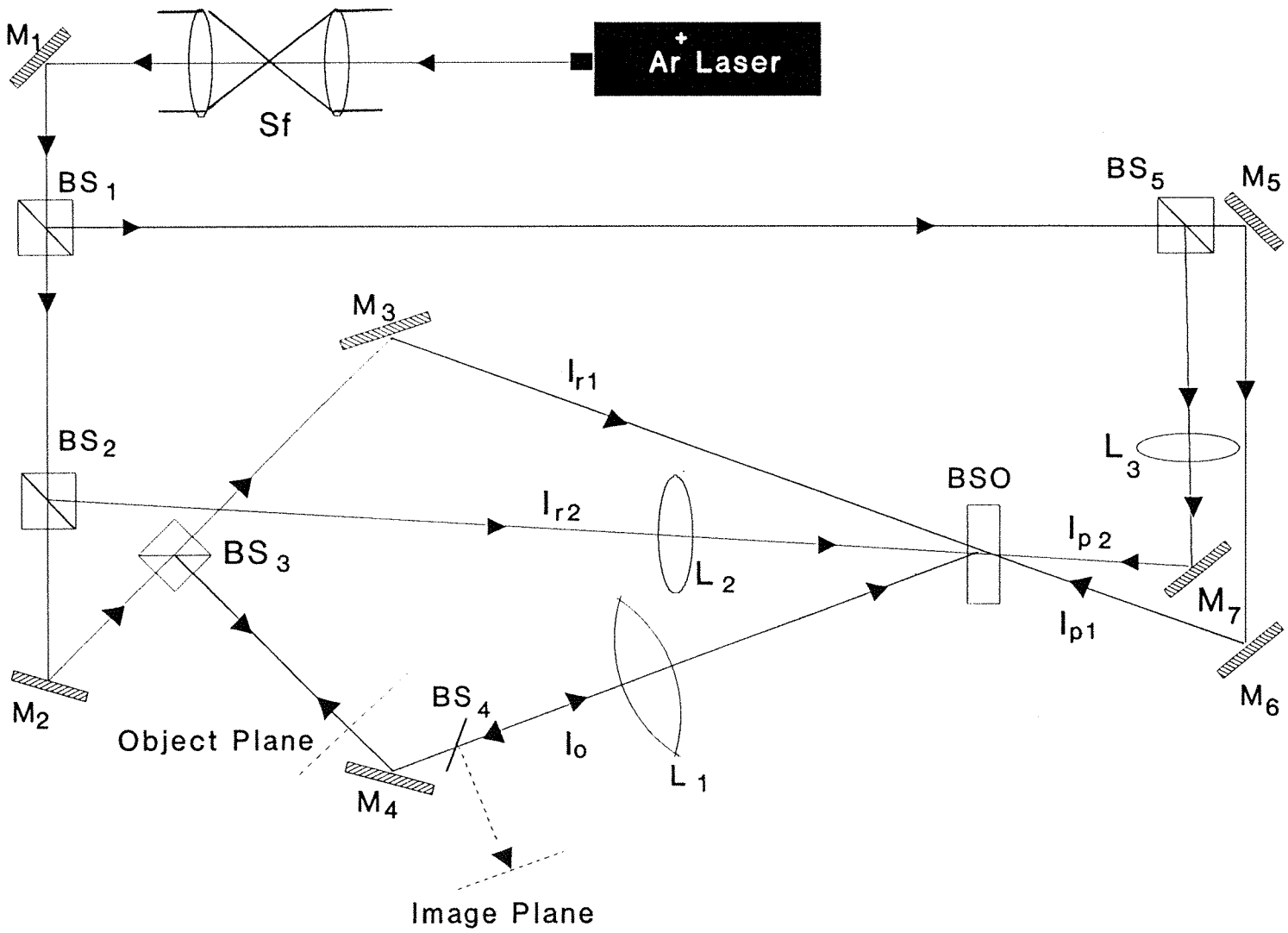

Figure 2.10 Experimental arrangement for contrast manipulation via multiplexed DFWM arrangement.

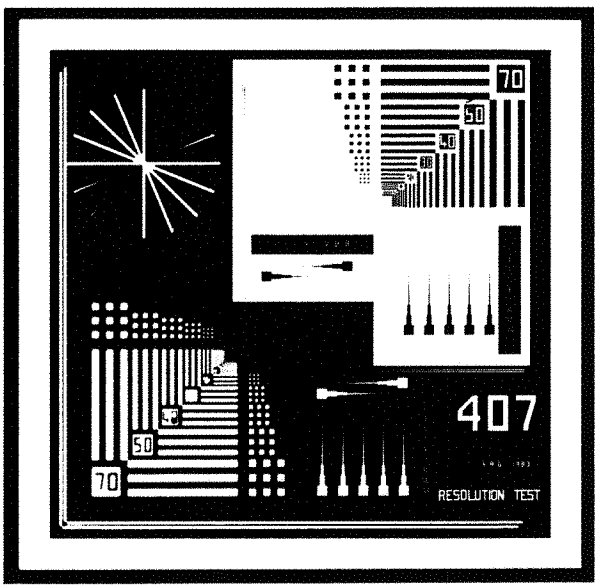

Figure 2.11 Shows an enlarged photograph of a resolution test chart which was placed in the object plane.

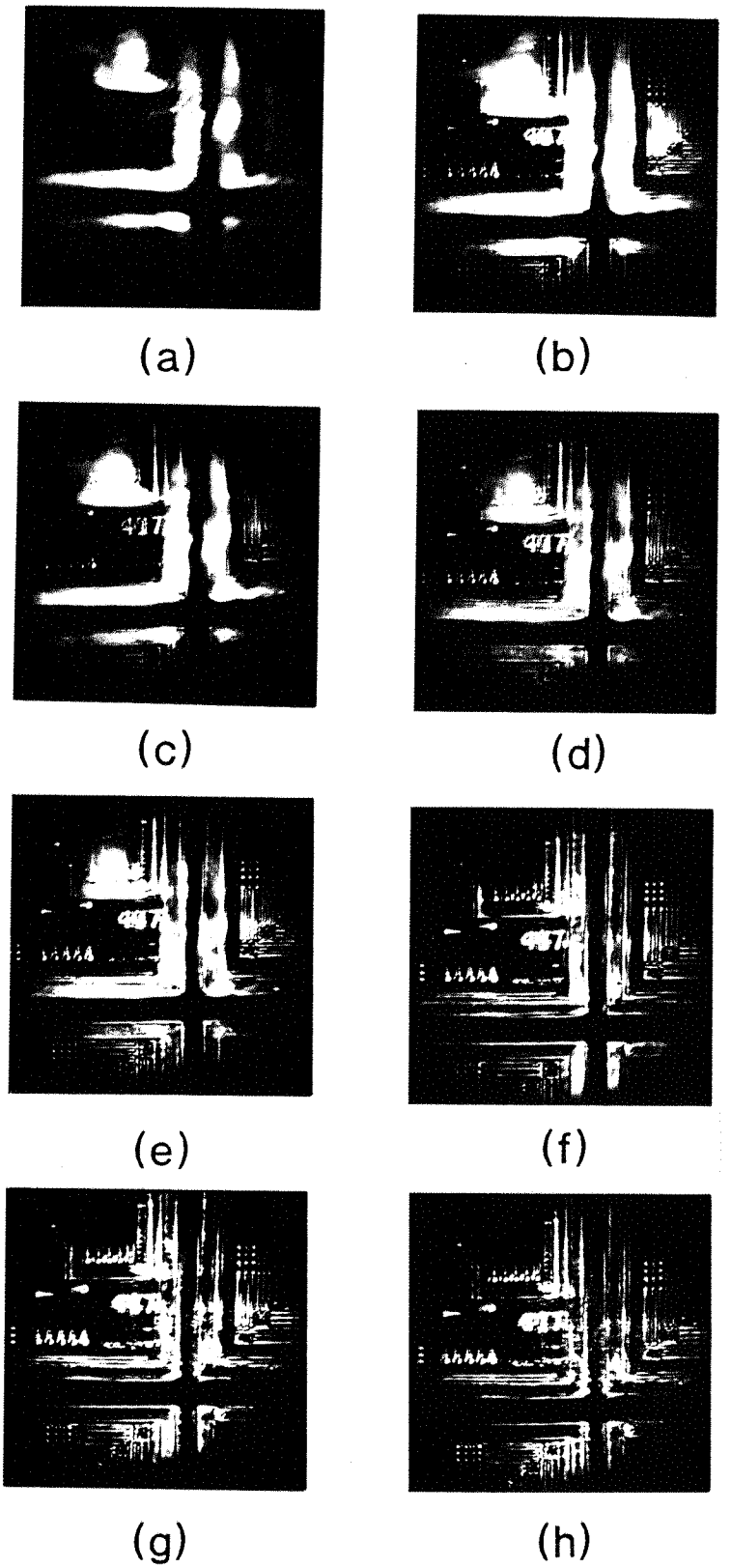

Figure 2.12 A sequence of photographs showing results of contrast manipulation of a binary object.

With further manipulation of the intensities of reference beams I_{r1} and I_{r2} we achieved the results which are shown in photographs (d) and (e). As it is apparent in these photographs the contrast of some of the higher order features is inverted while at the same time the DC is also present for these features. This is because the higher orders were recorded separately than the DC order. Therefore an edge enhanced image is achieved separately from the DC image, which may be a disadvantage of this technique. Photograph (f) shows that the DC output was further reduced via lowering of the intensity of the beam I_{r2}. Photograph (g) and (h) show the results when the intensity of the focused reference beam was reduced further so that almost no DC is recorded, and higher orders are dominant.

The above results show that we can control the level of DC and higher orders of the corresponding gratings by separate recording and readout process. These features of this technique made it possible to achieve an image which is bright, and also contains sharp higher order features. However, due to the separate recording and readout process for higher orders we achieved contrast inversion of some of the higher order features i.e., mainly periodic features.

2.6 Future work

A further technique for tunable contrast enhancement is proposed which relies on two DFWM configuration in a single photorefractive crystal such as BSO. The first DFWM arrangement is used to reconstruct the image which corresponds to higher Fourier orders while the second DFWM is used to reconstruct the DC or background distribution of the object. Figure 2.13, shows a schematic diagram to achieve such an operation of contrast manipulation of objects.

A beam-splitter BS_1 divides the input beam into two. The transmitted beam forms an object beam I_o, while the reflected beam is divided into reference beam I_r and a probe beam I_p. The reflected beam I_r is directed into the BSO crystal while the object beam after traversing through the object (transparency), is Fourier transformed by a lens L_1. A tiny mirror M_{DC} is placed in the zero order to reflect the DC component of the Fourier transform which is then directed towards the BSO crystal while higher orders are allowed to travel direct to the BSO crystal through a

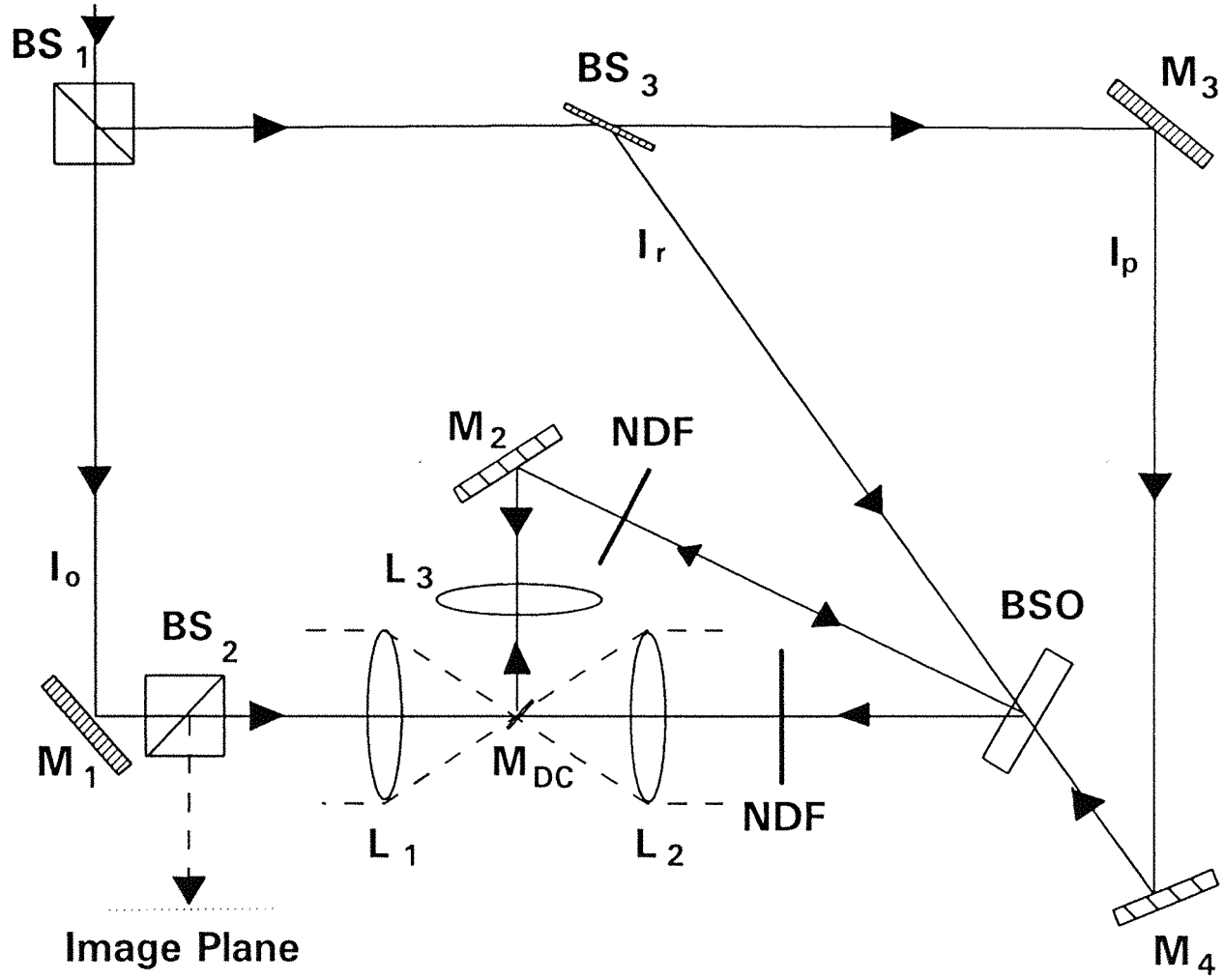

Figure 2.13 Proposed arrangement for tunable contrast manipulation.

lens L_2. A reverse situation can also be achieved where the DC is allowed to pass through a central transparent section of the mirror and higher orders are reflected.

Neutral density filters are placed in the two separate components of the Fourier transform to control their diffraction efficiencies independently. The intensity of the reference beam should be sufficiently higher than the object beam to recover the signal beam faithfully. Using such an arrangement, contrast of an input object can be manipulated by varying the input intensities of the two components of the Fourier transform. Good quality of edge enhancement is also possible by blocking (or reducing) the input DC light to the crystal. It is also possible to enhance preferentially a range of spatial frequencies by changing the beam intensity ratios of the higher orders to reference beam.

2.7 Conclusion

Two techniques of contrast manipulation are demonstrated which exploit the basic configuration of DFWM in a BSO crystal. The first technique is demonstrated via a single DFWM configuration in BSO and uses the diffraction efficiency characteristics of volume phase holograms described by Kogelnik's analysis. The diffraction efficiency of such a hologram depends on the beam intensity ratio of the object to reference beam intensities. We recorded a real time hologram between the reference beam and the Fourier transform of the object. By controlling the spatial position of the Fourier transform we varied the beam intensity ratio of the reference beam to various Fourier orders and therefore manipulated the contrast of the input object. We also used an extra incoherent erasing beam to erase the DC component to manipulate the contrast. However we did not achieve optimum results because of the edge enhancement which was present when the DC was partially suppressed. This also causes the overall illumination to be reduced.

To overcome these problems we proposed and demonstrated a technique which can be applied for contrast enhancement of images. The second technique relies on multiplexed hologram recording in a single crystal of BSO. One of the DFWM arrangements has a plane reference and probe beams to record and read mainly the higher orders, while the other has a focused reference and probe beam to record and

read the DC term of the object Fourier transform. By adjusting the intensities of the two reference beams we have achieved contrast manipulation of input objects. This technique can improve the contrast of objects without reducing the overall illumination of the object. One further technique of contrast manipulation is also proposed.

REFERENCES

2.1 Henry Stark, "Applications of optical Fourier transforms", Academic Press (1982).

2.2 R. H. Anderson, "Edge enhancement of coherent magnetooptic Images", Appl. Opt. **25**, 976 (1986).

2.3 R. W. Lewis, "Real time coherent optical edge enhancement", Appl. Opt. **17**, 161 (1978).

2.4 G. O. Reynolds, J. B. Develis, G. B. Parrent, B. J. Thompsons, "Physical optics notebook: Tutorials in Fourier Optics", SPIE Optical Engineering Press, Washington, 409 (1989).

2.5 J. O. White and A. Yariv, "Real-time image processing via four-wave mixing in a photorefractive medium", Appl. Phys. Lett. **37**, 5 (1980).

2.6 A. Yariv, "Introduction to Optical Electronics", 3rd ed. Holt Rinehart, Winston, 517-524, 1985.

2.7 P. Yeh and A. E. T. Chiou, "Optical matrix-vector multiplication through four-wave mixing in photorefractive media", Opt. Lett. **12**, 138, 1987.

2.8 Y. H. Ja, "Real time image division in four wave mixing with photorefractive $Bi_{12}GeO_{20}$ crystals", Opt. Commun. **44**, 24 (1982).

2.9 N. J. Wooder and J. C. Dainty, "Real time intensity inversion by four wave mixing in bismuth silicon oxide", Opt. Commun. **63**, 85 (1987).

2.10 J. P. Huignard and J. P. Herriau, "Real-time coherent object edge reconstruction with $Bi_{12}SiO_{20}$ crystals", Appl. Opt. **17**, 2671 (1978).

2.11 J. Feinberg, "Real-Time edge enhancement using the photorefractive effect",

Opt. Lett. **5**, 330 (1980).

2.12 H. Kogelnik, Bell Systems Technical Journal, **48**, 2909 (1969).

2.13 N. A. Vainos and R. W. Eason, "Real time edge enhancement by active spatial filtering via five wave mixing in photorefractive BSO", Opt. Commun. **59**, 167 (1986).

2.14 J. B. Develis, and G. O. Reynold, "Theory and application of holography", Addison Wesley, 151 (1967).

2.15 G. W. Stroke, "An introduction to coherent optics and holography", Academic press, 77-79 (1977).

2.16 M. W. McCall and C. Petts,"Grating modification in degenerate four wave mixing", Opt. Commun. **53**, 7 (1985).

2.17 N. Vainos, J. K. Khoury and R. W. Eason, "Real-time parallel optical logic in photorefractive bismuth silicon oxide", Opt. Lett. **13**, 503 (1988).

2.18 A. Kolodziejczyk, "Contrast reversal of a binary periodic object", Optica Acta, **33**, 867 (1986).

2.19 J. P. Huignard, J. P. Herriau and G. Rivet, "Phase-conjugation and spatial-frequency dependence of wave front reflectivity in $Bi_{12}SiO_{20}$ crystals", Opt. Lett. **5**, 102 (1980).

CHAPTER THREE

CONTRAST MANIPULATION AND CONTROLLABLE SPATIAL FILTERING VIA PHOTOREFRACTIVE TWO-BEAM COUPLING IN $BaTiO_3$

3.1 Introduction

The Fourier transform of a coherently illuminated object is one of the most important entities for optical image processing, and a number of spatial filtering operations can be performed in the back focal plane of a lens in such a filtering system. Among the common filtering systems are the zero spatial frequency stop, and horizontal or vertical slits in the centre of the Fourier plane. Others, which perform complicated filtering operations include complex spatial filters.

The operation of spatial filtering, which relies on blocking completely, or partially, certain frequency components, by insertion of masks, slits or other kind of objects, is a well established technique for optical image processing. Various filtering operations such as directional filtering, and high pass (edge enhancement) filtering are possible [3.1]. These conventional techniques, however, suffer from two serious drawbacks. Firstly the required mask fabrication may take a long time, and is usually designed for a specific configuration, so that therefore there is no possibility of updating or renewing these Fourier plane masks for real time processing, at for example, TV frame rates. Secondly the filtering operations are carried out by eliminating or **reducing** the amplitude of some of the spectral components while leaving others unchanged. Therefore we again have no possibility for amplifying some of the Fourier components at the expense of others.

Photorefractive materials, BSO and $BaTiO_3$ are perhaps the most commonly used. BSO, due to its requirement on writing and erasing energies $< 500\ \mu Jcm^{-2}$ [3.2], short response time, good optical quality and availability of relatively large size crystals makes it an important candidate for such real time applications. However applications where high gain may be required often use $BaTiO_3$ which is particularly attractive because of its large electrooptic coefficient that leads to correspondingly

large values of coupling between the interfering beams. DFWM is a widely used configuration for performing a variety of image processing operations using these materials.

As described in Chapter 2, certain parts of the hologram which are recorded by the Fourier transform of an input image and a reference beam are erased using an incoherent erasing beam to provide an efficient and real time spatial filtering technique upon readout. The other technique described in Chapter 2, shows contrast manipulation via quasi-Fourier transform hologram. However due to the dependence of the diffraction efficiency upon beam intensity ratio of the two input beams, contrast of the output image may not be optimum for all the spatial frequencies. To overcome this limitation we have also demonstrated another technique which depends on multiplexed DFWM and records different holograms for DC (or lower orders), and higher orders. This technique provides simultaneously the desired level of intensity for the DC and a range of Fourier orders but without any gain.

However despite several such possibilities, the basic DFWM configuration in BSO still inevitably reduces the amplitude of certain spatial frequency components rather than producing any enhancement. Due to these limitations, Fourier manipulation via DFWM has only limited application. On the other hand due to the relative simplicity and possibility of large gain, we have demonstrated the possibilities of Fourier plane modification using two beam coupling in $BaTiO_3$. Two beam coupling is an important technique in photorefractive materials due to its simplicity and gain specially in crystals having larger electrooptic coefficients such as SBN and $BaTiO_3$.

So far several techniques have been reported to achieve gain via two beam coupling along with different applications in these materials. The recording of a phase volume hologram in such materials leads to a stationary energy transfer between the two interfering light beams. This effect of energy redistribution which has been observed in these materials is due to the self-diffraction process of the reference beam into the signal beam when the dynamic phase grating has a phase shift of 90° with respect to the interference pattern. Photorefractive BSO has already been used for energy transfer via two wave mixing [3.3]. The 90° phase shift between

the volume phase grating and intensity pattern is achieved via recording the grating with moving fringe pattern at a constant velocity and applying an external electric field across the crystal. They achieved exponential gain coefficient of 7 cm^{-1}, and due to significant gain, they demonstrated the amplification of an input image.

Two beam coupling has also been demonstrated in $BaTiO_3$ which has certain advantages over BSO. In $BaTiO_3$ larger gains are achieved without any moving gratings. Two beam coupling characteristics in $BaTiO_3$ and its application for laser beam steering has been reported by Rak et al [3.4]. In their technique, they used two beam coupling with a low intensity probe beam, so complete energy exchange from the pump to the probe may be achieved. Similarly if another direction of the signal beam is selected the previous grating is erased while the new grating is recorded which deflects the pump in another direction.

They demonstrated this beam deflection for a limited number of positions and termed it laser beamsteering, using an array of piezomirrors to direct the signal beams towards the $BaTiO_3$ crystal in the focal plane of a lens. All except the selected one are excited with a ramp generator, which corresponds to the chosen direction of deflection. The moving piezomirrors introduce Doppler shifts in the signal beams which when interference with the pump beam takes place, gives moving interference patterns. When such shifts are large enough, no grating is recorded. However the selected signal beam has no Doppler shift, and therefore records a grating with the pump beam which is deflected (ideally) completely into the signal beam.

Chang et al [3.5] demonstrated a technique of spatial filtering which consists of manipulating an input image at its Fourier plane. Their technique is based on selectively amplifying the spatial frequencies via two beam coupling with a nonuniform pump beam in $BaTiO_3$ crystal. Therefore certain features of the image can be enhanced with respect to the overall image intensity by using the appropriate pump beam distribution. Therefore using this technique image brightness of unamplified portions remained of same intensity while desired components can be amplified.

Optical noise is usually a limitation in two beam coupling amplification of output

images. This noise arises due to beam fanning inside the crystal which is subsequently amplified via two beam coupling. Joseph et al [3.6] demonstrated a technique of two beam coupling with a high signal-to-noise ratio. Their technique of two beam coupling amplification consists of two stages. In the first stage they used a low power pump beam that has comparable intensity to that of the signal beam to record the grating with maximum index modulation and without considerable fanning noise. After the grating is recorded to its full strength, the readout process is achieved by increasing the intensity of the pump beam by about 1000 times and subsequently allowing it to read the grating for 20 msec which is less than the time constant of beam fanning. Therefore under such conditions improved signal to noise ratio is achieved and as they reported approximately tenfold increase in the gain is achieved over the conventional readout scheme of two beam coupling. The obvious limitation of their scheme is to read the previously recorded grating for only 20 ms, erasing this grating and then recording again. Such a technique may not be applied for continuous recording and readout of the grating in specific applications in image processing.

Another way to get ride of fanning noise is to record an achromatic grating in $BaTiO_3$. One such technique is demonstrated by Rabinovich et al [3.7] by recording a grating with white light in a symmetrical arrangement, where the bisector of the pump and signal beams was parallel to the crystal surface normal. However when this condition is not met refraction at the crystal surface tilts the gratings which are formed by different colours with respect to each other. They measured gain as a function of angle between the crystal normal and bisector of pump and signal beams recording a white light coupling gain of 0.24 cm^{-1}. Recording of volume holograms in non-linear materials with broad band spatially incoherent sources of light has obvious advantages. However, such grating formation occurs only under special and sensitive conditions.

3.2 Theoretical Considerations

When two mutually coherent beams interfere in a photorefractive medium they form a resultant refractive index grating. If this grating is not in phase with the irradiance grating, energy will transfer from one beam to the other, the direction of

which is determined by the crystal orientation and types of the charge carriers [3.8]. The magnitude of this coupling depends on intrinsic parameters of the material such as trap density, effective electrooptic coefficient etc, and extrinsic parameters as well, such as grating wavevector and its angle with respect to the c-axis of the crystal.

Figure 3.1 shows the standard configuration for two beam coupling experiments in photorefractive $BaTiO_3$. The angle between the two interfering beams is θ within the medium of length L. Energy is coupled from the reference beam I_r into the object beam I_o. There is no applied field across the crystal. The gain G experienced by the object beam I_o in this case can be deduced from a solution of the relevant coupled wave equations [3.9, 3.10, Appendix B] and is given by the equation

$$G=\frac{(1+r)\exp(\Gamma L_{eff})}{1+r\exp(\Gamma L_{eff})} \qquad (3.1)$$

Where r is the ratio of signal to reference beam intensity, Γ is the two beam coupling gain coefficient which depends on the angle θ between the interacting beams, their polarization direction and angle between the grating wavevector and the c-axis of the crystal. L_{eff} is the effective interaction length, which depends on the thickness of the crystal and geometry of the beams in the crystal. Equation (3.1) does not take into account any absorption or reflection losses the beams may suffer and is valid only in lossless case. It is, therefore, experimentally desirable to measure the gain G as the ratio of the object beam $I_o(L)$ with and without the presence of the reference beam.

In Figure 3.2 the gain G is plotted as a function of the beam intensity ratio r when the intensity of the reference beam is kept constant. Considering Equation (3.1), for $\Gamma L_{eff} >> 1$ and beam intensity ratio r=1 the gain reduces to a value of 2. For $r << 1$ however the gain approaches a saturated value which is given by

$$G_{sat}=\exp(\Gamma L_{eff}) \qquad (3.2)$$

For any intermediate value of r there is a third region which is experimentally interesting, where gain is inversely dependent on beam intensity ratio. Therefore an almost constant value of $I_o(L)$ can be observed for a wide range of values of signal intensity (several decades).

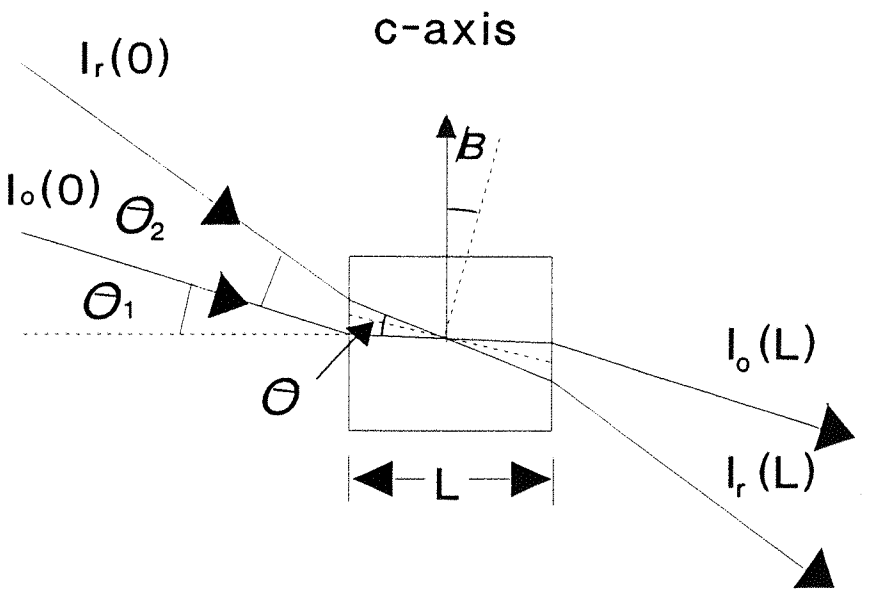

Figure 3.1 Geometry for reference and signal beams inside $BaTiO_3$ crystal.

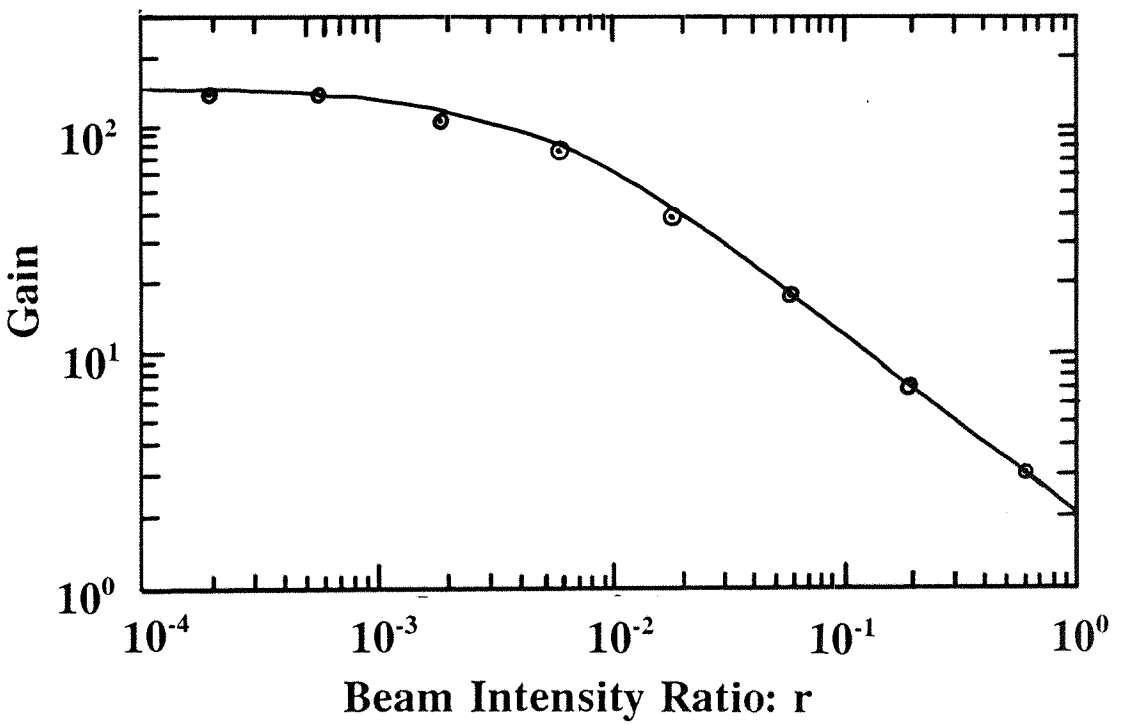

Figure 3.2 Plot of gain G, versus beam intensity ratio *r*, defined as $I_S(0)/I_R(0)$, for the geometry of Figure 3.1. The dots are experimental points and the solid curve is calculated according to Equation (3.1) using a value of $\Gamma L_{eff} = 5\ cm^{-1}$.

The object beam here is a Fourier transform of an object which occurs in the back focal plane of a transforming lens. The Fourier plane is arranged to fall inside the crystal in our case. When these Fourier orders couple with the reference beam inside the photorefractive $BaTiO_3$, the various spatial frequency components will experience gain according to their respective intensity ratios with respect to the reference beam.

It is possible to perform a number of spatial filtering operations that depend on the gain characteristics of the photorefractive material in a two beam coupling geometry. This has been recognised earlier for performing the operations of edge enhancement, where high spatial frequencies of an object have experienced higher gain compared to the lower frequencies and uniform image amplification in which the intensities of all the Fourier components should satisfy the saturation gain condition of Equation (3.2), [3.10].

Irrespective of these operations, we are extending the possibility here to consider explicitly other operations which rely on just this characteristic. We examine here contrast enhancement which requires preferential amplification of the higher spatial frequencies present in an object.

Merely removing the DC component from Equation (2.2) is not desirable as it will also eliminate the overall illumination in the image. This problem can be solved however by using non-linear coupling in $BaTiO_3$, by adjusting the intensity ratios according to the characteristic gain. At an appropriate point, the DC component will experience small gain, say around unity, while the higher frequency components should experience considerable gain. Background illumination therefore may not be affected at all, and remains approximately the same, while considerable improvement in contrast will result. Using this technique, problems of lack of illumination and edge enhancement, which are associated with the contrast enhancement operation using photorefractive BSO have largely been overcome [3.11].

Other filtering operations can also be achieved by amplifying a particular range of spatial frequencies to enhance specific features of the object. Similarly we may look at an input and selectively amplify spatial frequency dependent defects, for

example dust particles or scratches and contrast inversion of a periodic object can also be realised. Contrast inversion can be explained by the theory propounded by Kolodziejczyk [3.12] and has already been described in Chapter 2. In our case this phenomenon can be accounted for by the preferential amplification of discrete higher spatial frequencies in a periodic object. It can be considered to be the equivalent of absorbing some part of the DC component in conventional filtering or subtracting a plane wave from the image.

3.3 Experimental and Results

Figure 3.3 shows the experimental arrangement used for two beam coupling. The Kr^+ Ion laser was operating in multi-longitudinal mode at λ = 530.9 nm. Beam-splitter BS divides the input into two beams. The transmitted beam is expanded to a diameter of approximately 4 mm, and enters into the crystal of $BaTiO_3$ of dimensions 5 x 5 x 5.9 mm^3 at an angle of 42° with respect to the crystal normal. To avoid self pumping [3.13] and to maximize the coupling from reference to signal beams, the crystal is oriented such that $\theta_1 = 11°$, $\theta_2 = 32°$, $\theta = 12°$ and $\beta = 11°$. The measured intensity of reference beam I_r was 2.4 mW. The signal beam, transmitted through beam-splitter BS, traversed a variable neutral density filter VF. Various transparencies were placed at the object plane as shown. A lens of focal length 10 cm was adjusted such that the resultant Fourier transform achieved optimum spatial overlap with the reference beam inside the crystal. Figure 3.2 shows a plot of gain versus beam intensity ratio, indicating good agreement between measured and theoretical values for a value of $\Gamma L_{eff} = 5\ cm^{-1}$. It is, however, experimentally difficult to map the corresponding values of r for all the Fourier components in the object spectrum. The output image resulting from intensity dependent coupling is observed at the image plane via a camera and monitor combination.

The camera image is processed by a three dimensional scenic display generator, which proves a direct comparison between the intensities of various points in the image before and after the operation of contrast enhancement.

Figure 3.4 shows the experimental results obtained and illustrates the operation of contrast enhancement, feature extraction, defects enhancement and inversion of

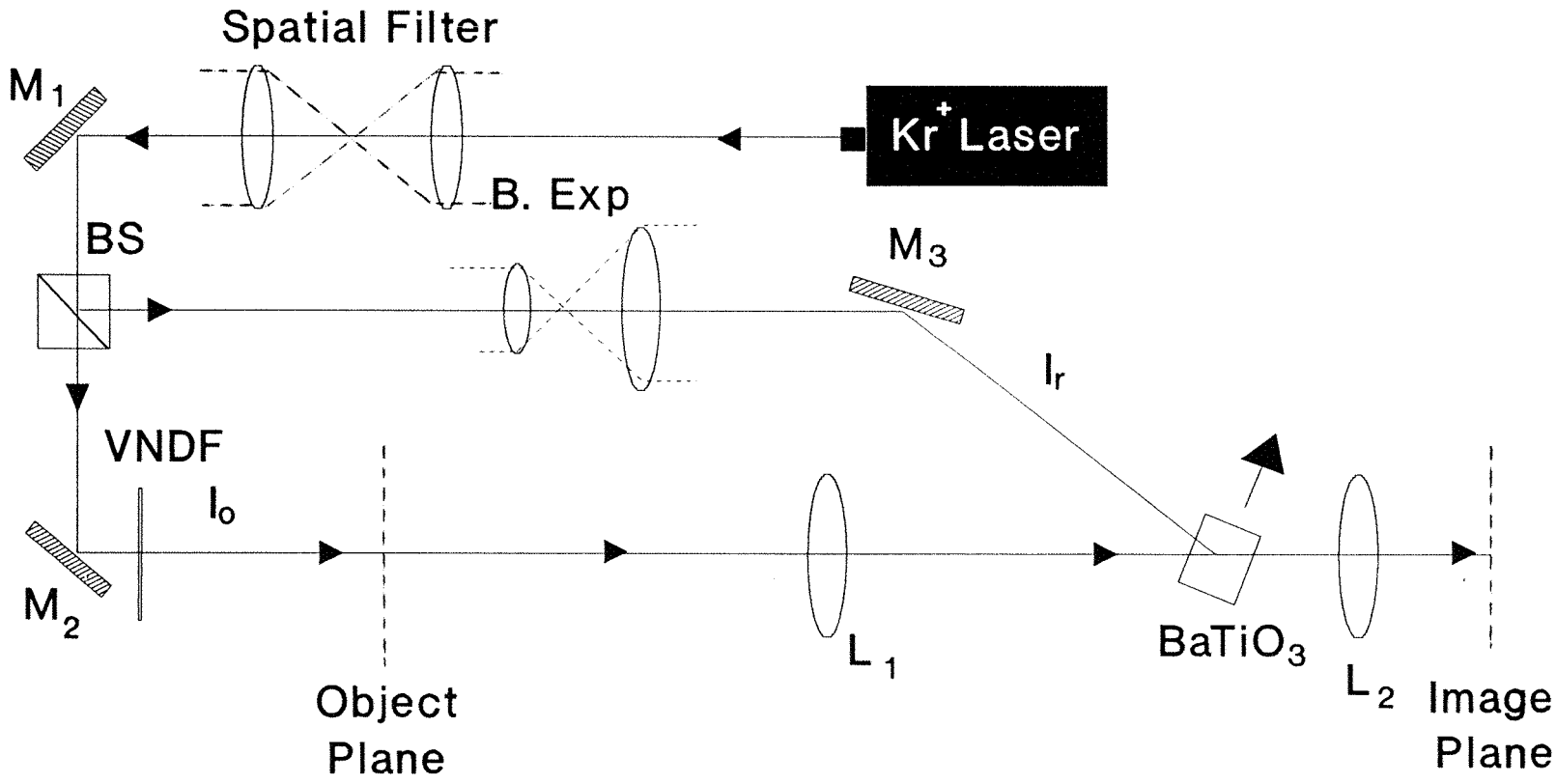

Figure 3.3 Shows experimental arrangement for contrast manipulation via two beam coupling.

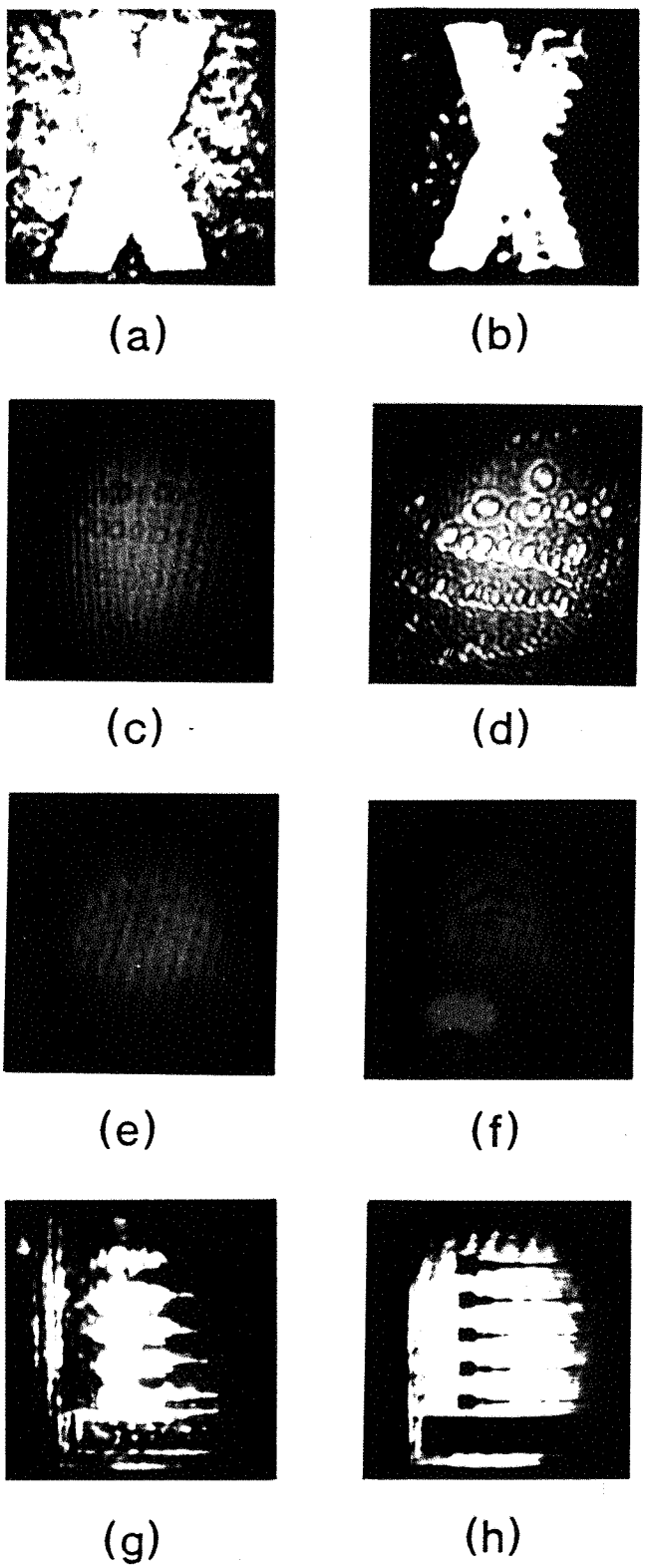

Figure 3.4 Results of contrast enhancement, feature extraction, defect enhancement and contrast reversal. Originals are (a), (c), (e), and (f); corresponding enhanced versions are (b), (d), (f) and (h).

periodic objects. Figure 3.4(a) shows a letter **X** of dimensions 1.2 mm x 0.6 mm that is obtained at the image plane when the reference beam was blocked. The poor contrast between the object and background was introduced photographically in the transparency. Figure 3.4(b) illustrates the results when object and reference beams (at $r = 1.1 \times 10^{-2}$) are coupled in $BaTiO_3$, such that the higher spatial frequencies corresponding to the letter **X** experienced preferential gain compared to the DC order. The illumination level of the letter **X** in (a) and (b) was measured to be equal.

To ensure this, the camera image was processed by the scenic display and we equalised the level of illumination of the **X** before and after the contrast enhancement operation. Figure 3.5 (a), illustrates the output of the scenic display of the input transparency of the letter **X**. It can be seen that a considerable background exists around the peak, corresponding to the **X**. In Figure 3.5 (b) the Fourier transform of the object is coupled with the reference beam, and it is clear that the level of background illumination is very low while the level of intensity of the letter **X** is kept at the same as that in Figure 3.5 (a). Figure 3.4 (c), shows an image of a slide of silicone oil with dust particles on it, as it appeared in the image plane when the reference beam was blocked. It can be assumed that dust particles behave like defects on a transparent surface, and therefore correspond to high frequency components in the image spectrum. Figure 3.4 (d) illustrates the enhancement of these defect sites on the slide when the reference beam was applied, showing that higher frequencies experience more gain. The beam intensity ratio for this case is equal to $r = 10^{-3}$. Figure 3.4 (e) shows the image of an object which is a smeared silicone oil film. Figure 3.4 (f), shows the enhanced version of a fringe pattern of Figure 3.4 (e) produced by interference in the smeared oil film when coupled with the reference beam at a value of $r = 10^{-3}$. Figure 3.4 (g) shows the image of a part of a resolution test chart which is periodic, and whose inverse is sought. A partial inversion is seen to occur when the reference beam is let through, at a beam intensity ratio of $r = 2.0$.

3.4 Comments

It can be seen from Figures 3.4(a) to 3.4(h) that during the operations of contrast enhancement and inversion the output images have lost some resolution. This loss

(a)

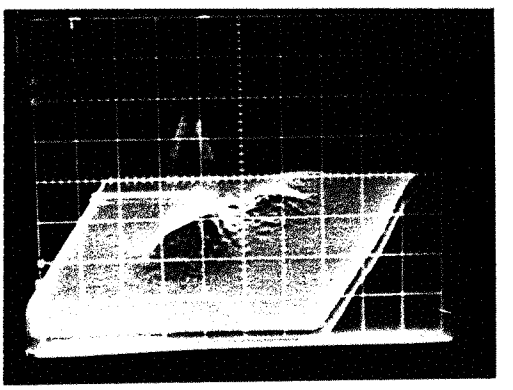

(b)

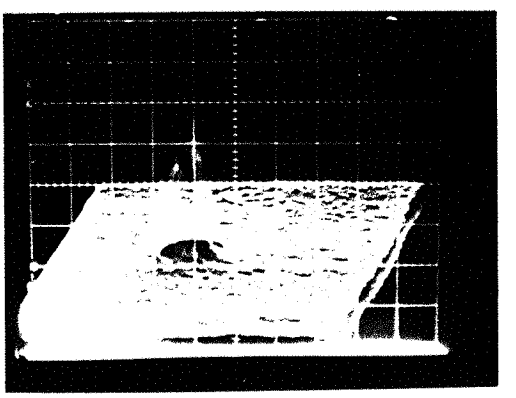

Figure 3.5 Scenic display output of the input transparency (a) without two beam coupling, (b) with two beam coupling.

in resolution can occur because of three main reasons. Firstly, the gain spatial bandwidth product is limited because, the various Fourier components of the object interfere with the reference beam at different angles. Therefore their effective interaction lengths inside the crystal are not the same and individual components may have different values of β. It is evident that the exponential gain coefficient Γ may not be equal for a group of spatial frequency components because Γ strongly depends on θ and β via a nonsymmetric and nonuniform dependence. This problem has also been encountered previously for amplification of images, and one suggestion for improving this situation relies on the use of a spherical reference beam [3.10]. Other factors that may affect the resolution include the Gaussian nature of the intensity profile of the interfering beams, and internal reflection inside the crystal. This latter problem may be solved by putting the crystal into suitable index matching media.

The operations that we have demonstrated above can be considered as high band pass filtering. However using the same experimental geometry while rotating the crystal through 180° we can perform a low band pass filtering operation with an object beam of higher intensity than that of the reference beam. Here higher spatial frequencies are removed because of their lower intensities and lower frequencies are passed because of their higher intensities.

3.5 Conclusion

We have demonstrated a technique of contrast manipulation and spatial filtering which relies on two beam coupling in photorefractive $BaTiO_3$. By appropriate choice of operating point on the gain curve, the operations of contrast enhancement, feature extraction, defect enhancement and contrast reversal have been achieved. Using this technique various orders experience variable gain rather than selective reduction in intensity of the object Fourier transform.

REFERENCES

3.1 S. H. Lee, "Optical Information Processing", Vol. **48**, Springer Verlag (1981).

3.2 J. P. Huignard and A. Marrakchi, "Coherent signal beam amplification in two-wave mixing experiments with photorefractive $Bi_{12}SiO_{20}$ crystals", Opt. Commun. **38**, 249 (1981).

3.3 H. Rajbenbach, J. P. Huignard and B. Loiseaux, "Spatial frequency dependence of the energy transfer in Two-wave mixing experiments with BSO crystal", Opt. Commun. **48**, 247 (1983).

3.4 D. Rak, I. Ledoux and J. P. Huignard, "Two-wave mixing and energy transfer in $BaTiO_3$ application to laser beamsteering", Opt. Commun. **49**, 302 (1984).

3.5 T. Y. Chang, J. H. Hong and P. Yeh, "Spatial amplification: an image-processing technique using the selective amplification of spatial frequencies" Opt. Lett. **15**, 743 (1990).

3.6 J. Joseph, P. K. C. Pillai and K. Singh, "High-gain, low-noise signal beam amplification in photorefractive $BaTiO_3$", Appl. Opt. **30**, 3315 (1991).

3.7 W. S. Rabinovich and B. J. Feldman, "Photorefractive two-beam coupling with white light", Opt. Lett. **16**, 708 (1991).

3.8 P. Gunter, "Holography, coherent light amplification and optical phase conjugation", Physics Report, **93**, 199-299 (1987).

3.9 N. V. Kukhtarev, V. B. Markov, S. G. Odulov, M. S. Soskin and V. L. Vivetskii, "Holographic storage in electrooptic crystals. II. Beam coupling - light amplification", Ferroelectrics, **22**, 961 (1979).

3.10 Y. Fainman, E. Klancnik and S. H. Lee, "Optimal coherent image amplification by two-wave coupling in photorefrective $BaTiO_3$", Opt. Eng. **25**,

228 (1986).

3.11 J. A. Khoury, G. Hussain, R. W. Eason, "Contrast manipulation and controllable spatial filtering via photorefractive two-beam coupling", Opt. Commun. **70**, 272 (1989).

3.12 A. Kolodziejczyk, "Contrast reversal of a binary periodic object", Optica Acta, **33**, 867 (1986).

3.13 J. Feinberg, "Self-pumped, continuous-wave phase conjugator using internal reflection", Opt. Lett. **7**, 486 (1982).

CHAPTER 4

CONTRAST MANIPULATION VIA POLARIZATION ENCODING OF FOURIER TRANSFORMS USING ACTIVE AND PASSIVE TECHNIQUES

4.1 Introduction

The number of repetitions per unit length that a cyclic pattern undergoes is known as the spatial frequency. When a plane monochromatic wave is diffracted by an object, a distorted wave front results. This wave front can be resolved into a set of plane waves each travelling in a specific direction, corresponding to different diffracted orders. A two dimensional Fourier transform of the light distribution in the object plane is generally as the Fraunhofer diffraction pattern on a very distant screen. However, by introducing a lens, the Fourier transform can be generated at its back focal plane. For a two dimensional periodic step function (a grating) as the input, with period **a** the fundamental spatial frequency of the grating is the reciprocal of **a**. As the orders **m** in the Fourier plane get farther from the central DC component, their associated spatial frequencies (m/a) increase correspondingly. Such a situation allows the insertion of obstructions i.e., masks or filters in the transform plane, and in so doing, we can block partially, or completely, certain spatial frequencies from reaching the image plane [4.1-4.3].

Caulfield and Soref [4.4] have reported a technique of contrast enhancement using a liquid crystal cell. Their technique depends on the dynamic scattering of light from the liquid crystal sandwich when a voltage is applied across it. The input object, which is four circular transparent electrodes deposited on the glass substrate is Fourier transformed and subsequently inverse transformed by two lenses. The spatial filtering is performed by stopping either the scattered light or non-scattered light via stops or masks in the Fourier plane. This technique has certain draw backs: the contrast of the output image is limited by the maximum scattering efficiency of the device, which depends on the composition of the liquid crystal, the thickness of its sandwich and the applied field. The other factors which contribute towards limited contrast are electrode imperfection, numerical aperture of the lens and the zero field

inhomogenities of the liquid crystal.

A real time optical edge enhancement technique has been reported by Lewis [4.5]. In this technique he employed the conventional method of optical spatial filtering. The incoherent input image is modulated via an image panel which is read in a specular reflection configuration from the front surface of the panel. The image is Fourier transformed and a high pass filter is used to stop the DC order and allow the higher orders to form an edge enhanced image at the output plane. The quality of the output image was degraded due to the surface imperfections and the non-uniformities which appear in the image panel. Due to the fixed mask used this technique is limited only to edge enhancement and cannot perform other dynamic operations on the images.

Anderson [4.6] has demonstrated an edge enhancement technique on images using a magneto-optic spatial light modulator (MOSLM). Due to the periodic array structure of the pixels of MOSLM it works as a mesh, and thus in the Fourier plane the input image is replicated. To perform the filtering operation in the Fourier plane, a mask of replicated DC blocking spots is used to achieve an edge enhanced image. He also achieved edge enhancement via an adjustable aperture in the Fourier plane, with a central DC blocking spot. The adjustable aperture allows higher Fourier orders of a Fourier transform to pass which gives an edge enhanced image on a dark background at the output plane. He further demonstrated that dark edges on a bright background can also be achieved by allowing the DC term to pass through when a variable aperture of diameter less than the diffraction order spacing is placed in the Fourier plane. Therefore both the positive and negative contrast edge enhanced images can be achieved via this technique. However this method is limited to edge enhancement only and the resolution of the output image is also lost during the filtering process.

Bartelt and Sauer [4.7] have demonstrated a technique of space variant spatial filtering. Their technique exploits a holographic lenslet array to produce local Fourier transforms of the object which are then filtered in parallel by a corresponding array of filters. These individual filters in the array perform the filtering operations on the Fourier transforms which then are inverse transformed by a common lens to yield the

the output image. The filter array has different filters in different regions which correspondingly filter the Fourier transforms to give the required output image. This technique provides the flexibility of space variant filtering on the input image. However the Fourier transform filter array for a particular image application may not be suitable for another type of filtering operation. The limitations of this technique are the crosstalk of the local spectra and diffraction effects caused by the finite size of the lenslet.

A different technique for edge enhancement has been reported by Brown [4.8], in which he used two holographic diffraction gratings in the Fourier plane of a spatial filtering set up. The two holographic gratings have slightly different spatial frequencies which were adjusted such that a 180° phase shift is introduced in the Fourier plane. A convolution takes place between the Fourier transform of the input object and the gratings which results in multiple images of the object in the output plane. A controlled degree of shift is introduced in the two overlapping images to achieve edge enhancement in one direction only. The alignment problem and the overlapping of other multiple images can also degrade the operation of edge enhancement using this technique.

Operations of correlation [4.9, 4.10] subtraction [4.11-4.15] and inversion [4.16, 4.17] have been performed using optical phase conjugation techniques. The operation of spatial filtering is used for feature extraction, pattern recognition, contrast enhancement etc. One of the spatial filtering operation is edge detection, the aim being to outline areas of equal brightness or similar texture with the end objective of feature recognition by shape identification. The preprocessing step of edge enhancement can clarify the image by removing extraneous detail from the scene. Two earlier techniques of edge enhancement with photorefractive materials were reported by Huignard and Herriau [4.18], and Fienberg [4.19].

A similar approach has been applied to enhance the defects of periodic objects in BSO [4.20]. The technique relies upon two observations: Firstly the Fourier transform of a periodic object is an array of discrete spikes, while a small defect in the periodic structure has a continuous Fourier transform with lower intensity than these discrete spikes. The second observation is that the diffraction efficiency of the

volume hologram is maximum when the intensities of the two writing beams are equal. Therefore in such a system a defect can be enhanced by focusing the Fourier transform of the mask in the BSO to record the hologram, and adjusting the relative intensities of signal and reference beams such that the intensity of the peak spectral component due to the defect is less than, or equal to, the intensity of the reference beam. At this stage the diffracted beam intensity from the hologram corresponding to the defect is maximum while that for the spikes is a minimum due to the low index of modulation. As a result defect sites are observed clearly against the dark background in the image plane.

A technique of edge enhancement has been reported by Vainos and Eason [4.21], which employs the DFWM configuration in BSO and an additional loosely focused beam is directed towards the lower spatial frequencies of the Fourier hologram to cause selective erasure. When this hologram is readout, the phase conjugate output produces an edge enhanced image. An extension of this technique of spatial (band-pass) filtering of phase conjugate images has also been performed in $BaTiO_3$ via two different holographic configurations [4.22]. In the first configuration a DFWM process is used to record and read out the Fourier hologram, while the second configuration used a signal beam to record a hologram with a self-pumped reference beam inside the $BaTiO_3$ crystal. The self-pumped phase conjugate beam reads the hologram of the signal beam to achieve phase conjugate output. In both cases, spatial filtering is performed by illuminating the transparencies of the spatial filter by an incoherent white light source, which erases selected Fourier orders of the object hologram and the reconstructed image is modified correspondingly. This technique provides an easy way to erase various Fourier orders to perform the required filtering operation considerably faster compared to other conventional optical techniques. However this technique has certain limitations as well. Firstly the erasure of Fourier orders in the self-pumped configuration may erase those fanning gratings which also providing the readout beam. The other limitation is that the various reconstructed Fourier orders may suffer nonlinear gain.

4.2 Theoretical Consideration

4.2.1 Phase Contrast Imaging

An amplitude object is observable against its surroundings because of the variations that it causes in the amplitude of the light which provides contrast with respect to its background. However the other category of objects called phase objects are ones that are transparent, and therefore show practically no contrast against their surrounding background. Additionally, the optical thickness of such objects generally varies from point to point, as either thickness or refractive index (or both) is spatially varying [4.1, 4.23].

Diffraction occurs when a portion of the wave-front is modulated in amplitude or phase. When a wave passes through a phase object it is modulated accordingly, and consists of two parts. One of the parts is modulated by the localized phase object, while the other part is effectively an un-modulated plane wave. The phase retardation may also be very small, which in turn gives rise to very small diffraction, for example a phase lag of only a quarter of a wavelength. After broadly diverging from the object, these higher order spatial frequencies are converged via a lens arrangement, on the image plane, where they interfere with a 90° phase shift with the DC to form the phase modulated image and apparently no image is perceptible.

For a phase change of i.e, less than a radian, as is the usual case, the phase shift of 90° is introduced in the un-diffracted central DC term. Such a phase shift is realized by inserting a spatial filter in the transform plane (of the objective). This filter could be a small circular indentation of the correct thickness etched in a transparent glass plate. Ideally, only the direct (un-diffracted), beam would pass through the indentation. A filter of this sort is known as a phase filter. If the net relative phase which is introduced by the phase object and phase filter is 180° between the DC and higher orders, destructive interference takes place. This give rise to dark contrast for the phase object against a bright background. However, in practice, not all phase objects are regular and therefore there may be random phase variations throughout the object. In this situation complete destructive interference takes place only between direct and diffracted paths when they have a relative phase

shift of 180°.

At the same time however there may also be diffracted light from other parts of the object which interferes constructively with direct (or DC), light provided they are in phase. There may also be regions in the object which introduce continuous intermediate phase shifts to the diffracted light which would lead to interference with 90° phase shifted, direct light to give an intermediate level of intensity. Therefore the visibility will be different for different regions of the object, and will also depend on the relative refractive indices in the object. For smaller refractive index features the amplitudes of diffracted light will also be smaller and to get maximum contrast for such features in the image plane the DC should also be of the same amplitude.

In conventional techniques this is achieved by introducing another filter to attenuate only the DC to a level similar to that of any particular feature. However it is difficult to fabricate and place such a filter or mask to attenuate the DC only. Also different attenuation filters are required for features with different light amplitudes, while positive and negative contrasts are achieved via different phase filters which is again a difficult and time consuming job. These attenuation filters may not achieve a continuous level of attenuation. Therefore using conventional techniques of phase contrast imaging, it is almost impossible to see all the individual features in the object plane with optimum contrast.

We present here a new technique which is based on polarization encoding of the Fourier transform of the light distribution in the object plane. When a transparent object is illuminated by (coherent) light, phase retardation takes place which gives rise to light diffraction. Figure 4.1 shows the three possible configurations of polarization encoding of the object distribution. However, we shall only consider scheme (a) here. As shown, a lens L_1 produces the Fourier transform of the object distribution in its back focal plane. In the Fourier plane the central DC term contains all the background information of the object while higher orders contain all the phase information.

Instead of introducing a 90° phase shift in the DC via a phase filter we place a half-wave plate (HWP), with a central hole to allow the DC to pass through, without

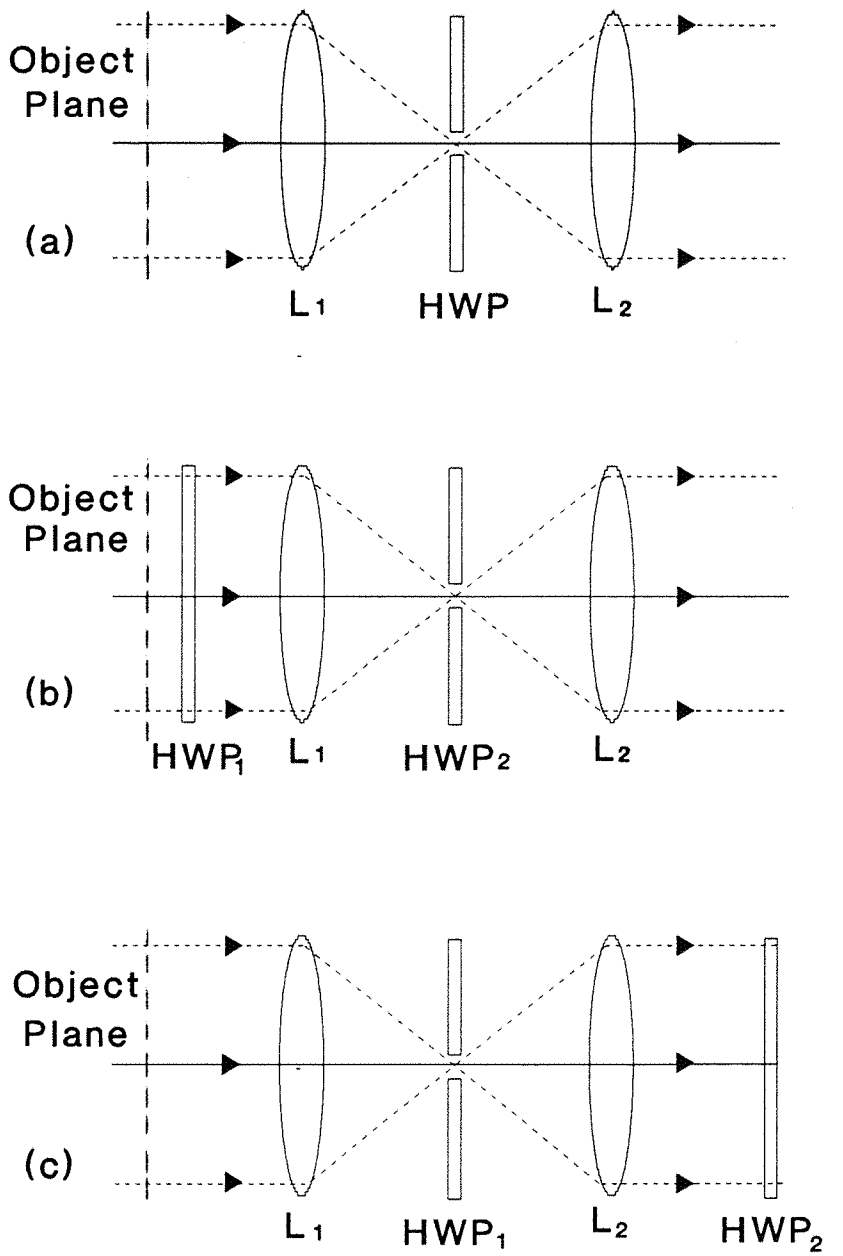

Figure 4.1 Different arrangements for polarization encoding using half-wave plates.

changing its polarization state (a non-birefringent index matching medium can be used for this purpose). However all higher orders do pass through the half-wave plate, and their polarization direction is rotated through an arbitrary angle. For the present case, let us consider a 90° rotation from their initial position. The polarization encoded Fourier transform is then inverse transformed by lens L_2 as shown in Figure 4.1. Due to the orthogonal polarizations of the background and higher order illumination no interference takes place at the image plane and therefore the image will be of poor quality. However, by placing an analyzer before the image plane, the DC and higher orders are resolved along and perpendicular to its transmission axis. All those components which are parallel to the transmission axis of the analyzer will interfere. Table 4.1 illustrates a sequence of polarization states for such an arrangement and can be expressed by

$$Re\left[A_1 e_{DC}^{i(\theta-\psi)} + A_2 e_{HO}^{i(\theta+\phi-\psi)}\right] = Output \qquad (4.1)$$

Where θ is the polarization angle between the DC and vertical axis, ϕ is the relative polarization angle between the direct light and diffracted light (we take here $\phi=90°$) while ψ is the angle between the vertical axis and transmission axis of the analyzer. A_1 and A_2 are the maximum amplitudes of the DC and higher orders which can be achieved at angles $\psi=\theta$, and $\theta+\phi$ respectively. Contrast of the object can be manipulated by varying any or all of the three angles described above.

Figure 4.2 shows the graphical representation of Equation (4.1), for equal amplitudes of DC and higher orders. The graph shows complete subtraction is achieved at ψ = 0°, 180° and 360°. At these positions, the amplitudes of DC and higher orders are out of phase, while at other positions a net output is always achieved. The visibility of the formerly less visible features in the object may be improved if some of the DC is attenuated to equate the light amplitudes of DC and those particular higher orders. In our technique it is quite easy to attenuate the DC or higher orders to any value from 0 up to their maximum value. This is achieved by rotating the transmission axis of the analyzer to attenuate the DC, while increasing the transmission of higher orders.

Unlike previous techniques of phase contrast imaging where special attenuation masks of particular values or steps are fabricated, our technique does not require

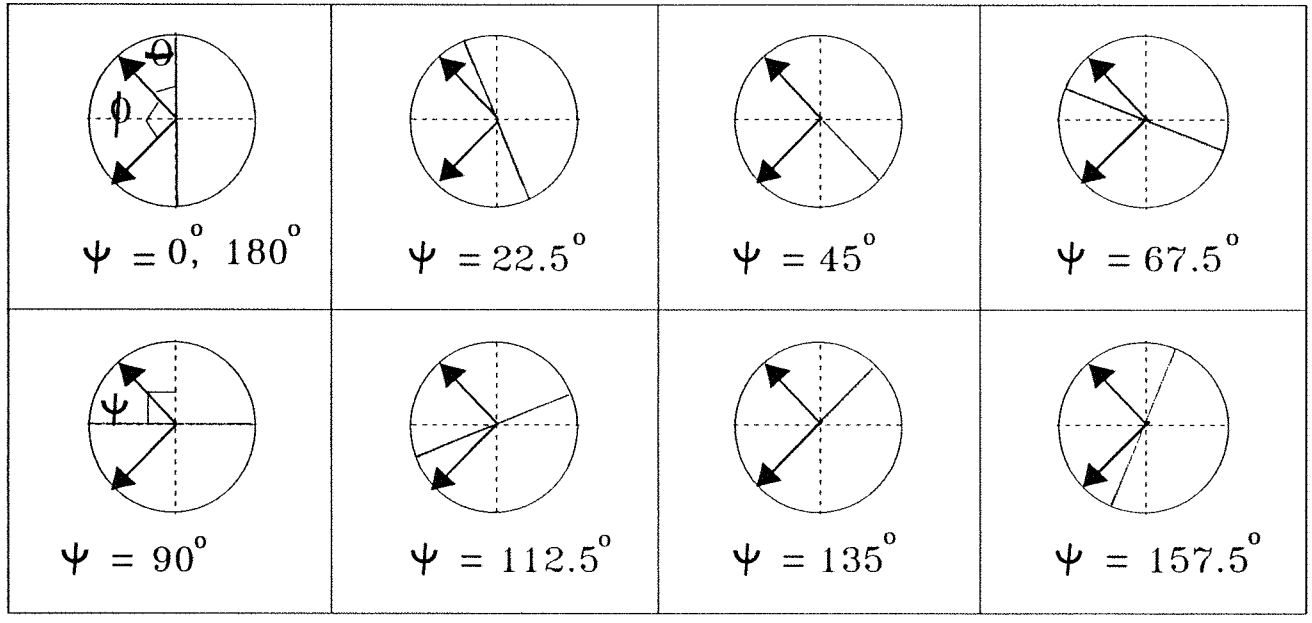

Table 4.1 Shows polarization states of DC and higher orders in a plane after the polarization encoding in a contrast manipulation arrangement.

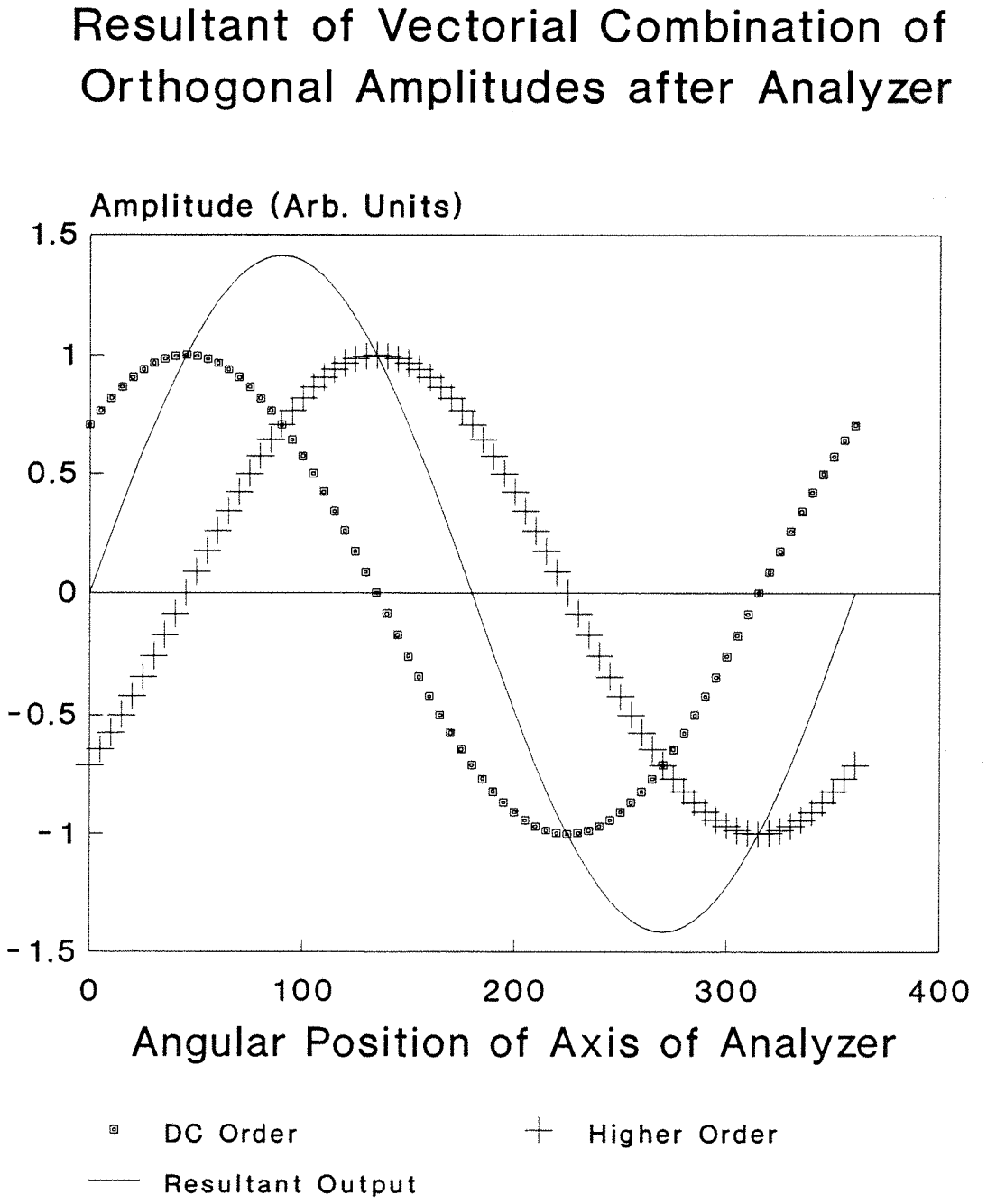

Figure 4.2 Theoretical plot of output amplitude at image plane for equal amplitudes of DC and higher orders versus angular position of transmission axis of the analyzer.

fabrication of any such mask, yet can attenuate the desired proportion of DC and higher orders. Therefore when the amplitudes of the DC and higher orders are not equal for example, (i.e. when higher orders have their amplitudes half, quarter or an eighth of the DC amplitude), total subtraction is still achieved at different angular positions of the analyzer. A graphical representation of this is shown in Figures 4.3-4.5, where it is clear that our technique is both easy and versatile.

Our technique can also be extended to other types of illumination schemes of the object and can be applied in phase contrast microscopy. A phase contrast microscope is used to observe, for example, unstained biological organisms because staining techniques may alter or damage biological structures and cannot be applied to living material. Therefore using our technique for variable phase contrast microscopy, the contrast of an unstained specimen can be continuously varied. The variable phase contrast microscope may only require the addition of a polarizer, an analyzer and replacement of the phase filter by a polarization rotation filter i.e, which may be such a modified half-wave plate.

Figure 4.6 shows the basic arrangement for illumination of the object, polarization rotation filter, and three schemes of polarization encoding of the light in the microscope. As is common in phase contrast imaging, our variable phase contrast microscope also incorporates an annular diaphragm below the condenser which directs a hollow cone of light to the transparent specimen as shown in Figure 4.7 (a). The objective collects the light and directs it towards a polarizer and a polarization rotation mask. Therefore the light which is diffracted from the object is rotated by the mask through an angle (such as 90°) while the un-diffracted light remains of the same polarization (or vice versa). Therefore the two components of light are of orthogonal polarizations and do not interfere with each other. However an analyzer placed at a plane in between the mask and detection plane, analyzes these two components of light. Figure 4.7 (b) shows a reflection microscope where variable phase (and) or amplitude contrast is achieved via illumination through the objective.

In conventional phase contrast microscopy, the light which is diffracted by the structural details in the specimen is a quarter-wave length out of phase with light

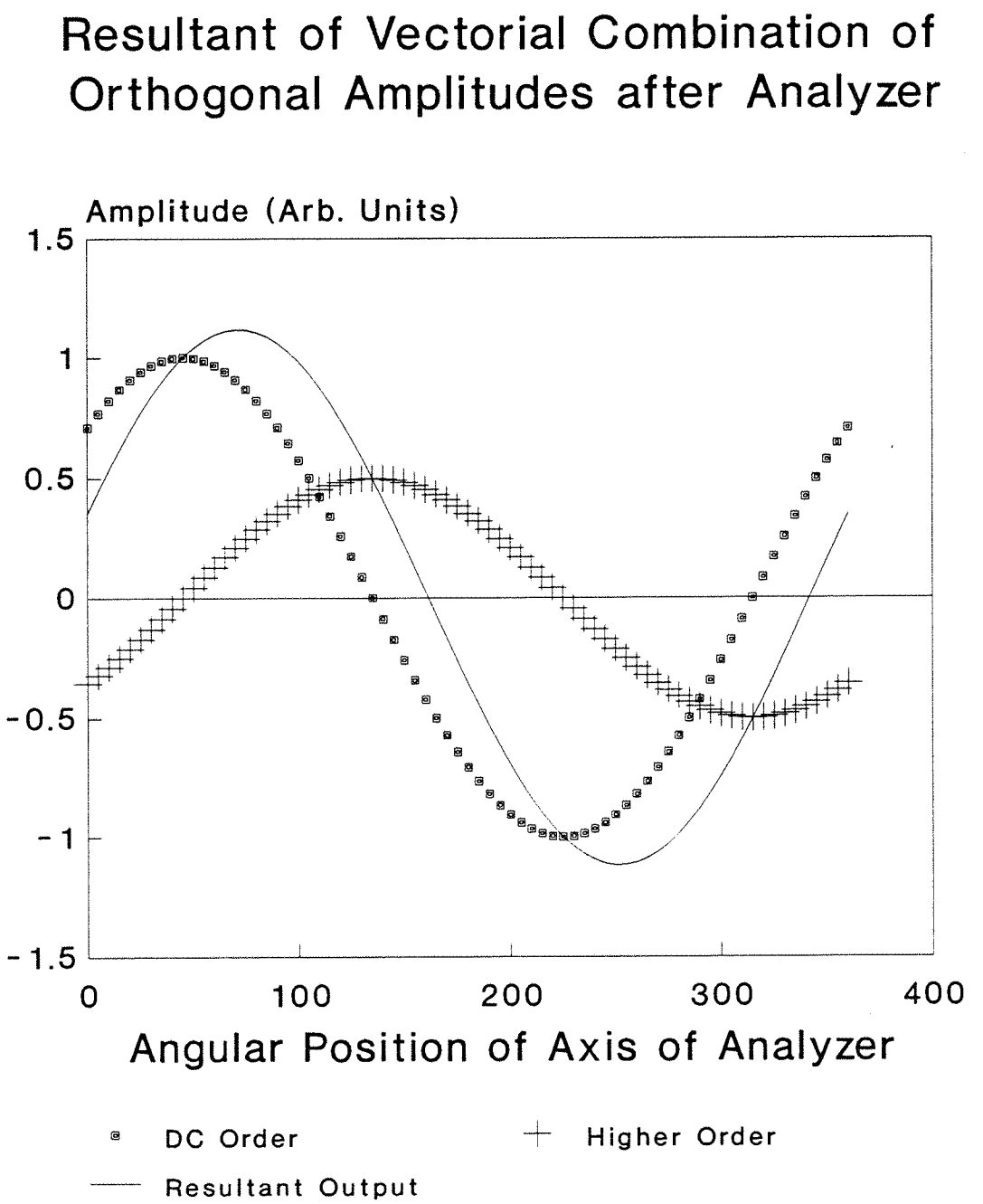

Figure 4.3 Theoretical plot of output amplitude at image plane for higher orders amplitude to be half of DC versus angular position of the transmission axis of the analyzer.

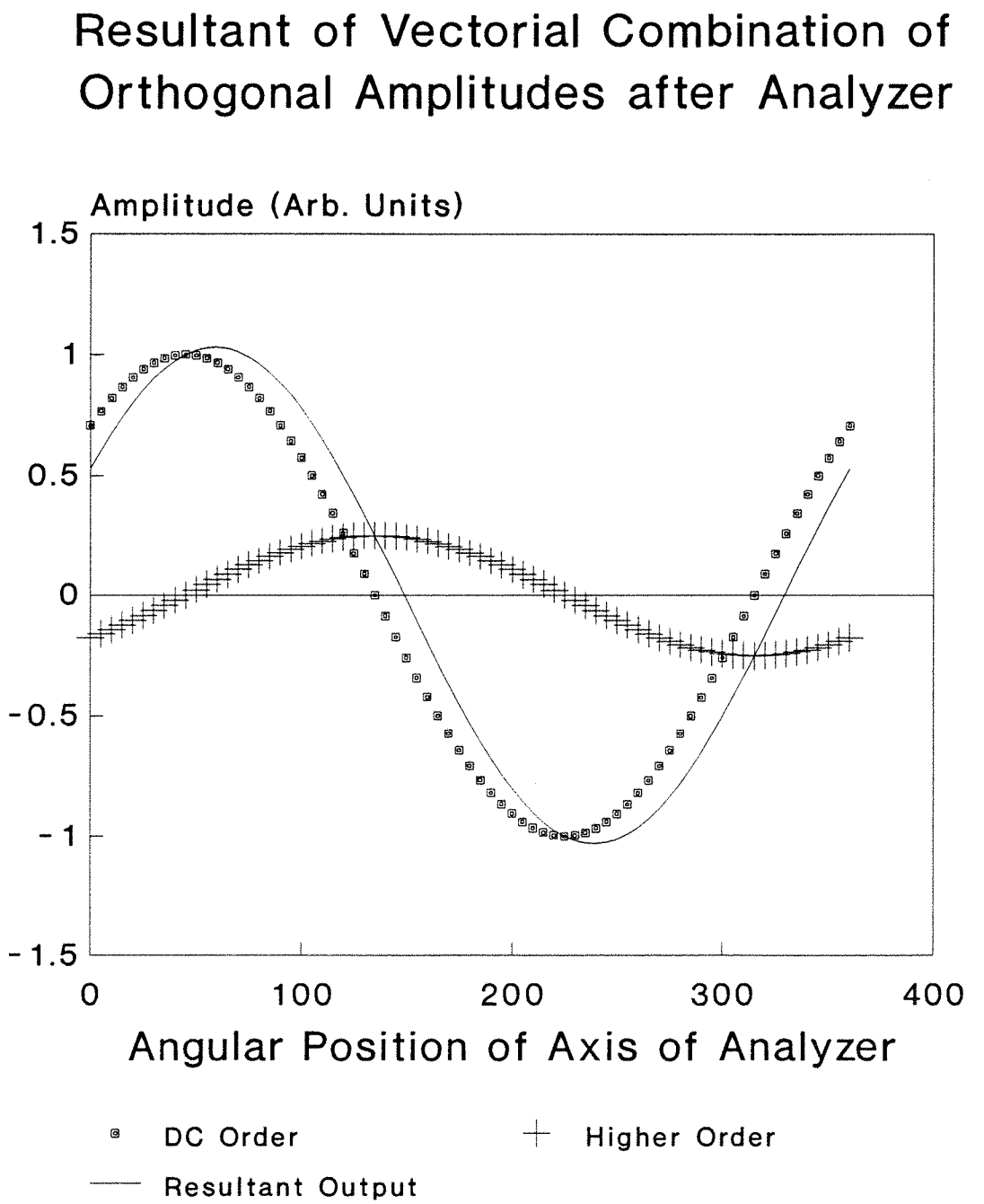

Figure 4.4 Plot of the output amplitude at the image plane when higher orders have the one-fourth amplitude as compared to DC versus angular position of the transmission axis of the analyzer.

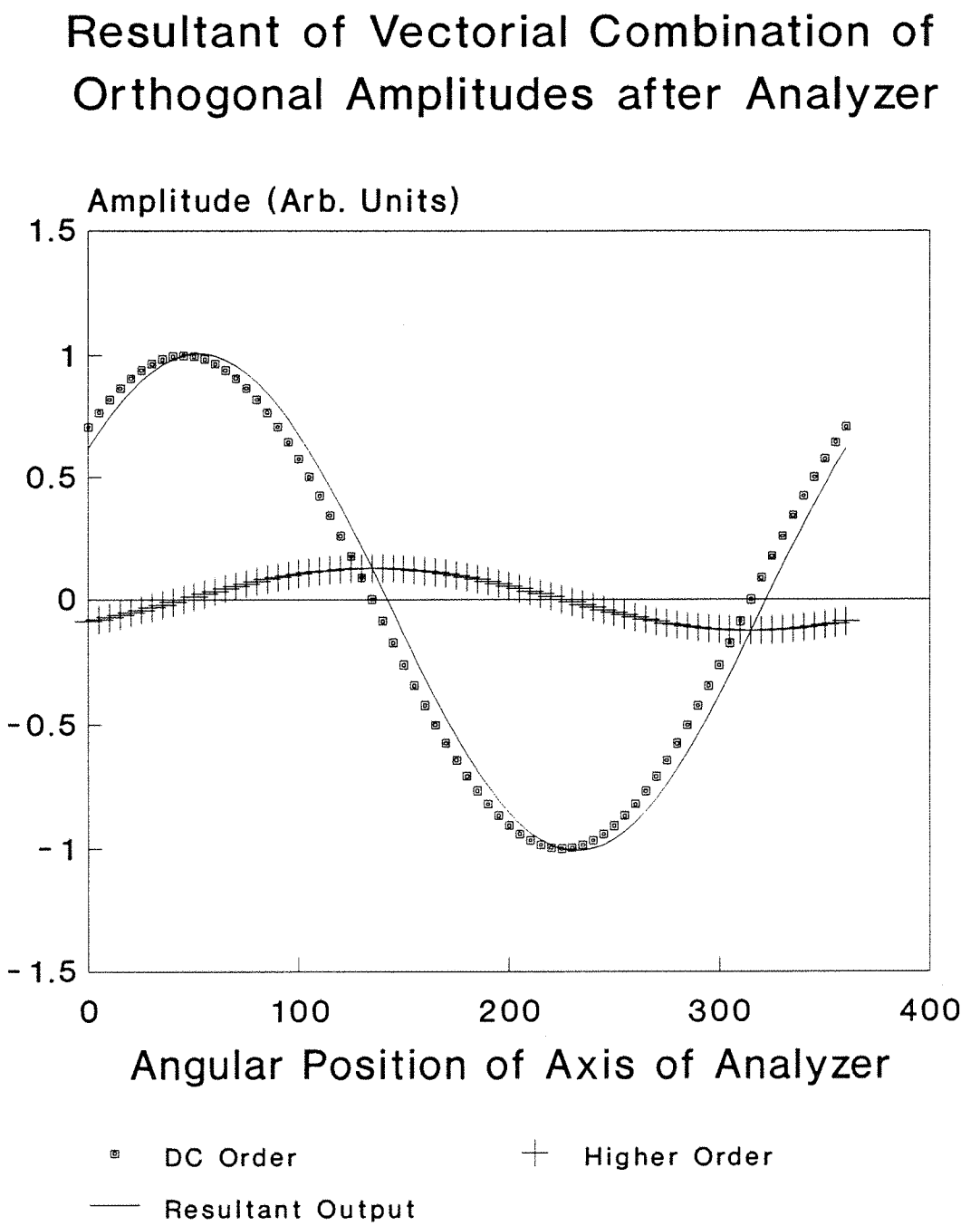

Figure 4.5 Theoretical plot of output amplitude at image plane for higher orders amplitude to be one-eighth of DC amplitude versus the angular position of the transmission axis of the analyzer.

which has not been diffracted. Usually the un-diffracted light is of considerably greater intensity than the diffracted light. Therefore, to compensate for the diffracted light, a ring-shaped amplitude filter is also used to reduce the intensity of the direct light and equalise its brightness to that of diffracted light to achieve the desired contrast. In addition to this absorption, as stated earlier, different phase plates are required to achieve positive and negative contrast images. A comparison of a conventional phase contrast microscope and our variable phase contrast microscope is illustrated via a schematic diagram in Figure 4.8. The basic set up is the same for both techniques. However positive and negative step phase filters are replaced by a single polarization rotation filter and a polarizer and an analyzer is added to the system.

Apart from Zernike's technique [4.24] for observing phase objects, there is another technique which is known as the dark ground technique [4.1]. In this technique, the un-diffracted (DC order) is removed completely by an opaque disk. Therefore the phase object is seen in the image plane as bright due to the localized diffraction of light on the dark background. This operation is also achieved using our technique by just rotating the analyzer to a position where its axis of transmission is parallel to the polarization direction of the diffracted light (higher orders), while perpendicular to that of un-diffracted light. This results in complete attenuation of the DC, and maximum transmission of higher orders. Therefore our technique not only improves on the previous techniques of phase contrast imaging but also combines these two techniques together.

In addition, visualization of fluid dynamics in wind tunnels is an important part of the structural test of aerodynamic systems. A flow visualization method in wind tunnels has been reported by Allario [4.25] which has been termed a **laser light sheet**. The plane of the light sheet can be moved along a model surface to observe the growth and dynamics of vortices.

We propose a technique of visualizing the wind structure along the model surface by illuminating it uniformly as shown in Figure 4.9. Subsequently taking the Fourier transform of the input distribution we can encode the Fourier transform by polarization rotation masks, and again analyzing the Fourier transform via an output

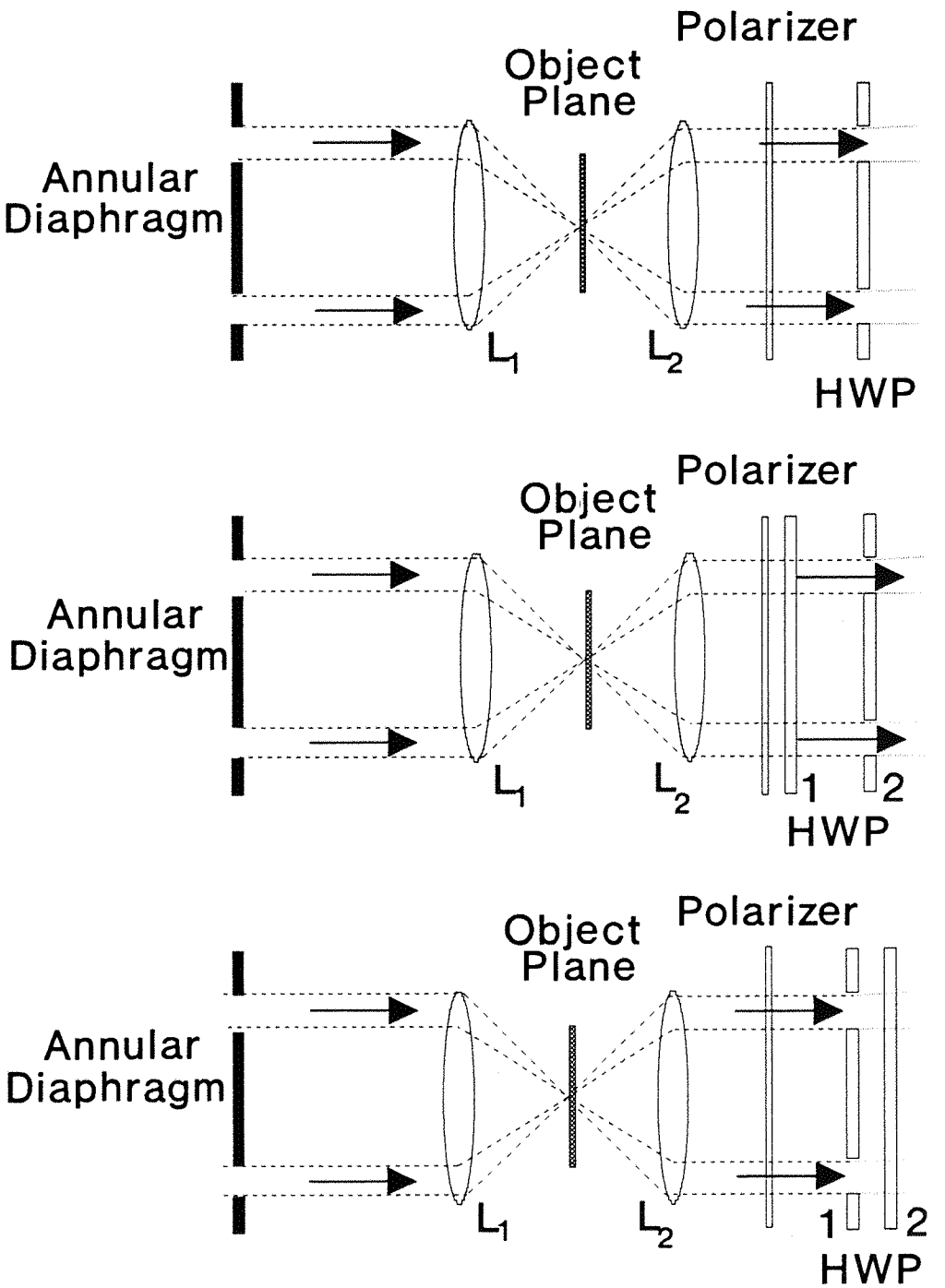

Figure 4.6 Schematic diagram shows the illumination schemes of an object and subsequent polarization encoding of the diffracted and non-diffracted light for variable phase contrast microscope.

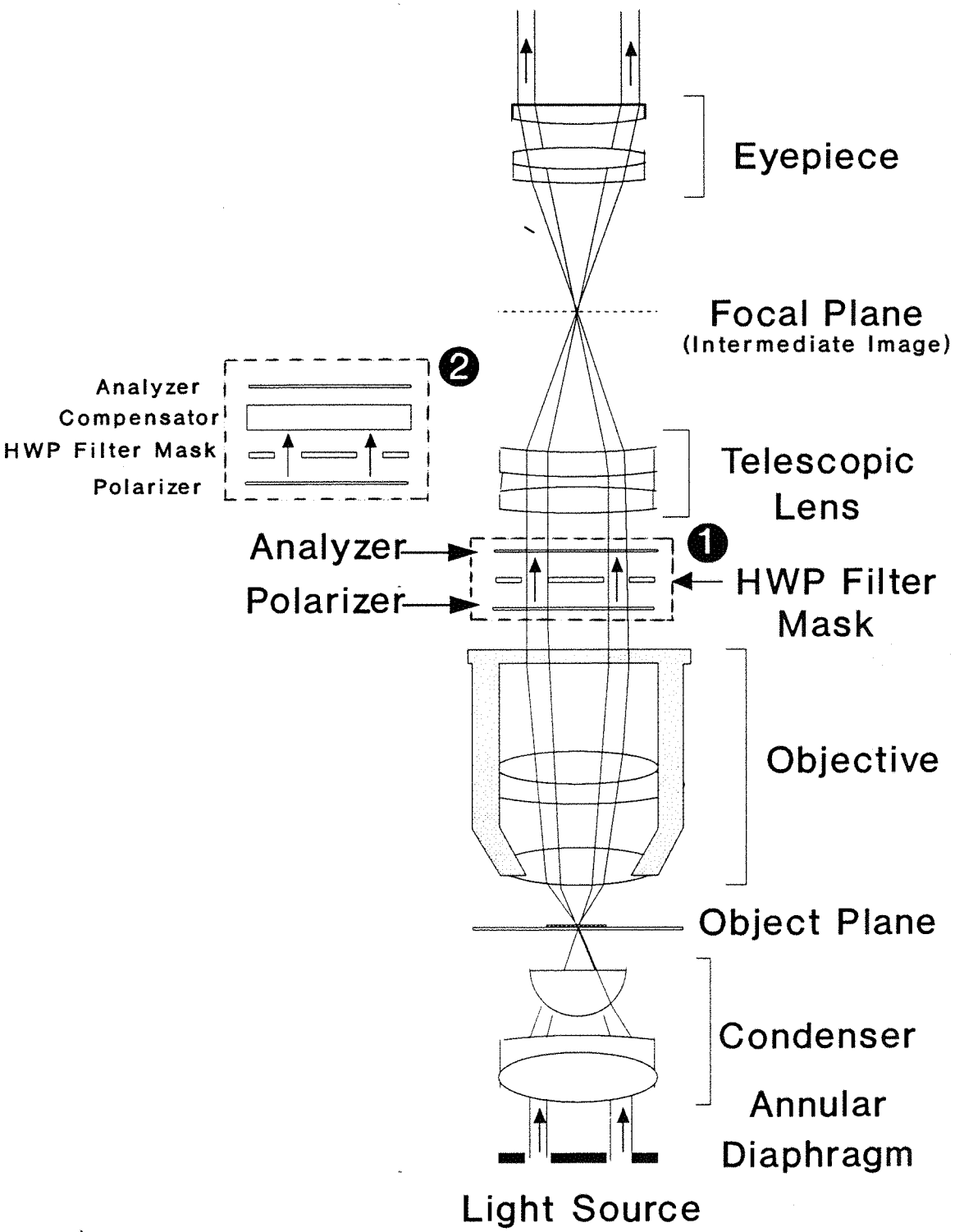

Figure 4.7 (a) Schematic diagram of variable phase and amplitude contrast microscope showing its basic features i.e, annular diaphragm, condenser, polarizer, a polarization rotation mask, and an analyzer.

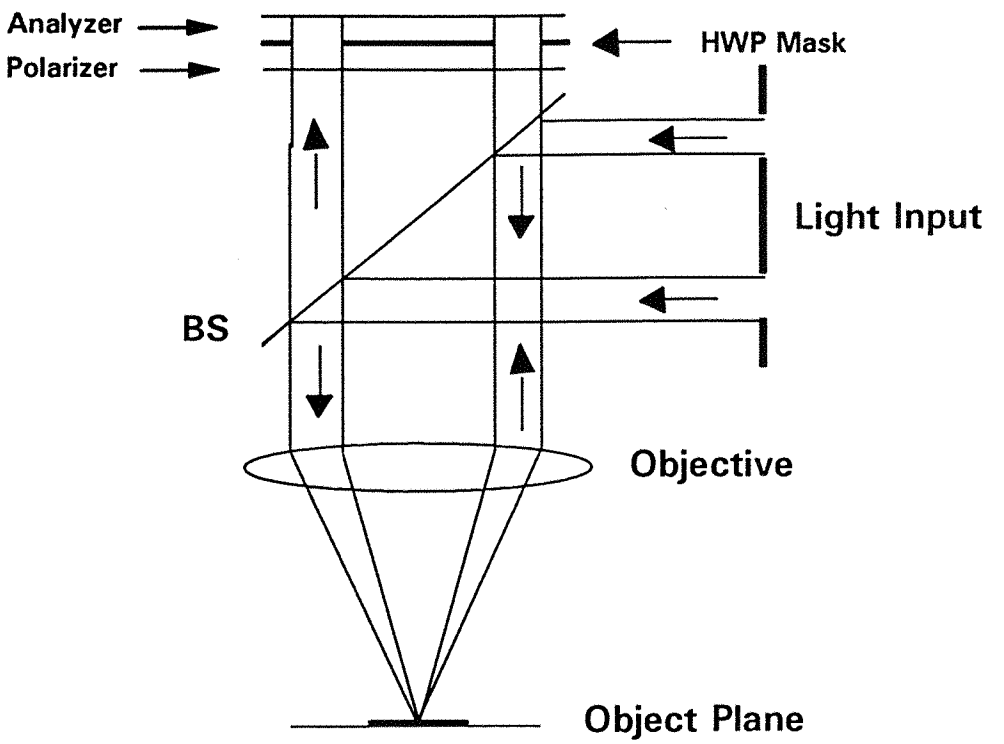

Figure 4.7 (b) Schematic shows the variable phase and amplitude contrast microscope in reflection mode.

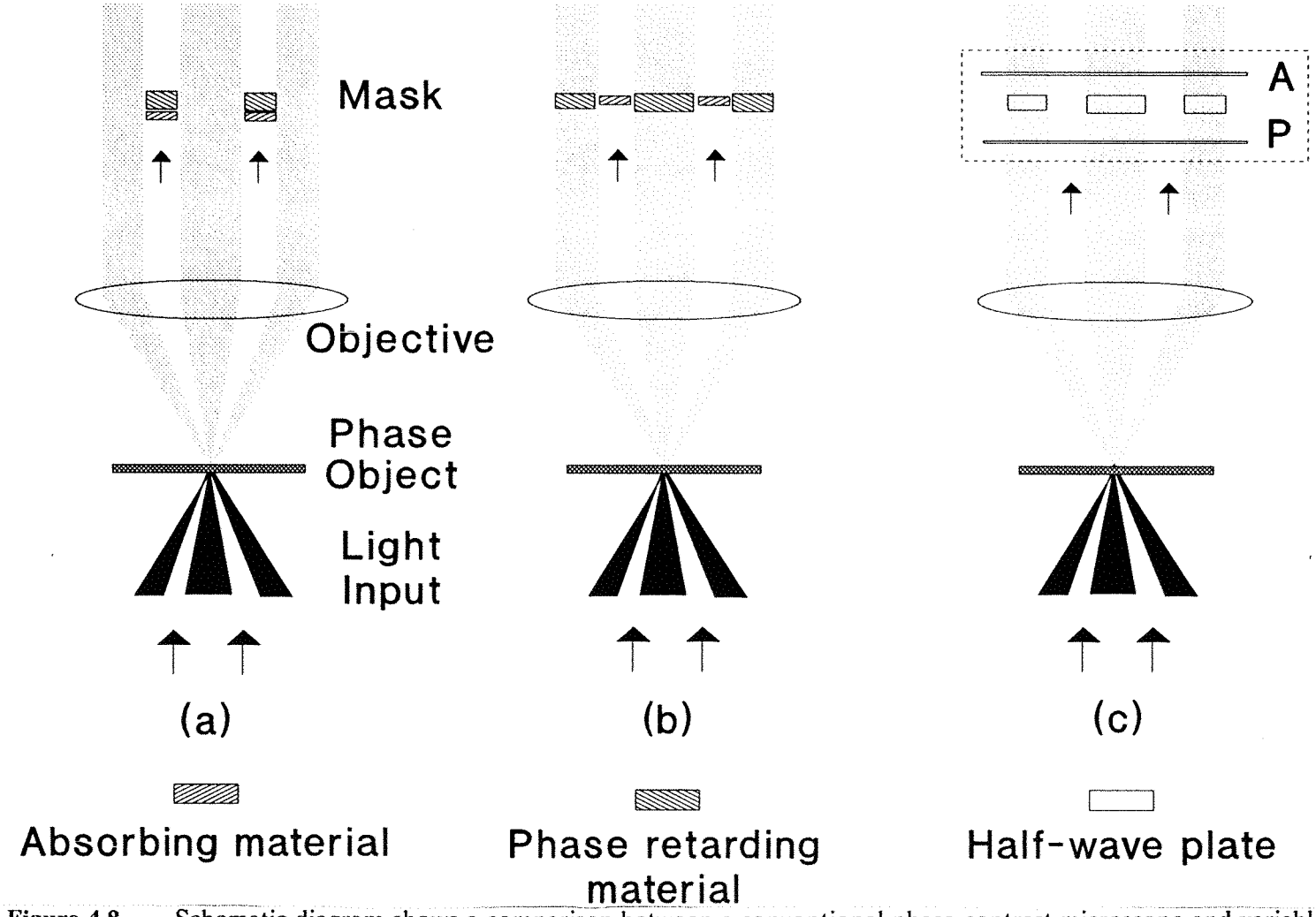

Figure 4.8 Schematic diagram shows a comparison between a conventional phase contrast microscope and variable phase contrast microscope. (a) and (b) shows arrangement for the conventional positive and negative phase contrast microscopes while (c) is a variable contrast phase microscope.

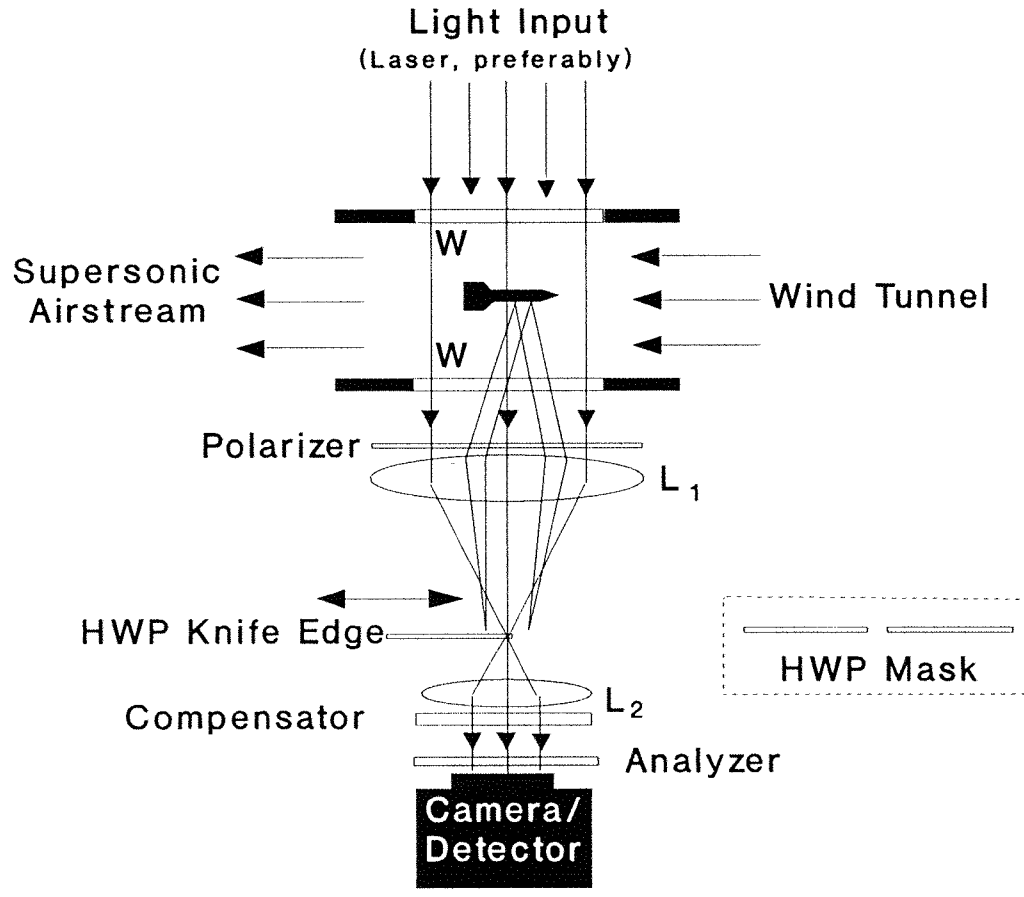

Figure 4.9 Schematic shows the optical arrangement for observing the aerodynamics in wind tunnels.

analyzer, to filter the DC component out, while allowing the diffracted light to pass. Such an arrangement will give rise to wind structure visualization around the model surface in the wind tunnel. However further manipulation of contrast can also be achieved via rotating the analyzer. Similarly other masks can also be placed in the Fourier transform plane, as will be discussed in Section 4.4, which will allow selection of different features (with optimum contrast also against the light background), within the field of view, such as some sharp feature in a particular direction.

4.2.2 Contrast manipulation using real time holography in BSO

The polarization encoding of the Fourier transform as described earlier can also be performed for amplitude objects by introducing a change in the direction of polarization of the zero and higher orders. As shown in Figure 4.1, where the three possible arrangements for polarization encoding of an object Fourier transform are illustrated we now consider here the arrangement (b). An input beam is passed through a (rotatable) half-wave plate which rotates the plane of polarization of the input. The input beam I_{in} then passes through the object transparency, lens L_1 forms the Fourier transform of the input light distribution in the back focal plane where a second half-wave plate HWP_2, is situated with a hole in the central region. The DC order passes through the central hole without changing its polarization direction while the higher orders undergo a second change in polarization on passing through the HWP_2. Lens L_2 performs the inverse Fourier transform of the light distribution in its front focal plane, to form the modified image of the object.

In a DFWM set-up as shown in Figure 4.10, the polarization encoded image interferes with a linearly polarized reference beam inside a photorefractive medium to record two multiplexed holograms, one of them corresponding to the zero order while the other to higher orders, in the Fourier transform plane.

The index of modulation inside the photorefractive medium (at the image plane), for the background illumination and higher spatial features can be expressed as

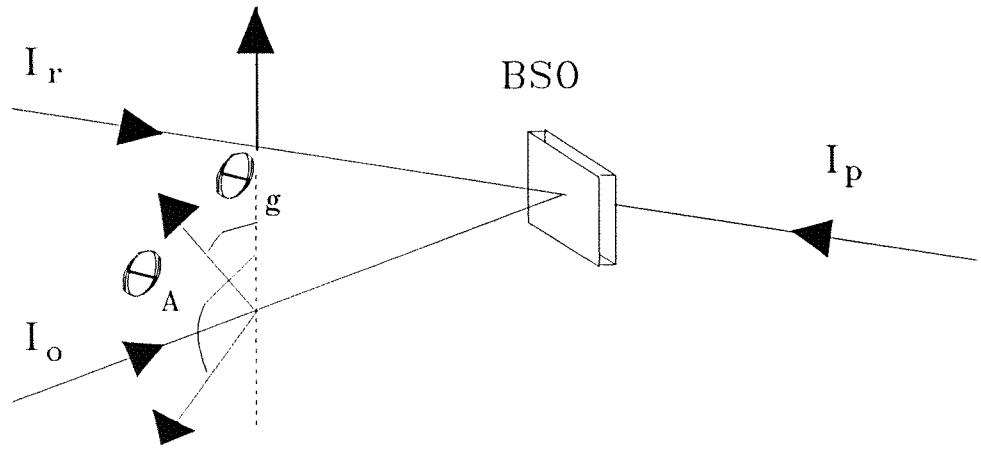

Figure 4.10 Schematic diagram shows the arrangement to record multiplexed holograms inside a photorefractive crystal of BSO.

$$m_A(x,y) = \frac{2E_r E_A Cos\theta_A}{(E_r^2 + E_A^2)} \qquad (4.2)$$

$$m_g(x,y) = \frac{2E_r E_g Cos\theta_g}{(E_r^2 + E_g^2)} \qquad (4.3)$$

Where E_r is the amplitude of the reference beam, E_A is the amplitude of the background illumination, E_g is the amplitude of the spatial features, θ_A is the angle between the direction of polarization of the reference beam I_r and background (zero order), illumination, and θ_g is the angle between the polarization of I_r and the polarisation angle of the light corresponding to the spatial information (higher orders).

4.2.2.1 Edge Enhancement and Low Pass Filtering

Equations (4.2) and (4.3) show that the index of modulation can be modified by changing the angles θ_A and θ_g. Therefore under a set of parameters such as beam intensities and angle between the beams, operations of contrast manipulation can be performed by varying the polarization of the interfering beams. Edge enhancement can be achieved when θ_g is 0° (or 180°), and θ_A is 90° (or 270°), i.e., m_g is maximum while m_A is zero. Similarly operation of low pass filtering can be achieved when θ_g is 90° (or 270°), and θ_A is 0° (or 180°), in which case m_g is zero and m_A is a maximum.

4.2.2.2 Positive and Negative Contrast Manipulation

Real time inversion of contrast is an important algebraic operation in signal processing. This simple operation needs a comparatively long time using digital electronics because of the serial nature of the process. Contrast inversion can also be achieved by our technique by recording the multiplexed gratings with opposite phases. For this purpose a BSO crystal can be used in the $K_g \perp <001>$, configuration which works as a half-wave plate (for an ideally thin crystal), [4.26], for the readout beam polarization.

Recording of multiplexed gratings in BSO with opposite phases will give rise to two gratings corresponding to the DC and higher orders. As we know that BSO is not a polarisation-preserving phase conjugator in the usual arrangement, and therefore polarization of the output phase conjugate beam will be different than that of the input signal, the direction of polarization of the phase conjugate output can be controlled via control of polarization of the readout beam, and optical path length. Because the gratings corresponding to DC and higher orders respectively are opposite in phase, the phase conjugate outputs will also have a relative phase shift of 180°, but with the same polarization direction.

The scheme of recording two such gratings in photorefractive BSO is illustrated via Table 4.2. Column (2), of the table shows the input polarization of the signal beam before the object plane; column (3), shows the direction of polarization of the DC order, which is same as the input polarization in the Fourier plane. The polarization of the higher orders is encoded via HWP_2 (with a central hole for the DC) and is shown in column (4). The object is imaged inside the BSO crystal where it interferes with a reference beam via multiplexed gratings. The two gratings may or may not be in-phase depending upon their relative initial phases. The polarization of the phase conjugate output DC and higher orders from the BSO crystal is shown in column (5). We assume here that the output polarization from the BSO is in the vertical direction (0°). Column (6), shows the polarization directions of the DC from the BSO crystal, while column (7), illustrate the polarizations of DC and higher orders after HWP_2. Column (8), shows the interference of polarized light at the analyzer where the oblique dotted line is the transmission axis of the analyzer.

We may consider cases (b) and (d), for negative image contrast at the image plane after destructive interference at the analyzer. In case (b), the polarizations of the DC and higher orders are at 45°, but on passage through HWP_2, the two spatial orders become out of phase. Therefore the two multiplexed gratings are recorded out of phase and the corresponding phase conjugate outputs will also be out of phase as shown in column 5(b). After they retraverse through HWP_2 the polarization of the higher orders is rotated to 90°. Consequently the DC and higher orders are now of orthogonal polarizations. By placing an analyzer before the image plane these two orders interfere via their resolved components along the transmission axis of the

(1)	(2)	(3)	(4)	(5)	(6)	(7)	(8)
	Input Polarization	Polarization of Input *DC*	Polarization of Input HO	Polarization of Output DC & HO	Polarization of Output		Interference at Analyzer
					DC	HO after HWP	
a	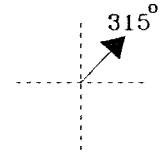	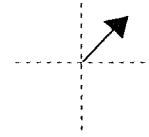	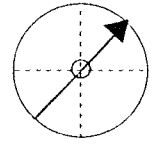	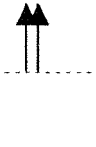	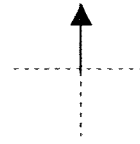	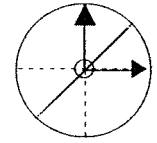	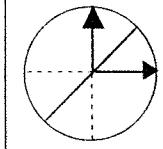
b	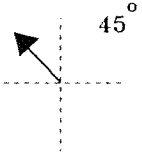	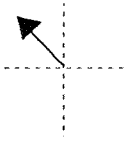	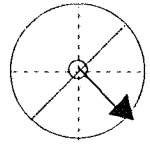	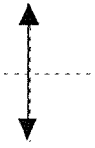	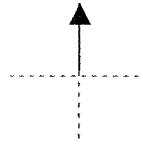	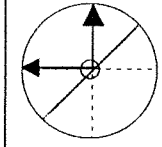	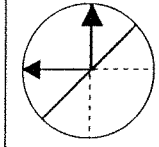
c	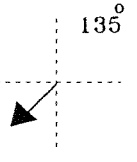	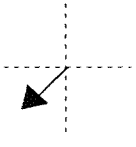	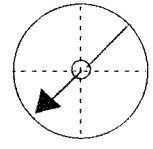		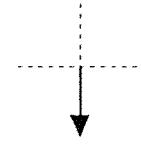	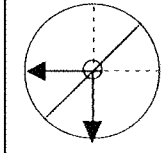	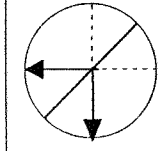
d	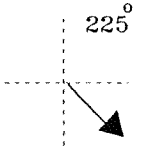	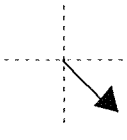	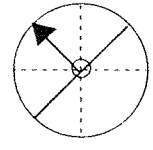	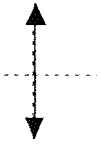	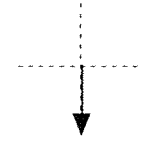	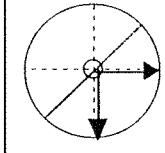	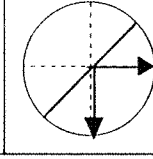

Table 4.2 Illustrate the polarization states for polarization encoding scheme of Figure 4.1(b), using DFWM in a BSO crystal.

analyzer, to produce a negative contrast image. Similarly in case (d), the input DC and higher orders polarization directions are at 225°. The interfering components of DC and higher orders are again out of phase inside the crystal, hence their outputs will also be out of phase. After higher orders pass through the HWP_2, the polarization directions of the phase conjugate DC and higher orders are orthogonal and the analyzer again produces a negative contrast image.

For a positive contrast output image, we consider cases (a) and (c). In (a), the input polarization is 315°. After passing through HWP_2 higher orders remain in the same polarization direction. The input polarization components of DC and higher orders are in phase therefore they record two in-phase gratings with a common reference beam. The phase conjugate output from the two gratings will therefore be in phase as well. At the Fourier plane, polarization of all higher orders is rotated to the horizontal direction, as shown in column 7(a). The in-phase, parallel components of the two orders along the transmission axis of the analyzer interfere constructively to give a positive contrast image. Similarly case (c), can be explained for positive contrast image.

As described in Table 4.2, which elaborates the polarization encoding scheme of Figure 4.1(b), the phase conjugate output does not re-traverse through HWP_1 and is directed towards an image plane. However the same polarization scheme can be used in polarization modulation mode when the phase conjugate output does re-traverse HWP_1 as well. Because the input and phase conjugate output polarizations are fixed, the phase conjugate output polarizations corresponding to DC and higher orders can therefore be manipulated via rotating either HWP_1 or HWP_2 or both.

Table 4.3, describes the polarization states using the above scheme, assuming the input polarization is at 90° and the polarization of the phase conjugate output is in a plane at 45°. The input beam passes through the object transparency and subsequently through the HWP_1. In case (a) column 3, the fast axis of HWP_1 is oriented at 0° therefore the polarization of the input beam is rotated to 180°, and remains in the same plane, and is subsequently Fourier transformed by a lens. In the Fourier plane, HWP_2 is placed with its central hole to pass the DC without further modulating its polarization. However, the higher orders are rotated as they pass

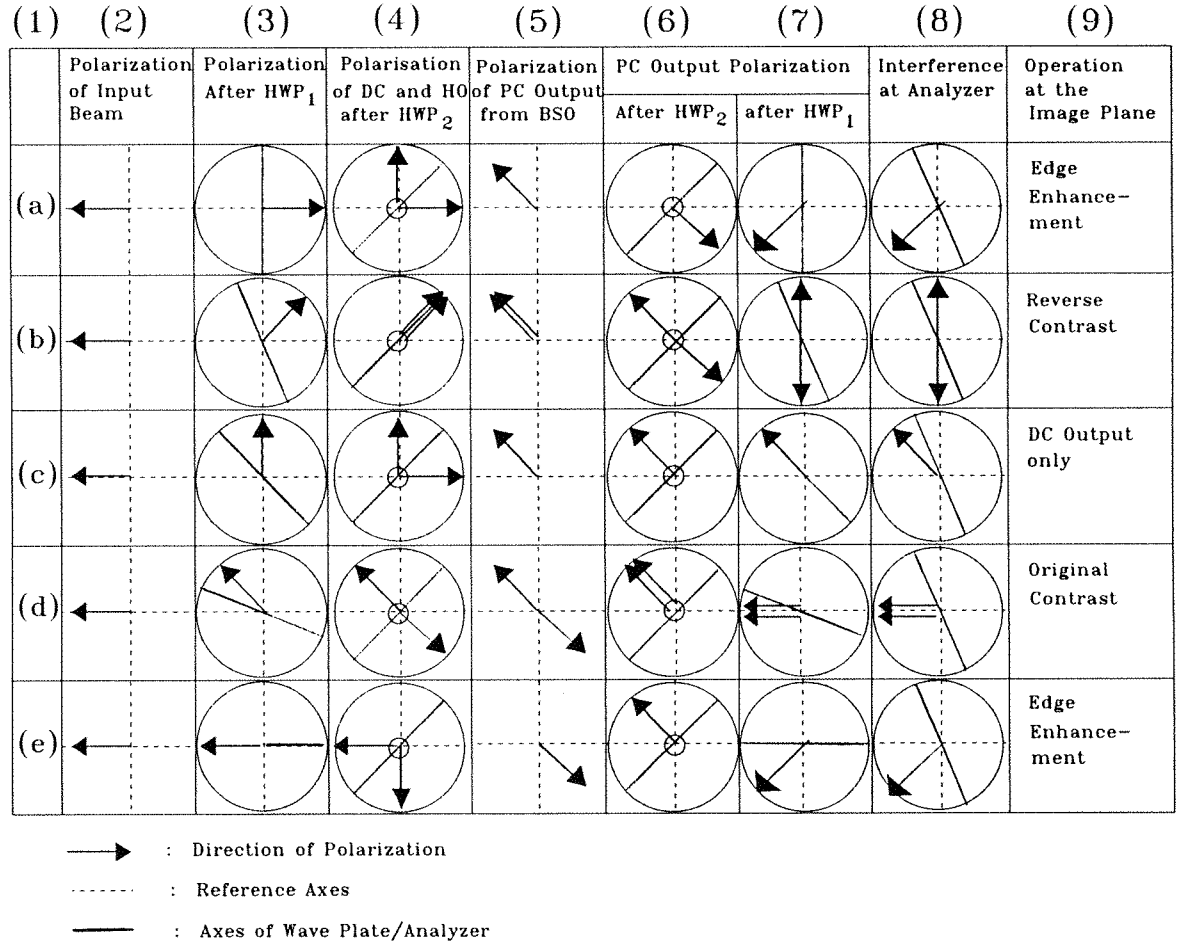

Table 4.3 Shows the polarization states for polarization encoding scheme of Figure 4.1(b), working in "polarization modulation mode" for phase conjugation output.

through HWP_2 whose fast axis is fixed at 135°. The phase conjugate output from BSO is in a plane at 45°. When higher orders traverse back through HWP_2 their polarization direction is rotated to 225°. Subsequently re-traversing HWP_1, their polarization is rotated to a position at 135°. An analyzer is placed at the output with its angle of transmission at say, 30°. The phase conjugate output is resolved along the transmission axis to give an edge enhanced image.

In case (c), the DC input to the BSO is in the vertical direction while higher orders are horizontally polarized. Therefore in the crystal plane only the DC component interferes with the reference beam which is also vertically polarized. In case (b), it is shown that the input polarizations of DC and higher orders are parallel and are at 315°. Therefore phase conjugate output polarizations of both sets of orders are in phase. However after higher orders pass through HWP_2 they undergo a rotation of 180° (or a phase shift of 180°), while the DC remains in the same initial direction. Consequently the DC and higher orders are out of phase. When they pass through HWP_1, both are rotated to the vertical, but are still out of phase. At the analyzer both orders are resolved along the transmission axis and are therefore subtracted to produce an inverse contrast image. In case (d), the input polarizations to the BSO are out of phase. Therefore the phase conjugate output from the BSO will also be out of phase. After passing HWP_2, both orders become in phase and are subsequently rotated to the horizontal direction when they both pass through HWP_1. At the plane of the analyzer both the orders are resolved along its transmission axis in phase to give a positive contrast image.

The third arrangement of polarisation encoding of Figure 4.1(c) is illustrated in Table (4.4). Cases (a) and (e), illustrate the polarization states at various stages when operation of DC pass is achieved.

The arrangement to achieve original contrast is illustrated via case (b). When the fast axis of the HWP_2 is at 90° as shown in case (c), the polarization of input higher orders is rotated through 180° in the vertical plane while the DC remains in the horizontal direction. Therefore only the higher orders record the gratings which therefore gives an edge enhanced image. Similarly case (d) can be explained for reverse contrast image.

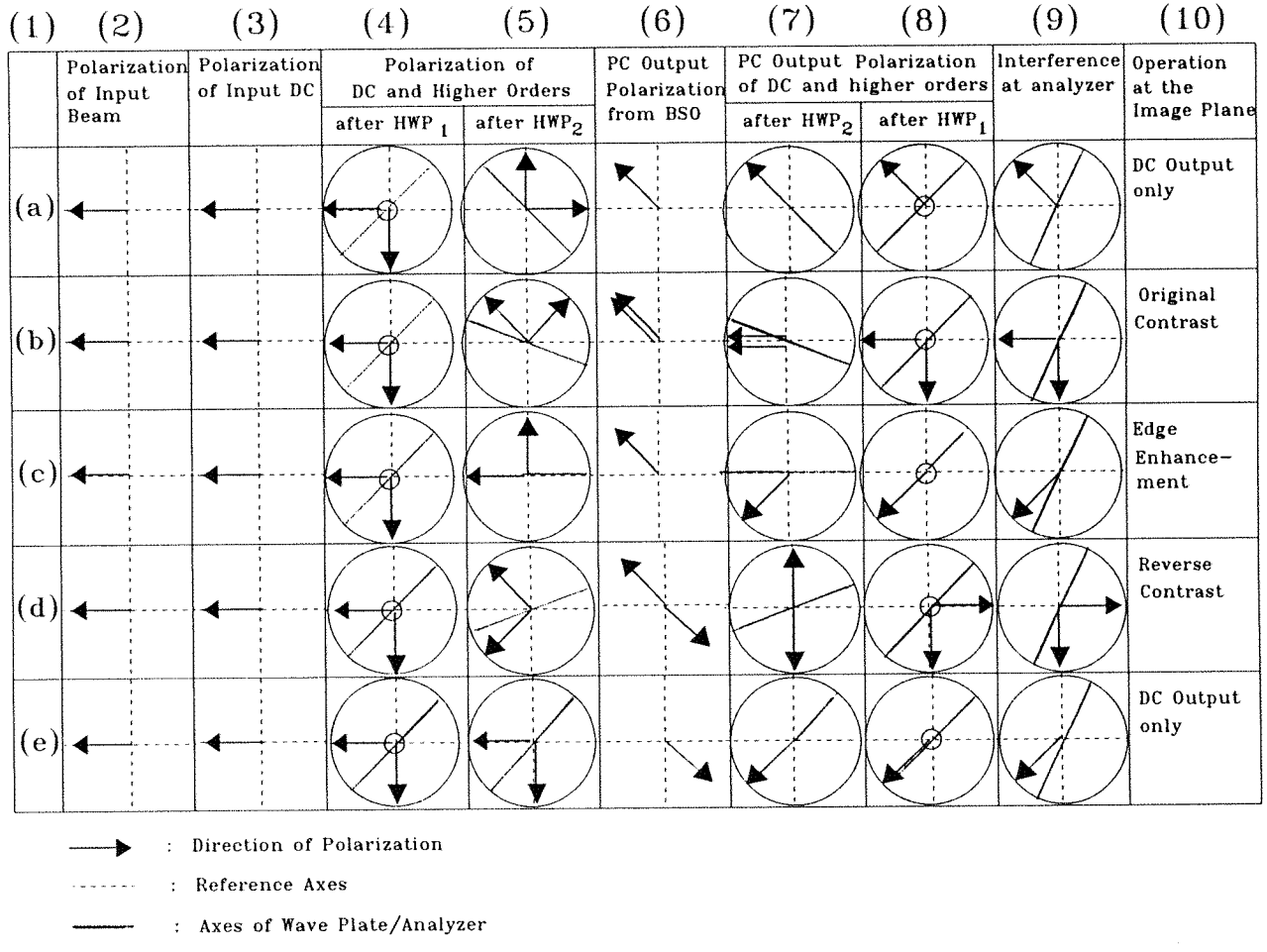

Table 4.4 Shows the polarization states for polarization encoding scheme of Figure 4.1(c), in "polarization modulation mode" for phase conjugate output.

Using the above mentioned configurations, contrast manipulation techniques such as edge enhancement, DC pass filtering, positive contrast, negative contrast and contrast enhancement of images can easily be achieved by rotating the polarizer at the output. To achieve a better contrast image, an optimum combination of light amplitude of the higher spatial frequency features with a certain DC illumination is required.

4.2.3 Selective Amplification via Polarization Encoding in Two Beam Coupling

Figure 4.11 shows the standard configuration for two-beam coupling in which two coherent beams intersect at an angle θ inside a photorefractive crystal, such as $BaTiO_3$. The direction of energy transfer between the two beams depends on the crystal orientation, experimental geometry and material parameters. In Figure 4.11 energy couples from the reference beam I_r, to the signal beam I_o and the gain is given by

$$G=\frac{I_o(L)}{I_o(0)} \qquad (4.4)$$

$$G=\frac{(1+r)\exp(\Gamma L_{eff})}{1+r\exp(\Gamma L_{eff})} \qquad (4.5)$$

Where r is the ratio of signal to reference beam intensity, L_{eff} is the effective interaction length and Γ is the exponential gain coefficient. Equation (4.5) shows that the gain experienced by the signal beam depends on the beam intensity ratio. For: (i) $r \approx 1$, the gain approaches a limiting value of 2; (ii) $r << 1$ gain approaches a saturated value i.e., $G_{sat} = \exp(\Gamma L_{eff})$; (iii) While for intermediate values of 'r' the gain is almost inversely proportional to the beam intensity ratio ($G \propto 1 / r$).

We have previously demonstrated contrast manipulation via two beam coupling using regions (i) and (iii) above, via two beam coupling in $BaTiO_3$. The DC in the object Fourier transform inside the crystal was in region (i), while the higher spatial frequencies lie within region (iii), and the gain in this region depends on the individual intensity ratios of all of the Fourier orders. Therefore in conventional two beam coupling the spatial filtering character mainly depends on r and preferential amplification takes place for low intensity (higher) orders. Using this technique we

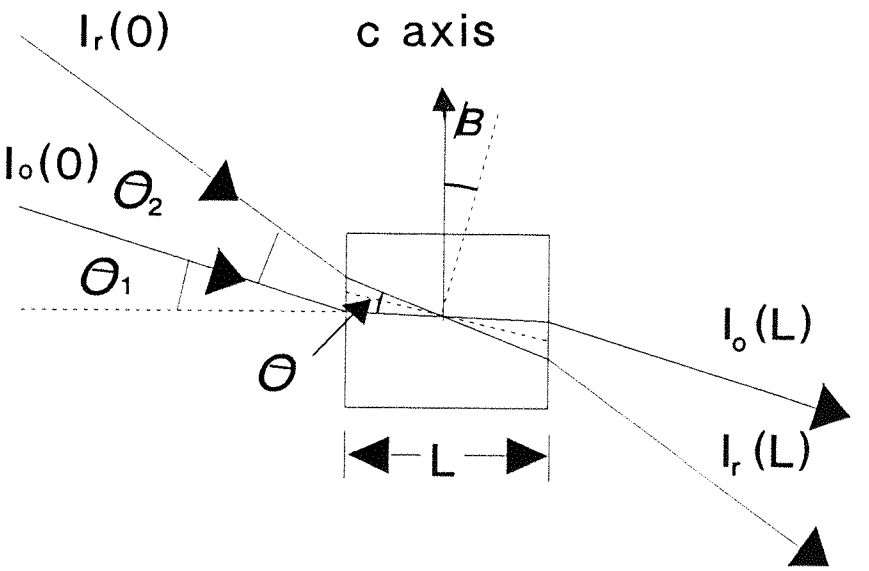

Figure 4.11 Shows the standard configuration for two beam coupling arrangement.

demonstrated contrast enhancement, defect enhancement and feature extraction in Chapter 3. In previously reported techniques of spatial filtering via two beam coupling, the controlling factor for variable gain is the beam intensity ratio only. The limitations of these previous techniques are clear, where the requirement is to amplify certain spatial frequencies only, while the others remain intact.

In photorefractive crystals in the absence of any intrinsic or applied field the total space charge electric fields E induced by the interference pattern is given by [4.27],

$$E=\left(\frac{k_B T}{q}\right)\frac{k_g}{\left(1+\frac{k_g}{k_o}\right)}e_1^{*}\cdot e_2^{*} \qquad (4.6)$$

Where k_BT is the thermal energy, q is the charge of mobile charge carriers, k_g is the magnitude of the grating wavevector, and e^*_1 and e^*_2 are unit polarization vectors of the two interfering beams. Equation (4.6) shows that by varying the unit polarization vectors e^*_1 and e^*_2 we can vary the space charge electric fields E. Therefore we can manipulate the two beam coupling gain not only by varying the intensity of the two beams alone but also by changing the relative polarizations of the interfering beams.

The techniques of polarization encoding described in Figure 4.1 can also be used in two beam coupling to achieve preferential amplification of the desired Fourier orders while leaving others unamplified. This can be realized by manipulating the polarization of the DC and higher orders. Therefore, as in the case of BSO, we can also record multiplexed gratings corresponding to DC and higher orders in $BaTiO_3$. However in this case, recording of complementary gratings to observe contrast inversion may not be realized because of the unequal amplification of higher orders as compared with the DC. Good contrast inversion can be achieved only if the ratio of intensities of the DC and higher orders in the image plane is the same as that in the object plane. Such a balance may be difficult to achieve in the case of two beam coupling in a medium where gain depends on beam intensity ratios. However, we may realize contrast inversion by recording complementary gratings in region (ii) of saturated gain described above, where all the orders receive almost equal gain.

4.3 Experimental Arrangement

4.3.1 Variable phase contrast imaging

Figure 4.12 shows the experimental arrangement of phase contrast imaging for the parallel illumination case. The laser input was spatially filtered and then expanded by a combination of two ordinary lenses L_1 and L_2. The object plane was at the front focal plane of L_3. The object, in the form of a transparency or glass slide, was placed in the object plane to be Fourier transformed in the back focal plane of L_3. Two different half-wave plates one with a central precision hole of 200 μm (drilled by Exitech, UK), and the other with a 600 μm hole are used as Fourier plane modulators. The DC component of the object passes through the hole and therefore remains of the same polarization, while the higher orders were rotated to an orthogonal direction as they pass through the half-wave plate. An analyzer is placed before the image plane to select the continuously variable proportion of DC and higher orders.

Figure 4.13 shows a sequence of photographs of a phase object (a transparent section of a leaf) on a microscope slide. Figure 4.13 (a) shows photographs of the original object which shows poor contrast while photographs (b)-(l), show the results of contrast manipulation when the analyzer is rotated to select the sequence of different proportions of DC and higher orders for both in phase and out of phase components.

Photograph (b) shows that only higher orders are passed and the DC is attenuated when the transmission axis of the analyzer was at 90°. Photograph (c) shows the contrast when the transmission axis of the analyzer was at 75° and horizontally polarized higher orders are transmitted more than the DC component. Photograph (d) shows the result when the axis of the analyzer was at 60°. Photograph (e) shows the contrast of the transparent leaf when the transmission axis of the analyzer was at 45°. At this position the DC and higher orders pass equally and we may say it is the positive contrast. Photograph (f) to (h) shows results when the transmission axis of the analyzer were at 30°, 15° and 0° respectively. Photograph (h) shows when all the DC (vertically polarized), is transmitted plus a small amount of higher orders,

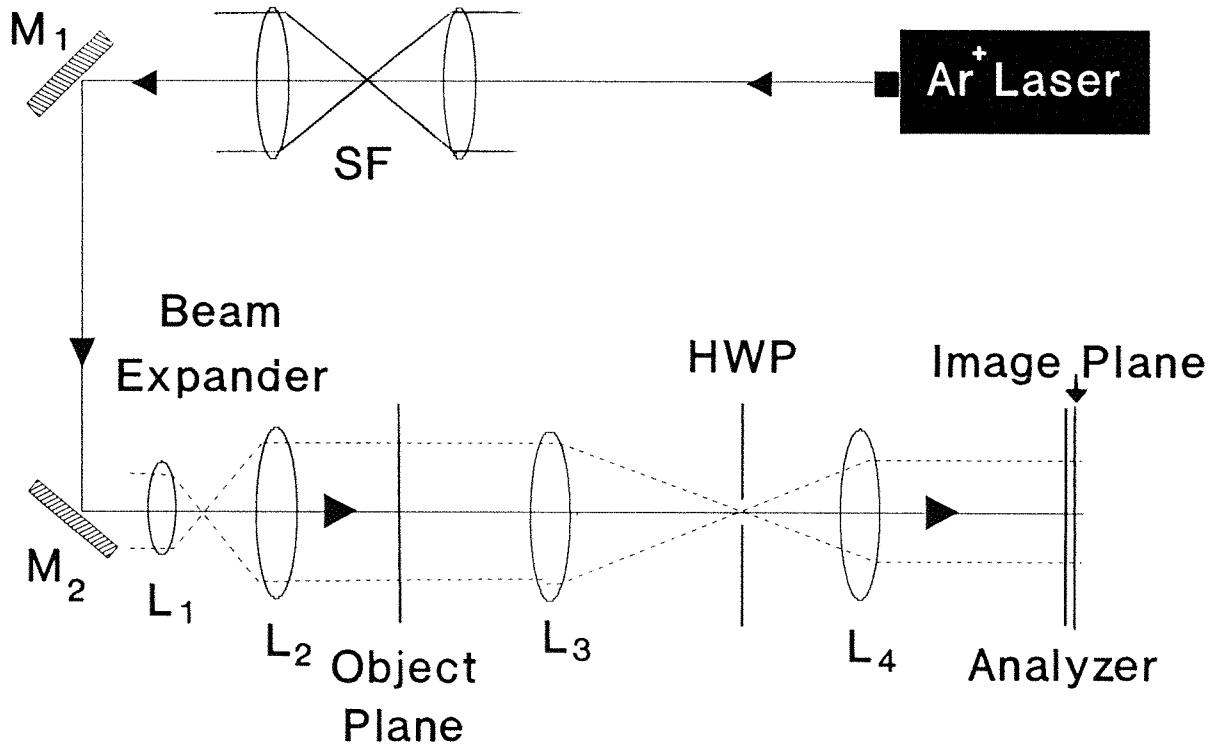

Figure 4.12 Experimental arrangement for phase contrast imaging.

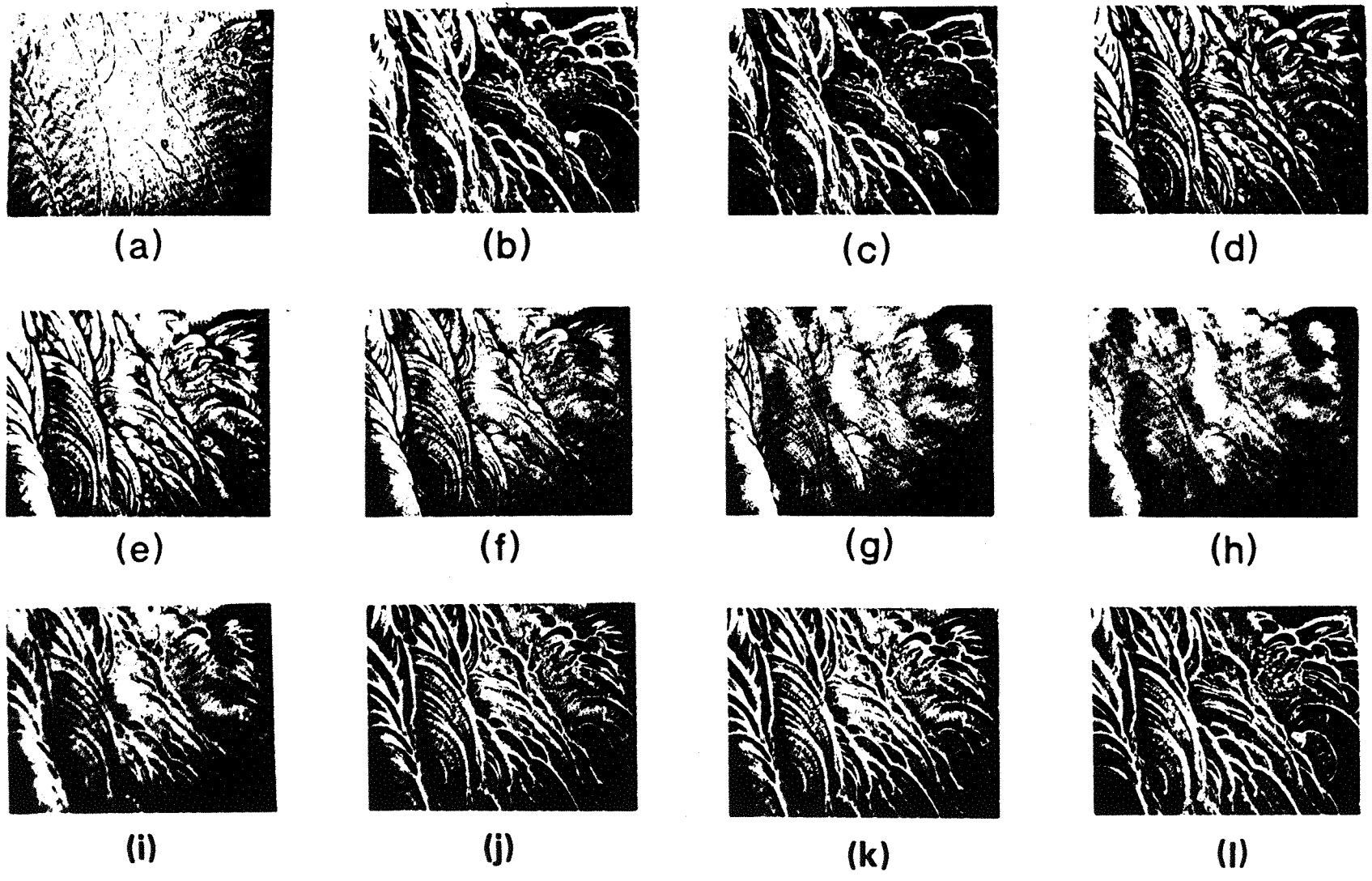

Figure 4.13 Shows a sequence of photographs of a transparent microscope slide of a leaf.

which may be due to the unintentional inclined axis of the analyzer or the polarizer of the higher orders. Photographs (i) to (l) shows results when the transmission axis of the analyzer were at 330°, 315°, 300° and 285° respectively. Photograph (j) shows reverse contrast to that of Photograph (e). In this case DC and the higher orders are equally transmitted and hence interfere with out-of-phase components.

Figure 4.14, shows a sequence of photograph of a phase object (in this case an oil smear). Photograph (a) shows the original object which shows little detail. Photographs (b)-(f) show the results of contrast manipulation at different angular positions of the analyzer. Photograph (b) shows the results when the analyzer was at 0° and all the vertically polarized higher orders were transmitted. Photograph (c) shows the results when the analyzer was rotated to 45° which means equal transmission of the background information as well as spatial features took place. This shows more details as compared to photograph (b) due to the mutual interference of the two components of light. Photograph (d) shows the results that are observed when the analyzer was placed at 90° to allow transmission of all the horizontally polarized background components. Photograph (e) shows the results when the axis of the analyzer is oriented at 135° to pass equal proportions of the DC and higher orders components, with opposite phases to that shown in photograph (c). Photograph (f) shows results when the polarization of the input light is changed to 135°, which means DC and higher order features are polarized in one plane and shows similar results to Photograph (c).

Our technique is not restricted to phase objects only but can equally well be applied to amplitude objects. We have additionally demonstrated the contrast manipulation of a grey level object which is in this case was a Cactus plant. Figure 4.15 shows a sequence of photographs of contrast manipulation for different angular positions of the analyzer. Contrast manipulation of a binary object is shown in Figure 4.16, which shows positive and negative contrasts as well as high and low pass filtering. The above experimental results suggests that our technique of passive contrast manipulation is a flexible and versatile technique which process the image very quickly unlike other conventional photographic or holographic techniques.

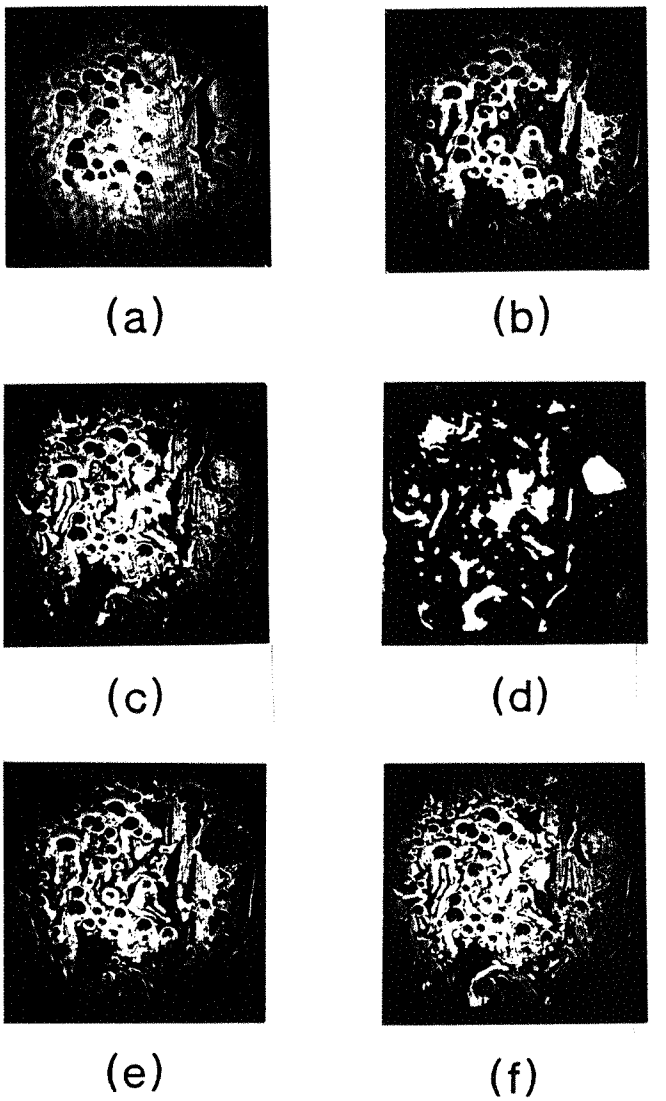

Figure 4.14 Photographs showing the contrast manipulations of an oil smear on a glass slide.

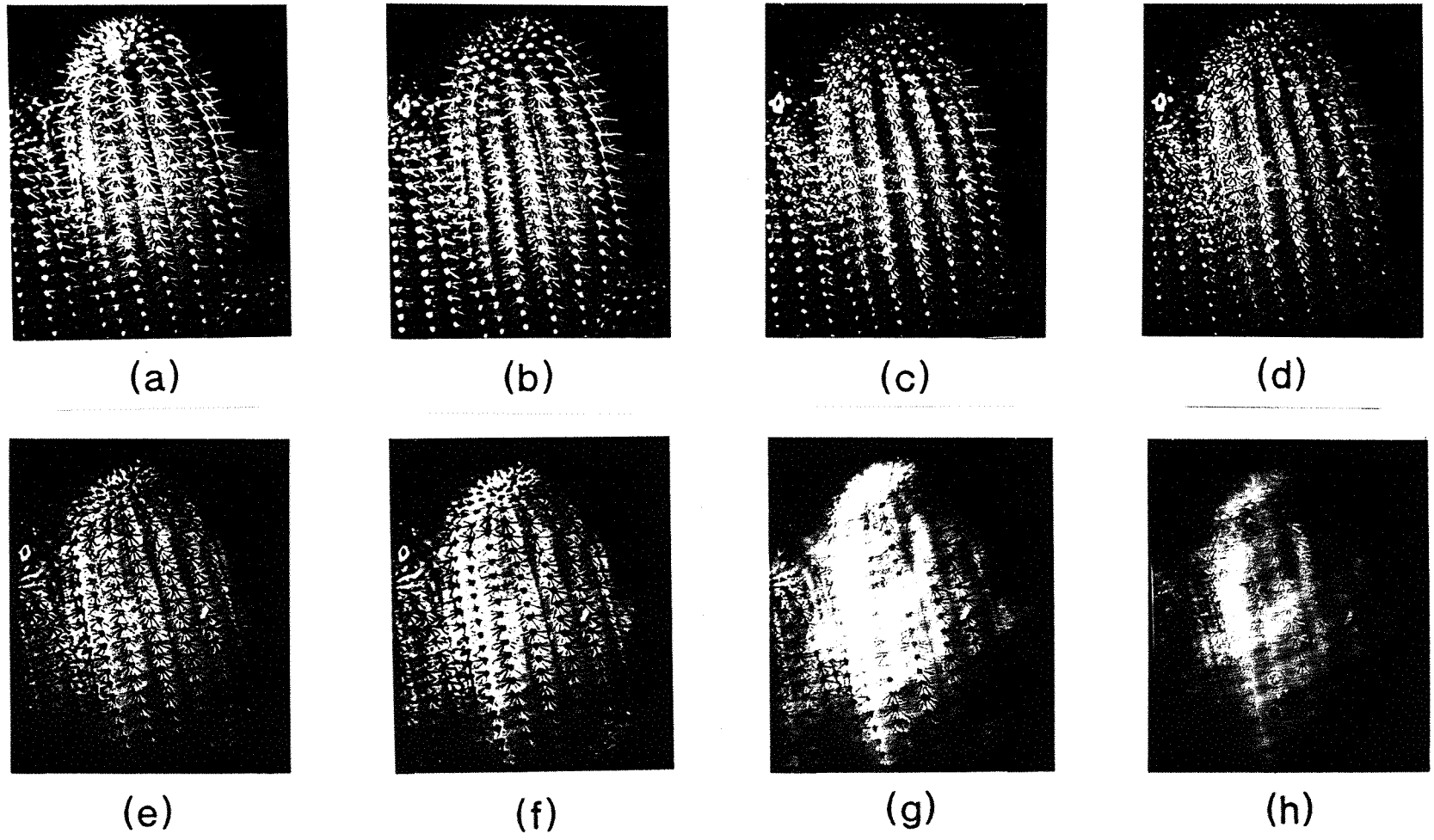

Figure 4.15 Sequence of photographs showing contrast manipulation of a grey level object.

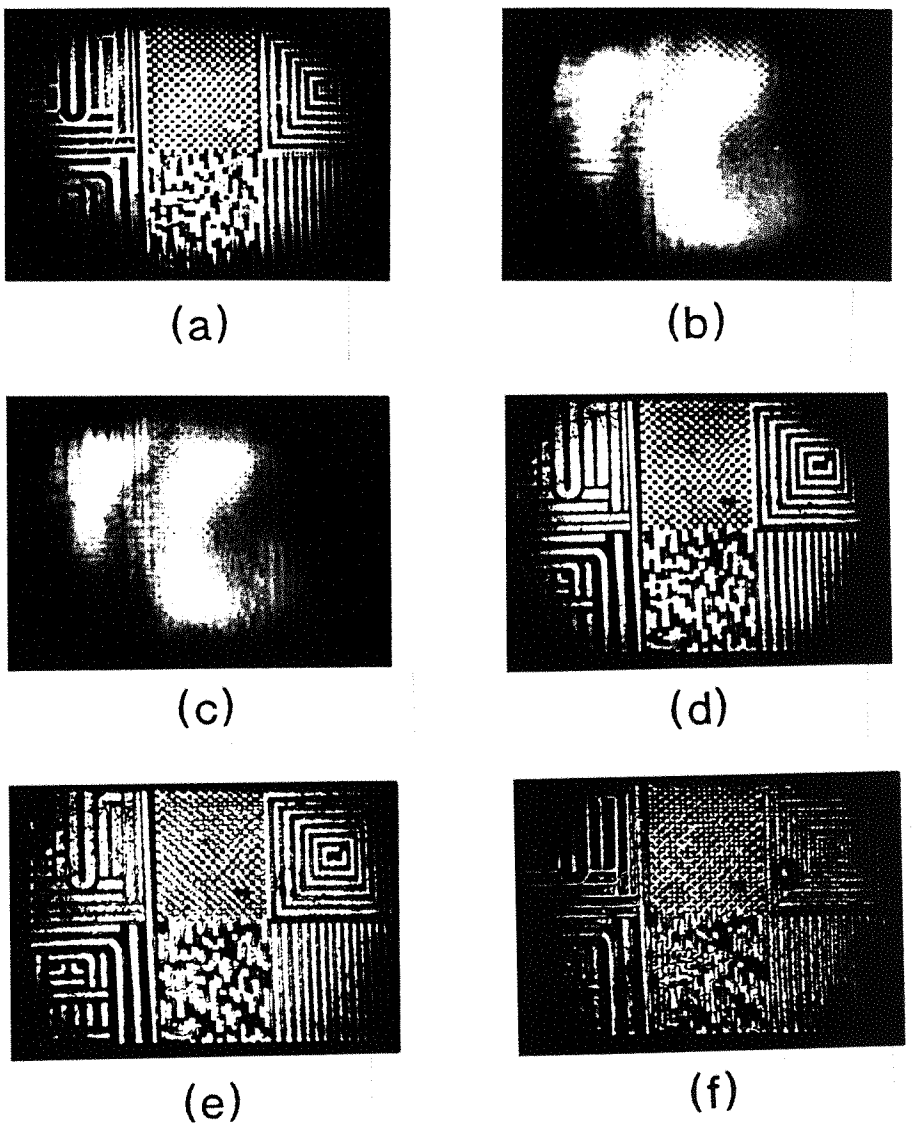

Figure 4.16 Shows photographs of a binary level object at different stages of contrast manipulation.

4.3.2 Contrast manipulation via DFWM in BSO

The experimental arrangement for contrast manipulation is shown in Figure 4.17, which is a basic DFWM configuration. An Argon Ion laser was used at 514.5 nm in multi-longitudinal mode. The laser output was filtered and expanded. Beam-splitter BS_1 divides the beam into two beams. The transmitted beam, after reflection from mirror M_2 was sub-divided by a beam-splitter BS_2. The transmitted beam was directed towards the BSO crystal (of dimensions 10 x 10 x 2 mm^3 which was additionally immersed in silicone oil), to act as a reference beam. The reflected beam from BS_2 was directed to pass through a half-wave plate, object transparency and a lens L_1. In the back focal plane of lens L_1 a half-wave plate with a hole in the centre was placed to allow the zero order to pass through uninterrupted. The higher orders undergo a polarization change on passage through this wave-plate. Lens L_2 forms the image of the object plane inside the BSO crystal.

Using the arrangement of polarization encoding which is illustrated in Table 4.2, we demonstrated contrast manipulation of a non-periodic binary object and Figure 4.18 shows a representative sequence of photographs. Figure 4.18 (a) shows the output image with original contrast which corresponds to the case (a) of Table 4.2. Photograph (b) shows an object with reverse contrast where the DC is dominant. Photograph (c) shows reverse contrast image while photograph (d) shows an edge enhanced image when the input DC was horizontally polarized and does not record a grating. These results are achieved when the transmission axis of the analyzer was at 140°.

We also performed contrast manipulation using the polarization encoding scheme of Figure 4.1(c) in DFWM configuration and the angle between reference beam I_1 and object beam I_2 was 54° outside the crystal (in air). The intensities of reference beam, object beam and readout beam were 3.00 mW, 3.5 mW and 6.50 mW respectively. As described in Section 4.2.2.2, contrast manipulation using this scheme can be achieved by rotating the second half-wave plate. The input polarization in the object beam to HWP_1 was horizontal. When there is an object transparency, higher orders pass through the HWP_1 and their polarization was rotated to the vertical direction. After passing through HWP_2 their polarizations were rotated as illustrated

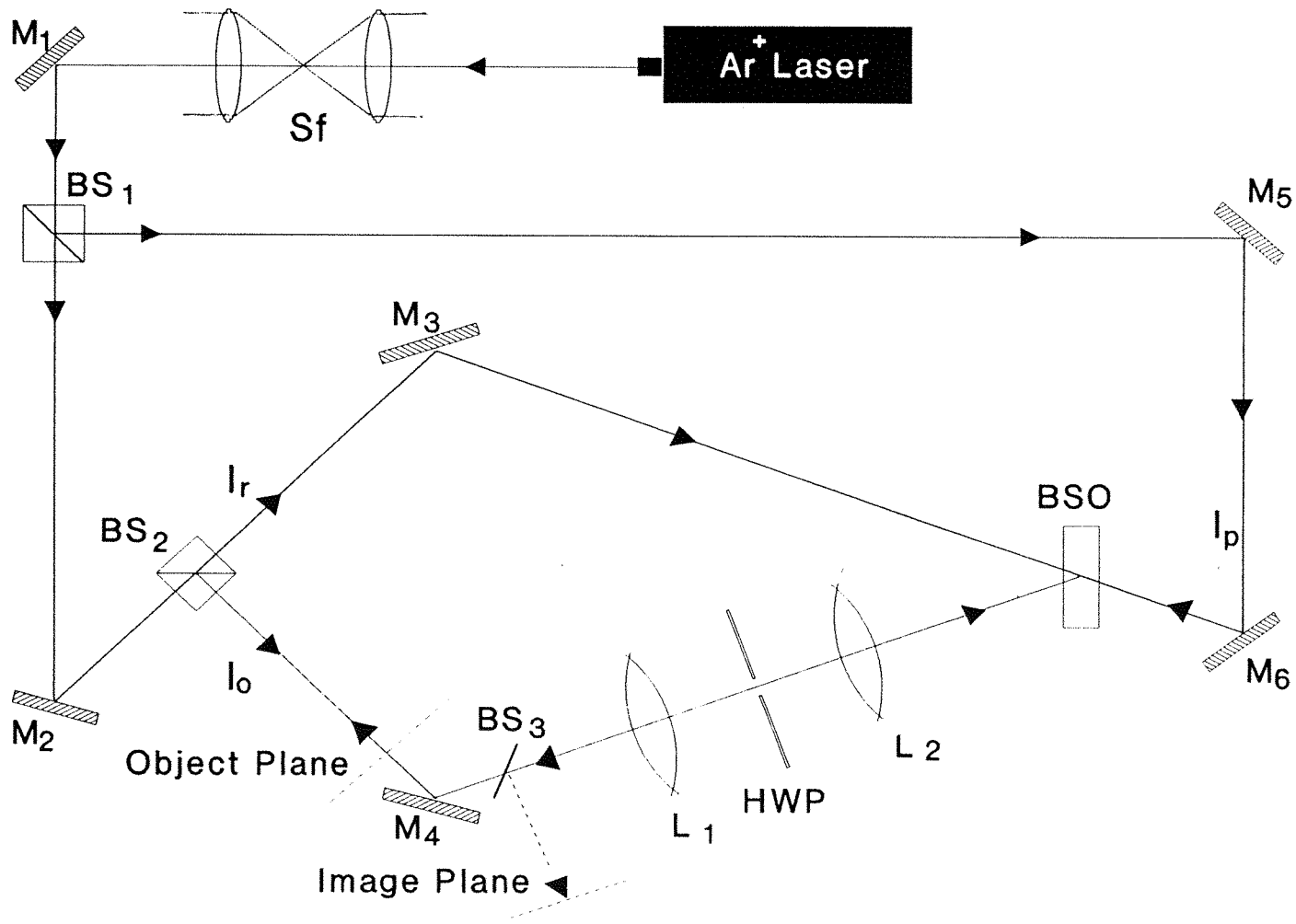

Figure 4.17 Shows the experimental arrangement in DFWM configuration for contrast manipulation where all three schemes of polarization encoding may be implemented.

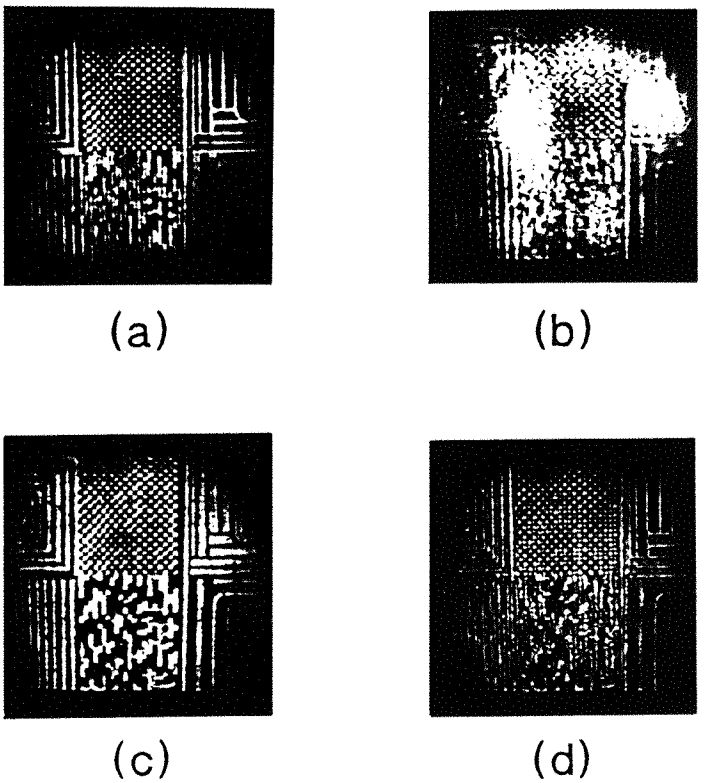

Figure 4.18 Shows contrast manipulation of a binary object via polarization encoding scheme of Table 4.2.

in Table 4.4, for the five different input polarizations. To achieve a continuous level of contrast manipulation we were able to rotate the HWP_2 to intermediate positions.

Photograph (a) in Figure 4.19 shows the object which was placed in the input plane. Photograph (b) shows image with original contrast while the higher orders are dominant and in-phase with the DC. Photographs (c) and (d) shows the results when only vertically polarized light corresponding to the DC order interferes with the vertically polarized reference beam inside the crystal. However, small proportions of light components corresponding to the higher orders are also interfering in- and out-of-phase with the DC to give positive and negative contrast images. Photograph (e) shows results towards contrast reversal when higher orders are dominant while photograph (f) shows a good contrast reversal image.

Using the same polarization encoding scheme we have also manipulated the contrast of objects such as finger prints, and a sequence of photographs of such contrast manipulation are shown in Figure 4.20. Photograph (a), shows the original finger print without any Fourier manipulation. Photograph (b) shows the finger print with negative contrast although, it is not very impressive partly because of restrictions imposed by numerical aperture considerations. Photograph (c), shows the DC or background illumination when higher orders are extinguished because they do not record any grating, while Photograph (d) shows original contrast with slightly greater proportion of DC than that of original object. Photograph (e) shows an original contrast image with slightly reduced DC level as compared to (d). Photograph (f) shows the edge enhanced version of the object which we can say in this particular case corresponds to **contrast enhancement** for a phase object such as the finger print.

4.3.3 Contrast manipulation via two beam coupling

We have also used two beam coupling in combination with polarization encoding scheme of Figure 4.1(a), in $BaTiO_3$ crystal for contrast manipulation and the arrangement is shown in Figure 4.21. The crystal was oriented such that the angle between the reference beam and signal beam was 50°, and the angle between the crystal normal and the signal beam was 10°. The measured power of the reference beam was 9.5 mW. The signal was expanded to a diameter of 2 cm, the intensity of

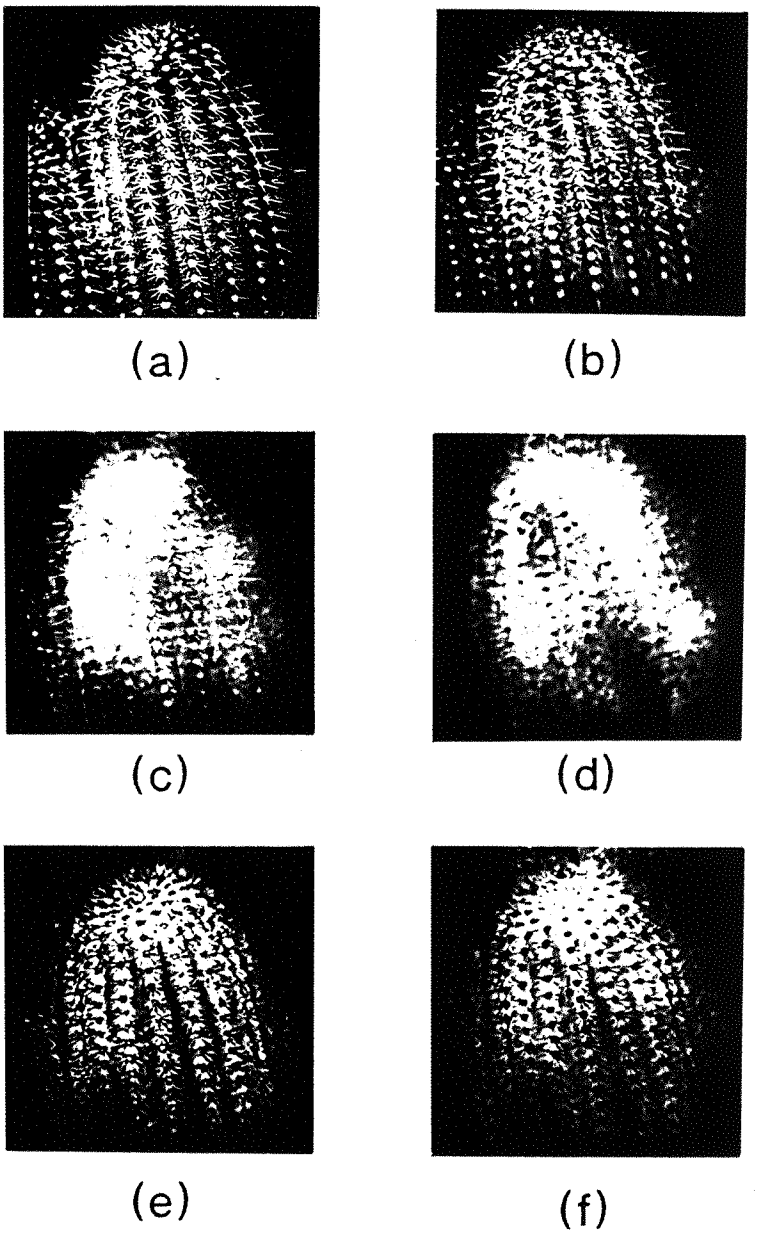

Figure 4.19 A sequence of photographs showing contrast manipulation using the polarization encoding scheme of Table 4.4.

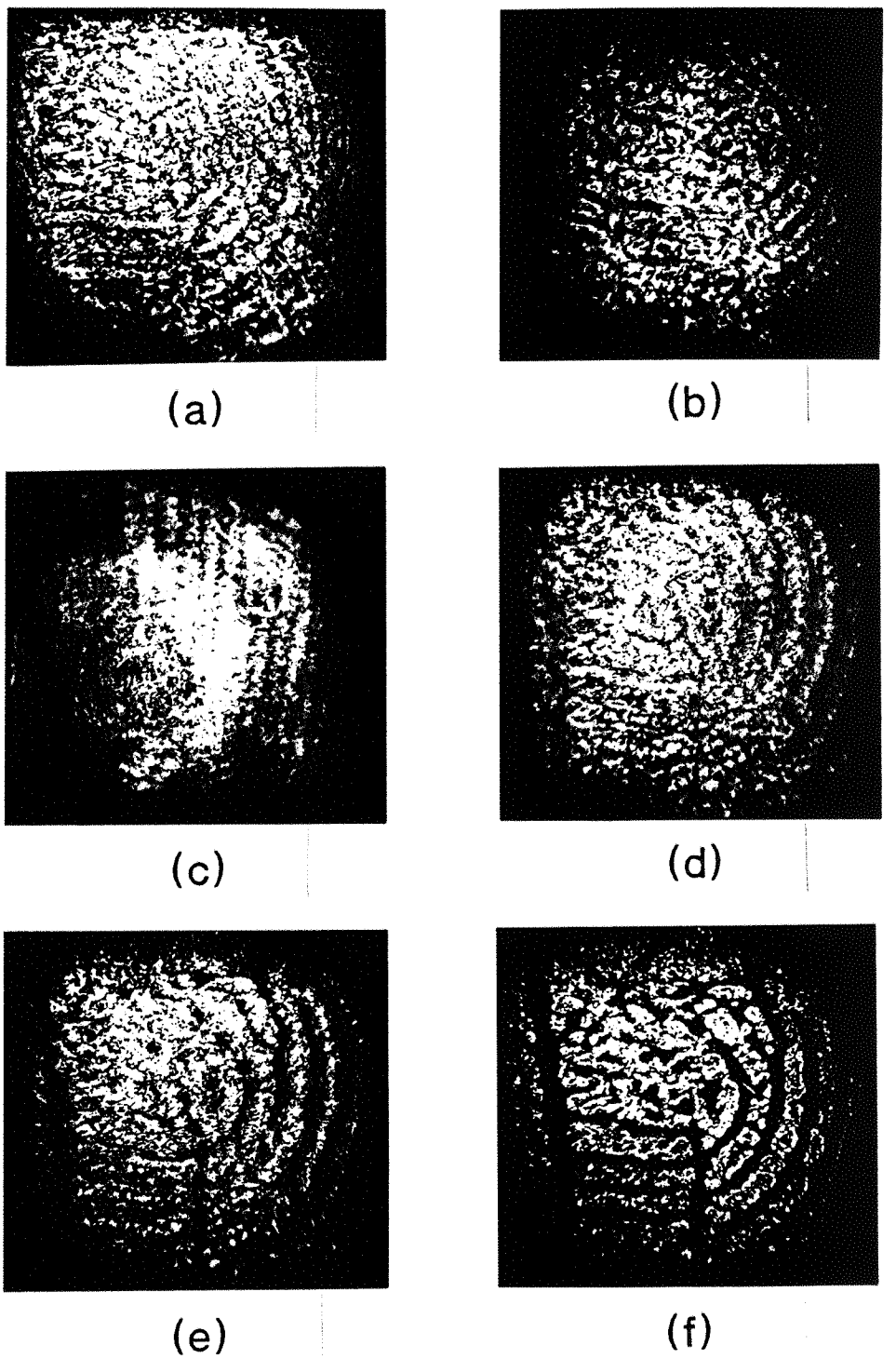

Figure 4.20 Contrast manipulation of a finger print using the polarization encoding scheme illustrated in Table 4.4.

which was controlled by a variable neutral density filter. The polarization of the reference beam and higher orders was set to be horizontal whereas the polarization of the DC was vertical. Therefore, in such a set up, only the higher orders saw gain, while the DC remained at the same level as that of the input object. The intensity of the object distribution after the transparency was 0.27 mW. In our experiment we observed gain for higher orders only due to the horizontal polarization however, due to the rapid build up of fanning gratings in $BaTiO_3$, a high degree of noise also developed, which severely degraded the output image at later times. We attempted the noise suppression technique of slowly rotating the crystal within a certain narrow range of angular motion [4.28]. In this method the gratings responsible for the noise are rotated with respect to the crystal constantly while the gratings corresponding to the image are rotated in a relatively slower and more controllable manner. Unlike the results reported in [4.28], we did not succeed in eliminating noise from the output image, so the output image is not as clear as intended.

Figure 4.22 shows the results of contrast enhancement of a finger print via two beam coupling. Photograph (a)-(c) show the results of passive contrast manipulation when the reference beam was blocked and an analyzer is placed after the $BaTiO_3$ crystal as shown in Figure 4.21. Photograph (a) shows the finger print when the transmission axis of the analyzer was at 45°, which allows the same proportion of DC and higher orders as that contained in the object, while photograph (b) shows mainly the DC component of the finger print. As the analyzer is rotated to an angle of 140° contrast of the finger print is reversed and the background is darker than the spatial features as shown in (c). As mentioned above this is due to the out of phase components of DC and higher orders. When the reference beam was unblocked, the grating between the reference beam and the Fourier transform of the object was recorded inside the $BaTiO_3$ crystal. The polarizer was now placed before the camera and the axis of the analyzer rotated to the vertical direction to allow all the DC component through and stop the horizontal polarized higher order features. However due to the large gain, of the order of 70 in this experiment, that we have achieved for the higher orders some of the output is still transmitted as shown in Photograph (d). Photograph (e) shows the results when the analyzer is rotated to an angle of 45°, and it is clear that the enhancement of the higher orders is significant and can be compared with the photograph (a) taken with the same angular position of the

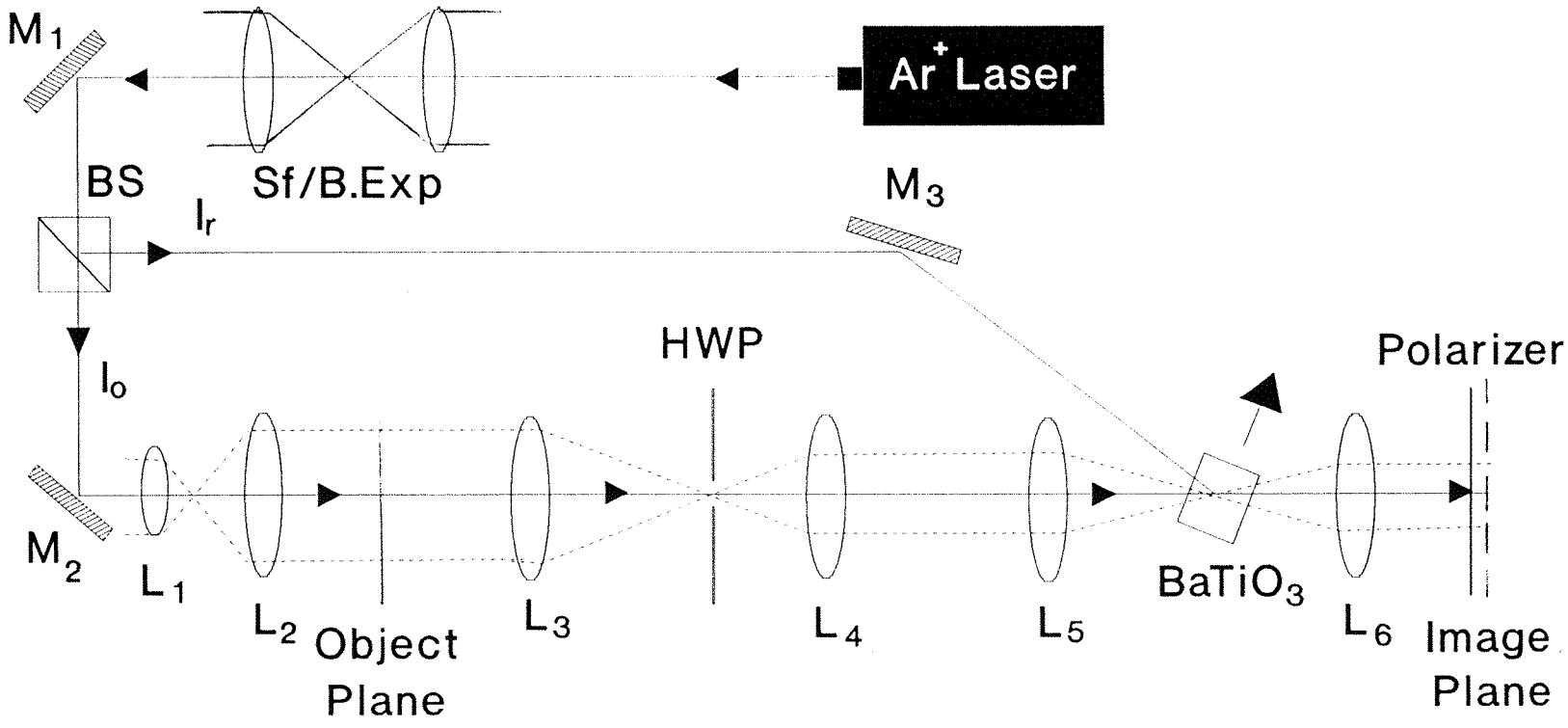

Figure 4.21 Experimental arrangement of two beam coupling for polarization encoded signal beam.

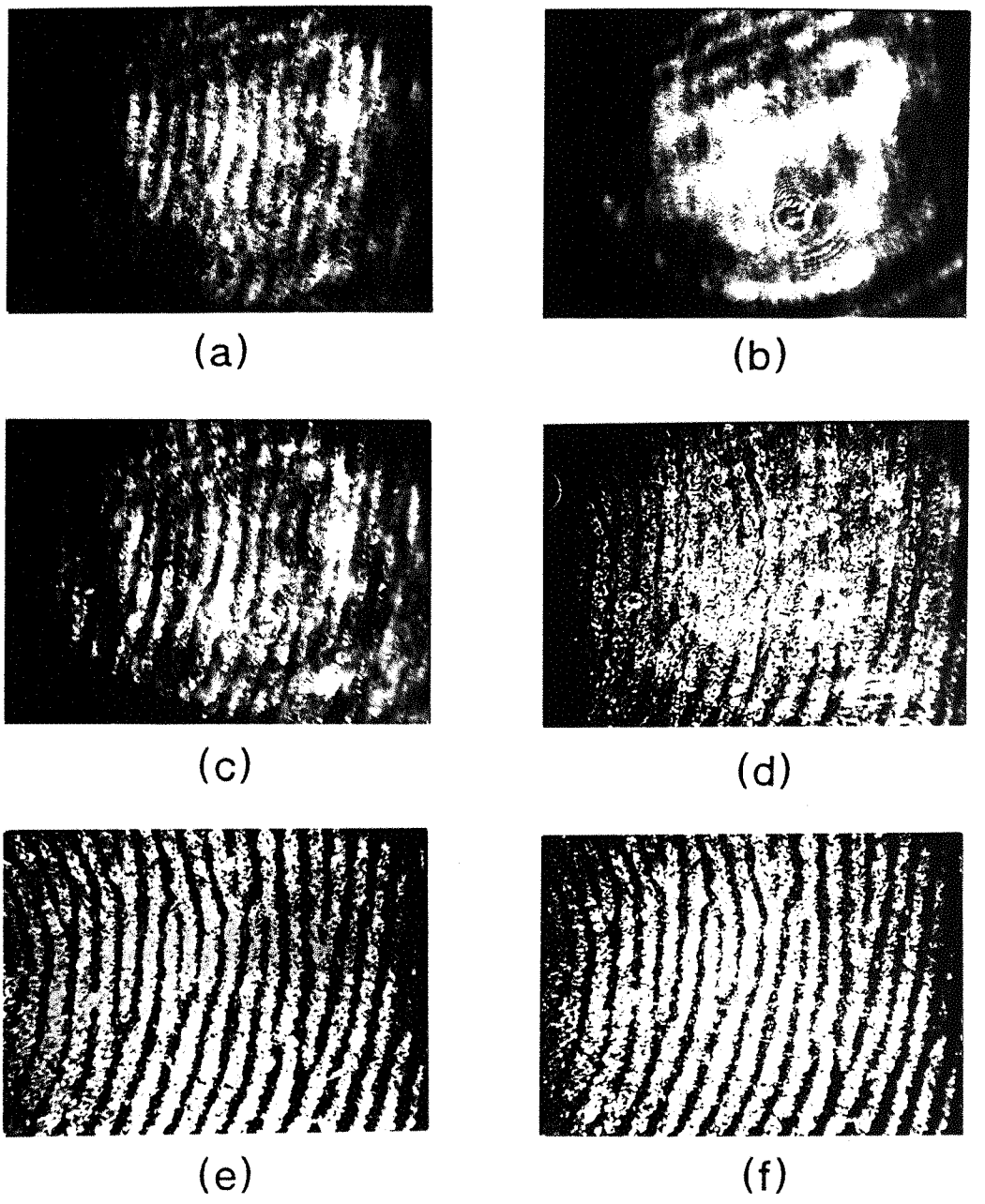

Figure 4.22 A sequence of photographs show contrast manipulation of a finger print via using an analyzer.

analyzer. Similarly Photograph (f) is taken when the polarizer was at 90° and all the higher orders are allowed to pass while the DC was eliminated. To achieve these results we used neutral density filters before the camera.

4.4 Further work and proposals

Previously Fourier transform techniques have also been used in combination with computer techniques. One such technique uses arrays of photo-detectors in the form of wedge and ring configurations [4.29]. These photo-detectors actually detect the Fourier transform power spectrum of the input object and subsequently sample it via a sequence of time consuming computer processing. Because of the shift invariance property of the Fourier transform, the object transform remains in the same position irrespective of its position in the object plane. Therefore the wedge-ring detector, in this case, loses the location information of the input object. The other drawback of such a technique is its processing, where the input is digitized and fed into a computer for subsequent processing. The output is mainly in the form of statistical data which is difficult to recognize visually.

Another technique of spatial filtering has been reported which uses a hybrid technique to process the input image [4.30]. It is often required in aerial imagery for example to be able to distinguish between different classes of regions of the scene. By such texture variance analysis of the original image it is possible to distinguish sharply textured areas from smooth textured areas. The variance of an object is realized optically by coherently illuminating a transparency of the object, forming its optical transform, blocking the DC component, and subsequently, inverse transforming the residual Fourier transform. The texture variance image, which is an edge enhancement version of the object, is imaged on a ground glass diffuser on which a TV camera is focused. The video output is fed into an image analyzer which separates the various texture classes in the image by varying the width of the electronic tone-texture window. This technique takes advantage of optics in the first stage of texture variance, while in the second stage, processing is electronic which may be time consuming and the output results are artificial in the sense that they are produced by the tone window of the image analyzer.

As an extension to our work on contrast manipulation via polarization encoding we propose a flexible and versatile technique which uses Fourier transform masks of various patterns instead of a wave plate with a hole in it. As we know Fourier transformation performs data compression and classification of different features of the object distribution in the form of spatial frequencies and their orientations. A single point in the Fourier transform may contain a global description of the object. Similarly a set of spatial frequencies in the Fourier transform plane may describe a texture class in the object plane. The set of spatial frequencies with reference to their orientation describe the texture class of a particular direction.

We propose designs of Fourier plane masks which consist of liquid crystal cells and can work as voltage controlled rotatable half-wave plates. In the Fourier transform, the spatial frequencies are distributed radially as well as angularly. Sampling of these spatial frequencies individually or in groups will allow contrast manipulation and other spatial filtering operations to be performed on a particular texture class, group of texture classes, or a single texture element.

The liquid crystal masks can replace a permanent half-wave plate and consequently provide greater control on the sampling of spatial frequencies in the Fourier plane. We will describe here basically two types of liquid crystal masks and two of their combinations. One of the mask consists of concentric stripes while the other consists of wedge shaped sectors and may also have a central circular disk pattern for DC order. The other two masks are combinations of these two masks and are shown in Figure 4.23. Constructional details are shown in Figure 4.24. Using combined mask patterns (a) and (b) of Figure 4.23, sandwich mask patterns can be built as shown in Figure 4.25.

Using these masks as shown in Figure 4.23, we can perform spatial filtering operations such as low pass, high pass, band pass, directional filtering and texture variance analysis. The radial orders of the Fourier transform provide information about the distribution of the spatial features in the object while the directional orders represent the features in a particular direction. However, when there is a rotatable analyzer at the output face of the mask, it is possible to achieve contrast inversion of the desired image features while leaving others intact. In this way we can achieve

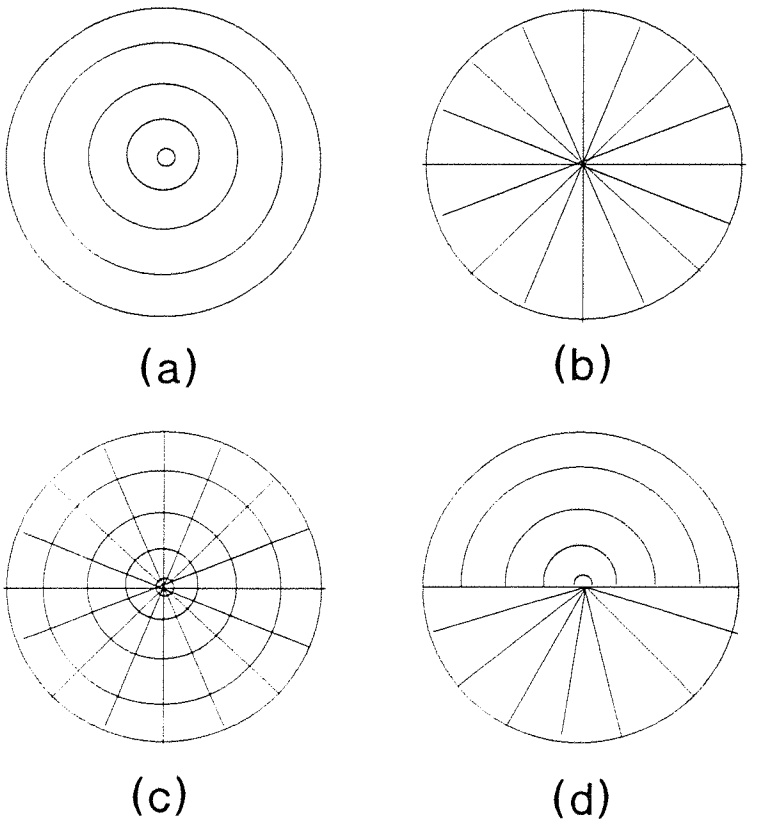

Figure 4.23 Shows four types of Fourier plane mask patterns.

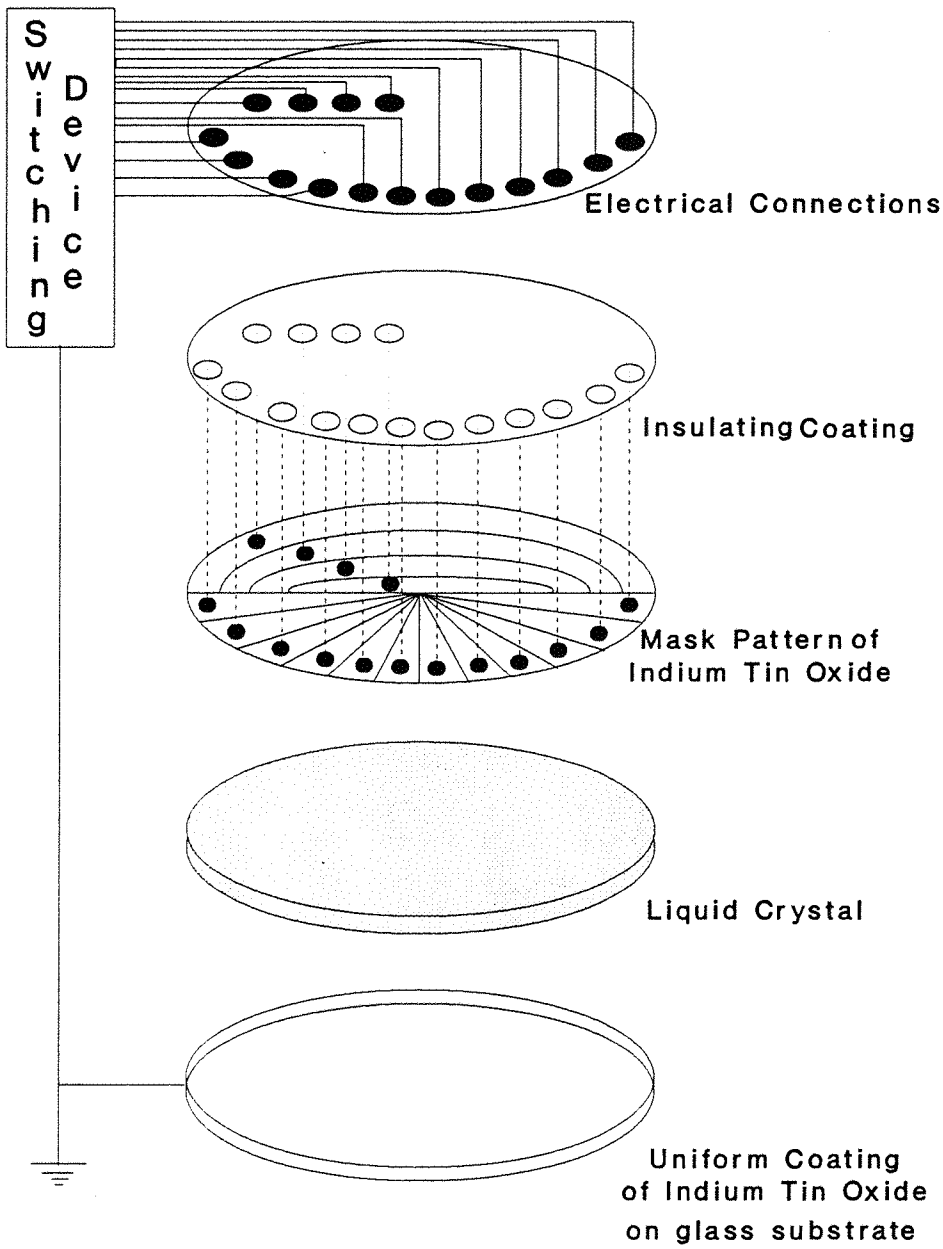

Figure 4.24 Shows the construction of a Fourier plane mask using liquid crystal as a polarization modulator.

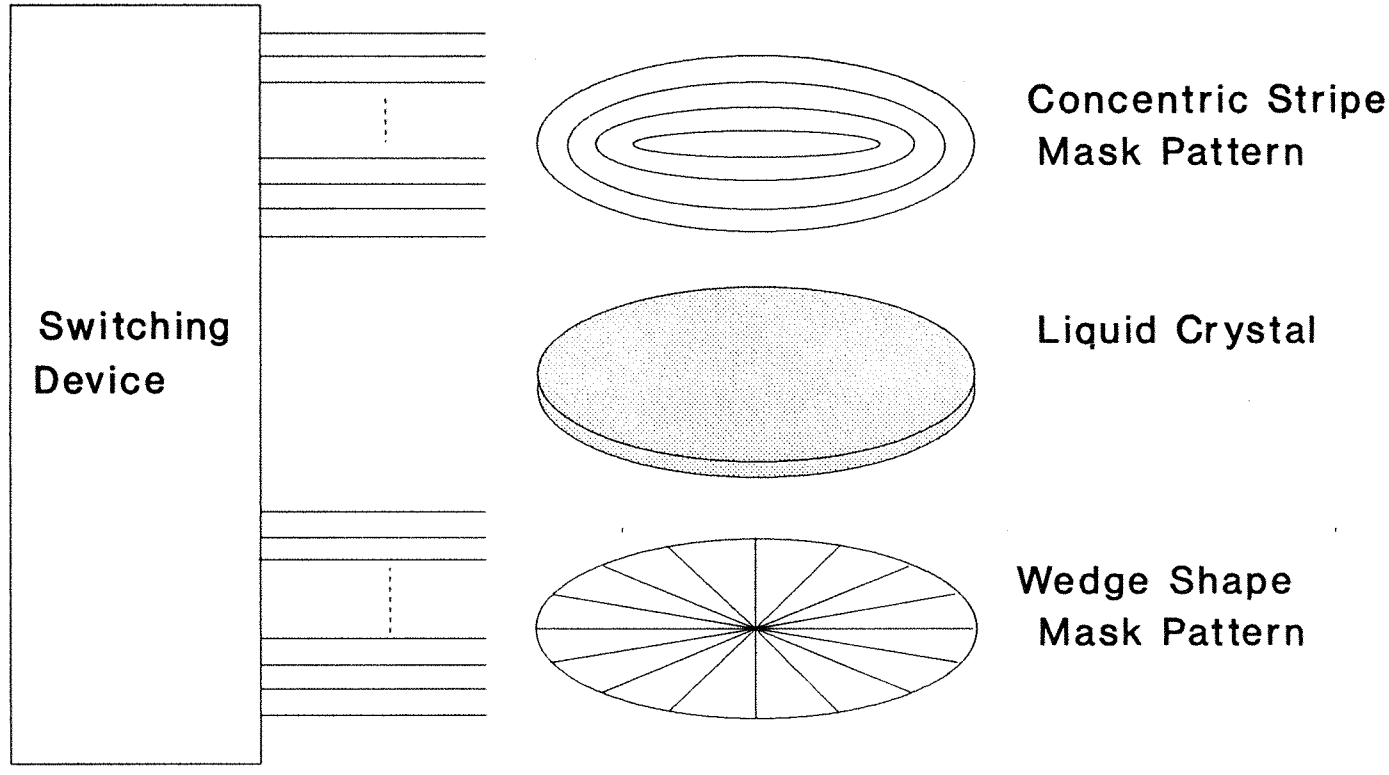

Figure 4.25 Schematic shows the Fourier transform spatial filter constructed via a combination of a wedge shaped and a concentric circular mask pattern.

for example a dark boundary between features of two grey levels (corresponding to lower orders), which will improve the distinction between various otherwise less distinguishable features in the object.

The commercially available Fourier transform sampling system consists of a detector array which consists of 32 wedge-shaped and 32 annular ring shaped photo-detectors arranged in the two semicircular regions of a circular detector [4.3]. The detector arrays sample the contents on the basis of distribution of input data with spatial frequency. This data is subsequently transmitted to a digital computer for analysis. Due to the translation invariance property of Fourier transformation information about the position cannot be detected by the detector.

The output from the computer is graphical and may sometimes be difficult to recognise and also requires longer processing times. We propose an arrangement which processes the Fourier transform optically in reflection as well as transmission modes, using liquid crystal masks described above. Our technique is shown in Figure 4.26, where transparent and opaque objects are placed in same object plane to achieve the optical Fourier transform via coherent illumination of the object from the top. However other illumination schemes can also be implemented. As shown in Figure 4.26 the input laser illuminates the object placed in the object plane. The reflected light is passed through a quarter wave plate, polarizing beam splitter and a lens to form a diffraction pattern in the back focal plane, where a liquid crystal mask is placed which is controlled by a computer for sampling the Fourier orders. Subsequently a video camera at the image plane detects the image and send the output to a computer and a monitor. The optically processed image can be post processed via computer techniques.

The optical preprocessing of the Fourier transform gives an advantage of instantaneous processing over the conventional Fourier transform sampling techniques. Operations like selecting particular grain size, directional filtering, and other similar spatial filtering operations can be achieved. This technique can also be used for surface inspection such as of metallic or glass sheets. Similarly in a scene such as a transparency of an aerial photograph containing mountains, trees, roads and other man made structures (i.e, regular directional features), can be

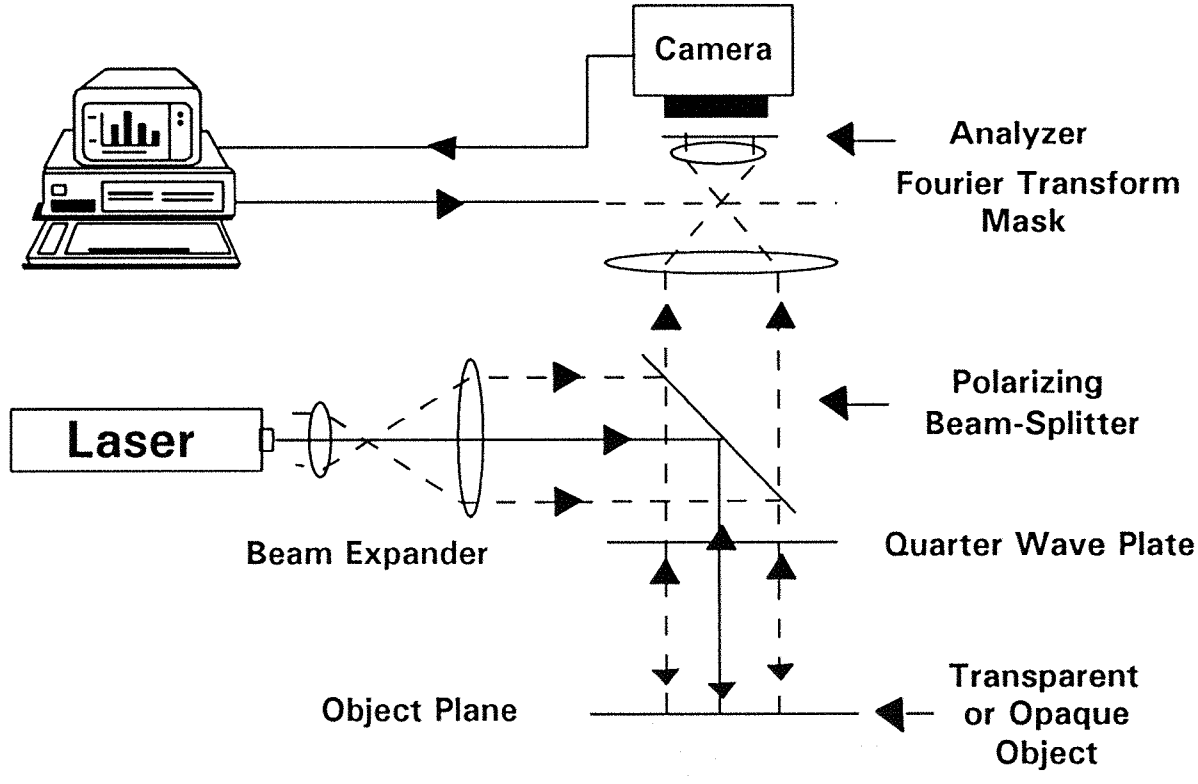

Figure 4.26 Schematic shows an arrangement for Fourier transform sampling.

distinguished by inverting the contrast of one with respect to the other or background. This will improve the distinction between directional regular or sharp man-made features in randomly distributed scenes such as trees and mountains.

4.5 Conclusion

We have demonstrated a range of techniques for contrast manipulation of objects which can be implemented passively or actively. In the case of a passive technique, it is based upon polarization encoding of the Fourier transform of the object and subsequent analysis via an analyzer. In our technique we placed a half-wave plate with a precision hole machined in the centre, in the back focal plane of a Fourier transforming lens. The DC order was allowed to pass through the hole without changing its polarization direction while higher orders are rotated to a selectable direction. Subsequently this polarization encoded information is analyzed by placing a rotatable analyzer before the image plane. Positive and negative contrast manipulation of images has been achieved, by selecting a variable proportion of amplitudes of DC and higher orders via the rotatable analyzer. This technique can be used for amplitude as well as phase objects. Results of contrast manipulation using this technique are presented for phase objects as well as amplitude objects (i.e, grey level and binary level).

We also proposed a further improvement in our technique by introducing a variable wave-plate. The variable wave-plate can be placed anywhere after the half-wave plate with the central hole, and before the analyzer. The variable wave-plate is used to introduce a controllable relative phase shift between orthogonally polarized DC and higher orders when the fast axis of the variable wave-plate is parallel to the polarization direction of either DC or higher orders.

This technique can also be used in combination with real time holography to achieve contrast manipulation and amplification of selected Fourier orders. We have also presented results of contrast manipulation via polarization encoding using DFWM and TBC in BSO and $BaTiO_3$ respectively.

Lastly we propose the fabrication of liquid crystal Fourier transform masks of various patterns. By selecting in real time the different Fourier orders using transmission characteristics of these liquid crystal masks we can process the image for almost any type of spatial filtering operation in real time.

REFERENCES

4.1 E. Hecht, "Optics", Addison-Wesley Publishing Company, (1987).

4.2 A. R. Shulman, "Optical Data Processing", John Wiley & Sons Inc, (1970).

4.3 S. H. Lee, "Optical Information Processing", Topics in Applied Physics,Vol. 48 Springer-Verlag, Germany (1981).

4.4 H. J. Caulfield and R. A. Soref, "Optical contrast enhancement in liquid crystal devices by spatial filtering", Appl. Phys. Lett. **18**, 5 (1971).

4.5 R. W. Lewis, "Real time coherent optical edge enhancement", Appl. Opt. **17**, 161 (1978).

4.6 R. H. Anderson, "Edge enhancement of coherent magneto-optic images", Appl. Opt. **25**, 976 (1986).

4.7 H. Bartelt and F. Sauer, "Space-Variant filtering with holographic multifacet elements", Opt. Commun. **53**, 296 (1985).

4.8 M. S. Brown, "Optical edge enhancement applied to scenes with natural vegetation backgrounds", Optica Acta, **32**, 549 (1985).

4.9 C. R. Petts, M. W. McCall, and L. C. Laycock, "Optical correlation in $Bi_{12}SiO_{20}$ at 632.8 nm", Elect. Lett. **20**, 32 (1984).

4.10 Y. Fainman, S. H. Lee, "Applications of photorefractive crystals to optical signal processing", SPIE Optical and Hybrid computing, **634**, 380 (1986).

4.11 J. P. Huignard, J. P. Herriau and F. Micheron, "Selective erasure and processing in volume holograms superimposed in photosensitive Ferroelectrics", Ferroelectrics, **11**, 393 (1976).

4.12 Y. H. Ja, "Real time image subtraction in four wave mixing with photorefractive $Bi_{12}GeO_{20}$ crystals", Opt. Commum. **42**, 377 (1982).

4.13 S. K. Kwong, G. A. Rakulijc, A. Yariv, "Real time image subtraction and **exclusive OR** operation using self-pumped phase conjugate mirror", Appl. Phys. Lett. **48**, 201, (1986).

4.14 A. E. Chiou and P. Yeh, "Parallel image subtraction using a phase-conjugate Michelson interferometer", Opt. Lett. **11**, 306, (1986).

4.15 P. Yeh, T. Y. Chang and P. H. Beckwith, "Real time optical image subtraction using dynamic holographic interference in photorefractive media", Opt. Lett. **13**, 586 (1988).

4.16 N. J. Wooder and J. C. Dainty, "Real time intensity inversion by four wave mixing in bismuth silicon oxide", Opt. Commun. **63**, 85 (1987).

4.17 P. Yeh, A. E. T. Chiou, "Real time contrast reversal via four wave mixing in nonlinear media", Opt. Commun **64**, 160 (1987).

4.18 J. P. Huignard and J. P. Herriau, "Real time coherent object edge reconstruction with $Bi_{12}SiO_{20}$ crystals", Appl. Opt. **17**, 2671 (1978).

4.19 J. Feinberg, "Real time edge enhancement using the photorefractive effect", Opt. Lett. **5**, 330 (1980).

4.20 E. Ochoa, J. W. Goodman, and L. Hesselink, "Real time enhancement of defects in a periodic mask using photorefractive $Bi_{12}SiO_{20}$", Opt. Lett. **10**, 430 (1985).

4.21 N. A. Vainos and R. W. Eason, "Real time edge enhancement by active spatial filtering via five wave mixing in photorefractive BSO", Opt. Commun. **59**, 167 (1986).

4.22 L.Pugliese and G. M. Morris, "Band-pass filtering in Barium Titanate", Appl. Opt. **27**, 4535 (1988).

4.23 G. O. Reynolds, J. B. DeVelis, G. B. Parrent, B. J. Thompson, "Physical optics notebook: Tutorials in Fourier Optics", SPIE Optical Engineering Press, Washington (1989).

4.24 F. Zernike, "Beugurgstheorie des Schneidenverfahrens und seinerverbesserten form, der phaseenkontrastmethod", Physica 1, 689, (1934).

4.25 F. Allario, "Laser remote sensing supports aviation research and safety", Laser Focus World, 59, April 1992.

4.26 A. Marrakchi, R. V. Johnson, and A. R. Tanguay, Jr, "Polarization properties of photorefractive diffraction in electrooptic and optically active sillenite crystals (Bragg regime)", J. Opt. Soc. Am. B, **3**, 321 (1986).

4.27 Y. Fainman, E. Klancnik and S. H. Lee, "Optimal coherent image amplification by two-wave mixing coupling in photorefractive $BaTiO_3$", Opt. Eng. **25**, 228 (1986).

4.28 H. Rajbenbach, A. Delboulbe and J. P. Huignard, "Noise suppression in photorefractive image amplifiers", Opt. Lett. **14**, 1275 (1989).

4.29 H. Stark, "Applications of Optical Fourier Transforms", Ch. 4, Academic Press (1982), New York.

4.30 H. Stark and E. Garcia, "An optical computer for texture analysis of images", Proc. Inter. Opt. Comput. Conf., Zurich, 5 (1974).

CHAPTER 5

OPTICAL TRACKING AND MOTION DETECTION USING PHOTOREFRACTIVE $Bi_{12}SiO_{20}$

5.1 Introduction

The operation of motion detection, velocity filtering and detection of change in a given scene are all important aspects for optical processing architectures and systems. An optical novelty filter is used to extract and display the moving features of a scene while any features that are static are not displayed. Fields in which this capability has immediate applications include industrial inspection, bio-medical screening techniques and machine vision. So far several different techniques have been implemented and will be discussed in the following paragraphs.

A hybrid technique of motion detection has been reported by Aida et al [5.1]. Their technique is based on an active matrix liquid crystal television (AMLCTV), a position sensitive device (PSD), and a TV frame memory. When there is any movement in the object against a stationary background the successive TV frames of the input video signals are fed to the frame memory and to a subtractor which generates frame difference signals which then extract the signal corresponding to the moving elements. The frame difference signal is fed to the AMLCTV, which converts the electrical signal into two dimensional optical images. This outlined image is projected onto the target of the PSD which detects the centre of the image at any instant provided the shape of the object does not change as it moves between successive frames. The centre of the outline image between the two successive frames is located between the centres of these moving image frames. However, this system cannot trace more than one object moving in the input plane or when the TV camera is panning.

Another hybrid technique has been demonstrated by Li et al [5.2] of a tracking novelty filter which uses a white light source and two liquid crystal TVs. Liquid crystal TVs work as polarizing devices when there is no external voltage applied,

rotating the input polarization through 90°. Li et al used two identical LCTVs in a cascaded configuration while removing the inner adjacent analyzer and polarizer from them. The polarizer and analyzer of the combined LCTV arrangement was adjusted so that they achieved an exclusive OR operation on the input signal.

Their tracking novelty filter was operated in two modes. The first one is a real time fixed reference comparison mode, in which one of the LCTVs is connected to a video camera, used to acquire the real time image. The other LCTV is connected to a video recorder, that displays a single frame image from a previously recorded videotape. For this case uniform dark output is displayed as long as real time image is identical to the stored one. However if any change appears in the real time image, the difference output is displayed. Therefore the real time input is continuously compared to a stored reference image. To activate this mode the video camera output is split into two parts, with one output directly connected to the first LCTV while the other output is connected to the second LCTV. The reference image is periodically updated and then compared with the real time image to give the differential output any change exists between them. This technique relies on pixel by pixel subtraction between a previously stored image and a constantly updated image. Due to the sequential nature of this technique, processing with this is a time consuming job and may not be applicable for high speed applications (higher than TV frame rates).

An optical novelty filter extracts and displays those features of a scene that are changed with respect to time. One form of optical novelty filter uses a real-time holographic medium for the memory i.e., a photorefractive crystal. Through recording of two such holograms with different response times, real time subtraction is performed on the input scene (static or moving), with the entire scene processed in parallel.

Soutar et al [5.3], have demonstrated a hybrid technique of optical novelty filtering using BSO as a dynamic holographic medium, and a computer for real time processing of the output. It is known that the diffraction efficiency of a grating recorded in drift-mode will have a transient peak due to the complex time constant: they found that this transient peak can be enhanced by illuminating the BSO crystal

with white light of uniform intensity across the crystal, acting effectively as an optical bias. The white light has two effects. First the additional intensity has the usual effect of reducing the modulation index, and hence the steady state diffraction efficiency (according to its approximate dependence on the square of modulation index). The second effect that they observed is that the transient peak intensity is increased as this decrease in steady state value of diffraction efficiency takes place.

They also found a linear relationship between the ratio of transient to steady state intensity and white light intensity, which means that by increasing the total intensity of the writing beams, at a fixed intensity of white light, does not affect the transient peak value (over a wide range of values). They observed however that it is the intensity of optical bias that alone determines the peak width. Therefore when the grating is stationary the diffracted output will be fixed at its stabilised, low intensity steady state value. However as the input image is moved a new grating is continuously being recorded in the crystal and transient enhancement for this grating is achieved. As a result, moving features appear brighter than the static parts of the image. In a further development, they converted this image into a binary intensity level using an electronic thresholding technique. Therefore the higher intensity features become **1** while the steady state and lower intensity features become **0**. As a result no output is achieved when an object is static. However as the object starts moving, those moving parts appear at the output. This technique while useful is basically a hybrid one, requiring therefore an extra stage of electronic processing.

A technique of **time differentiation** of coherent images has been reported by Cronin-Golomb et al [5.4]. Their technique relies on two beam coupling where the grating is recorded inside a $BaTiO_3$ crystal. The crystal orientation was such that the coupling results in energy transfer from the signal beam to the pump beam yielding a strong de-amplified signal. This is due to the 180° phase shift that occurs between the directly transmitted signal beam and the diffracted pump beam. When the input image is static the coupling is such that no net output is achieved in the signal beam. However when a time variation occurs in the object plane, coupling between the object beam and reference beam is disturbed, provided the changes in the object plane are faster than the response time of the crystal. As a result a bright output image is achieved which is actually the transmitted signal beam.

They have also suggested an alternative approach to achieve such an operation via implementation of a fanning optical limiter. Optical fanning, which arises due to the scattered light from small crystal defects, strongly de-amplifies the incident signal beam and almost all the beam energy is deviated into the fanning noise. However as the input varies, the fanning holograms written in the crystal adjust to the change, depending on the photorefractive response time. If the change is faster than the response time of the crystal, a bright image may be achieved at the output. However it is not a true time differentiation because when a beam is modulated from light to dark the output will be zero, whereas true time differentiation would yield an output.

A similar technique has been demonstrated by Cudney et al [5.5] and has been named as a **transient detection microscope**. Their technique also relies upon two beam coupling in $BaTiO_3$. A reference beam and an object beam interfere in the crystal to record a hologram in real time. The diffracted reference beam interferes destructively with the signal beam due to the net 180° phase shift. In steady state, the object beam exits the crystal with greatly reduced intensity. Therefore no image is apparent at the output port. However when any change occurs in the object plane which is faster than the response time of the crystal, a bright image of the moving feature is observed. They pointed out however two limitations in their technique; the first one is that the crystal should be of very high optical quality otherwise it will distort the image. Secondly, is the slow response time of $BaTiO_3$ crystals leads to multiple images and a faint tail may appear behind the moving object.

Kwong et al [5.6] have demonstrated a technique of motion detection using transient energy coupling. This type of operation is observed in photorefractive crystals which operate with a local response i.e., no phase shift between intensity and index gratings exists. In such a situation the two beam coupling constant is imaginary and therefore there is no energy transfer between the two beams in steady state. However phase transfer occurs between the two interacting beams, provided their intensities are unequal. Because of this, the equi-phase contour index grating is tilted in the steady state. When the light intensity of the beams is suddenly changed, the interference fringes also change their positions accordingly. Therefore transient phase mismatch occurs between the interference pattern and the pre-recorded index grating, which gives rise to transient energy coupling. However, when the input beam

intensities become stationary for a time longer than the response time of the material, the index grating catches up with the changes and energy transfer ceases. While they achieved motion detection using this approach, due to the two beam coupling nature, the output image may be degraded because of the poor surface quality of the crystal, or other associated optical components. Also, the output image shows a uniform background which reduces the contrast of the output image.

A technique which relies on the use of a phase conjugate Michelson interferometer (PCMI) has been reported by Anderson et al [5.7]. Their optical novelty filter exploits the differential response time of a PCMI using $BaTiO_3$. The two arms of the novelty filter share a the single phase conjugate mirror (a $BaTiO_3$ crystal in the self-pumped configuration). The two phase conjugate outputs interfere destructively at the output port of a polarizing beam-splitter. The spatial light modulator (without crossed polarizers) is used as an input device, and a combination of wave-plates was placed in the input beam of the PCMI. The input beam passes through the SLM and is divided into two by a polarizing beam-splitter and subsequently phase conjugated by a self-pumped $BaTiO_3$. The phase conjugate output re-traverses back through the input path, and LCTV, and interferes at the polarizing beam-splitter at the output. In the case when there is no motion in the object plane, the polarizations of the two phase conjugate beams are of the same polarization as to that of the input. Therefore no part of the beam leaves the interferometer and the output is null.

However when there is any change in the object plane the phase conjugate output when passing through the SLM will not compensate the polarization change to that of the input. As a result, the output polarization is different and therefore passes through the output polarizing beam-splitter as a changed or novelty output. The output will fade and disappear as the phase conjugator readjusts itself. However, there is a limitation of this technique, namely slow response time for the $BaTiO_3$ crystal used.

Liu and Cheng [5.8] have reported a technique of single pixel novelty filtering which is based on PCMI using GaAs. They investigated the relation between the recovery time after a change in the object and the nonlinear response time of the

medium. If the speed of the object is too fast, or the response time of the nonlinear medium is too long, a tail will follow the moving image at the output. Therefore any two features for example in the object will become un-resolvable, if they are separated by a distance shorter than the length of the tail, regardless of how large the space bandwidth product (SBP) is of the input device (i.e, SLM) is. They defined therefore the effective SBP which is a function of the response time of the nonlinear medium, the speed of the target, as well as the SBP of the input device for binary input images.

Khoury et al [5.9] have reported a technique of motion detection which uses time correlation in a nearly degenerate four wave mixing (DFWM) arrangement. They used a reference beam which is modulated to destroy the grating through rapid phase variations in the beam. When such a grating is readout, for the static object case, the intensity of the phase conjugate beam will be zero. However when the object is moved, the phase conjugate reappears under the constraints of time correlation detection. Therefore any phase changes in the signal beam may be detected and observed in the output image plane. However using this technique only phase objects are detectable.

Khoury et al [5.10] have also reported a new technique of novelty filtering which has the dual features of self-nulling and self-aligning. Their technique is based upon a FWM arrangement where all the three incident beams used interfere to record transmission and reflection holograms inside a BSO crystal. Therefore the two pump beams used are diffracted from transmission and reflection holograms as two simultaneous phase conjugate beams. To achieve the phase conjugate beams of opposite phases a crystal orientation where the coupling constants are opposite in phase was adopted. They arranged the differential response times by recording the gratings with different fringe spacings and the phase conjugate outputs from the reflection and transmission gratings will cancel each other in steady state. When the object is moved however, the gratings will undergo erasure, and rewrite themselves. In this situation the phase conjugate output from the reflection grating will lag behind that from the transmission grating, and destructive interference will not occur in the transient regime. Therefore an output moving image is observed at the output port.

5.2 Theoretical Considerations

In photorefrative materials the recording and decay times of a grating depend on several parameters such as grating spacing, total incident light intensity, crystal orientation and any external applied field [5.11, 5.12]. The erasing time τ_e can be represented through the expression [5.13],

$$\tau_e=\tau_{di}\,[1+f_D(\Lambda)+f_E(\Lambda)\,E_o^2] \qquad (5.1)$$

Where $\tau_{di}=\epsilon\epsilon_o/\sigma$ is the dielectric relaxation time and σ is the conductivity. E_o is any externally applied electric field and

$$f_D(\Lambda)=\frac{4\pi\mu\tau_R K_B T}{e\Lambda^2}$$

$$f_E(\Lambda)=\frac{4\pi^2 e(\mu\tau_R)^2}{(e\Lambda^2+4\pi\mu\tau_R K_B T)} \qquad (5.2)$$

Here Λ is the grating fringe spacing and τ_R is the carrier recombination time. It is clear from the above equations that in the diffusion regime the response time for writing holograms with large fringe spacings is faster than for those with small fringe spacings while the dielectric relaxation time τ_{di} is inversely proportional to the total incident intensity. By controlling the respective intensity and fringe spacing therefore, the response time of a photorefractive material can be varied. More importantly, for several different simultaneous inputs, the response time of each grating can be independently tuned for applications such as the differential device described here. The basic requirement for this optical image differentiation in time is the principle of coherent subtraction between two simultaneous phase conjugates under static conditions. For the differential device described here, in practice a suitable combination of angles and relative intensities for the two beams can always be found, thus ensuring complete subtraction.

The technique for subtraction that we use here relies on a phase conjugate Michelson interferometric configuration that has been reported earlier [5.14, 5.15]. This technique is based on the Stokes' relation that holds for a lossless dielectric beam-splitter. The intensity at the output port of the dielectric beam-splitter can be described by

$$r't^*+r^*t=0 \qquad (5.3)$$

where r and r′ are the amplitude reflection coefficients for the two phase conjugate beams, incident from opposite directions at the beam-splitter under conditions of true phase conjugation. Exact image subtraction can be achieved when the intensities of the phase conjugates are equal in both arms of the interferometer. This Stokes' principle has a physical interpretation, which is that under complete time reversal, no input from the image plane to the beam-splitter guarantees no corresponding output. As shown in Figure 5.1 the input image plane is behind the dielectric beam-splitter therefore any temporal change in the image will be input simultaneously into both arms of the interferometer. Due to the differing response times of each arm however, one phase conjugate output may lag behind the other, and destructive interference will not occur at the beam-splitter until a certain time has elapsed. Therefore, in a transient regime the reversibility in time is not valid. During the recording cycle the light amplitude at the output port of the beam-splitter BS_2 can be written as,

$$A_{out}(x,t) \propto A(x,[t-\tau_1]) - A(x,[t-\tau_2]) \approx \frac{\partial A(x,t)}{\partial t}(\tau_{1r}-\tau_{2r}) \quad (5.4)$$

where τ_{1r} and τ_{2r} are the response times for recording holograms with small and large fringe spacings respectively. Similarly the output at BS_2 during the erasure cycle can be given as

$$A_{out} \approx \left(\frac{\partial A}{\partial t}\right)(\tau_{1e}-\tau_{2e}) \quad (5.5)$$

Where τ_{1e} and τ_{2e} are the grating decay times for small and large fringe spacings respectively. From Equations (5.4) and (5.5) above it is evident that the insertion of any time varying signal at the input will result in the output predicted above, corresponding to either the recording cycle or the erasing cycle [5.16]. Detection of an output signal relies on two factors; the rate of change of the input signal $\partial A/\partial t$ and the differences in the response times for writing and erasing of the two gratings.

It is not necessary for the interference between the two phase conjugate signals to be destructive, as the amplitudes of the associated space charge fields are (i) not in steady state, (ii) may not have equal magnitude and (iii) the spatial phase shift will not equal $\pi/2$ in a non steady-state regime. The temporal development of the output

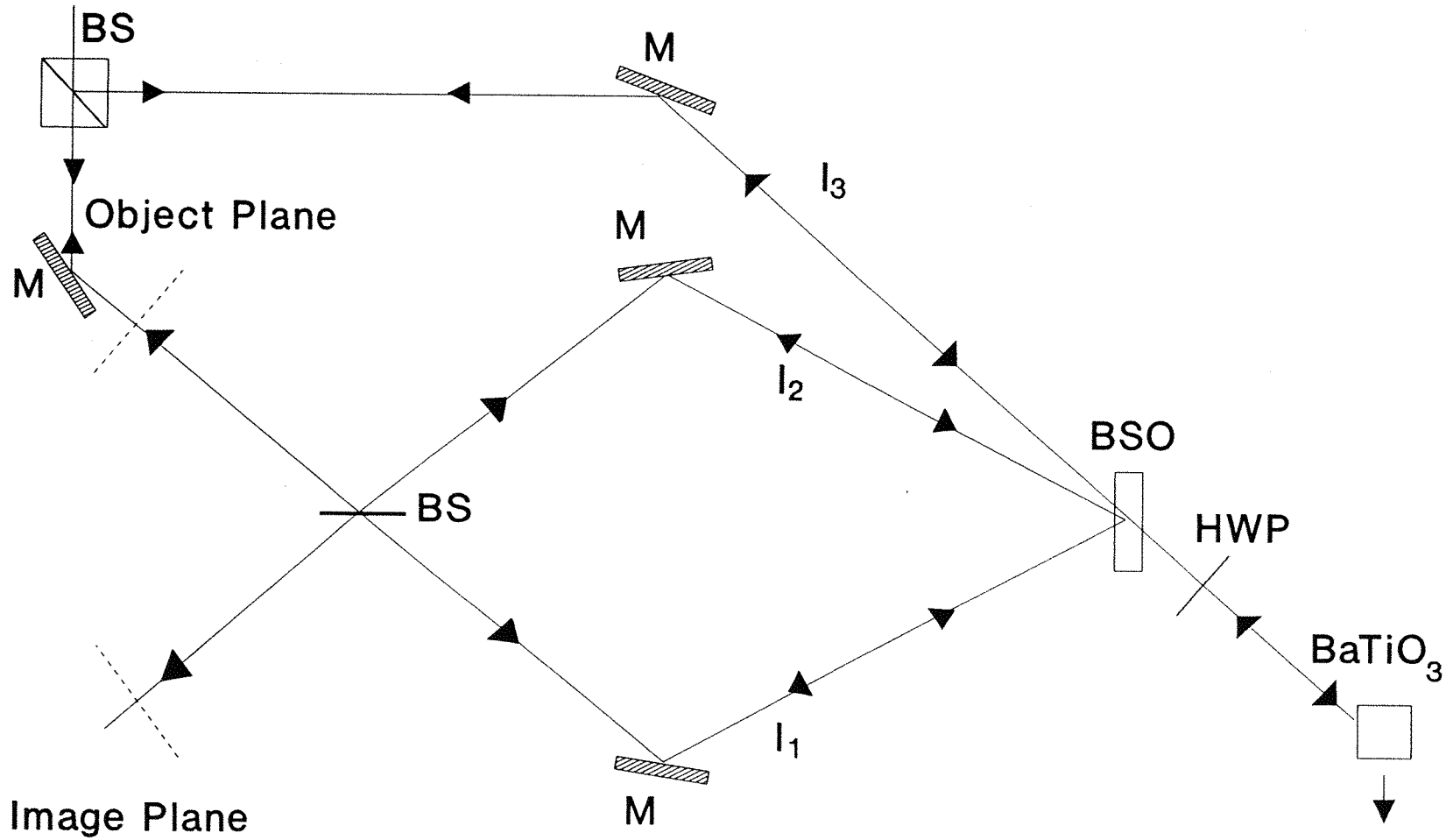

Figure 5.1 Schematic diagram for optical novelty filter, using two signal beams I_1 and I_2 and a common reference beam.

signal is related to the development of amplitudes and phases of the two space charge fields in time. The difference between the response times of the two gratings may be arbitrarily increased. This can be achieved by either reducing the total intensity of all the interacting beams or the readout beam alone, thereby limiting the differential output to the erasing cycle. Another possibility for increasing the response time difference between the two signals is by using an appropriate wavelength, for example orange or red, in the case of BSO, since the differentiation will then occur on both writing and erasing cycles.

5.3 Experimental arrangement and results

The experimental arrangement for motion detection is shown in Figure 5.2. A Krypton ion laser operating in multi-longitudinal mode at 568 nm with a total power I_o of 14 mW and a single BSO crystal of dimensions 10 x 10 x 2 mm^3 were used. The beam was spatially filtered, expanded to a diameter of ≈7 mm, and subsequently split by BS_1. The transmitted beam was divided by a dielectric beam splitter BS_2 into two input beams I_1 and I_2. A neutral density filter was placed in beam I_1 to reduce the intensity of the conjugate beam to equal that of I_2, and simultaneously to increase the response time of the grating. The measured intensities of the two input beams I_1, I_2 and the pump beam I_3 were 0.8 mW, 1.5 mW and 1.6 mW respectively. The pump beam on passing through the BSO crystal, half wave plate and converging lens L_3 was loosely focused into the $BaTiO_3$ crystal. The $BaTiO_3$ crystal acts as a self-pumped retro-reflector [5.17], and provides a readout beam that is the exact phase conjugate of I_3.

The use of $BaTiO_3$ greatly simplifies the experimental procedure for positioning of counter propagating pumps, and also provides optimum fidelity for the phase conjugate output, as the two pump beams are therefore mutually phase conjugate. Lenses L_1 and L_2 both of 300 mm focal length were used for 1:1 imaging of the input transparency into the crystal and of the phase conjugate to the image plane respectively. Beam I_1 was at an angle of 50° and beam I_2 at an angle of 7° with respect to the pump beam. Under the optimum conditions of overlap, two independent phase conjugates were obtained free of crosstalk. The two phase conjugates were subsequently recombined at BS_2 to produce mutual cancellation at

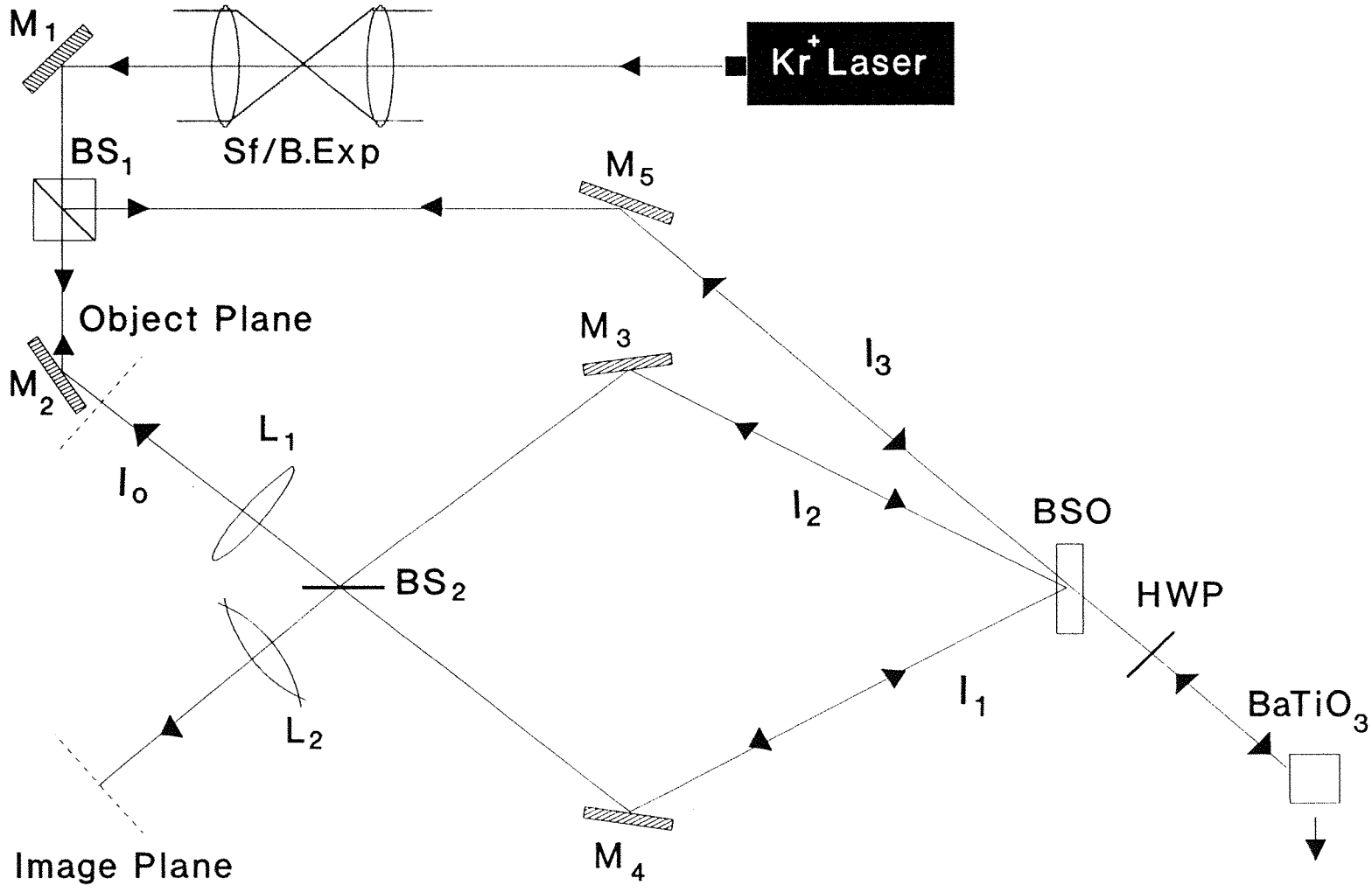

Figure 5.2 The experimental arrangement for optical motion detection using multiplexed gratings in a BSO crystal.

the output.

Figure 5.3 illustrates the basic operation of our technique when the input beam I_o was subject to chopping at a low frequency (1 Hz). Figures 5.3(a) and 5.3(b) show the phase conjugates of beams I_1 and I_2 respectively when the input was static (un-chopped); Figure 5.3(c) shows the resultant image subtraction obtained from the output port of BS_2 at the image plane, in which almost complete destructive interference has been obtained. When I_o was chopped however, the variation of response time for beams I_1 and I_2 does yield an output in the image plane, Figure 5.3(d), as completely destructive interference no longer occurs. It is clear therefore that any temporal change in the object plane may be observed as an output in the image plane.

Using an input wavelength of λ=568 nm, and at the low intensities available, the results shown in Figure 5.3 were obtainable up to a maximum chopping frequency of ≈10 Hz. Above this the rise time for grating formation for both beams was sufficiently long that no image was obtained at the image plane. When the λ=520.8 nm green line was used however, the maximum chopping rate at which almost complete subtraction occurred extended to ≈50 Hz. Between ≈70 Hz and ≈130 Hz, incomplete destructive interference occurred and the phase conjugate for one beam only appeared at the image plane.

Figure 5.4 shows twelve oscilloscope traces, recorded on a digital storage scope, of the light arriving at a photodiode placed at the image plane, when chopping of beam I_o occurred at 1, 5 and 10 Hz respectively. In the figure, the first column (A) shows the output from the interferometer arm whose response time was slower, while (B) shows the output from the faster arm. In each case these traces were recorded with the other arm blocked. Traces (C) show the results from the output port of BS_2 at the image plane when both phase conjugates interfere at BS_2, and traces (D) show the residual noise detected by the photodiode when the readout beam was blocked. This represents the amount of scattering, largely from the crystal surface, that was the main problem encountered in trying to achieve complete cancellation at BS_2. All the data shown was recorded at λ=568.2 nm.

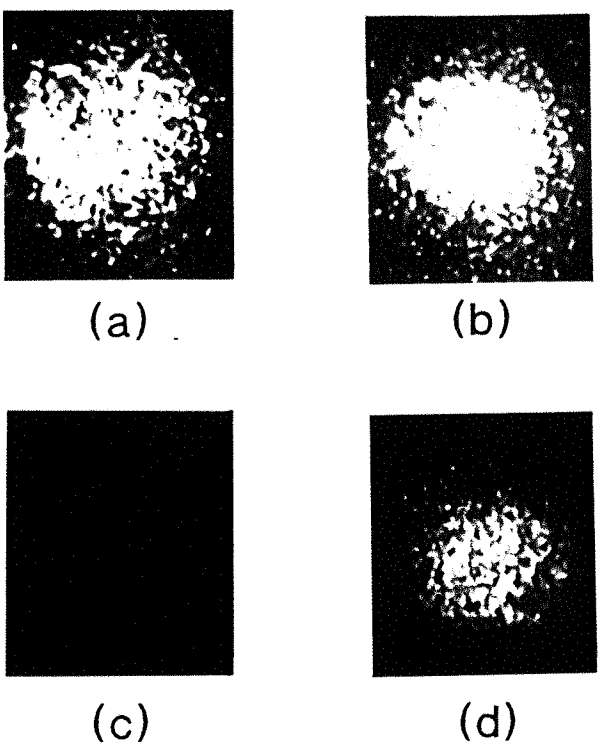

Figure 5.3 Illustrates the basic operation of the novelty filter: (a) Phase conjugate of beam I_1, (b) Phase conjugate of beam I_2, (c) Mutual cancellation of both beams under static conditions, (d) Output in the image plane when beam I_o is chopped at a frequency of 1 Hz.

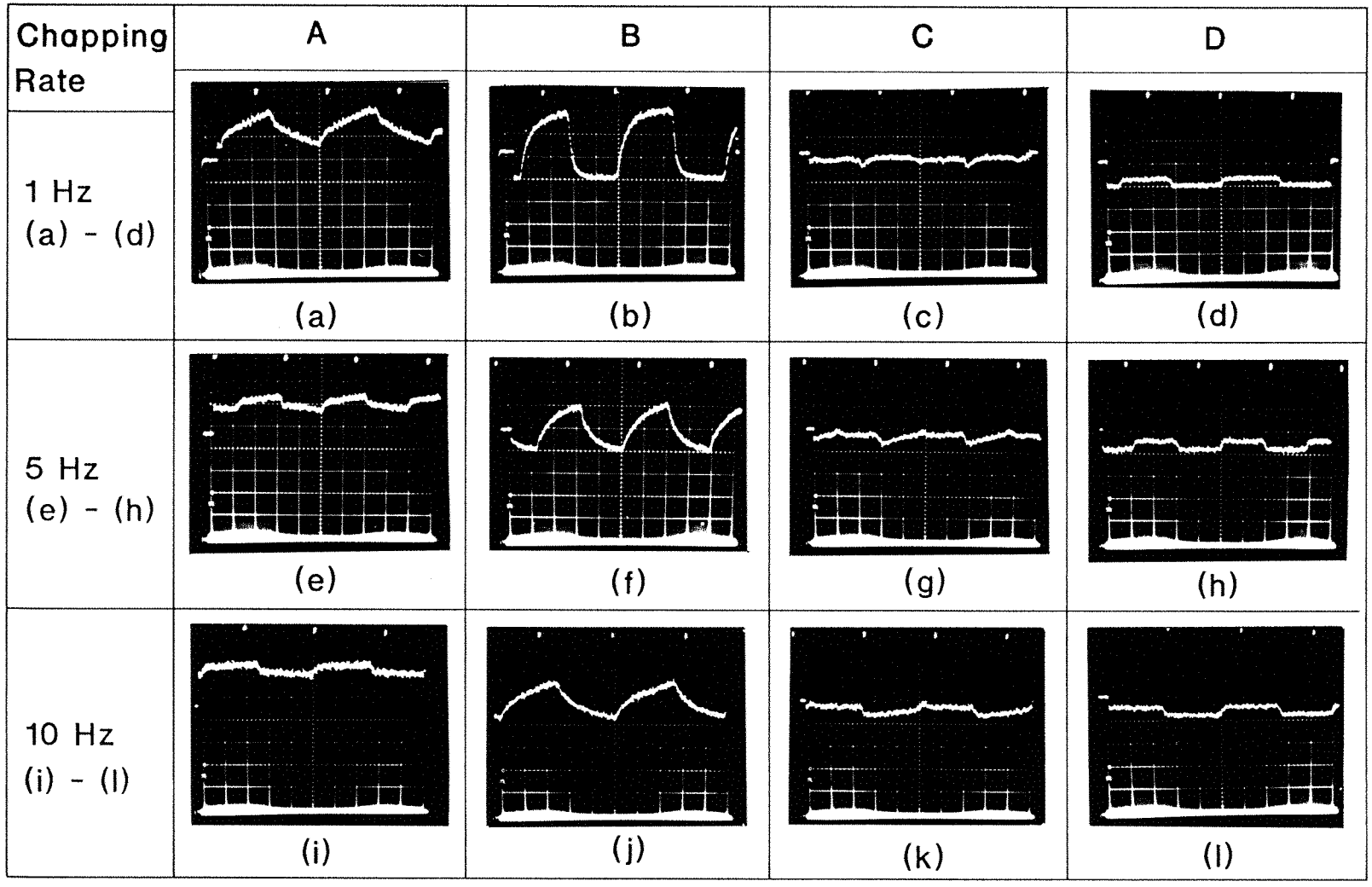

Figure 5.4 Output detected by a photodiode at the output port of BS_2 when beam I_o is chopped at a frequency of 1 Hz, 5 Hz and 10 Hz. (a) and (b) are the phase conjugates of beam I_1 and I_2 respectively. Transient interference between both beams is shown in (c). (d) shows the scattered background light (noise) during the chopping of I_o.

At a 1 Hz chopping rate, which is close to the response time of BSO at this wavelength and input power density, figure 5.4(a), for the slower arm, shows that the intensity of the phase conjugate neither saturates nor decays completely during the chopping cycle, whereas in figure 5.4(b) the faster response results in a conjugate output that follows the chopping profile much more accurately. Figure 5.4(c) is the output at the image plane which results from interference of the two conjugates at BS_2. Analysis of this profile is complicated, as we mentioned earlier for several reasons: the temporal development of both amplitude and phase of the two space charge fields is not independent, and mutual depletion must also occur during this non-steady state regime. The profile here also has a contribution from the scattering that is seen in figure 5.4(d).

At chopping rates of 5 Hz (Figures. 5.4(e)-(h)) and 10 Hz (Figures 5.4(i)-(l)), the results while qualitatively similar, show distinct differences. At 5 Hz, the slower arm (Figure 5.4(e)) can clearly no longer follow the rate of chopping. The output is smoothed or averaged and the contribution from noise is more apparent than at 1 Hz. The faster arm (Figure 5.4(f)) has an output that appears more saw-tooth than at 1 Hz, again due to the incomplete growth and decay of the conjugate output. At 10 Hz, the effect of the increased chopping rate is to reduce the output from the slower arm (Figure 5.4(i)) to effectively a DC component, and to reduce the output from the faster arm to resemble that in Figure 5.4(a). Comparing Figure 5.4(a) with Figure 5.4(j) therefore we see the ratio of the response times for **fast** and **slow** arms to be roughly 1:10. The corresponding output from BS_2 as shown in Figure 5.4(k) shows very little apart from the scattered noise contribution. When a TV camera is exchanged for the photodiode at this chopping rate, very low output is observed other than noise, a situation which holds for all higher chopping rates.

The performance of this device was also studied when a resolution test chart was placed in the object plane. Shown in Figure 5.5(a) is the conjugate image from beam 1 of the interferometer (with beam 2 blocked), and Figure 5.5(b) the result of static cancellation as viewed in the image plane. When the test chart was moved slowly, or temporarily displaced, a bright image transiently appeared, Figure 5.5(c), which disappeared again when static conditions resumed.

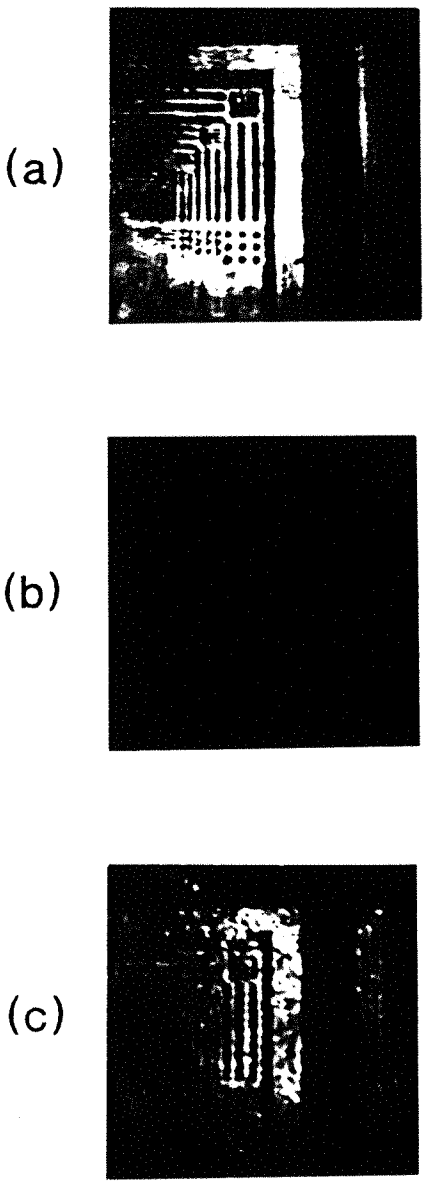

Figure 5.5 Photographs showing the response of the system to sudden motion in the object plane. (a) Output image of part of test chart from one of the arms of the interferometer. (b) Subtraction of the two images under static conditions. (c) Appearance of the object when displaced slightly from its static position.

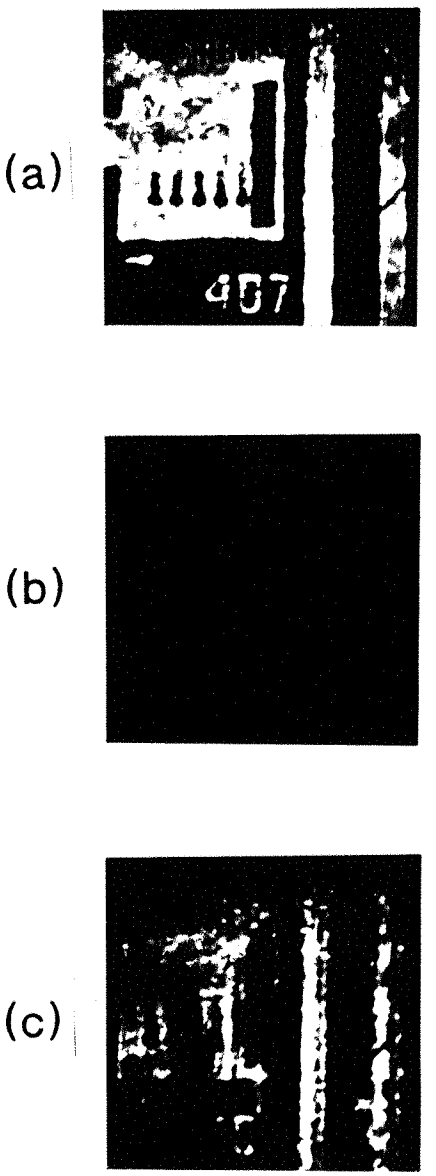

Figure 5.6 Results of directional motion of object seen at the image plane. (a) Output from one of the arms. (b) Cancellation of the two images when object is static. (c) Image of the moving object observed at the output port of BS_2.

Directional motion was also examined by slowly translating the object in one direction only. Figures 5.6(a) and 5.6(b) show a different part of the test chart under conditions similar to those in Figure 5.5. When the chart was translated slowly in the x-direction (horizontally), the output mainly consists of those features which are in the y-direction (vertical). Although the quality of these results is poor, it does show the application to spatial differentiation. The difference in response times for each arm results in the appearance of two simultaneous shifted images which are subtracted preferentially in those areas of maximum temporal overlap. The width of the resulting lines, which have a similarity to edge enhanced features, may be used to measure velocity for example. The minimum detectable velocity here would be determined by the minimum between $(\tau_{1e}-\tau_{2e})$ and $(\tau_{1r}-\tau_{2r})$ according to

$$V=\frac{d}{\min[(\tau_{1e}-\tau_{2e}),(\tau_{1r}-\tau_{2r})]} \qquad (5.6)$$

where d is the minimum resolvable feature.

A final technique for observing motion involves examination of the Fourier transform of the information generated via interference at BS_2 and output at the image plane. When a second lens is used to generate the transform of the output, a typical spectrum of the input transparency is observed as shown in Figure 5.7(a) for beam 1 alone. On static cancellation Figure 5.7(b) shows near perfect subtraction for all Fourier orders other than the **DC**, which is present largely due to the unavoidable residual background noise. In principle, this residual noise content can be quantified and steps taken such as index-matching, to reduce these deleterious effects to a minimum. Such steps were not taken here, as clearly further refinement is possible at a later stage. As the chart was translated slowly in the x-direction however, only Fourier orders also in the x-direction appeared, corresponding to those features in the image in the orthogonal y-direction, Figure 5.7(c). An entirely similar result was obtained for corresponding motion in the y-direction Figure 5.7(d).

For Figure 5.7(c) for example, the number or extent of Fourier orders that appear is a measure of the speed of translation of the original object. The greater the speed, the less orders appear. This technique has a clear application in directional filtering or velocity selection of moving objects.

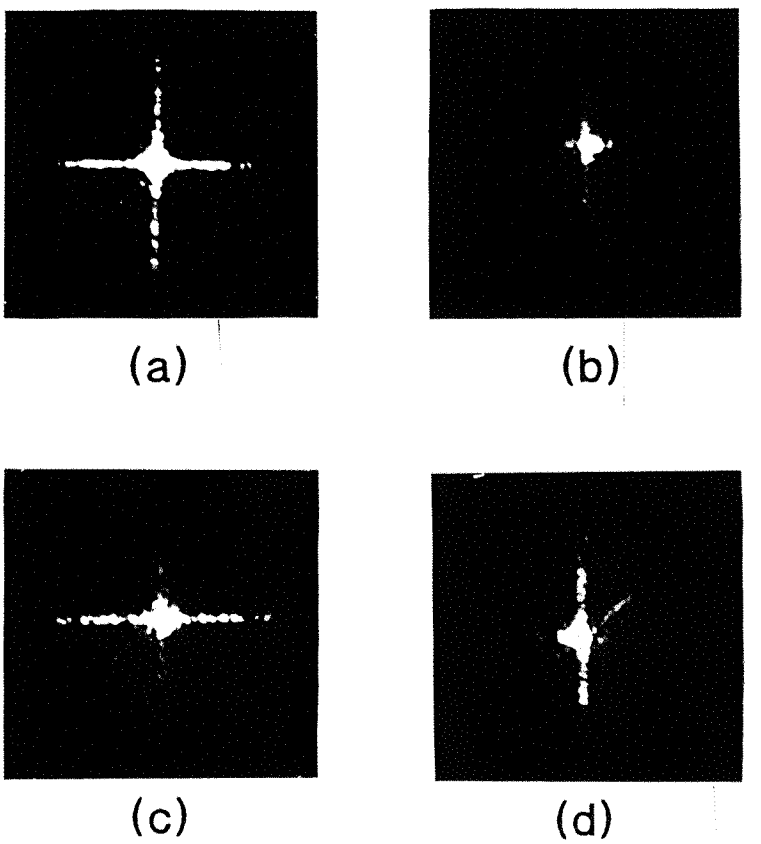

Figure 5.7 Fourier transforms of image demonstrating directional filtering. (a) Fourier transform of image from one arm only. (b) Fourier transform of resultant output at image plane under conditions of static cancellation. (c) Output when object undergoes translation in the horizontal direction. (d) Similar results to (c) above for vertical motion only.

5.4 Further work

5.4.1 Optical tracking and motion detection using photorefractive BSO and $BaTiO_3$

We propose a new technique for optical novelty filtering which is shown in Figure 5.8. This technique relies on the basic configuration of a phase conjugate Michelson interferometer, in which on of the arms has a BSO crystal as a phase conjugate mirror while the other one has a $BaTiO_3$ crystal. The BSO, being the faster material, is used to write a real time hologram, whereas in $BaTiO_3$ the hologram is electrically fixed. This hologram fixing in Iron doped $BaTiO_3$ has been demonstrated by Micheron and Bismuth [5.18].

The simultaneous readout of the two gratings will give rise to two phase conjugate beams which may be of unequal intensities. This intensity mismatch can be compensated by reading the holograms with different intensity beams or putting a neutral density filter in the writing beams. When the real time and fixed gratings are recorded of a scene, both the phase conjugate images will cancel each other at a dielectric beam-splitter, under static conditions. However when some change occur from within the scene the real time hologram of this whole scene will be recorded in the BSO, whereas nothing will be recorded by the fixed grating. As a result motion or any novelty in the image plane will be detected.

This technique may prove more efficient in some respects than the one that we have demonstrated. However, the ability to detect moving objects of the proposed device does not depend on the difference of response time of the BSO crystal alone. Hence the device can detect moving objects having a wide range of speeds and therefore, can detect the change, even if it is static which was not possible with the demonstrated technique.

For the case when some change occurs within the scene (say in a museum a painting is displaced) the device senses both the old and new places. This device may also find a variety of applications in the field of engineering as well, such as civil engineering. Erosion and other deformations in dams bridges, roads etc, can be seen. To detect such defects the holograms of these structures should be fixed at final

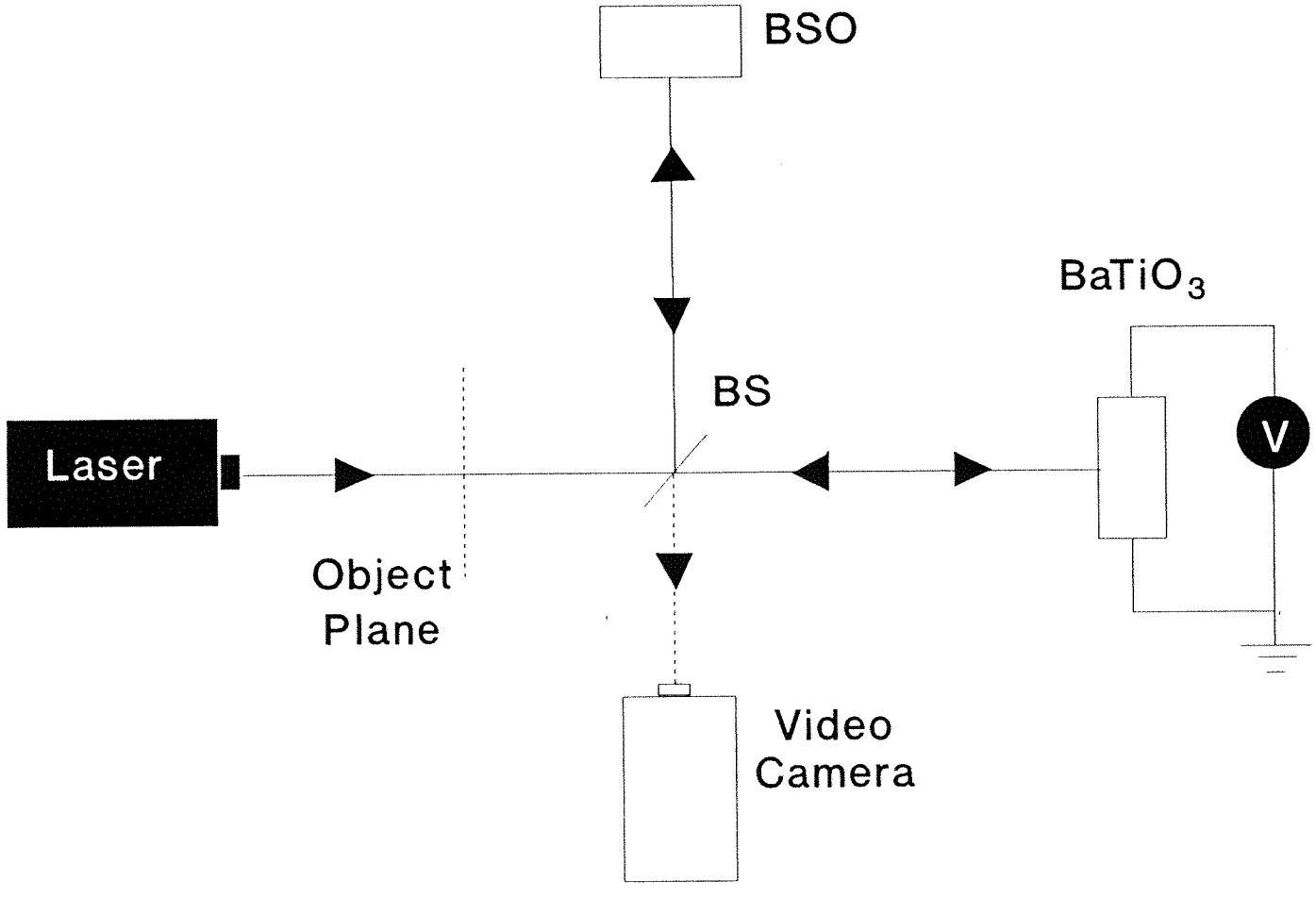

Figure 5.8 Shows a schematic diagram for optical motion detection using a real time grating in BSO and a fixed grating in $BaTiO_3$ in the PCMI configuration.

construction stage, so that in later routine inspections these can be used and subtracted from the real time holograms to detect any possible deformation.The technique is flexible enough so that the fixed holograms can be erased electrically at room temperature. Which will re-enable the device for a new scene. Similarly SBN crystal can also be used in place of $BaTiO_3$ to fix the grating electrically [5.19].

5.4.2 Optical novelty filtering via polarization encoding of PC outputs from reflection and transmission holograms

We further suggest a different scheme for optical motion detection that is based on a single FWM geometry. We use here a transmission and reflection gratings configuration in a photorefractive crystal with a single object beam. Figure 5.9 shows the schematic of the novelty filter. Beam-splitter BS_1 divides the input beam into two and BS_2 divides the transmitted beam further into beams I_o and I_{r1}. Beam I_o, which is the object beam, interferes with the beam I_{r1} inside a photorefractive crystal (i.e. BSO), to record a transmission grating, while the beam I_{r2} is incident from the other side of the crystal and interferes with the object beam to record a reflection grating. All the three incident beams to the crystal are therefore mutually coherent. As shown in Figure 5.9 the grating written between I_o and I_{r1} is readout by I_{r2} while the grating recorded by I_o and I_{r2} is readout by I_{r1}. Due to the usual geometry for recording reflection and transmission gratings, the fringe spacing for transmission gratings is larger while that of the reflection grating is less. The response time can therefore be controlled (apart from via applied field and total intensity incident on the crystal) by the angles between the three interfering beams. Therefore, in crystals such as BSO, gratings with larger fringe spacing will have shorter response times while gratings with smaller fringe spacing will have longer response times. Due to the different response times of the two gratings their phase conjugate outputs will have a time lag and any moving object is observed at the output.

Taking advantage of the large optical activity of BSO, its crystallographic orientation, and manipulating the polarization of the readout beams, it is possible to vary the polarization of the two phase conjugate outputs. It may also be possible to achieve orthogonal polarization of these outputs at certain input polarizations of the readout beams. Further use of this idea is discussed more extensively in Chapter 7.

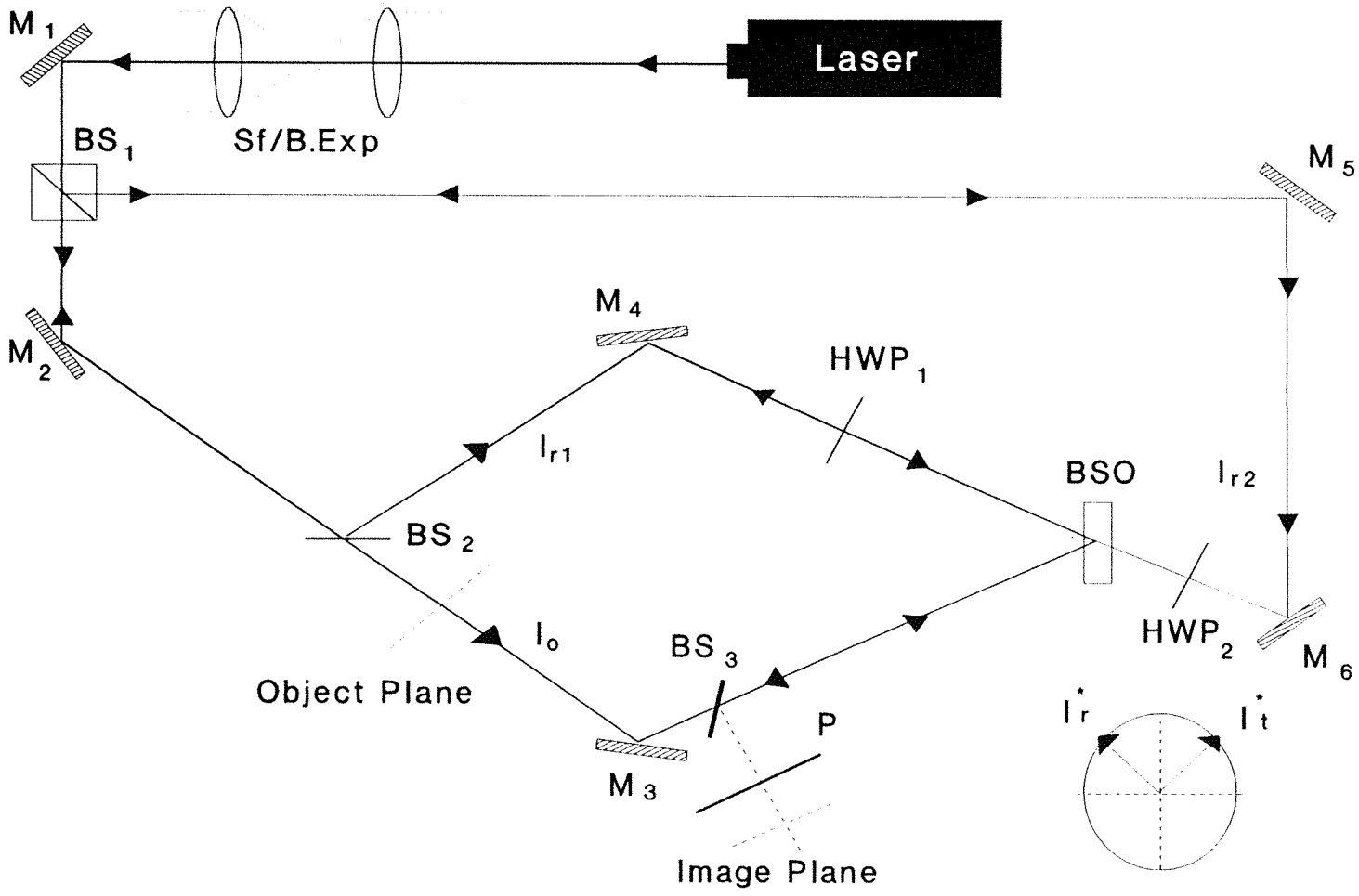

Figure 5.9 Shows the schematic diagram for optical motion detection via polarization encoding of the phase conjugate output from transmission and reflection holograms in a DFWM arrangement.

Rotating the analyzer at the output we can achieve constructive and destructive interference between the two phase conjugate outputs. When there is an object in the signal beam I_1, the phase conjugate outputs can be analyzed for positive and negative contrasts by interfering in-phase and out-of-phase components. When the object is static, a positive contrast phase conjugate image is achieved for constructive interference of the two outputs, while for the destructive interference case no output is achieved. However when there is any movement in the object plane, the two gratings will respond to the change according to their response times and give rise to an output as time differentiation of the input. For the constructive interference case, the moving objects would appear less bright (or darker), due to the output from only one grating, or no output from either of the two gratings depending on the response times and speed of the change while the static parts will be brighter. However for the destructive interference case all the static parts of the object will be subtracted while any moving features appear bright as a novelty output.

Our proposed technique has certain advantages over the previous techniques which may make it a likely candidate for future applications. For example when the diffraction efficiency of the two gratings is different, which may arise due to the different input polarizations of the interfering beams, different fringe spacings etc, it is possible to achieve equal output intensities of the phase conjugate outputs by rotating the analyzer. Therefore different relative proportions of the two phase conjugate outputs can be achieved. Similarly, the other advantage is that it is possible to achieve positive (constructive interference) contrast as well as negative (destructive) contrast at the output plane for static and moving objects.

The positive contrast output case is particularly useful for situations where moving object positions are also relevant to static objects such as a car chase which needs to be observed for example from above. Moving cars in this case would appear dark on a relatively bright background of static features. Similarly, it can also be applied for industrial inspection applications where moving objects are of no interest while static objects need to be inspected constantly. An example of this may be a moving conveyer belt where the objects are transported against the static surroundings. In the monotony mode of operation, moving objects will not be observed however, while static surroundings will appear bright. Such an operation

could be used to observe wear and tear of the static surroundings for example.

5.4.3 Optical novelty filtering via polarization encoding of PC outputs from Multiplexed transmission holograms

Another scheme of optical motion detection is proposed which is based on a two DFWM arrangement. Figure 5.10 shows the configuration for motion detection where an input beam is divided by a beam-splitter BS_2 into an object beam and a transmitted beam, which is further divided by BS_3 into two reference beams. All the three beams interfere in a photorefractive crystal such as BSO, to form two DFWM arrangements with a common signal beam. The two reference beams are at different angles to the signal beam, to control the fringe spacings arbitrarily, and hence achieve differential response times. The readout of these two gratings is carried out by probe beams I_3 and I_4, which are counter propagating with respect to I_1 and I_2.

For better results, self-pumped phase conjugates of the reference beams can be used to read out the two gratings. Exploiting the large optical activity and the orientation of BSO, the polarization of the two phase conjugate outputs can be manipulated by rotating the polarization of the readout beams. Therefore we may take orthogonal polarizations of the two phase conjugate beams. By using an analyzer, we can manipulate the interference between the two phase conjugate outputs to be constructive or destructive at the output. To achieve such an operation here we do not need to bother about the input polarization of the three interfering beams unlike the previous proposal. Therefore interference at the analyzer can be manipulated by rotating the polarization of one, or both of the readout beams.

This final proposed technique of motion detection has a number of advantages over the previously demonstrated techniques. It is easy to demonstrate because only one object beam required. It is not based on a Michelson interferometer which requires the intensity of the two phase conjugates to be equal and also their direction of polarizations to be in the same plane at the lossless beam-splitter, to achieve interference. Constructive and destructive interference takes place by rotating the analyzer before the image plane. It is easy to vary the angles between the reference beams and signal beams, by changing the angular position of reference beams.

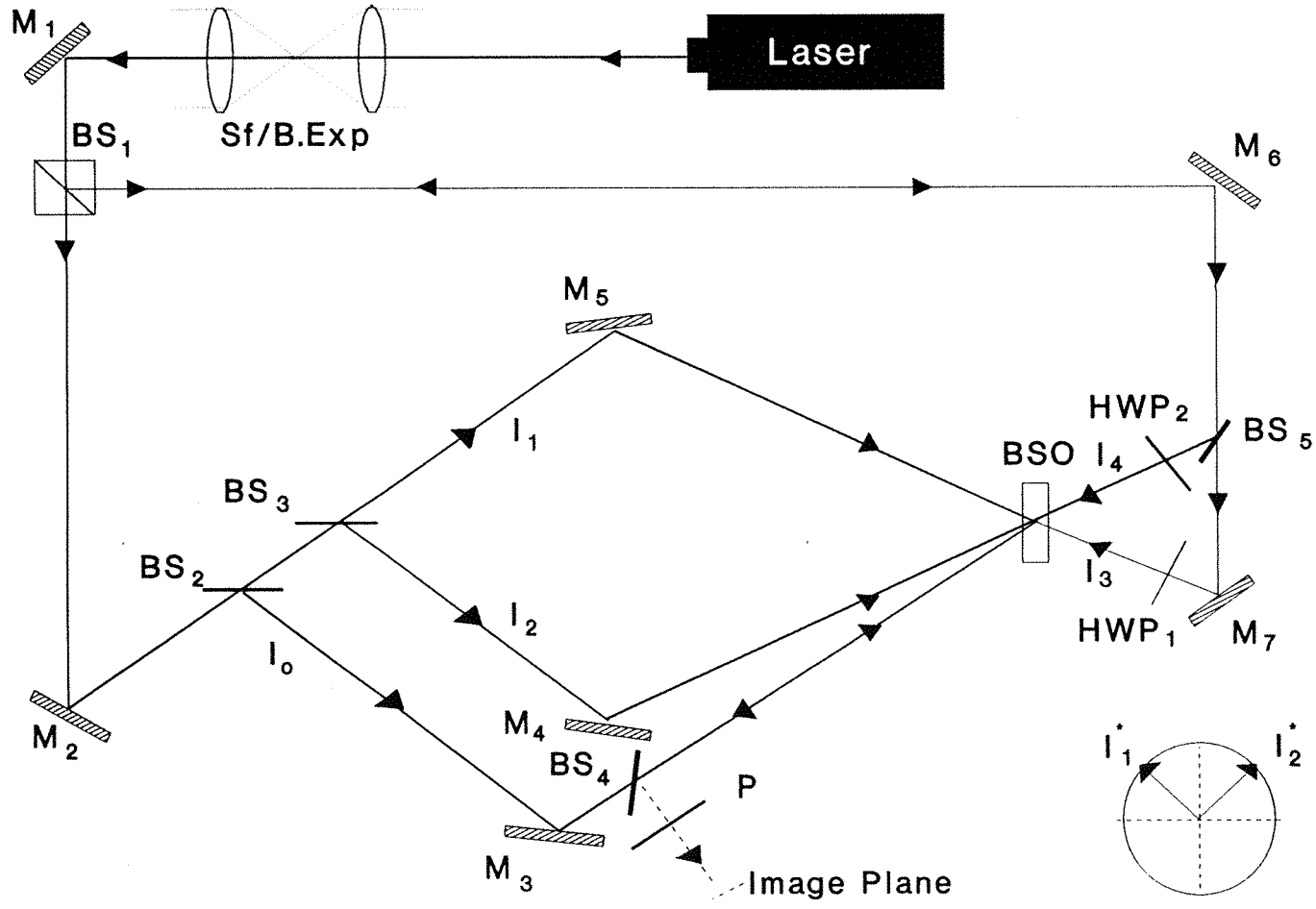

Figure 5.10 Shows the arrangement for recording multiplexed holograms with a single object beam for motion detection based on polarization encoding of the phase conjugate outputs from the two holograms.

Finally operation of novelty filtering can be performed even if the phase conjugate output from the two gratings are of unequal strength.

5.5 Conclusion

A technique for optical motion detection and image differentiation in time has been demonstrated that exploits the variable response time of multiplexed grating formation in a single crystal of BSO in a phase conjugate Michelson interferometer configuration. The detection characteristics and differential signal output can be varied via a tunable response time for the each arm. Experimental results are presented for motion detection in the image plane as well as in the Fourier plane.

Three new techniques for optical novelty filtering are also proposed. A technique which relies on a phase conjugate Michelson interferometric arrangement has a BSO crystal in one of its arms while the other arm has an SBN (or $BaTiO_3$) crystal. The BSO crystal records the real time hologram while the SBN (or $BaTiO_3$) records and fixes the same hologram by applying an electric field. Any subsequent change in the image will be detected even if this is very slow or even stationary. Therefore the motion detection by this device only depends on the response time of the BSO. A second technique involves two types of gratings sharing a common object beam, recorded with different response times. The polarization of the two phase conjugate beams is manipulated to be orthogonal which is subsequently analyzed by a polarizer.

The third technique relies on two DFWM arrangement to record two transmission gratings with different fringe spacings. By exploiting the optical activity of BSO and crystallographic orientation dependent polarization, the phase conjugate beams are rotated to orthogonal directions and subsequently be analyzed.

REFERENCES

5.1 T. Aida, K. Takizawa, and M. Okada, "Real-time tracking of a moving object in a television image using an optical system consisting of a liquid-crystal television and a position-sensitive device", Opt. Lett. **14**, 835 (1989).

5.2 Y. Li, A. Kostrzewski, D. H. Kim, and G. Eichmann, "Liquid crystal TV-based white light optical tracking novelty filter", Appl. Opt. **28**, 4861 (1989).

5.3 C. Soutar, C. M. Cartwright, W. A. Gillespie and Z. Q. Wang, "Tracking novelty filter using transient enhancement of gratings in photorefractive BSO", Opt. Commun. **86**, 255, (1991).

5.4 M. Cronin-Golomb, A. M. Biernacki, C. Lin, and H. Kong, "Photorefractive time differentiation of coherent optical images", Opt. Lett. **12**, 1029 (1987).

5.5 R. S. Cudney, R. M. Pierce and J. Feinberg, "The transient detection microscope", Nature, **332**, 424 (1988).

5.6 N. S. K. Kowng, Y. Tamita and A. Yariv, "Optical tracking filter using transient energy coupling", J. Opt. Soc. Am. B, **5**, 1788 (1988).

5.7 D. Z. Anderson, D. M. Lininger and J. Feinberg, "Optical tracking novelty filter", Opt. Lett. **12**, 123 (1987).

5.8 D. T. H. Liu and L. J. Cheng, "Resolution of a target-tracking optical novelty filter", Opt. Eng. **30**, 571 (1991).

5.9 J. Khoury, V. Ryan, C. Woods and M. Cronin-Golomb, "Photorefractive time correlation motion detection", Opt. Commun. **85**, 5 (1991).

5.10 J. Khoury, C. L. Woods and M. Cronin-Golomb, "Photorefractive holographic interference novelty filter", Opt. Comm. **82**, 533 (1991).

5.11 G. C. Valley, M. B. Klein, "Optimal properties of photorefractive materials for optical data processing", Opt. Eng. **22**, 704 (1983).

5.12 P. Gunter, "Holography, coherent light amplification and optical phase conjugation", Physics Report, Phys. Lett. **93**, 199 (1983).

5.13 J. Strait and A. M. Glass, "Time resolved photorefractive four wave mixing in semiconductor materials", J. Opt. Soc. Am. B. **3**, 342 (1986).

5.14 N. A. Vainos, J. A. Khoury and R. W. Eason, "Real time parallel optical logic in photorefractive bismuth silicon oxide", Opt. Lett. **13**, 503 (1988).

5.15 A. E. Chiou and P. Yeh, "Parallel image subtraction using a phase-conjugate Michelson interferometer", Opt. Lett. **11**, 306 (1986).

5.16 J. Feinberg, "Self-pumped, continuous-wave phase conjugator using internal reflection", Opt. Lett. **7**, 486 (1982).

5.17 J. A. Khoury, G. Hussain and R. W. Eason, "Optical tracking and motion detection using photorefractive $Bi_{12}SiO_{20}$", Opt. Commun. **71**, 138 (1989).

5.18 F. Micheron and G. Bismuth, "Electrical control of fixation and erasure of holographic patterns in Ferroelectric materials", Appl. Phys. Lett. **20**, 79 (1972).

5.19 F. Micheron and G. Bismuth, "Field and time threshold for the electrical fixation of holograms recorded in $(Sr_{0.75}Ba_{0.25})Nb_2O_6$ crystals", Appl. Phys. Lett. **23**, 71 (1973).

CHAPTER 6

VELOCITY FILTERING USING COMPLEMENTARY GRATINGS IN PHOTOREFRACTIVE BSO

6.1 Introduction

The operations of motion detection, velocity filtering and detection of change in a given scene are all important aspects for optical processing architectures and systems. Fields in which this capability has immediate applications include industrial inspection, bio-medical screening techniques and machine vision. So far several different techniques have been implemented and these have already been discussed in Chapter 5.

Image subtraction is one of the basic operations which is required for motion detection applications, and in recent years the need for faster techniques of image subtraction has been realized. Optics, due to its inherent parallel nature of processing, has an important application in optical image subtraction. Several image subtraction techniques have been reported in recent years and have also been used to perform motion detection [6.1-6.3].

A technique of multiplexed hologram recording has been reported by Vainos and Eason [6.4] in photorefractive BSO. Here they recorded four multiplexed holograms in a single crystal of BSO using four angularly multiplexed input beams which separately interfere with a single reference beam. Using a variation of this technique, two multiplexed holograms have been recorded such that when these holograms are simultaneously readout the phase conjugate outputs interfere destructively at the output of a beam-splitter to generate the operation of subtraction. Novelty filtering using this principle has already been reported by Anderson et al [6.5] and also by the author, as mentioned in Chapter 5. In this technique the required phase shift of 180° between the two phase conjugate outputs is achieved via the reflection and transmission characteristics of a dielectric beam-splitter.

Here we will discuss some of the image subtraction techniques upon which our technique of velocity filtering is based which have already been reported in the literature. One of the earliest techniques of image subtraction has been reported by Gabor et al [6.6], who used double exposure holographic recording with a 180° phase shift introduced between the two exposures. The obvious limitation of this technique is that exposure and subsequent chemical processing of the permanent holograms is required. Conventional holography is therefore impracticable for real time image subtraction applications. Fortunately photorefractive crystals provide the means for recording and erasing of real time holographic input.

6.2 Theoretical Considerations

Volume holographic gratings recorded via induced nonlinear electro-optic effects in materials such as BSO and BGO have been studied extensively for more than fifteen years now, and are discussed in detail in [6.7]. Spatial multiplexing of two such gratings is also possible in these materials with an arbitrary spatial phase shift between the two gratings. For a 180° phase shift these two gratings are termed **complementary** and such complementary grating recording techniques have already been implemented in $LiNbO_3$, and BGO crystals [6.8, 6.9], where sequential recording followed by continuous readout gave rise to subtraction between the two phase conjugate outputs: the **Exclusive OR** operation has also been demonstrated for non identical sequential inputs.

The technique of multiplexed grating recording in real time has been reported by Ja [6.9] in which he employed the technique of double exposure to record two gratings in photorefractive BGO using relatively slow response conditions for grating recording and erasing times. Therefore the two gratings are recorded sequentially and are continuously readout in a FWM geometry. A phase shift of 180° was introduced between the two holographic recordings which when readout give rise to subtraction between the outputs from these two holograms. However this technique is used for subtraction of static images which can only be observed at a particular instant in the cycle when the strength of the two gratings is equal. Clearly such equal strengths for the two gratings will occur for only a short time in between the two extreme values of the grating strength.

Optical motion detection however can benefit considerably from the use of a reasonably fast material, such as photorefractive BSO. We demonstrate here a scheme for motion detection and velocity filtering which uses a single object beam with a periodically phase modulated reference beam to record two spatially multiplexed gratings in real time with a resultant phase shift of 180° in the BSO crystal [6.10]. Under static conditions in the output plane the diffraction from these multiplexed gratings leads to destructive interference. For the case of motion however, an output image is seen as the former complete subtraction no longer occurs.

We consider an approach that uses complementary grating recording, in which the reference beam is subject to a periodic phase modulation in transmission geometry. When the two gratings recorded in this way experience a relative phase shift of one half of the grating period, a subtraction in the phase conjugate output occurs.

The principle of subtraction can be described by considering the photoinduced index modulation Δn_A and Δn_B of the two volume holograms recorded for the same object beam with the 180° phase modulated reference beam. The resultant superposed index modulations are thus

$$\Delta n_A = N_A \cos [Kx + \phi_A(x)]$$

$$\Delta n_B = N_B \cos [Kx + \phi_B(x)] \qquad (6.1)$$

Where x is the spatial co-ordinate and K is the grating wavevector. Subtraction is realized when both multiplexed gratings are of identical strength ($N_A = N_B$) and also $\Delta n_A + \Delta n_B = 0$. Here N_A and N_B contain all the information regarding grating modulation strength etc and ϕ_A, ϕ_B are the relative lateral phase shifts of the two gratings.

In the case of a static object these grating profiles are identical and the phase conjugate output is ideally reduced to zero. If any movement occurs in the object plane however these multiplexed gratings will undergo dynamic change and any resultant output will indicate motion within the object plane. For the case of change

that is too fast however new gratings cannot be continuously written and the technique does not work well. If the change is slow however, information recording is efficient, and the phase profile will be almost be same for the two gratings and hence subtraction is achieved. However any particular features that move at a precise speed are exactly of the right combination to record the new grating while the old grating is decaying gradually. In such a situation dynamic subtraction exists between the two outputs and motion can be observed whose character depends on the speed and size of the moving features. A Fourier transform of the output intensity distribution also shows the various orders corresponding to the motion of features of various dimensions at a range of speeds in both **x** and **y** directions.

6.3 Experimental arrangements

Figure 6.1 shows the details of the experimental arrangement for motion detection via this multiplexed degenerate four wave mixing configuration. An Argon Ion laser operating in multi-longitudinal mode at 514.5 nm was spatially filtered and expanded to a diameter of $\approx$ 5 mm and split by beam splitter BS_1. The reflected beam was directed towards mirror M_2 which was mounted on a piezoelectric pusher driven by a variable frequency square wave AC voltage. M_2 reflected the incident beam towards the BSO crystal to act as the reference beam. The beam transmitted through BS_1 was split by BS_2 to form an object beam I_2 and a mutually incoherent counter propagating readout beam I_3. Beam I_2 was incident on the BSO, after traversing an object, beam splitter BS_3, and imaging lens L_1 (f=15 cms).

The intensities of the beams I_1, I_2 and I_3 were arranged to be 7.0 mW, 3.5 mW and 1.7 mW respectively. Lens L_1 was adjusted for 1:1 imaging of the input light distribution into the BSO crystal. The angle between the beams I_1 and I_2 outside the crystal was 40°. Under normal conditions (i.e., when no voltage was applied to the piezo-electric pusher) normal DFWM occurred. To write the complementary gratings a square wave AC voltage was applied to the piezoelectric pusher in the reference beam with a controllable frequency in the range of 0-100 Hz and driving voltages of 0-30 volts.

Figure 6.2 shows the phase conjugate output, measured by a photodiode at the

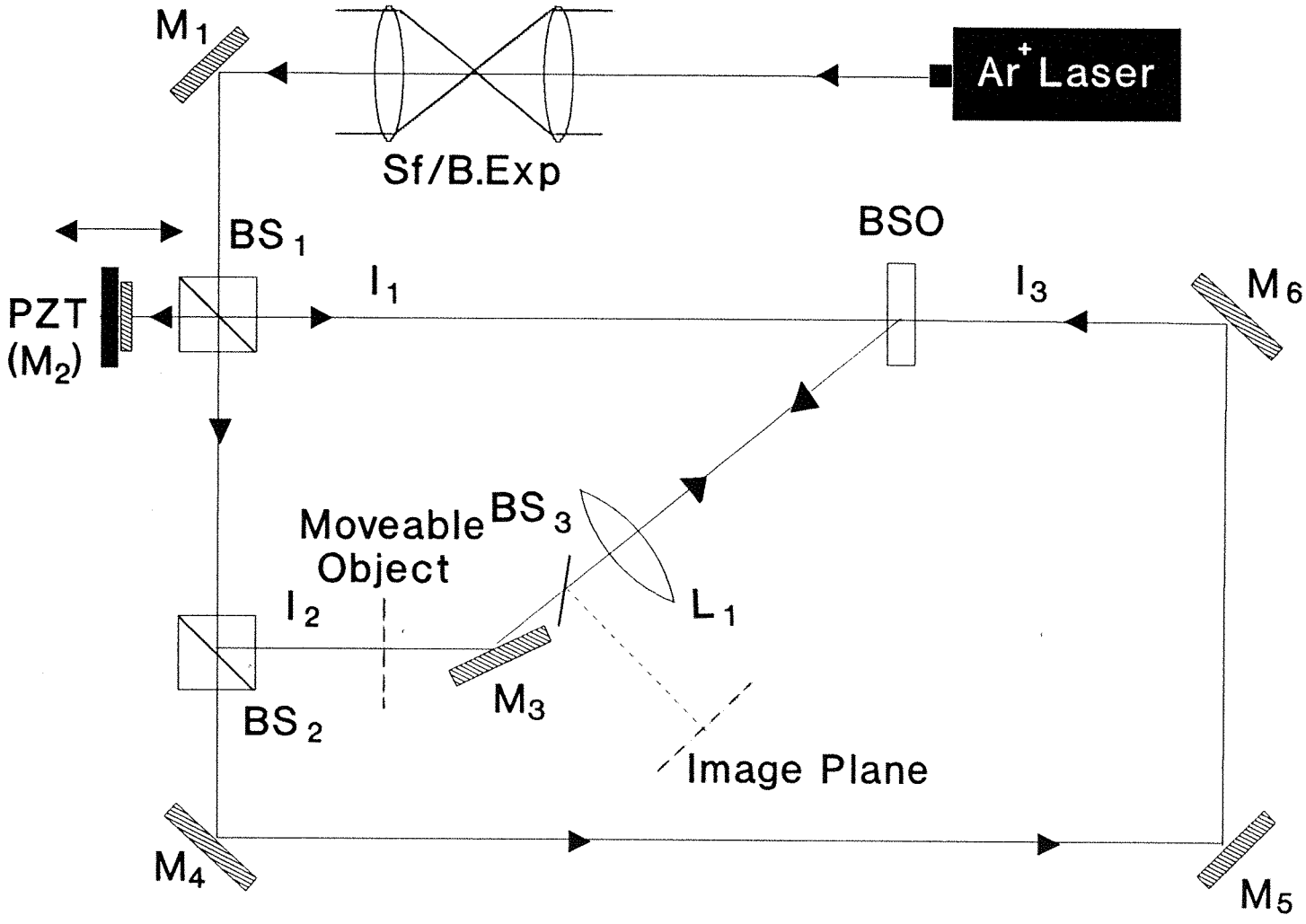

Figure 6.1 The experimental arrangement for velocity filtering using complementary gratings in photorefractive BSO.

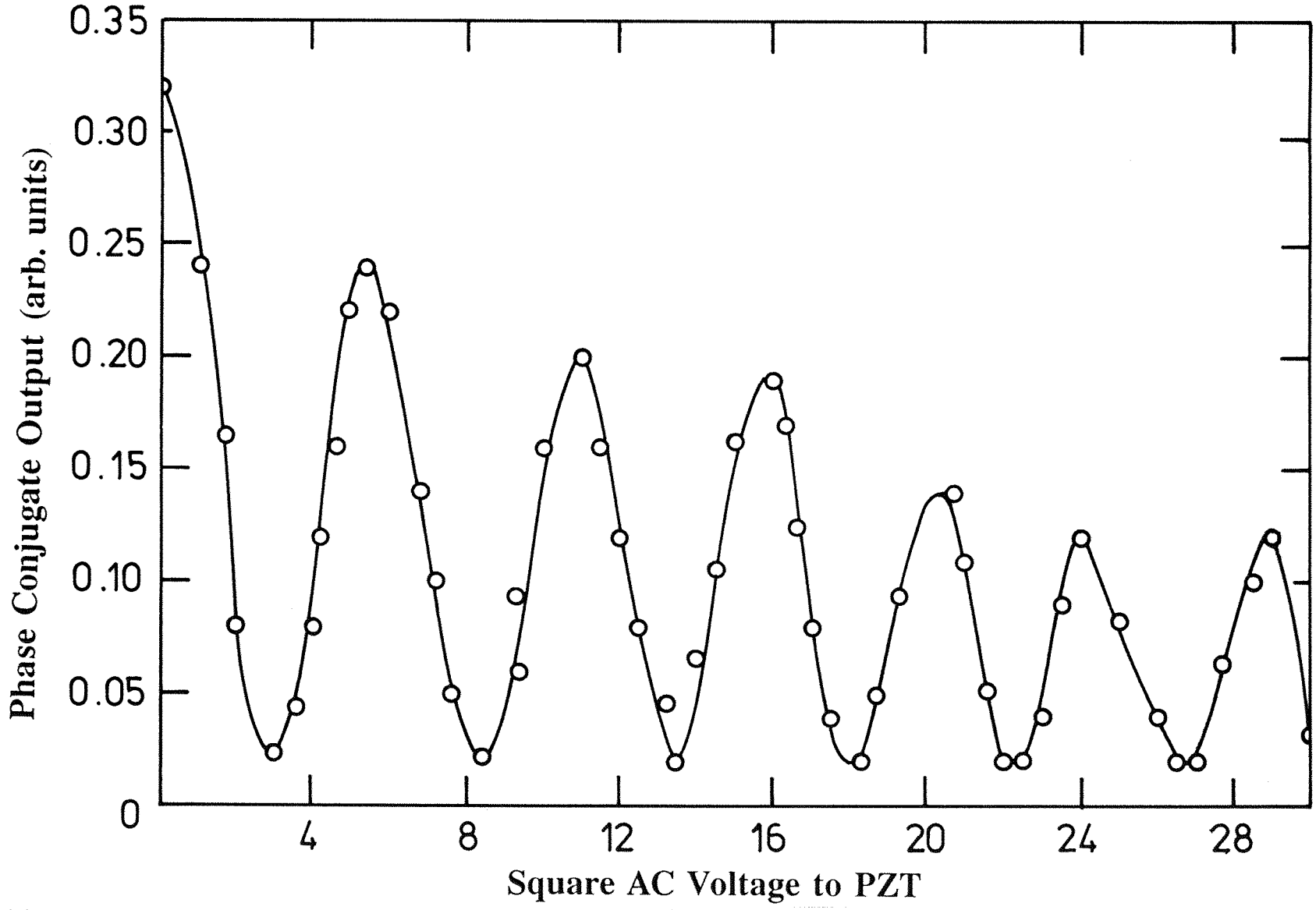

Figure 6.2 Phase conjugate output from complementary gratings versus amplitude of the square waveform AC voltage applied to the piezo-electric pusher (fit to data points is visual only).

image plane, versus the amplitude of the square waveform AC voltage applied to the pusher for the above input laser intensities. The curve shows several minima in the output intensity which correspond to subtraction of the two outputs. At these voltage values the pusher introduces a net phase shift of π (or odd multiples of π) between the two gratings. It was observed that at higher incident laser intensities, appropriately higher frequencies of the AC waveform were required due to the shorter recording and erasing time of the multiplexed gratings. After the first maximum in the phase conjugate output, a decrease in the subsidiary intensity maxima occurs, which is likely to be due to erasure effects caused by 'sweeping' of the gratings through the BSO for progressively larger AC voltages applied to the piezo-electric pusher.

Such subtraction by complementary gratings can be illustrated via a model shown in Figure 6.3, which considers the simultaneous presence of two spatially multiplxed gratings of variable photoinduced index modulation. For this simulation both curves (dashed and dotted lines) have a single exponential decay and growth constant during each of the indicated 100 time step intervals. For this case we have assumed that the decay and growth time constants τ_1 and τ_2 are not equal, which may experimentally be the case, and have set them at 25 and 20 time steps respectively, so that the exponentially decaying grating strength is of the form

$$A(t) = A_o \exp(-t/\tau_1) \qquad (6.2)$$

and the growth curve, during this interval, follows the form given by

$$B(t) = B_o [1 - \exp(-t/\tau_2)] \qquad (6.3)$$

Between time step 1 to 100 in Figure 6.3, the pusher is stationary, and the resultant subtraction is shown as the solid curve. It is clear from this idealized model, that a time occurs when the output is reduced to zero (time step $\approx$15) and complete subtraction has been obtained. This situation however will not last for the whole of the cycle covered by this time-step range, due to the constantly varying growth and decay dynamics; therefore the subtraction curve shows an imperfect subtraction for much of this range.

If however, we choose to either increase the time constants τ_1, and τ_2, or

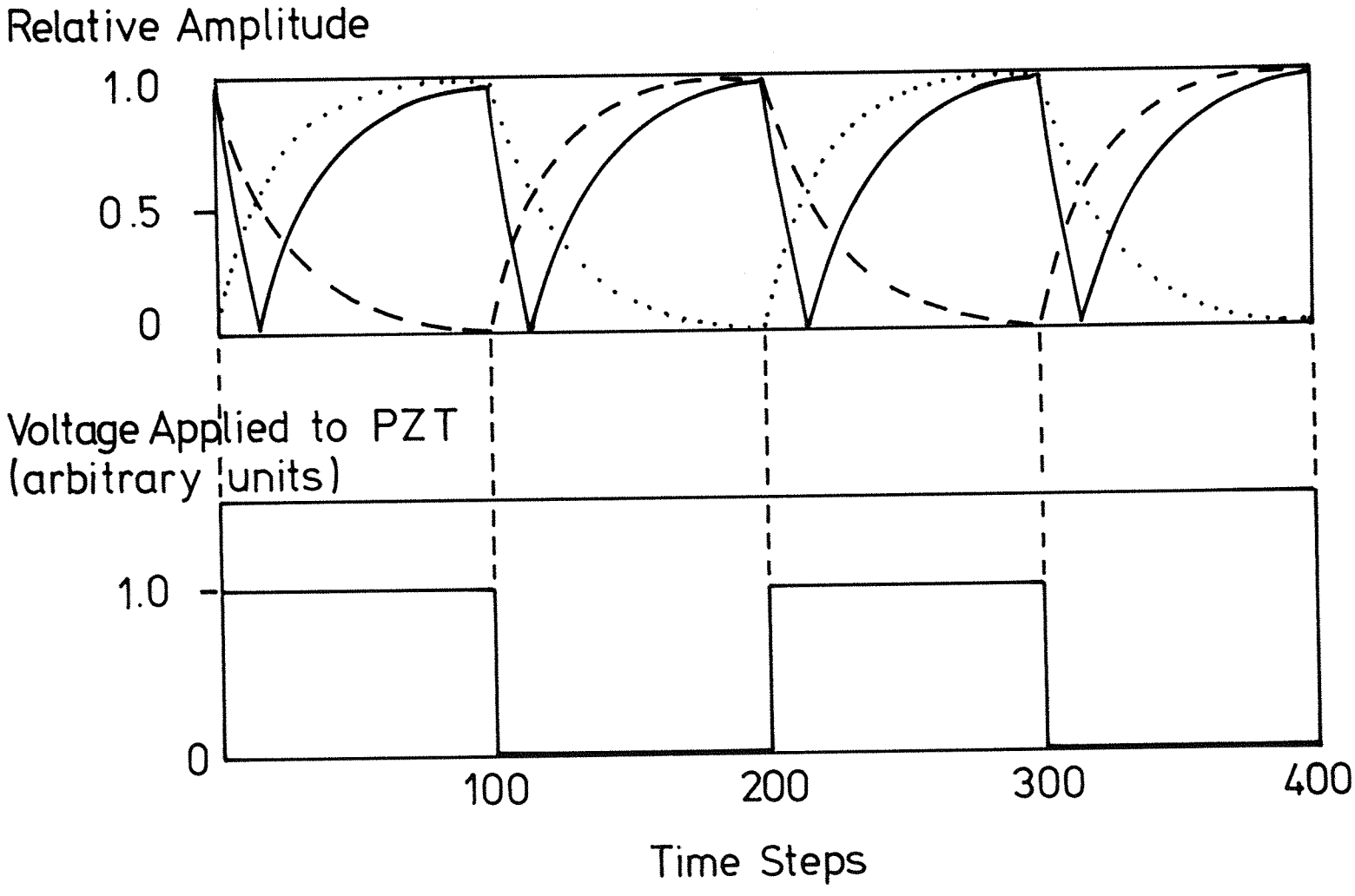

Figure 6.3 Result of simulation for the complementary gratings build up, decay, and the differential output. Dotted and dashed lines indicate decay and growth of the two gratings respectively. The solid line indicates differential output.

equivalently, to increase the pushing frequency (for given values of τ_1 and τ_2), we would expect to see improved subtraction over essentially the complete cycle. Note that in both cases, the sequence above is reversed for the interval between time steps t=101 and 200. The subtraction curve demonstrates a frequency doubling compared to the pushing frequency. For practical implementation of such a scheme, one must consider the temporal build up, and decay, of both these sequentially recorded gratings. If either the writing or erasure times are comparable with the applied periodic phase modulation, then any such subtraction is also dynamic, and ideal subtraction will therefore be compromised. Deliberate motion of the input object will also produce non-optimum subtraction, so that moving areas within an input field will be seen in the output.

Figure 6.4 column (i), shows oscilloscope traces, recorded on a storage scope of the phase conjugate output from the complementary gratings detected at the image plane by a photodiode. The intensities of beams I_1, I_2, and I_3 were 7.0 mW, 3.5 mW and 2 mW respectively. Curve (a) shows the output when no AC square voltage waveform was applied to the pusher, and therefore one grating is present only. Traces (b), (c), (d), (e), (f), (g), and (h) shows the output from the complimentary gratings for 1 Hz, 2 Hz, 5 Hz, 10 Hz, 20 Hz, 30 Hz, and 40 Hz respectively.

When the pusher was driven at a frequency of 30 Hz, output trace (g) shows almost perfect subtraction. Any further increase in pushing frequency would produce better subtraction but is less usable for motion detection, to be discussed below, due to the higher rate of phase modulation. Figure 6.4, column (ii), shows results of a simulation based upon the model shown in Figure 6.3, at pushing frequencies corresponding to those used experimentally. It is clear from this simulation that experiment and modelling are in good qualitative agreement.

Figure 6.5(a) shows the photograph of a resolution test chart whose phase replica was placed in the object plane to demonstrate the results of this velocity filtering technique. Figure 6.5(b) shows the result of image subtraction when complementary gratings are recorded at a pushing frequency of 30 Hz, for the intensities described above.

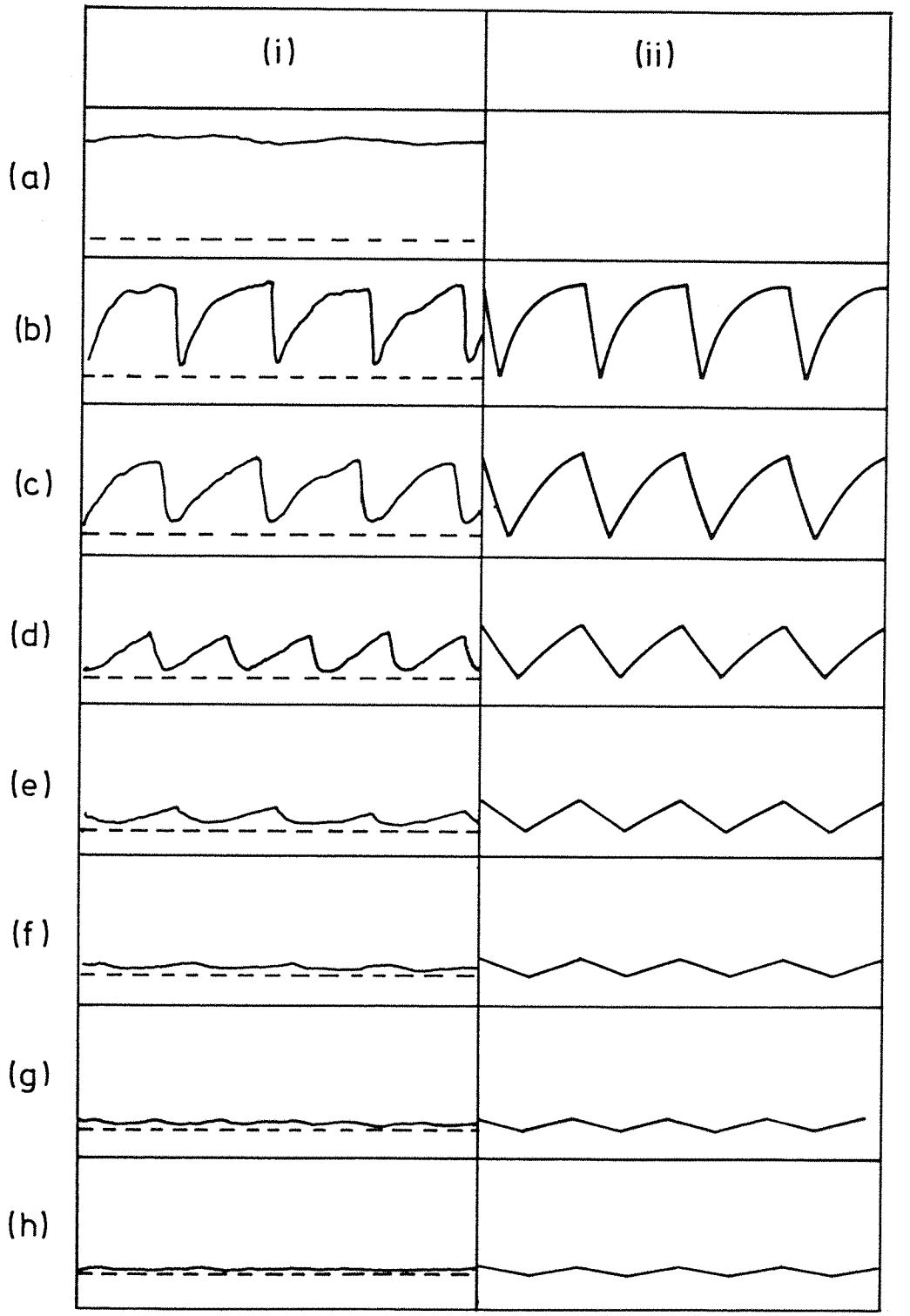

Figure 6.4 Column (i): oscilloscope traces of the phase conjugate output. Column (ii): corresponding simulations for piezo-electric pusher frequencies of 1 Hz (b), 2 Hz (c), 5 Hz (d), 10 Hz (e), 20 Hz (f), 30 Hz (g), and 40 Hz (h) respectively.

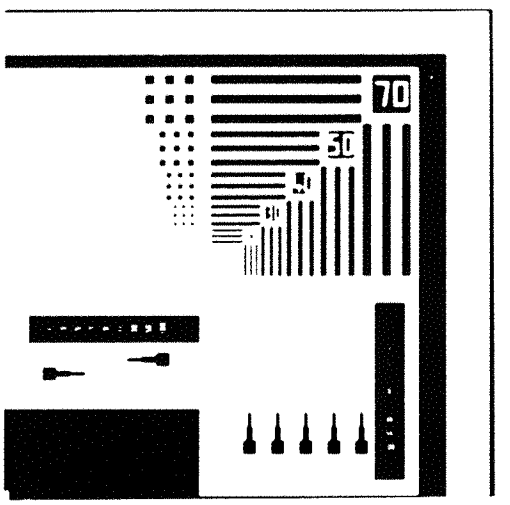

Figure 6.5 (a) shows a photograph of resolution test chart whose phase version was placed in object plane. (b) shows the image subtraction under static condition.

Figure 6.6 shows the results of dynamic image subtraction however in which specific intensity features are observed; a sequence of such output images is shown in Figures 6.6(a)-(i). In all these figures even though all parts of the test chart were moved with identical speeds, the subtraction process has isolated particular features within the general field of motion. While smaller features introduced rapid change which could not be recorded efficiently. Photograph 6.6(a) reveals only horizontal features within the object as vertical features were moving with, with too high a speed. This is clearly due to the limited response time of the BSO phase conjugate mirror under such conditions. In all cases the motion of the object was simple harmonic (pendulum-like behaviour). The overall displacement along the vertical axis was much smaller than along the horizontal axis which gave rise to preferential observation of all horizontal features. In photograph 6.6(b) however, predominantly vertical features are observed, as the induced motion was much slower than that in 6.6(a).

Figures 6.6(c)-(i) show a sequence of outputs, representing specific times within the cyclic oscillatory motion for the same input phase object, but revealing the feature extraction aspects of this new velocity filtering technique. It is seen that for any specific velocity within the overall velocity range, only a specific dimensional feature is readily apparent. The feature sizes shown here, vary from 70 μm width in Figure 6.6(c), to the smallest features observable with the limited numerical aperture in our experimental arrangement, of 20 μm. It can therefore be concluded that the observed features depend on a unique combination of size and velocity, which allows an accurate size estimate to be made, knowing the velocity, and vice versa.

A different aspect of velocity detection is shown in Figure 6.7 where the object was merely subjected to a fast, small amplitude damped simple harmonic, displacement in the vertical direction. Because, in this case, a repetitive continuous range of velocities is present, no discrimination occurs between respective feature sizes as was apparent in Figure 6.6. In this latter case therefore, a differentiation in time is produced and the small amplitude, high frequency motion does not discriminate against size.

The final aspect of this technique illustrates the implementation of a Fourier

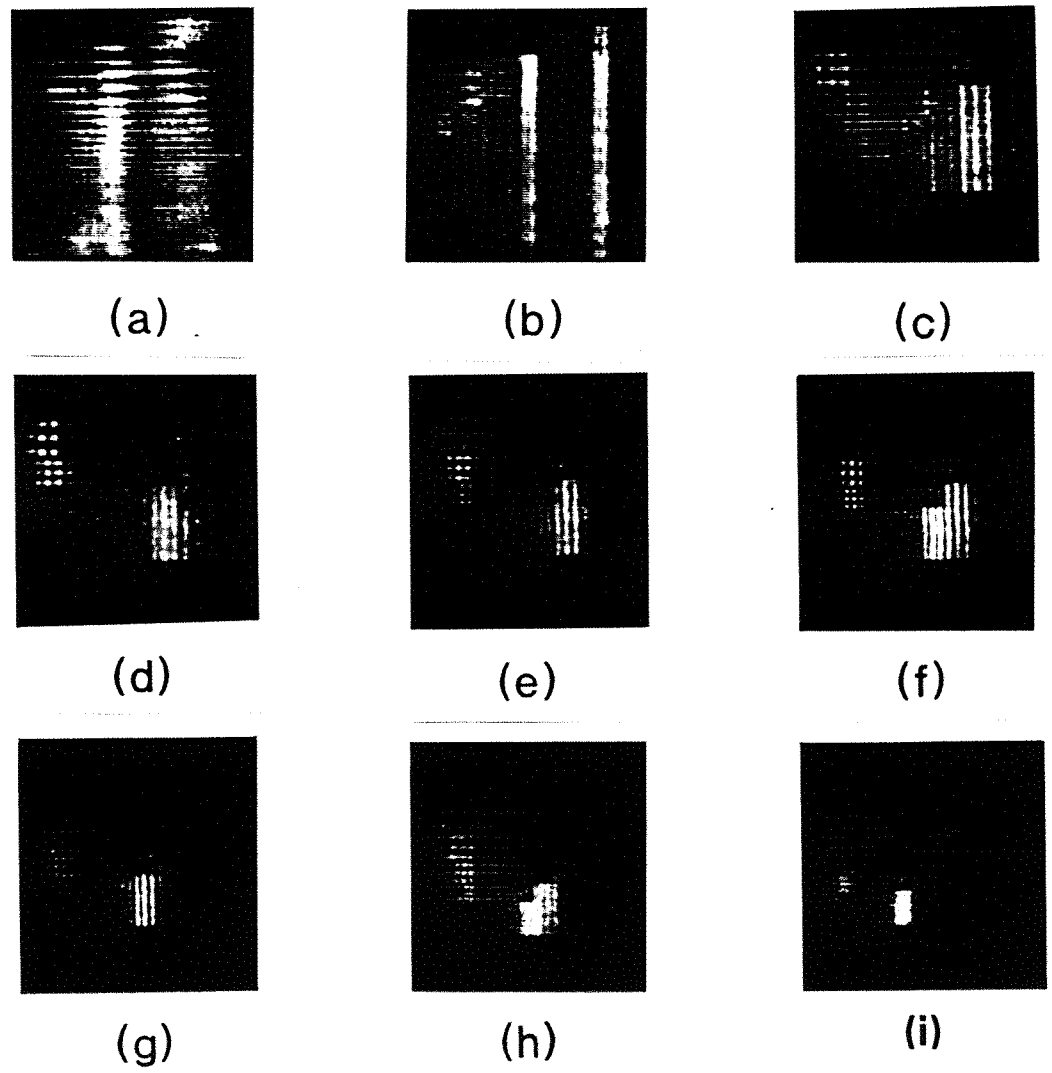

Figure 6.6 Sequence of photographs showing velocity filtering detection of features of particular dimensions only are observed at specific speeds.

Figure 6.7 Photographs showing different stages of motion detection when the object was subjected to damped simple harmonic motion in the vertical direction.

transform stage, in a similar manner to that of Chapter 5, where directional motion detection was also reported, but now, with the added capability of identifying specific feature sizes. Figure 6.8(a) shows the Fourier transform of subtraction achieved via complementary gratings. Figure 6.8(b) shows higher order vertical Fourier components, corresponding to the appearance of horizontal detail in the output image as observed in Figure 6.6(a) for example. Figures 6.8(c)-(f) show a similar sequence to the results of Figure 6.6, where the benefit of the added Fourier stage are observed. In Figure 6.8(e) for example, the orders that appear are directly interpretable as distinct feature size within the output image plane.

6.4 Suggestion for Optical motion detection using fixed and real time gratings in photorefractive crystal such as $BaTiO_3$

As an extension to the previous technique and its implementation, we further propose a technique of optical motion detection which relies on complementary gratings which may be recorded in for example $BaTiO_3$ crystal as shown in Figure 6.9. The two complementary gratings exist simultaneously in the crystal volume, but the recording of these gratings is accomplished via recording one permanent grating, and the other a real time grating with a phase shift of 180°. The fixing of such gratings (permanent grating) has already been reported by Micheron and Bismuth [6.11, 6.12], in which they demonstrated the electrical fixation and erasure of grating in an iron doped $BaTiO_3$ crystal at room temperature using an Argon ion laser at 488 nm wavelength. Therefore recording of real time and permanent gratings can be performed in a single crystal in a DFWM configuration, whereby an arbitrary phase shift can also be achieved between these gratings by introducing a phase shift in one of the beams when recording the real time grating.

A 180° phase shift can be introduced between permanent and real time gratings to achieve complete subtraction between the two identical gratings when readout by a common probe beam. However, when the two gratings contain different information, subtraction is achieved, in the form of a differential output. The above situation corresponds to a novelty filter where the real time and the fixed gratings can have identical information and show no output under static conditions while in case of movement the two gratings are different and a net output is achieved in the

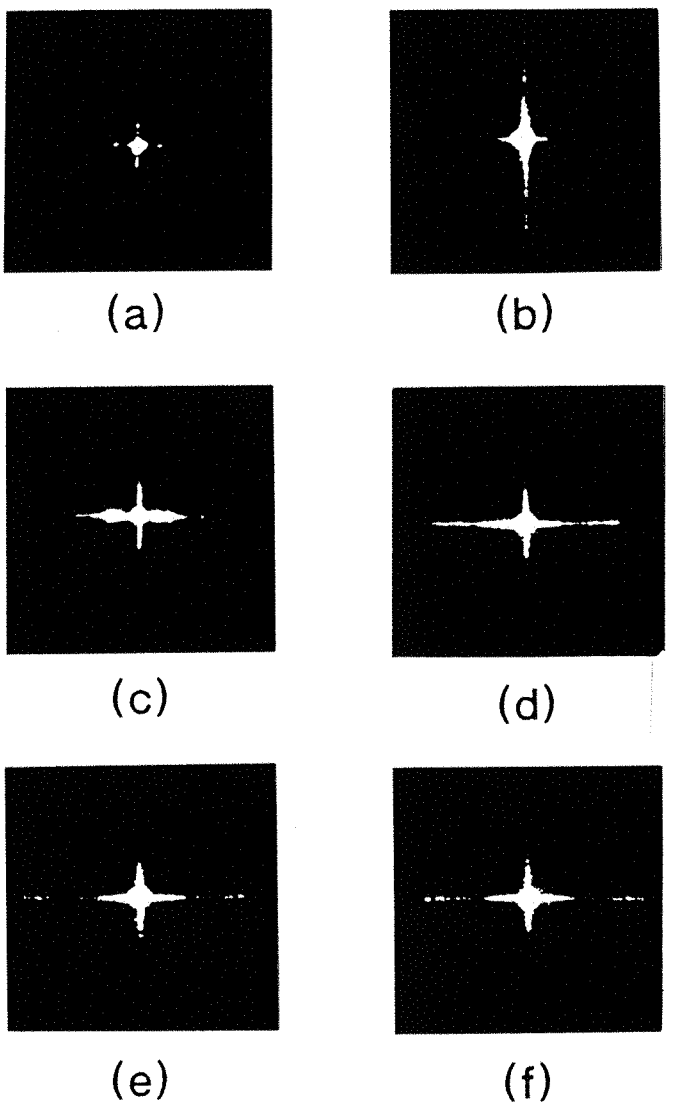

Figure 6.8 Results of directional motion detection via a Fourier transformation stage. (a) Fourier transform of subtraction of a static resolution chart showing faint DC term only. (b) Appearance of vertical orders only due to horizontal features present in the output image. (c) shows no discrimination between horizontal and vertical orders at a lower speed. (d), (e), and (f) show a sequence of higher horizontal orders due to the lower speeds.

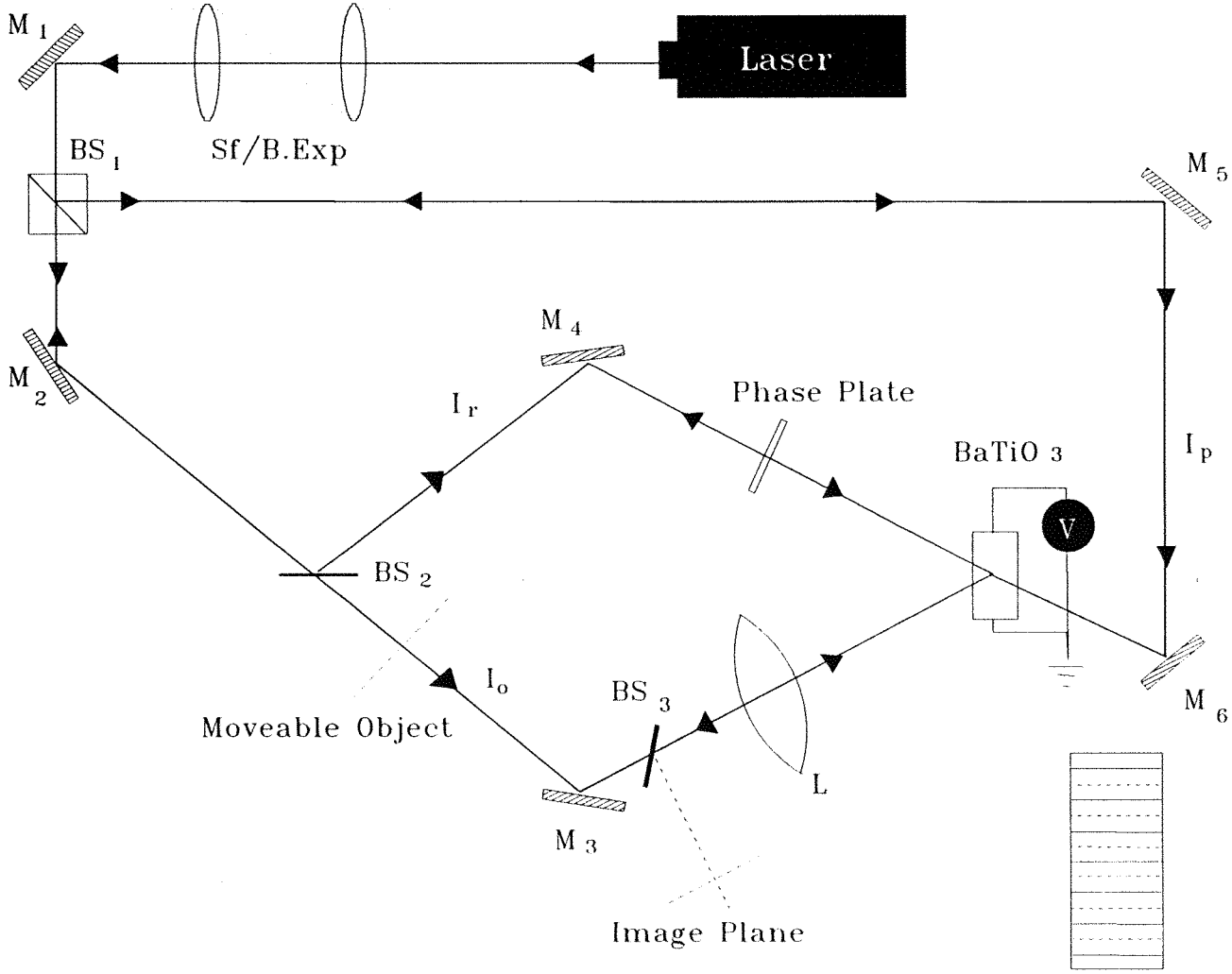

Figure 6.9 Shows an arrangement of motion detection via complementary gratings in a $BaTiO_3$ crystal.

form of a moving object. In the present case the difference in response times between the two gratings can be considered infinitely large and hence an arbitrarily slow change can therefore be observed. Therefore due to the fixed grating all the identical static real time features are subtracted while any change whether slow or fast which occurs in the real time grating can be observed.

6.5 Conclusion

A novel technique for velocity filtering has been demonstrated. Our technique is based on complementary (multiplexed) grating formation in a single crystal of BSO, in a DFWM arrangement. Under static conditions no output is observed; however under induced motion, we observe a bright output image whose features depend on the particular speed. At speeds above and below this the output image intensity is greatly reduced and experimental results are presented to verify this velocity filtering operation. Results are also presented for Fourier transform implementation. We have also proposed a new technique of motion detection which is also based on recording of complementary gratings.

REFERENCES

6.1 N. A. Vainos, J. A. Khoury and R. W. Eason, "Real time parallel optical logic in photorefractive bismuth silicon oxide" Opt. Lett. **13**, 503 (1988).

6.2 S. K. Kwong, G. A. Rakuljic and A. Yariv, "Real time image subtraction and exclusive OR operation using a self-pump phase conjugate mirror", Appl. Phys. Lett. **48**, 201 (1986).

6.3 A. E. Chiou and P. Yeh, "Parallel image subtraction using a phase conjugate Michelson interferometer", Opt. Lett. **11**, 306 (1986).

6.4 N. A. Vainos and R. W. Eason, "Spatially multiplexed phase conjugate imaging and processing in photorefractive BSO", Opt. Commun. **62**, 311 (1987).

6.5 D. Z. Anderson, D. M. Lininger and J. Feinberg, "An optical tracking novelty filter", Opt. Lett. **12**, 123 (1987).

6.6 D. Gabor, G. W. Stroke, R. Restrick, A. Funkhouser and D. Brumm, "Optical image synthesis (complex amplitude addition and subtraction) by holographic Fourier transformation", Phys. Lett. **18**, 116 (1965).

6.7 P. Gunter and J.-P. Huignard, "Photorefractive Materials and their Applications", Topics in Applied Physics, Vols. **61, 62**, Springer-Verlag, Berlin (1988).

6.8 J. P. Huignard, J. P Herriau and F. Micheron, "Selective erasure and processing in volume holograms superimposed in photorefractive Ferroelectrics", Ferroelectrics, **11**, 393 (1976).

6.9 J. H. Ja, "Real time image subtraction in four wave mixing with photorefractive $Bi_{12}GeO_{20}$ crystal", Opt. Commun. **42**, 377 (1982).

6.10 G. Hussain, R. W. Eason, "Velocity filtering using complementary gratings in photorefractive BSO", Opt. Commun. **86**, 106 (1992).

6.11 F. Micheron and G. Bismuth, "Electrical control of fixation and erasure of holographic patterns in Ferroelectric Materials", Appl. Phys. Lett. **20**, 79 (1972).

6.12 F. Micheron and G. Bismuth, "Field and time thresholds for the electrical fixation of holograms recorded in $(Sr_{0.75}Ba_{0.25})Nb_2O_6$ crystals", Appl. Phys. Lett. **23**, 71 (1973).

CHAPTER 7

OPTICAL LOGIC OPERATIONS VIA POLARIZATION ENCODING IN A PHASE CONJUGATE MICHELSON INTERFEROMETER

7.1 Introduction

In recent years digital electronic processing of images has proved to be very reliable and versatile. Its speed however, is fundamentally limited by its serial nature. During the last decade it has become apparent that optical techniques have considerable potential in implementing logic and other operations in ways that are fundamentally different from those of electronic techniques. In optical systems the input and output are usually two dimensional spatial light patterns and therefore operation is expected to be intrinsically faster due to the in-built parallelism.

In many optical systems, beams of light cross each other without interfering. Light of different wavelengths may also be superimposed without any cross talk, providing reliable interconnection capabilities. Apart from these promising features optical beams are capable of free space propagation. These features may be the main asset of any optical processor and it is much simpler to design parallel architectures in optics.

Optical Boolean logic gates are the basic elements of digital optical processors. So far various optical techniques have been demonstrated. A technique of image subtraction of complex amplitudes of light was first demonstrated by Gabor et al [7.1], who used a double exposure holographic method. However, this technique can only be applied on permanently recorded data. Yu et al [7.2] reported a technique of optical logic operations based upon magneto-optic spatial light modulator (MOSLM). They used two MOSLM in two different configurations to demonstrate the basic logic operations for two inputs. This technique require highly collimated beams and critical alignment to preserve a one-to-one pixel relationship. However an intermediate level is produced due to the bias term of binary patterns. They also could not perform the operation of XNOR. Their results were reported to be non-

optimum, and binary outputs also had grey levels (instead of the ideal values of 1 or 0). The resolution of the output images may also suffer because of size and number of pixels in MOSLM devices.

Yu et al [7.3] have demonstrated Boolean operations via an opto-electronic technique which relies on a micro-channel spatial light modulator and liquid crystal TVs. The operation of the device again depends on the material properties of MOSLM and applied bias voltages, which need to be properly adjusted for different modes, to perform the various different logic operations. The mode of operation of MOSLM was controlled by a computer and associated electronics. This technique suffers from output image distortion which mainly comes from imperfections of MOSLM operation.

A single pixel logic operation which gives both the sum and carry outputs of full addition has been demonstrated by Tooley et al [7.4]. Who used the reflection and transmission characteristics of a nonlinear Fabry-Perot interferometer to achieve sum and carry for full addition. The 0 and 1 logic levels in their system correspond to low and high output optical powers from the etalon. The discrimination between low and high levels of input and output is critical. This technique, however, suffers from alignment problems and requires sufficient gain in the system to overcome the losses from various optical components.

An optical logic technique which is based upon spatial filtering has been demonstrated by Weigelt [7.5]. In this technique the input of array cells with the logical value 1 is encoded by statistical structures, fringe speckles etc while the logical value 0 is encoded as transparency. The two objects are placed in a cascaded spatial filtering set up in two different Fourier planes. These logical levels 0 and 1 are distinguished in the Fourier plane where 0 appears as an unscattered bright intense DC term and 1 as higher spatial frequencies. Various logic operations have been performed using different combinations of high and low pass filters in the two Fourier planes. However, the encoding of the input in this way is complex and time consuming. The resolution and intensity is also lost at every stage of the spatial filtering, and specific Fourier plane spatial filtering masks are required for each different logic operation.

The technique of polarization based logic has been reported by Lohmann and Weigelt [7.6], a scheme which relies on polarization encoding. In the output plane every array cell is illuminated by light of either horizontal or vertical planes of polarization. A half wave plate is used to switch the polarization into the correct orientation, which corresponds to a logic operation in the form of a truth table. The technique is reported to perform the logic operation at non-real time because of the slow rate of encoding the input and output.

Optical subtraction (XOR) and addition have also been implemented by the use of classical interferometric techniques such as Mach-Zender or Michelson interferometers [7.7]. In these techniques subtraction of optical fields is obtained via a 180° relative phase shift between the two arms of the interferometer by mechanical means. However it is known that such interferometers require a high degree of stability, are extremely difficult to adjust, and are difficult to maintain a fixed path length between the two arms. In addition only the central fringe is useful for image subtraction and addition purposes which in many cases is not enough to cover the full image field.

Use therefore of conventional optical techniques of image subtraction, addition and logic operations is limited due to the alignment of the optical systems which is difficult to maintain in practice. Some of these techniques require encoding of the input data which is often complex and time consuming. Also due to the phase fluctuations, ambient air currents or thermal drift, overlapping image intensities often drift between the extrema.

In recent years OPC, by degenerate four wave mixing in nonlinear media such as photorefractive crystals has emerged as a versatile low power technique for implementing optical data processing schemes.

Optical image subtraction has been achieved by OPC via double exposure methods. Huignard et al [7.8] reported a technique of image subtraction and parallel optical logic in $LiNbO_3$. Their technique based on the recording of two complementary gratings, allows a readout beam to read the two gratings, and generate destructive interference due to the 180° phase shift between the two phase

conjugate beams. A similar technique has also been reported by Ja [7.9] involving a reflection grating configuration in BGO. These techniques however exploit **sequential** grating recording and erasing, which severely limits their usefulness.

By replacing the conventional mirrors in a Michelson interferometer with phase conjugate mirrors, we can combine the advantages of both systems, to construct a Phase Conjugate Michelson Interferometer (PCMI). Due to the dynamic nature of the photorefractive recording and readout process, we therefore ensure both temporal stability of the output, against variations in the optical path length of the two arms, thermal drifts etc., and any phase irregularities due to the optical components used, due to the exact cancellation via the double pass nature of OPC. Furthermore, the interferometer is also self aligning. Normally, under conditions of polarization preserving phase conjugation, destructive interference at the output of such a PCMI usually occurs; Using such a scheme, some of the basic logic operations have already been demonstrated [7.10, 7.11, 7.12].

7.2 Theoretical Considerations

Our basic PCMI is illustrated in Figure 7.1, in which a BSO crystal is used as the phase conjugate mirror to record spatially multiplexed gratings [7.13]. An input beam is split via a beam-splitter BS_2, to form separate inputs I_1 and I_2. Beam I_1 subsequently passes through a half-wave plate, and is directed towards the BSO. Beam I_2 passes through a second half-wave plate, and is also directed towards the BSO. A reference beam I_r interferes with these two beams inside the BSO, to record two angularly multiplexed gratings. The transmitted reference beam is phase conjugated via a self-pumped $BaTiO_3$ crystal, to provide the horizontally polarized readout beam.

The BSO crystal was used in the $K_g \perp \langle 001 \rangle$ configuration where it functions as a half-wave plate with respect to the polarization direction of the readout beam (for the ideal thin crystal case) [7.14]. In such a set up as Figure 7.1, it is easy to implement a polarization preserving phase conjugator. When the input polarizations of the two signal beams I_1 and I_2 are set in a horizontal plane before passing through the half-wave plates, and are both rotated to a vertical direction on passing through

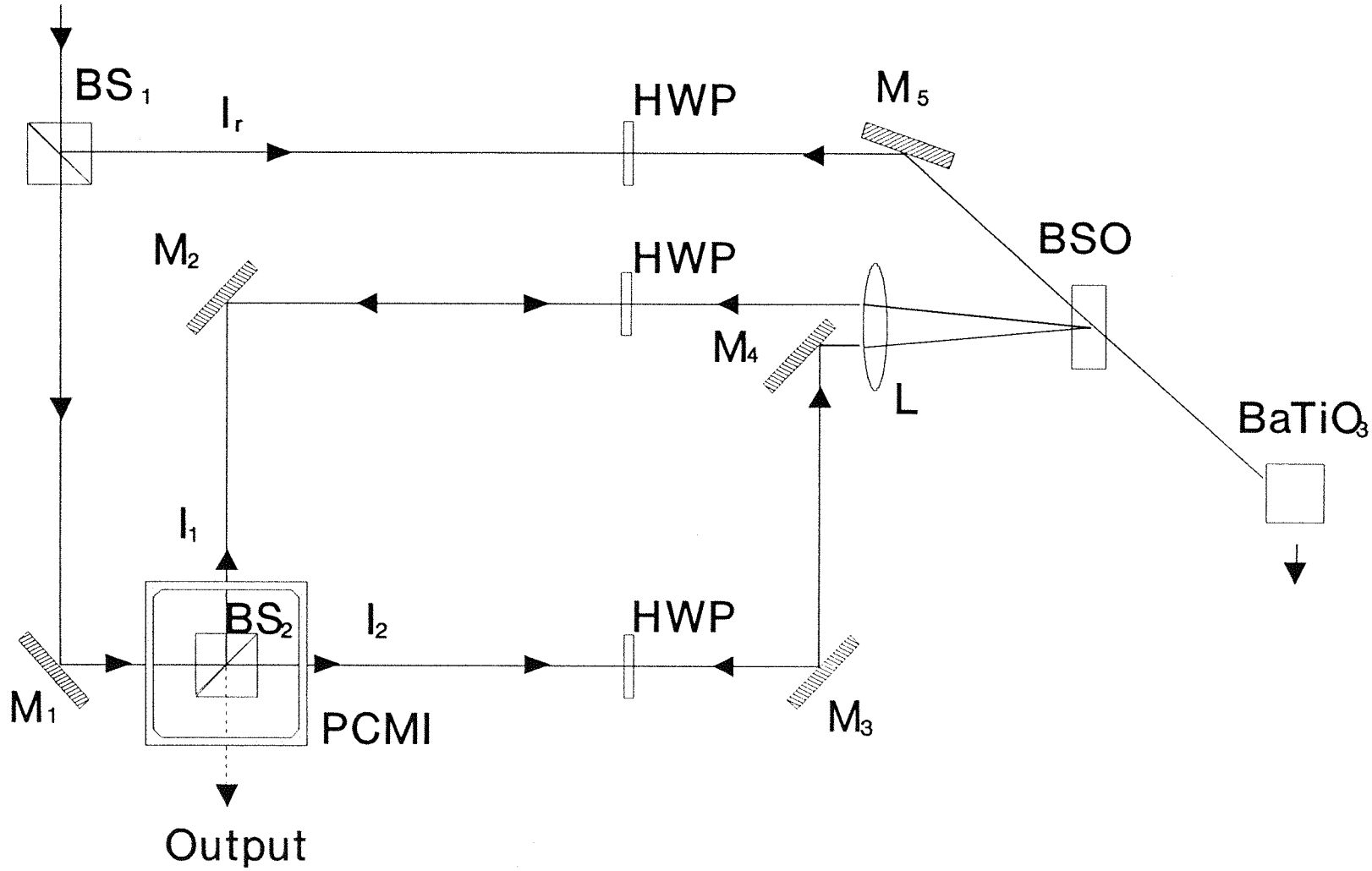

Figure 7.1 Shows a basic configuration of PCMI , where a BSO crystal is used as a phase conjugate mirror and a self-pumped $BaTiO_3$ is used to provide a readout beam for the two holograms. BS: Beam-splitter, M: mirror, HWP: half-wave plate.

the half-wave plates, they will interfere with a vertically polarized reference beam I_r and write the two independent gratings inside the BSO.

Due to the optical activity in BSO however, which is of the order ~45°/mm at 514.5 nm [7.15], the polarization of the transmitted beam I_r can be adjusted to be horizontally polarized by changing the path length in the crystal . The transmitted beam is phase conjugated to produce a readout beam which is also horizontally polarized. The polarization of the diffracted beams from the two recorded gratings will be vertically polarized due to the BSO configuration adopted, and the polarizations of these diffracted beams I_1^* and I_2^* will subsequently be rotated to the horizontal direction after passing through the half wave plates, to subsequently recombine at the beam-splitter BS_2. Under these conditions and for a lossless beam-splitter, the Stokes' principle of reversibility of light is fulfilled and total subtraction is achieved at the output port of BS_2 and a complementary output i.e., an addition of I_1^* and I_2^* will be achieved at the input port of BS_2. We may consider this as a **polarization preserving** mode of our PCMI.

However, when the half wave plates in the interferometer are rotated, a change occurs in the polarization directions of the input light to the BSO crystal. The vertical components of these two beams interfere with the vertically polarized reference beam I_r as before, to record the two multiplexed gratings. The diffracted (phase conjugate) beams, in this set up, will be vertically polarized. On the return path, the vertically polarized beam I_1^* passes back through the half wave plate and is rotated to a different angle, which depends upon the orientation of the fast axis of the appropriate half-wave plate. The resultant polarization direction of the phase conjugate beam after retraversing each half-wave plate, in this second case, will be different from that of the input light, which was initially horizontally polarized. In addition, there may be other components such as metal mirrors which will introduce a non-reciprocal phase shift for the phase conjugate non-horizontally polarised beam. This mode of operation therefore is clearly **not** polarization preserving.

The above description shows that the phase conjugation process in both cases will not, in general, be polarization, or phase preserving. When two such phase conjugate beams recombine at the beam-splitter BS_2, their interference behaviour

will depend on both polarization angle and relative phase difference. The output intensity can therefore be expressed by

$$I_{out}=2I_o(1+\cos\theta\cos\phi) \qquad (7.1)$$

Where ϕ is the phase angle between the two linearly polarized beams and θ is the polarization angle between the two beams at the BS_2. I_0 is the intensity of the individual phase conjugate beams at the output port of the BS_2. In this case, the polarization angle can be varied by rotating one or both of the wave plates. The phase difference generated is more complicated however, as this depends on relative phase shifts introduced in vertical and horizontal polarized components on reflection for example from metal coated mirrors.

7.3 Applications to Logic Operations

The PCMI described above can be used quite generally for the construction of optical logic gates. A three dimensional plot of Equation (7.1) shown in Figure 7.2, illustrates that a continuous level of output intensities can be achieved from I_{out} = 0 to $4I_0$. The same output intensity can be achieved for various different combinations of ϕ and θ from two inputs of initially equal intensities. However, this present two beam arrangement cannot achieve all of the basic logic operations. Binary Logic operations such as XOR, OR, Addition (coherent and incoherent) and non-binary intermediate operations are achievable from a range of combinations of ϕ and θ. The three dimensional plot also shows that the non-polarisation preserving quality is an added advantage for our PCMI. We describe here the four combinations of phase angle ϕ and polarization angle θ between the two phase conjugate beams to achieve the logic operations mentioned above.

Case I. Operation XOR: When the interferometer works in polarization preserving mode, the input and output polarizations and phases are preserved. In such a situation $\phi=180^\circ$, $\theta=0^\circ$ and according to Equation (7.1) zero output is achieved at

---

Figure 7.2 Shows a computed three dimensional graph of output intensity as a function of phase angle ϕ and polarization angle θ between the two phase conjugate outputs at the beam-splitter, (see next page).

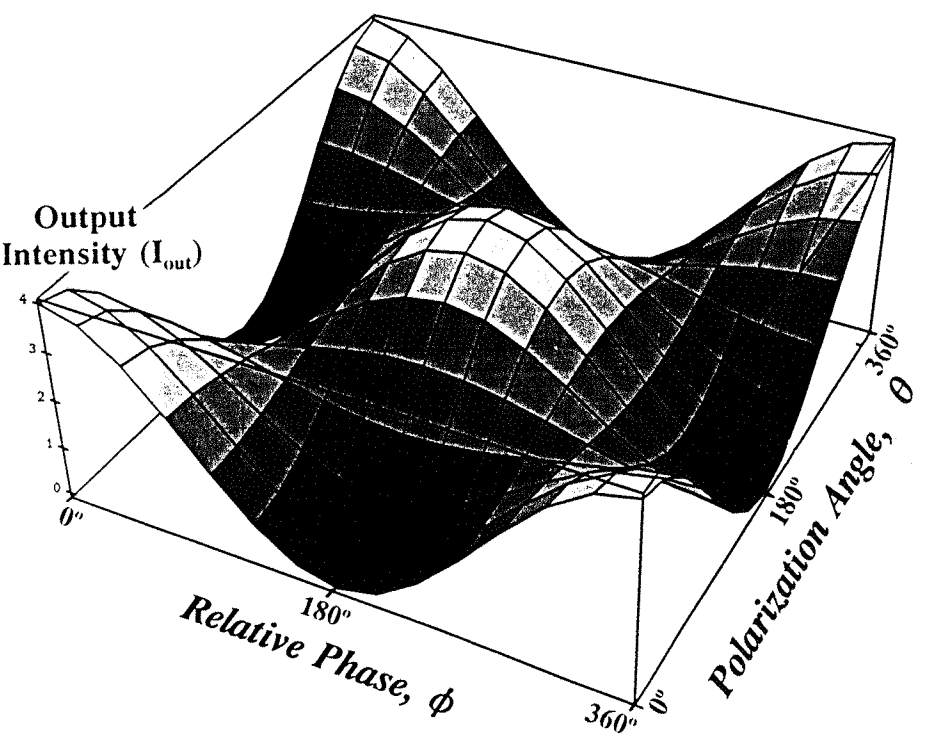
Output
Intensity (I_{out})
4
3
2
1
0
0°
180°
360°
Relative Phase, ϕ
0°
180°
360°
Polarization Angle, θ

the output port of BS_2.

Case II. Coherent Addition: When the relative phase $\phi=0^\circ$ and polarization angle $\theta=0^\circ$ between the beams I_1^* and I_2^*, constructive interference occurs at the output port of BS_2 and the intensity in this case will be $4I_o$.

Case III. Incoherent Addition: Addition of the two outputs can also be achieved when the relative phase has any arbitrary value from 0° to 360° and the two beams are of orthogonal polarization i.e., $\theta=90^\circ$ and hence will not interfere at all. Therefore the addition in this case is an incoherent one and the output will always be $2I_o$.

Case IV. Operation OR: An OR operation is achieved when the phase angle $\phi=180^\circ$ and $\theta=60^\circ$ or $\phi=0$ and $\theta=120^\circ$. For these combinations of ϕ and θ the output is equal to I_o, which corresponds to an OR operation. The complementary output from the above operation is observed at the input port of the same PCMI as shown in Figure 7.1.

Taking note of these basic operations of the PCMI via multiplexed holographic recording in BSO, it is simple to cascade another PCMI with the existing one. To construct such a system an additional beam, and a half-wave plate, is added to the BSO set up as shown in Figure 7.3. This interferometer now consists of two PCMIs, the phase conjugate output (at the input port of BS_3), from the second interferometer serves as a direct input to the first one. Both the PCMIs can equally perform operations of XOR, OR, Addition (coherent and incoherent) between the outputs from all three arms of the cascaded interferometers. Using such a system all sixteen basic logic operations of the two variables can be achieved. These logic operations can be performed in two stages. For the first stage $(PCMI)_2$ performs one of the above four logic operations between outputs I_2^* and I_3^* at its input port (a complementary operation also being performed at the output port of $(PCMI)_2$). Secondly, the output from $(PCMI)_2$ and I_1^* perform one of the above four logic operations. Such operations can be represented by the general relation

$$I_1^* \Delta (I_2^* \Delta I_3^*) = \textit{Logic Operations} \qquad (7.2)$$

Where Δ represents any of the above four operations. We shall now describe the

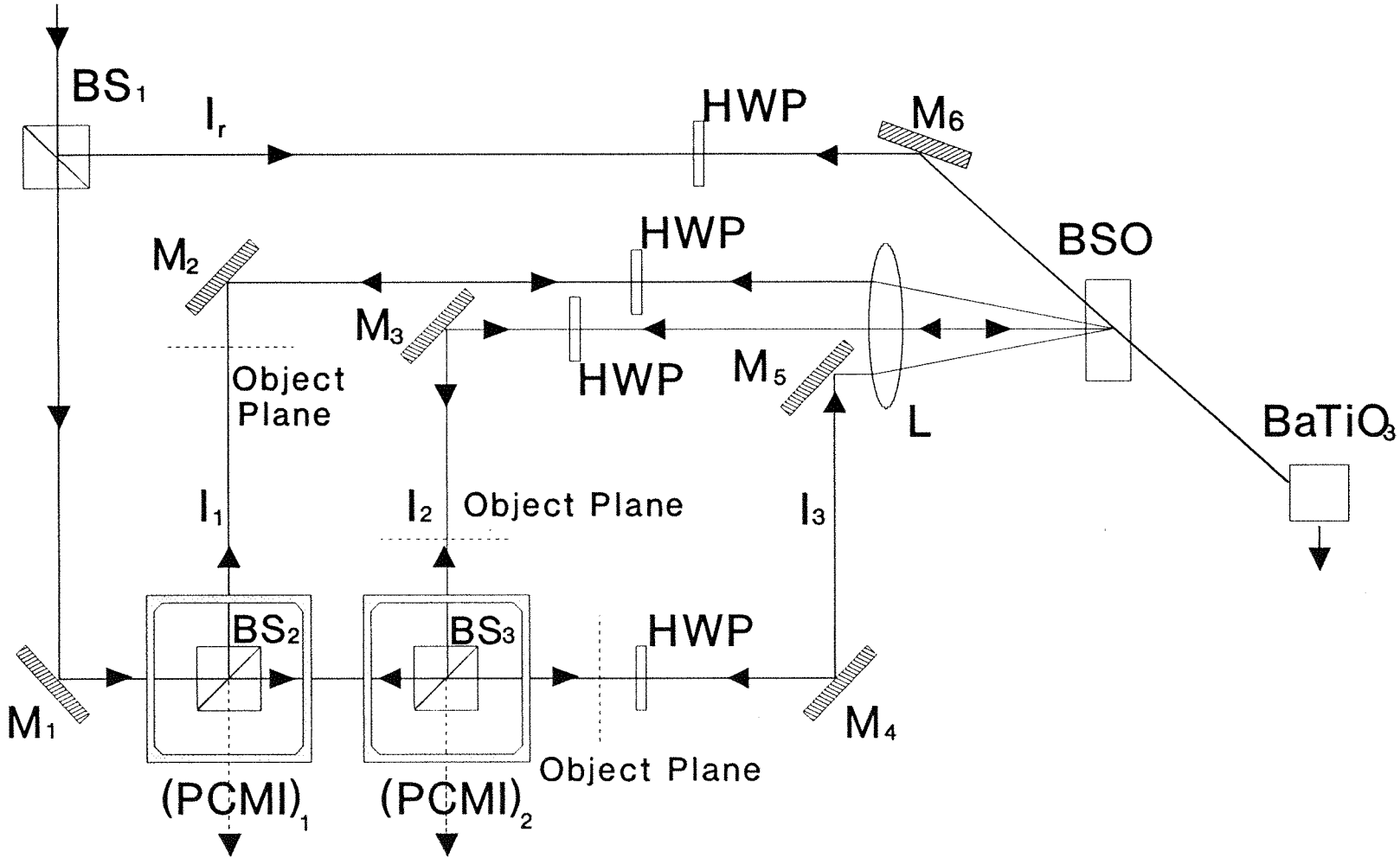

Figure 7.3 Shows a cascaded PCMI scheme where the phase conjugate output at the input port of $PCMI_2$ serves as one of the inputs to $PCMI_1$. All fifteen basic logic operations can be performed using this system.

application of this basic mechanism to perform all sixteen basic logic operations on the two variables. The following descriptions are detailed rigorously, as considerable effort has been expended to ensure that all such operations can be achieved.

7.3.1 Operation A OR B

This operation can be performed by blocking the beam I_1 of the first interferometer and putting the objects A and B in beams I_2 and I_3. The second PCMI works in addition mode at the output port of BS_3 such that the output intensity is $3I_o$. Therefore at the input port of BS_3 an intensity I_o is present and an OR operation is performed at the output port of BS_2. Similarly the OR operation can also be observed at the output port of BS_3.

7.3.2 Operation A XOR B

This operation is also be performed at the input port of BS_3, while blocking the beam I_1. In this case $PCMI_2$ works in coherent addition mode at its output port. Therefore subtraction (XOR) output is observed at BS_2. This operation can also be observed at the output of $PCMI_2$ when working in subtraction mode.

7.3.3 Operation $\overline{A}$ OR B

To perform this operation we use all three beams of the two cascaded $PCMI_s$. Object A is placed in beam I_2 while object B is placed in beam I_3. The two objects are incoherently at the input port of BS_3 and serve as an input at BS_2. Beam I_1^* which is a plane beam (without any object), performs simultaneously the XOR operation with object A addition with the object B respectively.

7.3.4 Operation A OR $\overline{B}$

This operation can be performed simply by changing the polarization of beam I_1 to be parallel to that of I_3, such that it performs the XOR operation with object B in beam I_3. The object A is added incoherently because of its orthogonal polarization to the other two beams.

7.3.5 Operation A AND B

The AND operation can be performed using only one of the beams in the cascaded PCMI while blocking the other two beams. The two inputs are placed one after the other (in sequential configuration). The phase conjugate output can be observed at the output port of either of the beam-splitters in the PCMI.

7.3.6 Operation A NAND B

This operation can be performed using only one interferometer. Therefore by blocking beam I_2, operation of A AND B can be performed in beam I_3 then an XOR operation is performed between the beam I_1^*, which is a plane beam and A AND B at the (output port of) BS_2 to achieved the operation A NAND B.

7.3.7 Operation $\bar{A}$ AND B

To perform this operation we need to put the object A in beams I_1 and I_2 while object B is placed in beam I_3. The second PCMI performs an OR operation between objects A and B at the input port. The first interferometer performs the XOR operation between the object A and (A OR B). Therefore, at the output of BS_2 only those parts of A and B which are not common are observed.

7.3.8 Operation A AND $\bar{B}$

This gate can be constructed using any two of the three arms of the cascaded PCMI. If beam I_2 is blocked and object A is placed in the common input beam the object B is placed in beam I_3. Both of the phase conjugate beams perform the XOR operation at the output of BS_2 to give the operation A and (A AND B).

7.3.9 Operation A NOR B

All three beams of the PCMIs are used to achieve this operation. The input objects A and B are placed in beams I_2 and I_3 respectively. At the output port of BS_3 they show coherent addition such that the output intensity is $3I_o$. A complementary

output (an OR operation) is directed towards BS_2 where it interferes destructively with I_1^* and operation A NOR B is observed at the output of BS_2.

7.3.10 Operation A XNOR B

This gate is constructed when the $PCMI_2$ works in subtraction mode at its output port, which give a coherent addition at the input port. This intensity distribution interferes with a plane beam I_1^* in subtraction mode which give zero output where only one of the objects is present. An output intensity which corresponds to logic level $I_o = 1$, is observed where both the objects are present.

7.3.11 Operation A

This operation is performed by placing the object A in beam I_1 and object B in the common input beam to $PCMI_2$. The second PCMI is working in coherent addition mode at its output. Therefore no phase conjugate output is observed at BS_2 and object A is observed at the output port of BS_2 only.

7.3.12 Operation $\overline{A}$

This operation can be performed by putting object A in beam I_2 and B in beam I_3 while beam I_1 is a plane beam. In the first stage an OR operation is achieved between beam I_1^* and B and in the second stage an XOR operation occurs between this output and beam A, giving $\overline{A}$ at the output port of BS_2.

7.3.13 Operation B

This gate can be constructed using all three beams of the two PCMIs. The object B is placed in beam I_3 and object A is placed in beams I_1 and I_2. In the second interferometer, objects A and B are added incoherently, while first interferometer is working in subtraction mode with beam I_2^* and is not interfering with beam I_3^* at all due to the orthogonal polarization. Therefore object B is observed at the output port of BS_2.

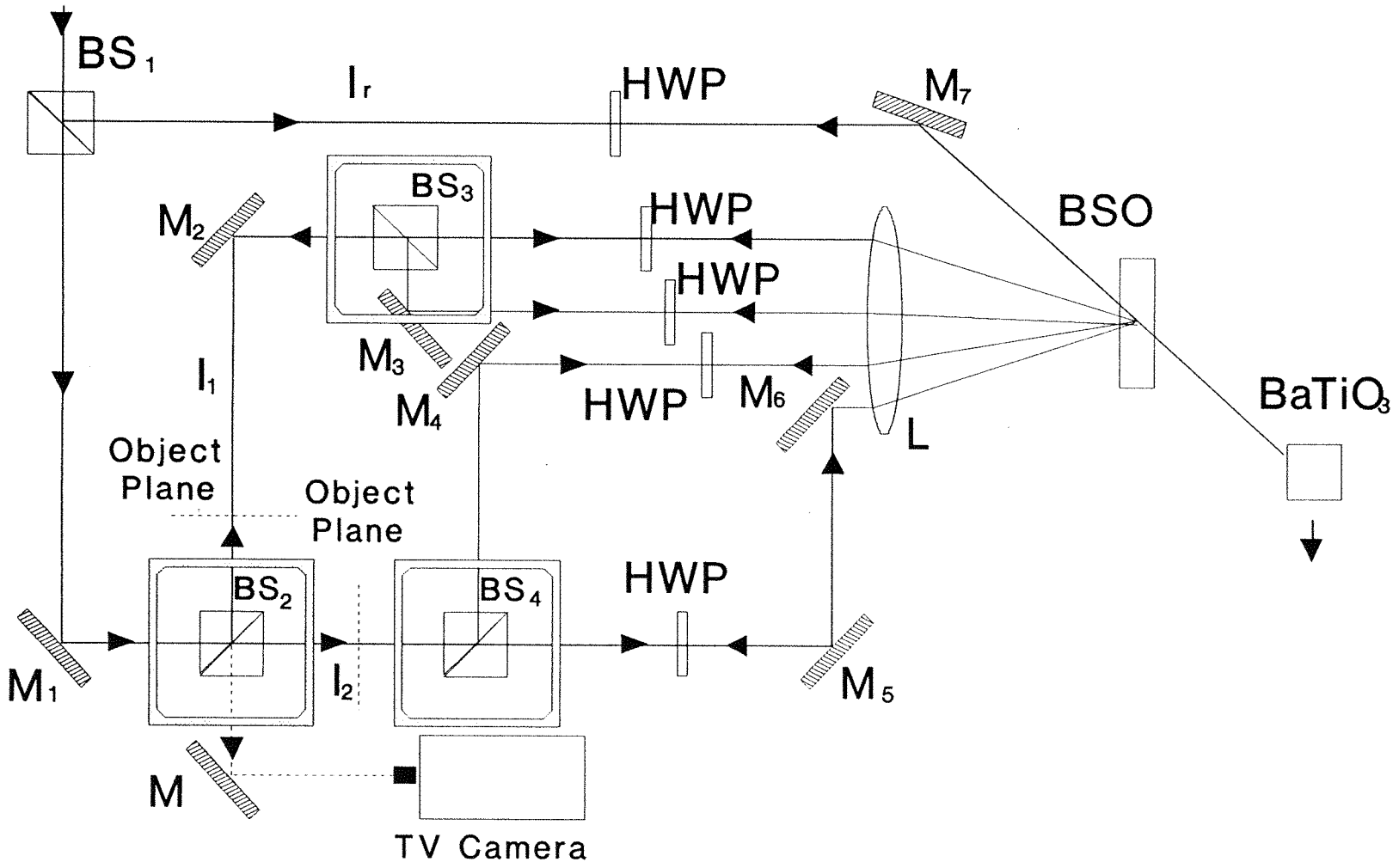

Figure 7.4 Schematic diagram shows the experimental arrangement for optical logic operation '0'.

7.3.14 Operation $\overline{B}$

Similarly in the first stage, operation OR is performed between beams I_1 and I_2 which has object A in it. Secondly subtracting the beam I_3 from the OR output at BS_2 we can achieve operation B.

To achieve the total set of sixteen operations, we include the remaining two only for completeness.

7.3.15 Operation 1

To perform this operation the phase conjugate output coming from the second PCMI should be in OR mode, while the first PCMI also works in OR mode at its output port, to produce the same intensity I_o everywhere at the output.

7.3.16 Operation 0

One of the simple ways to perform this operation is to change the polarization of the any two object bearing beams to horizontal direction when the reference beam is vertically polarized. In this way no grating is written and no phase conjugate output is achieved. The other technique is to split the beam I_1 of Figure 7.3, to construct two independent PCMIs which are cascaded to form a third interferometer as shown in Figure 7.4. The objects A and B are placed in beams I_1 and I_2 while adjusting the polarization of all four beams such that phase conjugate outputs from the two PCMI should be zero at BS_2, therefore achieving the operation 0.

Figure 7.5 shows a block diagram of a two stage cascaded PCMI of Figure 7.3. The phase conjugate outputs I_1^*, I_2^* and I_3^* interfere in $PCMI_2$ and $PCMI_1$ to give X, $\overline{X}$ Y and $\overline{Y}$ logic outputs.The X and Y represent the usable logic outputs from the output ports of $PCMI_1$ and $PCMI_2$ respectively. While $\overline{X}$ and $\overline{Y}$ represent the complementary logic outputs at the input ports of these PCMIs. We use X and Y alternatively depending on the logic operations. The complete set of sixteen logic operations is summarised in Table 7.1.

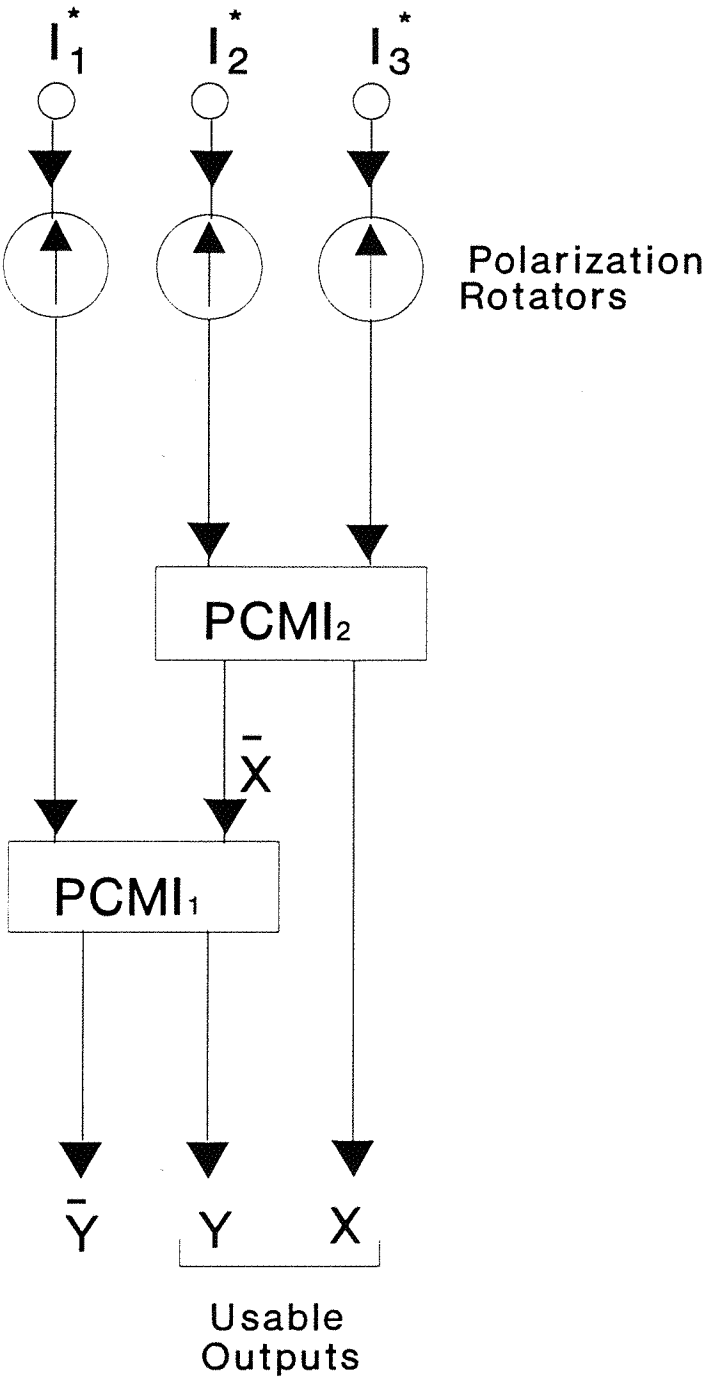

Figure 7.5 Shows a block diagram of cascaded PCMI. X or Y are the useable outputs depending on the operation performed

Operation	$\bar{X}$	X	Y
A OR B	(A + B) ▲	A OR B	(A + B) ▲
A XOR B	(A + B) ●	(A − B)	(A + B) ●
$\bar{A}$ OR B	A OR B	(A + B) ▲	(A − 1) OR B
A OR $\bar{B}$	A OR B	(A + B) ▲	A OR (B − 1)
A AND B	A AND B	A AND B	A AND B
A NAND B	A AND B	A AND B	(A AND B) − 1
$\bar{A}$ AND B	A OR B	(A + B) ▲	(A OR B) − A
A AND $\bar{B}$	A AND B	A AND B	(A AND B) − A
A NOR B	A OR B	(A + B) ▲	(A OR B) − 1
A XNOR B	(A + B) ●	A − B	(A + B) ● − 1
A	B − B	(B + B) ●	(B − B) + A
$\bar{A}$	*	*	A − (B OR 1)
B	(A + B) ■	(A + B) ■	(A + B) ■ − A
$\bar{B}$	*	*	(A OR 1) − B
1	A OR B	(A + B) ▲	(A OR B) OR 1
0	B − B	(B + B) ●	(B − B)+(A − A)

■ : Incoherent addition i.e, equal to $2I_o$

● : These additions are fully coherent and equal to $4I_o$

▲ : These additions are partially coherent and do not yield the maximum value for addition i.e, $2I_o < I < 4I_o$

* : These operations were not recorded

▭ : For these cases only X is used as the output

Table 7.1 Describes all sixteen basic logic operations.

7.4 Experimental Arrangement

Figure 7.6 shows the complete arrangement, in which an Ar^+ laser was used at 514.5 nm in multi-longitudinal mode. A single crystal of BSO with dimensions 2x10x10 mm^3, was used to record the angularly multiplexed gratings. The laser output was spatially filtered and divided by a beam-splitter BS_1 into a reference beam I_r and input beam I_{in} to the interferometer. Beam I_{in} was sub-divided by a beam-splitter BS_2, and the transmitted beam was further divided by BS_3. Beams I_1, I_2 and I_3 pass through the separate half-wave plates and imaging lens systems before entering the BSO crystal. Lenses L_1, L_2 and L_3 were of 30 cms focal length, while lens L_4 was 25 cms focal length. The polarizations of the reference and all three signal beams were horizontal before they passed through any half wave plates. The intensity of I_r at the input face of the BSO crystal was 32 mW while the maximum intensities of beams I_1, I_2 and I_3 (in our test case), were 25 mW, 16 mW and 14.5 mW respectively. However, the phase conjugate intensities of the three beams were made comparable via neutral density filters in the three signal beams. The reference beam transmitted through the BSO crystal was phase conjugated by a self-pumped $BaTiO_3$ crystal. This configuration which provides a very precise pair of phase conjugate pump beams for the FWM interaction is an important aspect of the PCMI described here. We have already used this configuration for multiplexed novelty filtering experiments [7.16], as it ensures fringe-free images at the beam-splitter output ports. We now consider the implementation of the two modes of polarisation preserving and polarization non-preserving PCMI.

Case: 1. Polarization Preserving Mode

For this case we consider only one PCMI and therefore block beam I_1. The polarization of beam I_r before the BSO crystal was rotated to the vertical plane by a half-wave plate. Similarly the polarization directions of the input signal beams I_2 and I_3 were also rotated to the vertical. Due to the intrinsic optical activity, the polarization of the transmitted reference beam was rotated to the horizontal direction. This beam was phase conjugated by a self-pumped $BaTiO_3$, and subsequently readout the two multiplexed gratings. The phase conjugate beams I_2^* and I_3^* were vertically polarized; tracing back their original paths, these beams passed back through the half-wave plates which again rotate their polarizations to

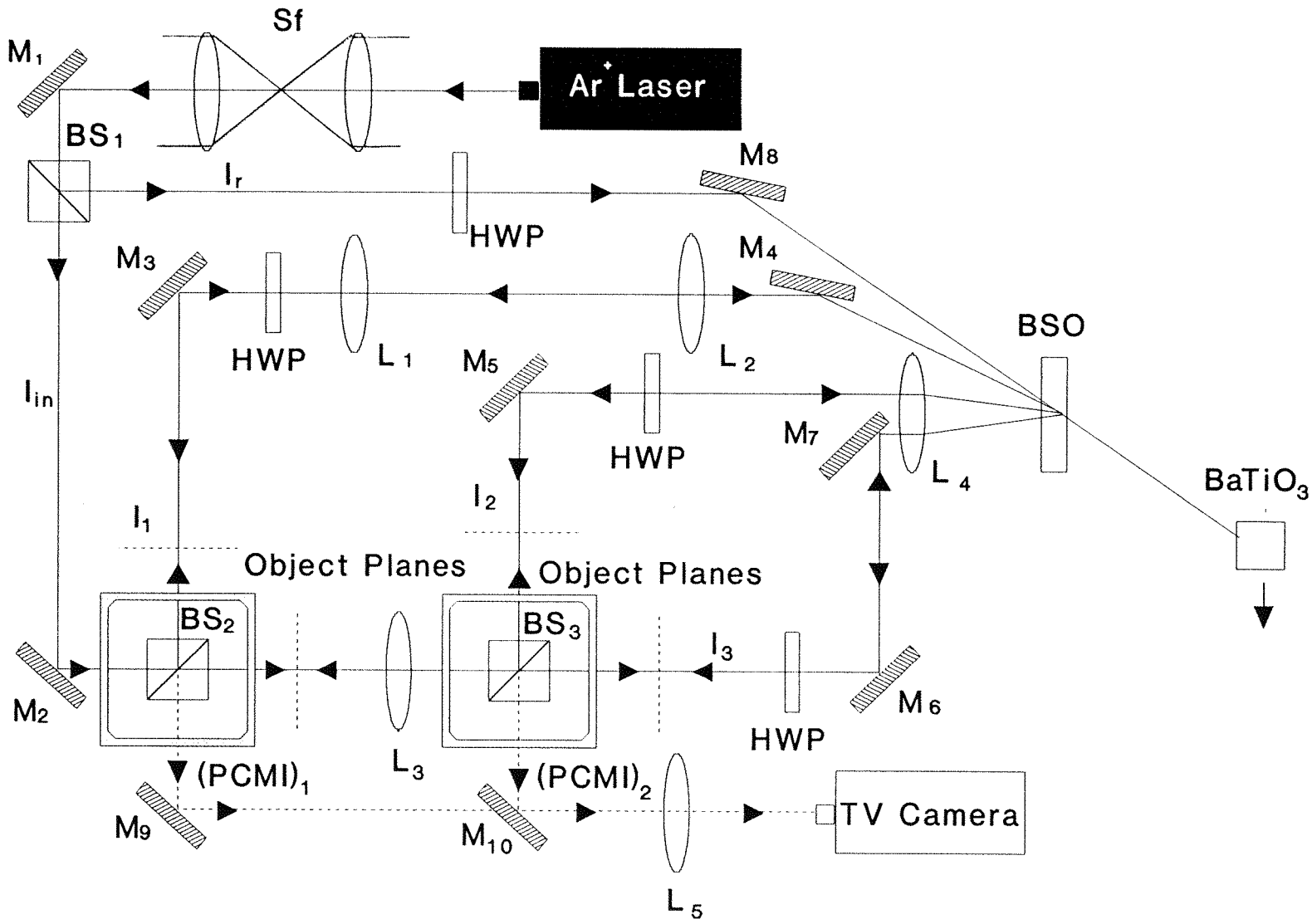

Figure 7.6 Shows the experimental arrangement to perform the basic logic operations.

the horizontal direction. At the beam splitter BS_3 they interfere destructively due to the 180° relative phase shift introduced between the two beams on reflection from BS_3. It is worth noting that due to the preservation of polarization, the relative phase shift of 180° between the two beams was also preserved on phase conjugation.

The fulfilment of these conditions ensured that the Stokes' principle of reversibility holds and we observe no light at the output port of BS_3 (XOR operation). A complementary output was observed at the input port of BS_3 which corresponds to coherent addition.

Case:II. Non-polarization preserving Mode

As in Case.I, the polarization of beams I_2, I_3 and the readout beam was initially horizontal. After passing through the half-wave plates, the polarizations of the two beams were at 295° and 65° (from the vertical plane). The vertically polarized phase conjugate beams I_2^* and I_3^* pass back through the half-wave plates with their polarization directions at +12° and 340° (from the vertical plane). Subsequently the beam I_2^*, reflected from a metallic mirror, M_5, and interference at the output port of BS_3, with beam I_3^*, leads to constructive interference. The measured polarizations of beams I_2^* and I_3^* at the output port of BS_3 were 5° and 345° (with respect to the vertical). Therefore both the beams now have vertical components (s-polarized components), which were not present initially in the input beams. We observe coherent addition at the output port of BS_3 and a complementary output (XOR operation), was observed at the input port of BS_3. We believe the reason for the coherent addition is that these s-polarized components have undergone an additional relative phase shift. Any such phase shift depends on the exact geometrical and material arrangement of reflecting surfaces, and therefore cannot be compensated or reversed during phase conjugation because of the initial absence of any such s-polarised light.

The operations of coherent addition and subtraction represent the two extremes of the system. By selecting any specific polarization rotation, we can achieve a continuous operation between the two extremes. The OR operation is achieved when the polarization angles of the output phase conjugate beams I_2^* and I_3^* were 290° and 248° respectively (assuming a relative phase shift of 180° between the two

beams, which is consistent with Equation 7.1).

By exactly similar reasoning the operation of a series of cascaded PCMI can be considered. We have performed all sixteen basic logic operations on the two variables, as shown in Figure 7.7. To summarize this operation A AND B was performed by using only one beam. Operations of A OR B, A XOR B, A AND $\overline{B}$ and A NAND B were performed using two of the three beams, operations of $\overline{A}$ AND B, $\overline{A}$ OR B, A OR $\overline{B}$, A NOR B, A XNOR B, A, $\overline{A}$, B, $\overline{B}$, And 1 were performed using all three beams. For completeness operation 0 was performed using four beams in a cascaded PCMI configuration of two individual PCMIs.

7.5 Proposal for further improvements

A Faraday isolator can rotate the plane of polarization of incident light when a magnetic field is applied in the propagation direction. The rotation of the plane of polarization depends on the direction of magnetic field (parallel or antiparallel) to the propagation direction of light.

The angle β through which the plane of light is rotated is given by

$$\beta = VBd \qquad (7.3)$$

Where B is the static magnetic flux density (in gauss), d is length of the medium traversed (in cm) and V is a factor of proportionality known as the Verdet constant, which varies with both incident wavelength and temperature of the medium.

Here we can use a Faraday Isolator to rotate the direction of polarization of the phase conjugate output from a self-pumped $BaTiO_3$ as a readout beam to PCMI. As

---

Figure 7.7 Shows the experimental results of all sixteen basic logic operations. For all cases, we show the simulated results to be expected, for comparison with the experimentally achieved results. (a) A OR B, (b) A XOR B, (c) $\overline{A}$ OR B, (d) A OR $\overline{B}$, (e) A AND B, (f) A NAND B, (g) A AND B, (h) $\overline{A}$ AND B, (i) A NOR B, (j) A XNOR B (k) 1, (l) 0, (m) A, (n) B, (o) A, (p) B, (see next page).

Inputs	Ideal Case Results	Truth Tables A B Output	Experimental Results
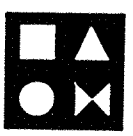 A 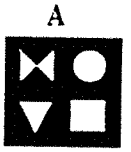 B	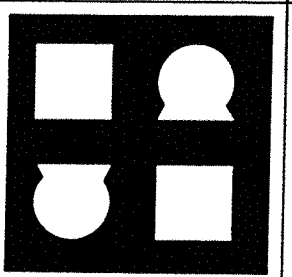 A OR B	1 1 1 1 0 1 0 1 1 0 0 0	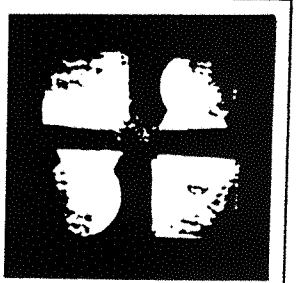 a
	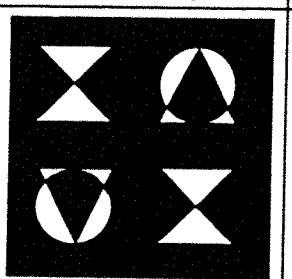 A XOR B	1 1 0 1 0 1 0 1 1 0 0 0	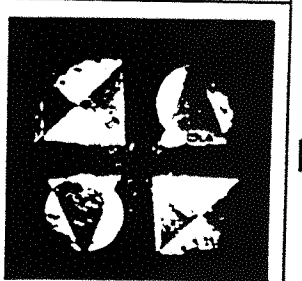 b
	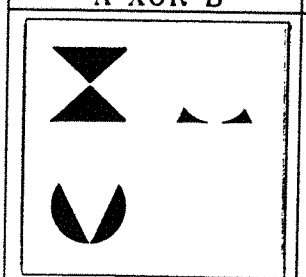 $\bar{A}$ OR B	1 1 1 1 0 0 0 1 1 0 0 1	 c
	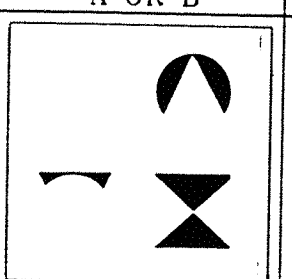 A OR $\bar{B}$	1 1 1 1 0 1 0 1 0 0 0 1	 d

Inputs	Ideal Case Results	Truth Table A B Output	Experimental Results
 A	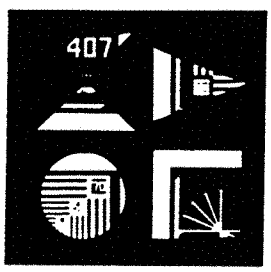 A AND B	1 1 1 1 0 0 0 1 0 0 0 0	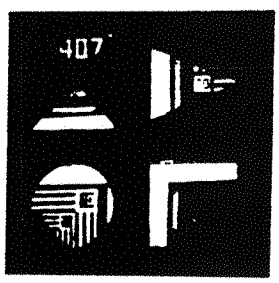 e
Resolution Chart B	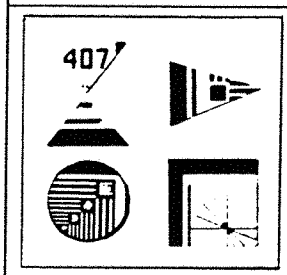 A NAND B	1 1 0 1 0 1 0 1 1 0 0 1	 f
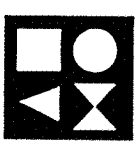 A	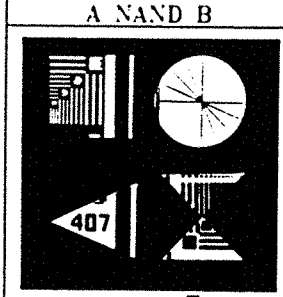 A AND $\bar{B}$	1 1 0 1 0 1 0 1 0 0 0 0	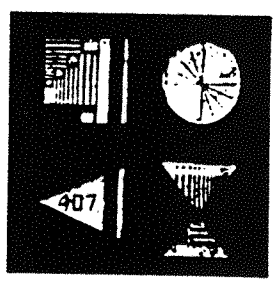 g
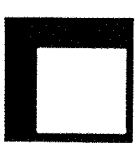 A 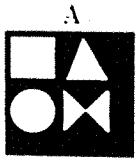 B	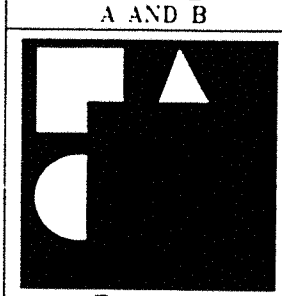 $\bar{A}$ AND B	1 1 0 1 0 0 0 1 1 0 0 0	 h

Inputs	Ideal Case Results	Truth Tables A	B	Output	Experimental Results
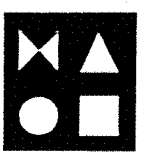 A	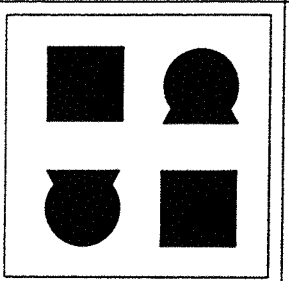 A NOR B	1	1	0	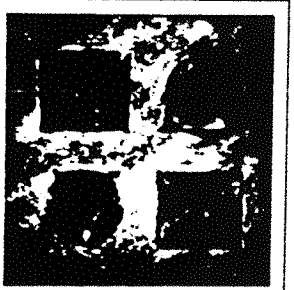 i
		1	0	0	
		0	1	0	
		0	0	1	
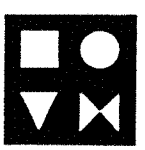 B	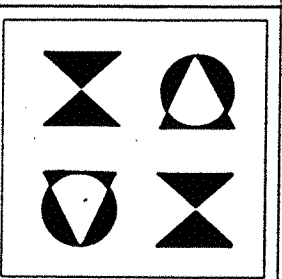 A XNOR B	1	1	1	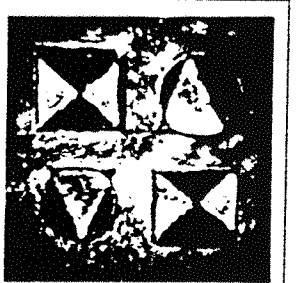 j
		1	0	0	
		0	1	0	
		0	0	1	
	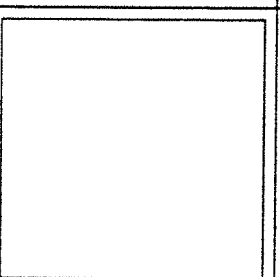 1	1	1	1	 k
		1	0	1	
		0	1	1	
		0	0	1	
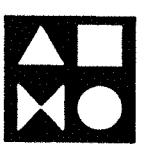 A	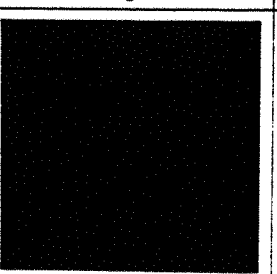 0	1	1	0	 l
		1	0	0	
		0	1	0	
		0	0	0	
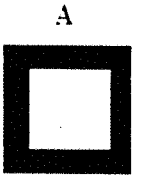 B					

Inputs	Ideal Case Results	Truth tables A	B	Output	Experimental Results	
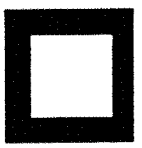 A	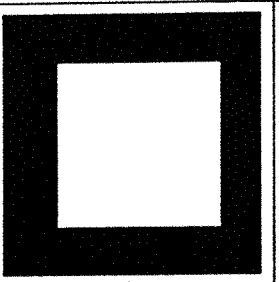 A	1	1	1	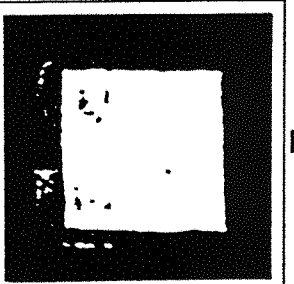	m
		1	0	1		
		0	1	0		
		0	0	0		
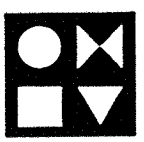 B	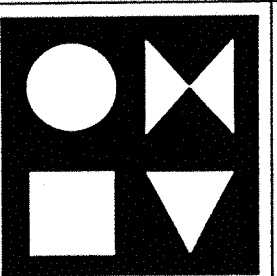 B	1	1	1	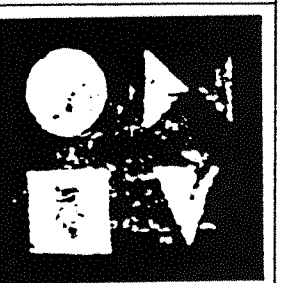	n
		1	0	0		
		0	1	1		
		0	0	0		
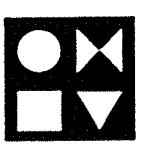 A	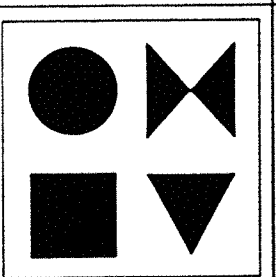 $\bar{A}$	1	1	0		o
		1	0	0		
		0	1	1		
		0	0	1		
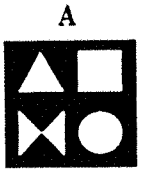 B	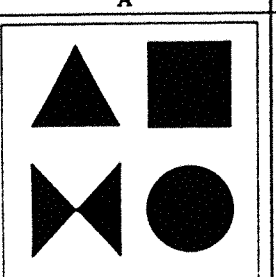 $\bar{B}$	1	1	0		p
		1	0	1		
		0	1	0		
		0	0	1		

shown in Figure 7.8, the PCM in the interferometric system is a BSO crystal in Kg $\perp \langle 001 \rangle$ configuration. Therefore the polarization of the phase conjugate beams will be of orthogonal polarizations to that of the readout polarization. The phase conjugate beams I_1^* and I_2^* pass through the half-wave plates and are rotated. Subsequently they are directed back towards BS_2 where they interfere. The interference of these beams is governed by Equation (7.1). The logic operations can be performed using such a set up by: (i) rotating the polarizations of beams I_1^* and I_2^* primarily through half-wave plates, (ii) rotating the polarization of the readout beam via a Faraday isolator (iii) rotating the polarization of both readout and phase conjugate beams simultaneously. Here we consider four cases to perform the operations of XOR, addition (coherent), addition (incoherent), and OR.

Case (I). Operation XOR

In this case as before the input beams have horizontal polarizations. After they pass through half-wave plates their polarizations are rotated to the vertical. The two vertically polarized signal beams interfere with a vertically polarized reference beam and record two gratings. A readout beam of horizontal polarization which is controlled by a Faraday isolator reads these two gratings. The polarizations of the phase conjugate beams I_1^* and I_2^* are vertical which will be rotated by a half-wave plate to the horizontal direction. Therefore the polarizations of phase conjugate beams are preserved and they will interfere destructively, due to the phase shift of 180°, at the output port of BS_2 to give the XOR operation.

Case (II). Operation Addition (incoherent)

As in the previous case the input polarization of the two signals is horizontal. The polarizations of these beams are rotated individually by the two half-wave plates. These beams record the two gratings as in the previous case (I). The polarization of the readout beam is now rotated to 315° from the vertical position. The polarization of the phase conjugate beams is now the same and will not be rotated by the crystal, because it is parallel to one of the two principal electro-optic axes. The fast axes of the two half wave plates are at a position where they make angles of 292.5° and 337.5° with the vertical respectively. Beam I_1^* is rotated to horizontal polarisation after it passes through the half wave plate. Whereas beam I_2^* is rotated by the half wave plate to a vertical polarization. At BS_2 both the beams

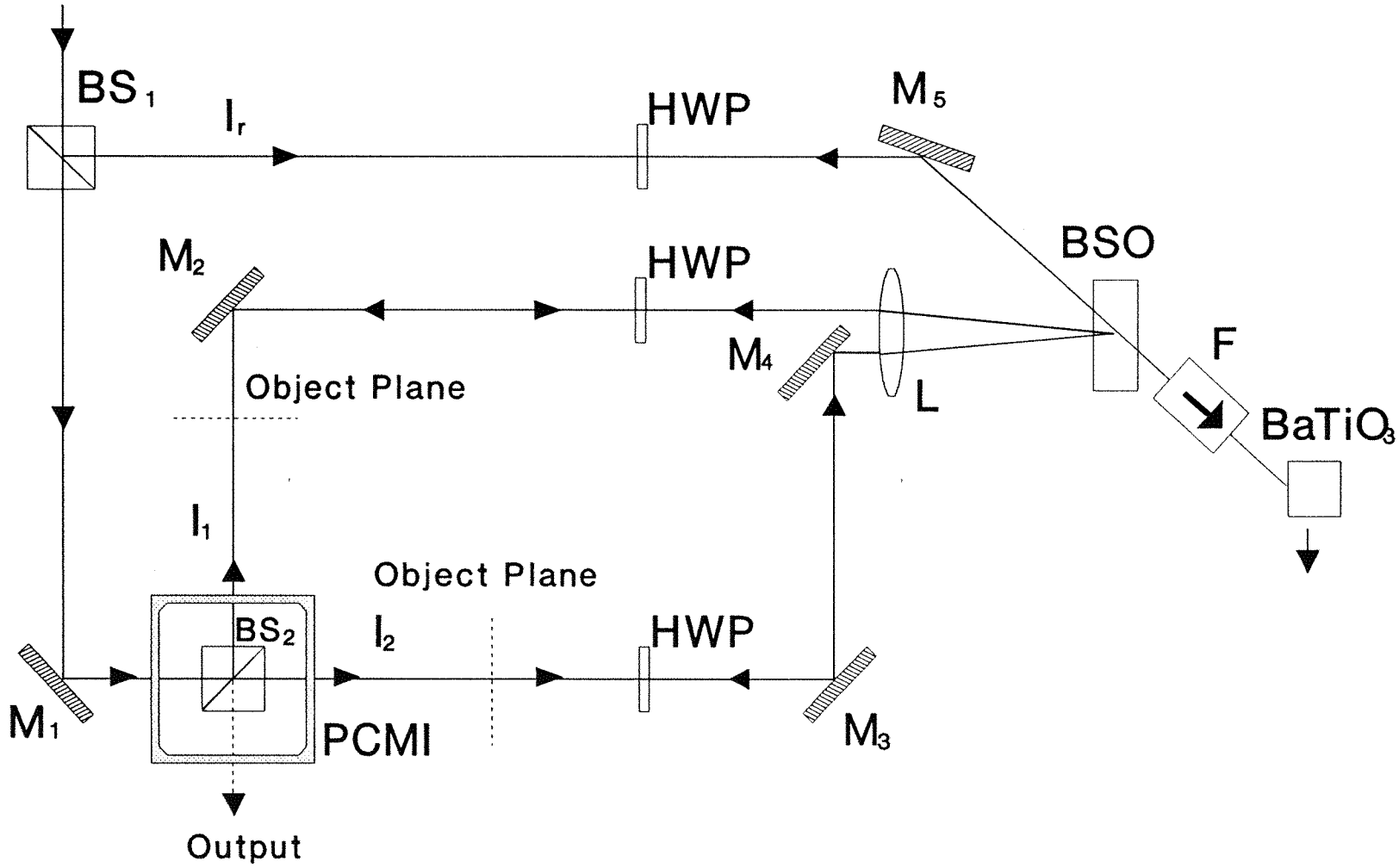

Figure 7.8 Shows a PCMI where a BSO crystal is used as a phase conjugate mirror and a self pumped $BaTiO_3$ crystal. A Faraday rotator is placed in the readout beam to rotate the plane of polarization of the beam.

have orthogonal polarizations and are transmitted and reflected without interfering with each other. Therefore an incoherent addition occurs at both input and output ports of BS_2.

Case (III). Operation Addition (coherent)

Coherent addition can be achieved when the polarization of the readout beam is vertical. The diffracted readout beam from the two gratings will have horizontal polarization. When the beams I_1^* and I_2^* pass through half-wave plates their polarization is rotated to the vertical. Due to the non-preservation of polarization the phase is not reversed on the return path. When the two beams reach BS_2 they interfere constructively, depending on their relative phase.

Case (IV). Operation OR

The operation OR can be achieved when the polarization of the readout beam is 330° from the vertical. In this situation the polarization of the phase conjugate output beams I_1^* and I_2^* would be 300° from the vertical because of the electro-optic axes in this crystal configuration. If the wave plate through which beam I_1^* passes has its axis at 315° it will rotate the polarization to 330°.While the polarization of beam I_2^* is arranged to be rotated to the horizontal direction via a half-wave plate. The two beams are directed towards the beam splitter BS_2 where they interfere to give an OR operation provided the relative phase shift between the two beams is 180°.

7.6 Optical Logic operations in Phase Regime

When a birefringent crystal plate is cut parallel to the optic axis the normally incident o- and e-waves travel with different speeds along a common direction in the crystal. In this case the o- and e-waves will emerge from the crystal plate with different relative phases. We can build a compensator as shown in Figure 7.9, which resembles a Babinet compensator. The compensator consists of the two independent wedges of the same birefringent material, with the optic axes of both the wedges parallel. A normally incident o-wave passing through the input face of the device at some arbitrary point will traverse a thickness of d_1 in the first wedge and d_2 in the second one. Therefore it will undergo a certain phase change after it emerges from the compensator. Similarly an e-wave undergoes a different phase change than that

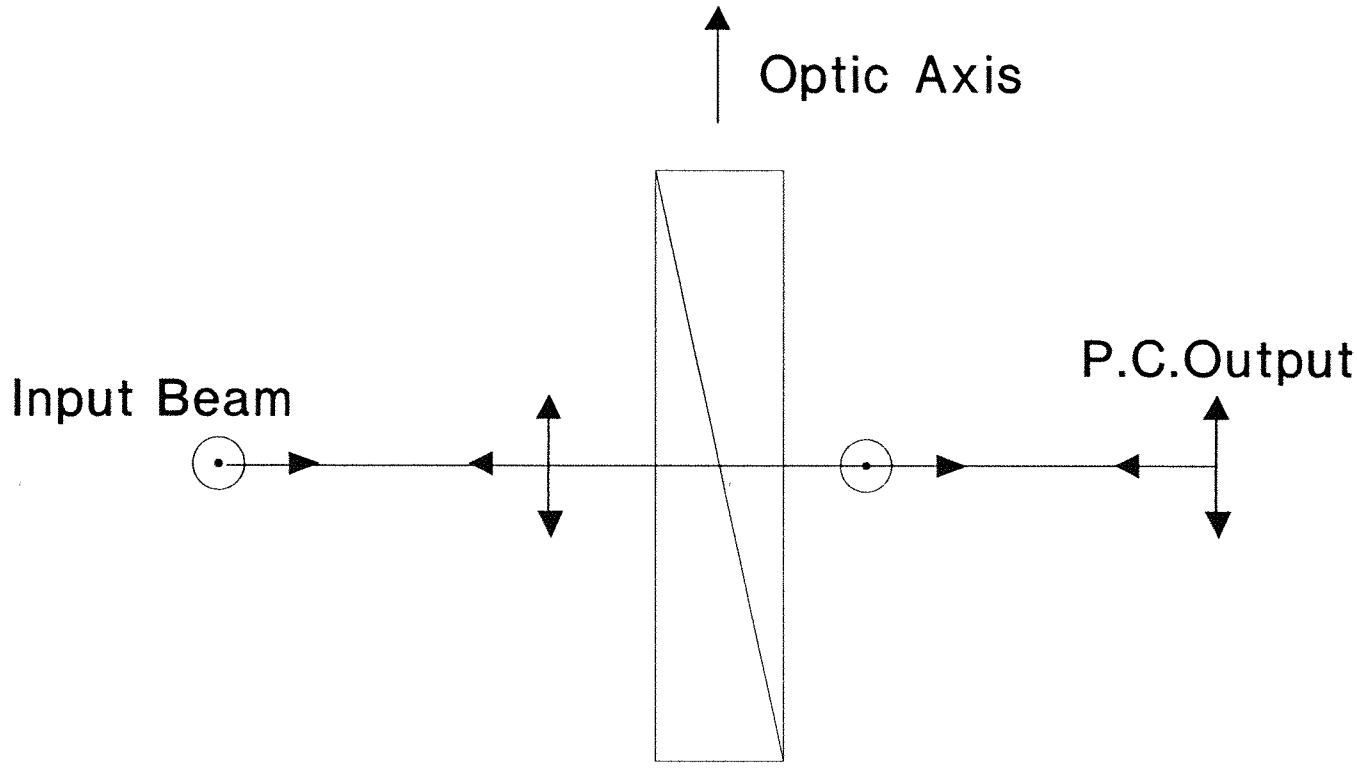

Figure 7.9 Shows two birefringent crystal wedges with parallel optic axis to achieve variable phase shift between orthogonally polarized light.

of o-wave. The phase shifts of the two waves depend on the refractive indices for the e- and o-waves and the thickness of the crystal plate and wavelength of the incident light. Therefore for a particular medium and wavelength we can control the phase shift of the e- and o-waves by varying the thickness of the compensator by sliding one wedge over the other.

$$\phi = \frac{2\pi (n_o - n_e)(d_1 + d_2)}{\lambda} \qquad (7.4)$$

Where n_o and n_e are the refractive index of o- and e-waves respectively, λ is the wavelength of the light, and d_1 and d_2 are the thickness of the crystal wedges.

Since the compensator can introduce variable phase shifts for the e- and o-waves, we can use such a technique in our PCMI to be able to control the relative phase shift between the interfering beams. Such a system can perform the logic operations in phase regime when the polarizations of the two beams are parallel. Figure 7.10, shows a PCMI configuration with such a compensator in one of the arms. As before, the phase conjugate mirror is a BSO crystal in the Kg $\perp$ $\langle 001 \rangle$ mode. The polarization of the input signals is horizontal, and beam I_1 passes through the compensator as an e-wave. Subsequently the signal beams are rotated to a vertical polarization via half-wave plates in the beams I_1 and I_2. The two beams interfere with a single reference beam of vertical polarization to record two gratings. A readout beam whose polarization is adjusted by a Faraday isolator to be vertical, reads the gratings. The polarization of the phase conjugate beams I_1^* and I_2^* is horizontal, which is then rotated to the vertical direction after passing through the half wave plates. Beam I_1^* passes through the compensator on its way back to the beam splitter. However this time the phase conjugate beam I_1^* passes through the compensator as an o-wave. Therefore the phase shift which is imposed on the o-wave is different than that on e-wave. When the beam I_1^* reaches BS_2, it interferes with the beam I_2^*. Since the polarizations of the two phase conjugate beams are in the same direction the interference will depend on the phase angle between the two (coherent) beams only. Therefore the degree of interference can be controlled by varying the relative phase between the two beams via the compensator. We can consider four general cases of operations for this configuration.

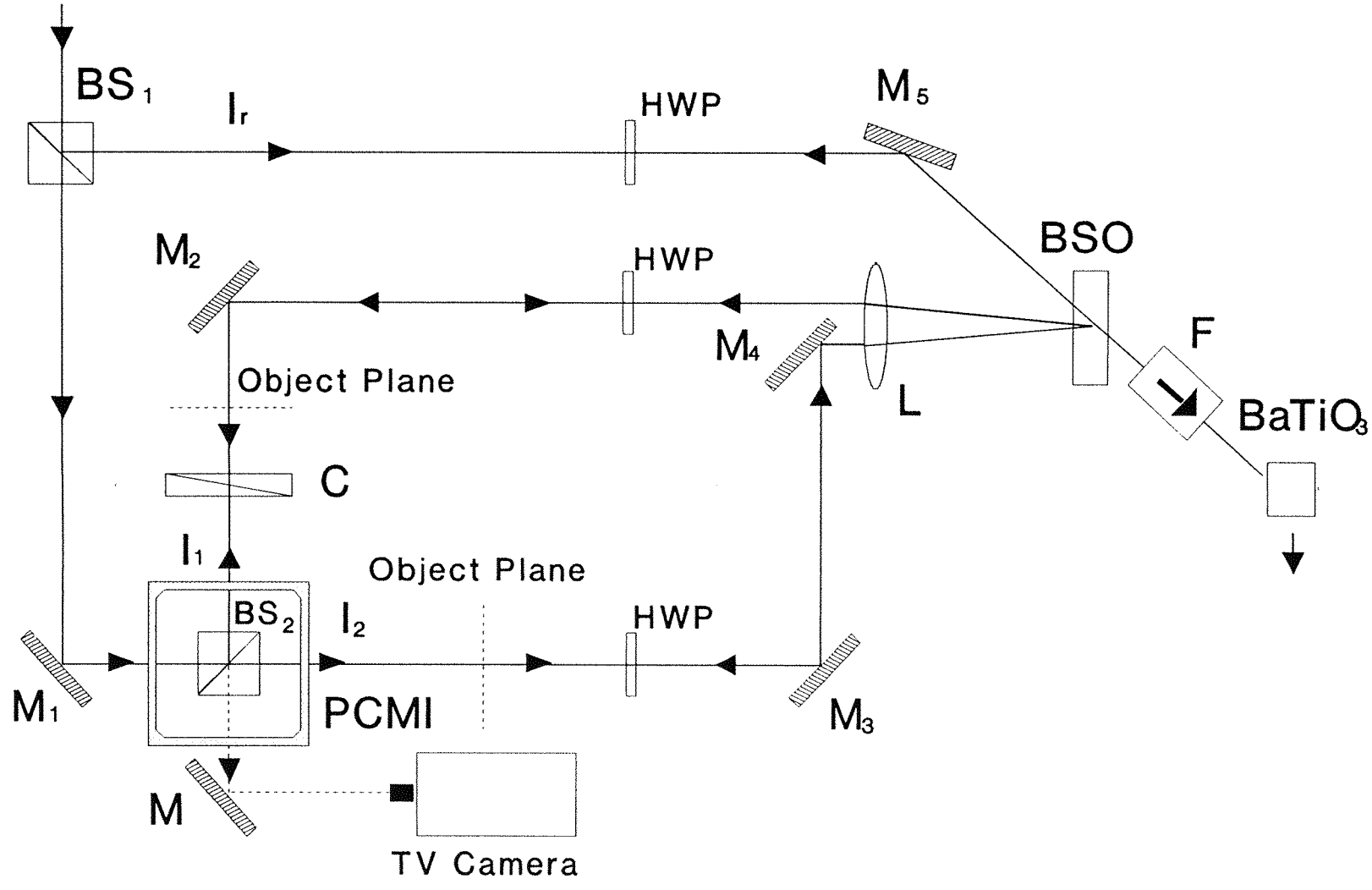

Figure 7.10 Shows a compensator as shown in Figure 7.9, in one of the arms of a PCMI to introduce a relative phase shift between the two phase conjugate outputs.

Case (I). Operation XOR

As shown in the Figure 7.2, when the angle between the plane of polarization is 0° all the operations are performed in the phase regime. Therefore an operation of XOR is achieved when 180° phase shift is introduced between the two beams. A complementary output which shows coherent addition is achieved at the input port of BS_2.

Case (II). Coherent Addition: $4I_o$

Coherent addition with output intensity $4I_o$ is also achieved at the output port of BS_2 when the phase shift of either 0° or 360° is introduced between the two beams. Similarly a complementary output in this case performs an operation XOR at the input of BS_2.

Case (III). Coherent Addition: $2I_o$

A coherent addition is achieved with output intensity $2I_o$ when there is a phase shift of 90° between the two phase conjugate beams. A complementary output, which is the same intensity will also be achieved at the input port of BS_2.

Case (IV). Operation OR

This operation is also easy to achieve in the phase regime by introducing a phase shift of 120° between the two beams. The intensity at the output port of BS_2 is I_o while a complementary output at the input port is $3I_o$.

The technique of logic operations in phase regime can be extended to a cascaded PCMI system. Such a system is shown in Figure 7.11. in which beams I_1 and I_2 both have compensators. All sixteen basic logic operations on two variables can be performed by simply varying the phase shifts in beams I_1^* and I_2^*.

The technique of performing logic operations in the phase regime has certain advantages over previous techniques which may make this a reliable potential scheme for optical logic operations. These are as follows:

(i). The polarization of the phase conjugate beams are fixed once rotated to 90° with respect to input polarizations and have $\theta=0°$.

(ii). To perform the above mentioned operations or any continuous operation

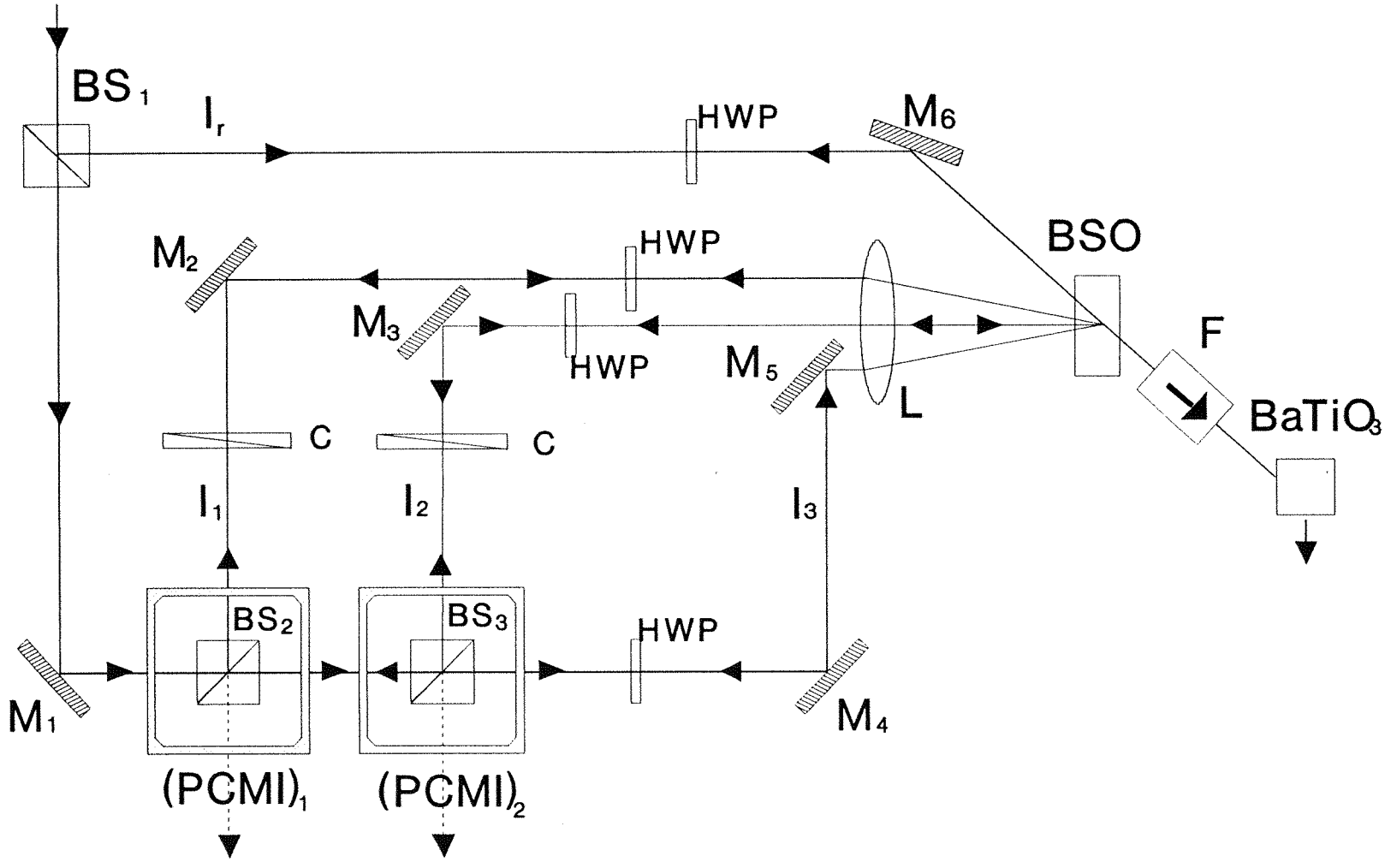

Figure 7.11 Shows a cascaded PCMI with compensators in two of its arms to achieve logic operations in phase regime.

between them we just need to introduce a required phase shift between the two beams via the compensators which is easy to achieve.

(iii). Unlike previous techniques where we have to control the polarization with an arbitrary change in phase due to reflection etc., between the two beams, we have full control of the relative phase of parallel polarizations. This ensures that operations of XOR, coherent Addition and all continuous operations between these two extremes are easily achievable.

7.7 Implementation of Boolean Functions via Optical Logic Scheme

In digital electronics there are two main problems i.e., design itself and simplification in the design of economical logic circuits. The first problem is solved by defining forms of logic expressions which are derived from truth tables. In the second stage these expressions are solved by algebraic methods or by a procedure for minimizing Boolean functions known as the "Karnaugh Map" [7.17, 7.18]. The map presents a visual diagram of all possible ways a function may be expressed in a standard form. By selecting various patterns, one can derive alternative algebraic expressions for the same function, from which the simplest one can be selected.

Consider a Boolean function

$$F=\overline{A}BC+A\overline{BC}+A\overline{B}C+AB\overline{C}+ABC \qquad (7.5)$$

The group of variables, which is separated by '+' sign is called minterm. Two or more minterms are joined in the logic diagram by OR gates. While all the variables in a minterm are joined by AND gates. Figure 7.12, shows the logic diagram of Equation (7.5). However the circuit is less simple and has five AND gates, five inverters and one OR gate with five inputs. An equivalent optical logic circuit is shown in Figure 7.13. Here the optical circuit exploits cascaded PCMIs operating in phase regime configuration with multiplex holographic recording in BSO. There are five OR gates, fives AND gates and five NOT gates involved to perform the Boolean function of Equation (7.5). By taking advantage of the minimisation procedure of logic functions i.e., Karnaugh Map method we can simplify the lengthy and complex Boolean functions into simplified ones. The resultant minimal form of logic circuits

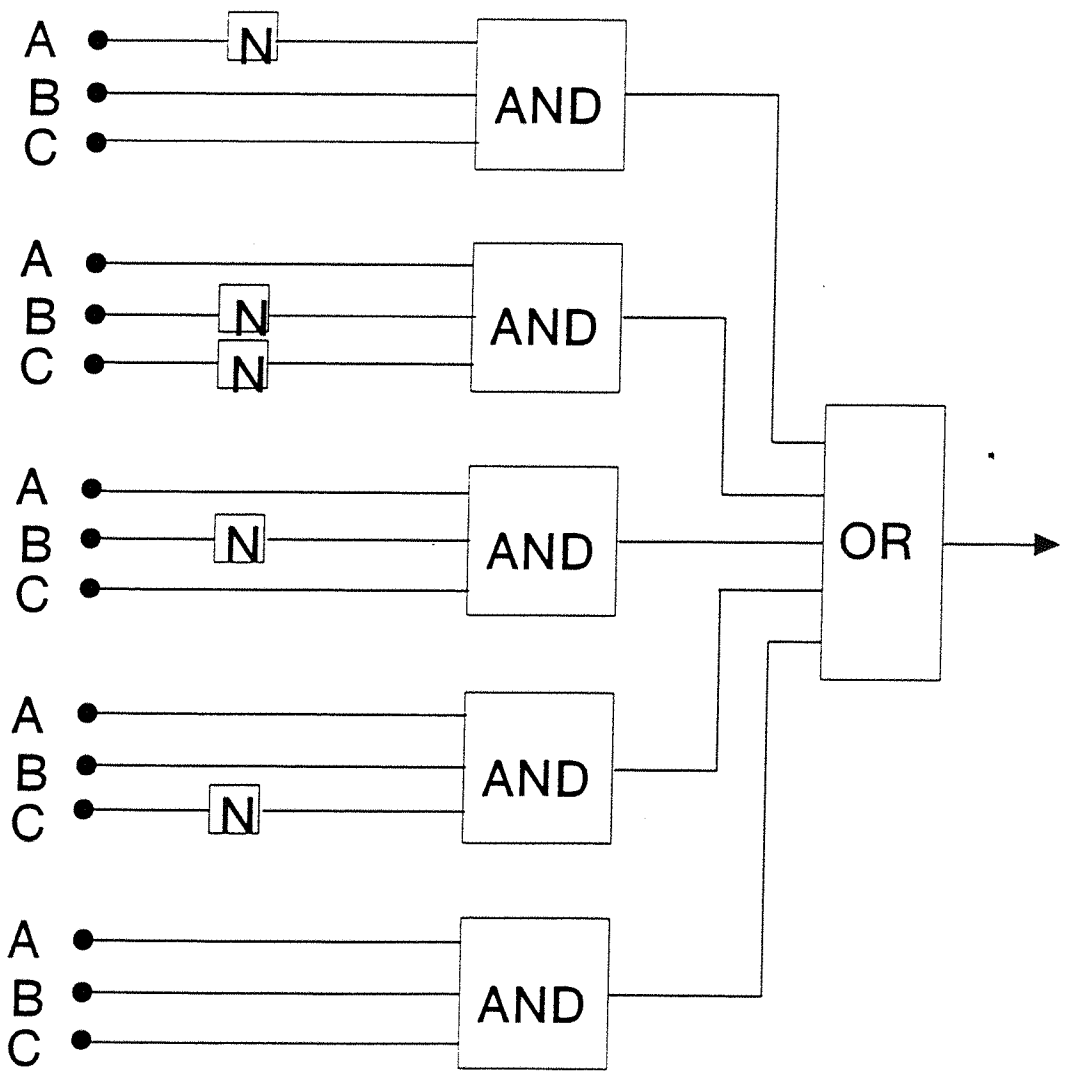

Figure 7.12 Shows logic diagram of Equation (7.4).

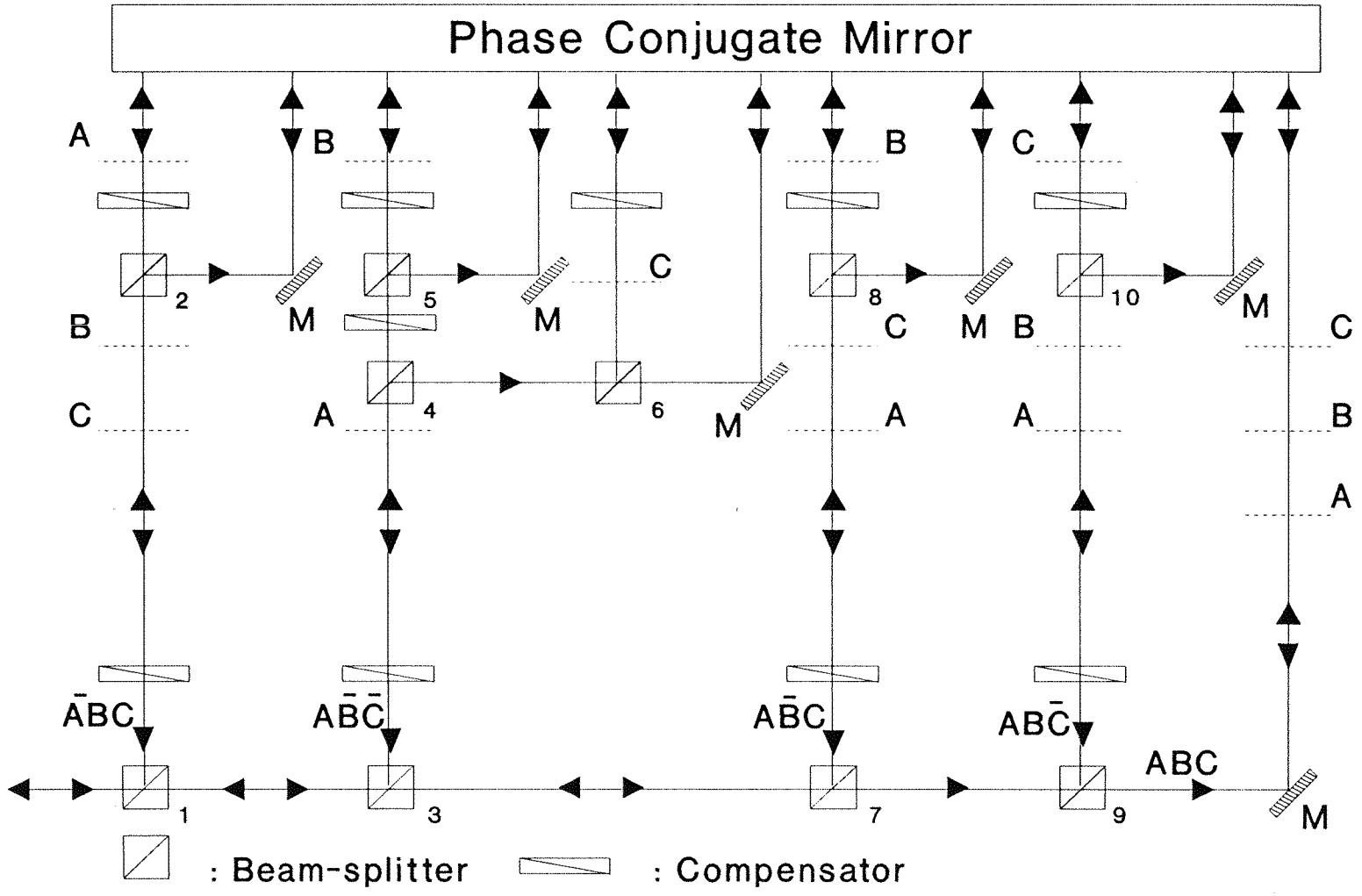

Figure 7.13 Optical logic circuit equivalent to the logic diagram of Figure 7.12.

are simple and have fewer gates. Therefore Equation (7.5) is reduced to its minimal form and is given by

$$F=A+BC \qquad (7.6)$$

The logic circuit diagram is shown in Figure 7.14(a), and has one AND and one OR gates. Such a function is performed using the optical logic technique with great simplicity. Similarly, its equivalent optical logic circuit is shown in Figure 7.14(b). The optical logic circuit has, like its electronic counterpart, only one AND and one OR gate. Such a system can perform the operations with BSO crystal as PCM with the speed of 1ms at $1W/cm^2$ intensity level. However, **unlike its electronic counterparts** a large number of pixels can be processed in parallel which may surpass the speed of sequential processing in electronics.

7.8 Discussion and Conclusion

A technique of optical logic on two variables is described using PCMI in cascaded form with a single crystal of BSO. Multiple signal beams with a single reference beam is used to record multiplexed gratings. Subsequently the reference beam is phase conjugated via a self-pumped $BaTiO_3$ crystal to read all the gratings. The technique relies upon changing the polarizations of the two phase conjugate beams, with specific phase shifts between them. Therefore interference at the output depends on their relative polarizations and phases. Complete subtraction is achieved when PCMI was working in polarization preserving mode. However, when the PCMI was not working in polarisation preserving mode and the two phase conjugate beams were s-polarized we have achieved coherent addition. Other continuous intermediate operations are observed when the polarizations of the phase conjugate beams were rotated between these two extremes.

Using these basic operations in cascaded PCMI we have demonstrated all sixteen logic operations on two variables. We feel the main advantage of our technique is that it is simple, stable and versatile since this type of cascading is almost impossible to implement in previous techniques. We also proposed improvements in the existing technique which may make our technique a potential candidate for building blocks in an optical computing system. According to these improvements operation of

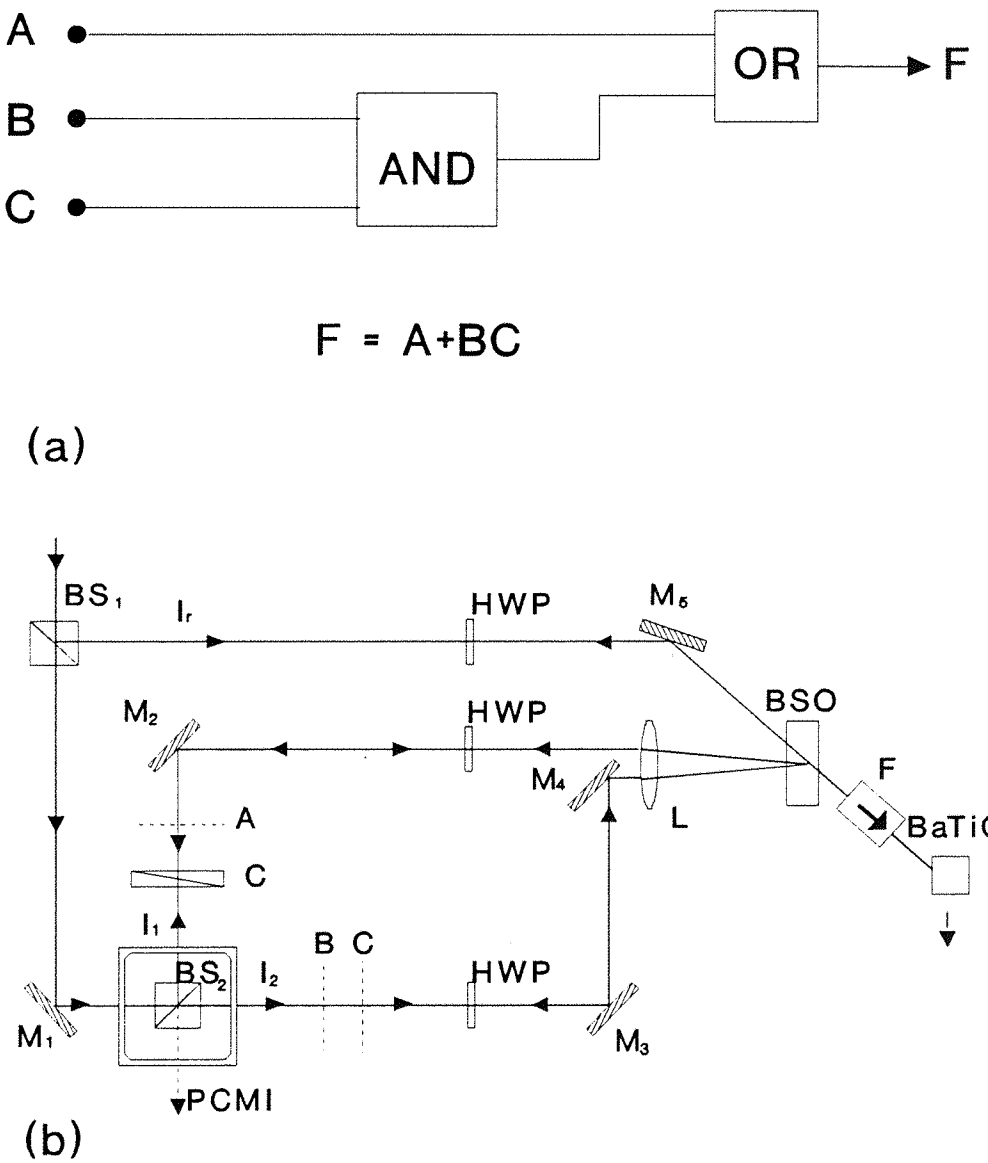

Figure 7.14 (a) Shows the minimum form of the logic diagram shown in Figure 7.12. (b) Shows the optical logic diagram equivalent to the logic diagram shown in (a).

cascaded PCMI can be controlled better if we rotate the polarization of the readout beam at certain fixed positions of the axes of half-wave plates in the two arms of PCMI. Another improved scheme is proposed in which one of the arms has a compensator. The input and phase conjugate beam polarizations in that arm are arranged to be o- and e-waves for the compensator respectively. In such an arrangement the compensator introduces a variable phase on the input and phase conjugate output beams which can be used to control the interference between the two phase conjugate beams at the output. This technique can be used in cascaded PCMI systems.

We think that these optical logic gate techniques can provide the possibility to perform the same logic functions using techniques of minimization or simplification of long and complex switching (Boolean), functions i.e, Karnaugh Mapping. However the advantage here with the optical logic gates is the capability of handling enormously large number of gates in parallel. This may be further improved with the development of nonlinear crystals with higher gain and shorter response time.

REFERENCES

7.1 D. Gabor, G. W. Stroke, R. Restrick, A. Funkhouser and D. Brumm, "Optical image synthesis (complex amplitude addition and subtraction) by holographic Fourier transformation", Phys. Lett. **18**, 116 (1965).

7.2 F. T. S. Yu, S. Jutamulia and Taiwei Lu, "Optical parallel logic based on magneto-optic spatial light modulator", Opt. Commun. **63**, 225, (1987).

7.3 F. T. S. Yu, Q. W. Song and X. J. Lu, "Implementation of Boolean logic gates using a microchannel spatial light modulator with liquid-crystal televisions", Opt. Lett. **12**, 962 (1987).

7.4 F. A. P. Tooley, N. C. Craft, S. D. Smith and B. S. Wherrett, "Experimental realisation of an all-optical single-gate full-adder circuit", Opt. Commun. **63**, 365 (1987).

7.5 J. Weigelt, "Binary logic by spatial filtering", Opt. Eng. **26**, 28 (1987).

7.6 A. W. Lohmann and J. Weigelt, "Spatial filtering logic based on polarization", Appl. Opt. **26**, 131 (1987).

7.7 A. E. Chiou, P. Yeh and M. Khoshnevisan, "Nonlinear optical image subtraction for potential industrial applications", Opt. Eng. **27**, 385 (1988).

7.8 J.P. Huignard, J. P. Heriau and F. Micheron, "Selective erasure and processing in volume holograms superimposed in photosensitive Ferroelectrics", Ferroelectrics, **11**, 393 (1976).

7.9 Y.H. Ja, "Real-time image subtraction in four-wave mixing with photorefractive $Bi_{12}GeO_{20}$ crystals", Opt. Commun. **42**, 377 (1982).

7.10 S. Kwong, G. A. Rakuljic and A. Yariv, "Real time image subtraction and **exclusive OR** operation using a self-pumped phase conjugate mirror", Appl.

Phys. Lett. **48**, 201 (1986).

7.11 A. E. Chiou and P. Yeh, "Parallel image subtraction using a phase-conjugate Michelson interferometer", Opt. Lett. **11**, 306 (1986).

7.12 N. A. Vainos, J. A. Khoury and R. W. Eason, "Real-time parallel optical logic in photorefractive bismuth silicon oxide", Opt. Lett. **13**, 503 (1988).

7.13 N. A. Vainos and R. W. Eason, "Spatially multiplexed phase conjugate imaging and processing in photorefractive BSO", Opt. Commun. **62**, 311 (1987).

7.14 A. Marrakchi, R. V. Johnson and A. R. Tanguay, "Polarization properties of photorefractive diffraction in electrooptic and optically active sillenite crystals (Bragg regime)", J. Opt. Soc. Am. B, **3**, 321 (1986).

7.15 P. Gunter and J.-P. Huignard, " Photorefractive Materials and their Applications", Topics in Applied Physics Vols. **61**, Springer-Verlag, Berlin (1988).

7.16 J. A. Khoury, G. Hussain and R. W. Eason, "Optical tracking and motion detection using photorefractive $Bi_{12}SiO_{20}$", Opt. Commun. **71**, 138 (1989).

7.17 I. Aleksander, "**Introduction to logic circuit theory**", George G. Harrap & Co. Ltd, London (1970).

7.18 M. Morris Mano "**Digital Design**", Prentice Hall, Inc, Englewood Cliffs NJ, USA (1984).

CHAPTER 8

OBSERVATION AND MODELLING OF DYNAMIC INSTABILITIES IN THE MUTUALLY PUMPED BIRD-WING PHASE CONJUGATOR IN $BaTiO_3$

8.1 Introduction

Photorefractive materials provide an ideal medium for performing the process of phase conjugate of an input optical beam. The more traditional beam geometry to achieve this process uses externally controlled interacting beams inside the photorefractive material. Self-starting oscillations in the output can occur in an arrangement which rely upon feedback in a photorefractive medium with large gain coefficient such as $BaTiO_3$. Such oscillations have been observed in self pumped $BaTiO_3$ crystal and may be regular or chaotic. It was observed that the frequencies of the oscillation was proportional to $I^{0.89}$ and a frequency shift in the phase conjugate output has also been observed. The character of the oscillations depends upon crystal orientation, reflectivity of the corners of the crystal, beam intensity and spot size [8.1].

Oscillations in the phase conjugate output from the self pumped phase conjugator have also been observed by Smout et al [8.2]. The characteristics of the oscillations depend upon the position and angle of incidence of the input beam and the distance of the beam from the +c face. The complex pattern of the beams inside the crystal suggests that the oscillations were the result of the competition between the different self pumping loops.

Instabilities in the output have also been observed in the bird-wing phase conjugator. In the subsequent section we present a brief review of various phase conjugators which rely upon pump beams which are generated inside the photorefractive medium.

8.2 Mutually pumped phase conjugator (MPPC)

A novel class of phase conjugators has emerged during the last few years which generate phase conjugate outputs of two mutually incoherent input beams. Phase conjugation in such conjugators, is implemented without the need for any externally applied pump beams. These new types of phase conjugators, implemented in a range of different geometries, exhibit however basically similar properties to other phase conjugate schemes and are therefore termed MPPC (Mutually pumped phase conjugators). The basic mechanism which is involved in this process is FWM. When the two beams enter the crystal, they interfere with their own fanning light [8.3]. Due to such a randomly oriented interference pattern, a range of holograms is recorded. Subsequently, light incident from the opposing beam is scattered from these holograms and emerges from the crystal as a phase conjugate output. Various types of MPPC are shown in Figure 8.1.

8.2.1 Double Phase Conjugate Mirror (DPCM)

In a DPCM as shown in Figure 8.1 (a), two mutually incoherent pump beams are incident on opposite faces of a photorefractive crystal e.g., $BaTiO_3$. The two input beams are fanned and record individual gratings which subsequently overlap, and are bent into one another due to the light which is scattered from these gratings as a result of the four wave mixing process. It has additionally been observed that the two phase conjugate beams that result are generated without significant crosstalk between them [8.3-8.6].

8.2.2 Bird Wing Phase Conjugator (BWPC)

When two (preferably incoherent), beams enter a photorefractive crystal such as $BaTiO_3$ in the BWPC orientation through opposite faces, they undergo fanning towards the +c face of the crystal and are internally reflected as shown in Figure 8.1 (b). The fanned light from one beam can Bragg diffract off the fanning grating recorded by the other beam to generate a phase conjugate output [8.7]. Further details about the BWPC including the inherent instabilities involved will be given in Section 8.3.

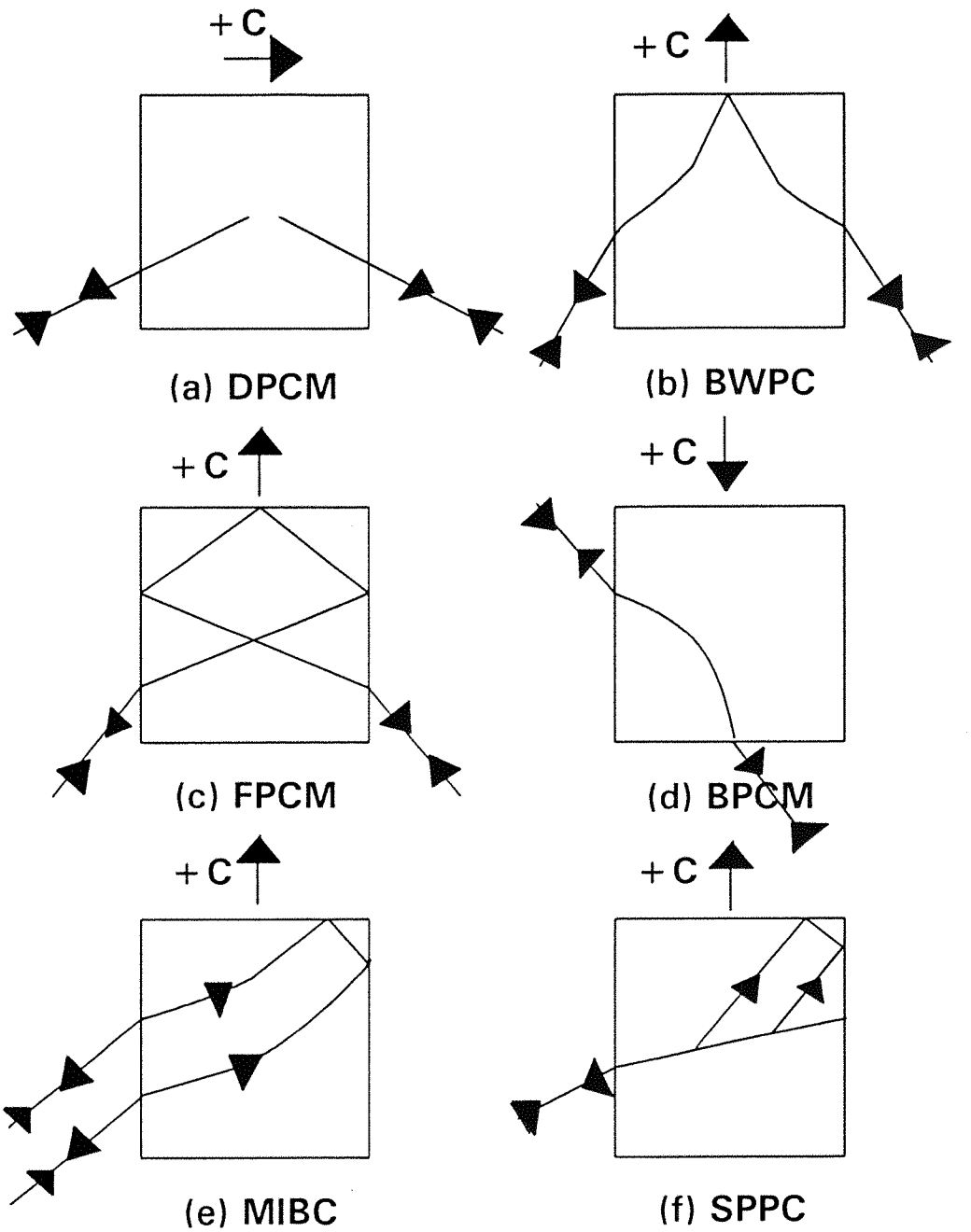

Figure 8.1 Shows various types of Mutually pumped phase conjugators.

8.2.3 Frog-Legs Phase Conjugate Mirror (FPCM)

The Frog-legs MPPC is the most recent kind of phase conjugator which relies upon three internal reflections between the two distinct interaction regions inside the photorefractive crystal as shown in Figure 8.1 (c), [8.8]. Again, two (incoherent) optical beams are incident on the two opposite faces of the crystal. After travelling a short distance i.e., 1 mm or so, the beams spontaneously deviate from their its incident paths to fan towards the +c axis. The deflected beams then strike the opposite faces of the crystal and are subsequently reflected from the +c face towards their incidence faces before deflecting from the other self-written gratings.

The reflectivity for the FPCM is comparable with that of the BWPC for similar incident beam intensity ratios. However the response time for the FLPC is over 100 times longer than for the BWPC for similar intensity levels [8.8]. The grating formation time will not necessarily become shorter if the incident beams are more tightly focused, because the phase conjugate gratings are initiated by the fanning light.

8.2.4 The Bridge Phase Conjugator (BPC)

The bridge conjugator is a more recent type of MPPC as shown in Figure 8.1 (d) and is similar to the DPPM in that there is no total internal reflection of the coupling channel from the crystal faces. However it is thought that BPC has two interaction region channels for coupling of the two mutually incoherent beams [8.9, 8.10]. The typical PC reflectivities from the BPC is reported to be 30 %. Due to the beam geometry involved in this type of MPPC, self pumping may occur for one of the beams, which would lead to competition between the two processes, and hence possible instabilities.

8.2.5 The Mutually Incoherent Beam Coupler (MIBC)

In the MIBC, two mutually incoherent beams are incident upon the same face of a photorefractive $BaTiO_3$ crystal so that self-fanning occurs in the direction of +c axis. Some of the fanned light from the two beams undergoes two total internal

reflection and thus becomes approximately counter propagating to the fanned light from the other beam. If the Bragg conditions are satisfied by these two beams, scattering takes place from the fanning gratings which results in phase conjugate outputs of the two input beams. The process can occur equally well for both the beams, and the fanned light is observed to condense to form a counter propagating coupling loop that appears to connect two distinct interaction regions as illustrated in Figure 8.1 (e). The phase conjugate outputs and the detailed interaction dynamics from the MIBC is a function of beam intensity ratio of the two interfering beams [8.11].

8.2.6 Self Pumped Phase Conjugator

The SPPC is a self contained device and consists of a photorefractive crystal such as $BaTiO_3$ [8.1, 8.2]. SPPC employs a DFWM process inside the photorefractive crystal such that the two counter propagating pump beams are derived from the incident beam in the crystal and never leave the crystal. One of the edges of the crystal acts as a corner cube reflector and via total internal reflections gives rise to a loop of counter propagating light. This loop of light provides the readout beam for the PC output as shown in Figure 8.1 (f).

8.3 Theoretical Considerations

The BWPC is one of the MPPC described in the previous section which generates two simultaneous PC outputs via the interaction of the two mutually incoherent beams. The two beams incident on the opposite faces of the crystal, undergo fanning towards the +c face of the crystal. As a result, a set of photorefractive holograms is generated that channel the two beams towards the c-face of the crystal as shown in more detail than previously, in Figure 8.2.

After the two beams are internally reflected the hologram sharing process takes place due to the overlap of the fanning gratings. All the overlapping fanning gratings which are produced by the two incident beams independently of each other will wash out, and the only gratings that will survive are recorded by mutually phase conjugated beams. The fan of light adopts a narrower channel of light whose shape resembles

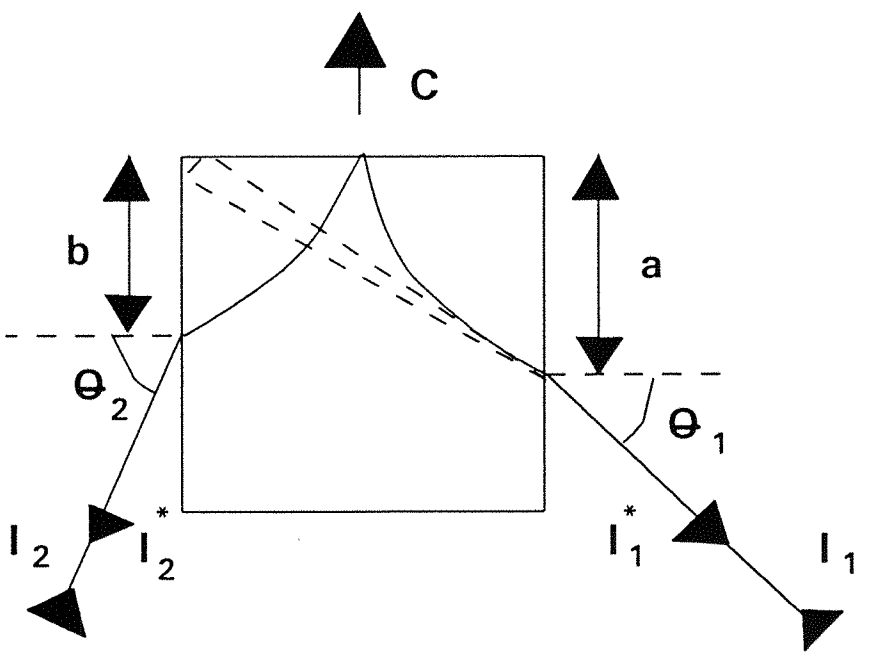

Figure 8.2 Shows schematic diagram of the Bird-Wing Phase Conjugator.

a set of bird's wings as it narrows. As a result simultaneous PC output is generated from both the input beams, such that beam I_1 provide the photons for beam I_2^* and beam I_2 provide the photons for beam I_1^*.

The beam configuration in the BWPC however, also allows one or both the beams to undergo self pumped phase conjugation in the cat geometry. These two processes may occur simultaneously and therefore it is possible for a competition between the two processes to exist. Such a potential competition between the BWPC and SPPC has already been noted by Ewbank [8.7] but no experimental work on this effect has previously been reported.

We have observed oscillations in the BWPC which are periodic as well as chaotic in character, depending on the input beam geometries [8.12]. The pattern of the beams inside the $BaTiO_3$ helps to clarify the behaviour of oscillations which is described in the following cycle and is illustrated in Figure 8.3. After the formation of the BWPC channel a SPPC loop takes place between beam I_1 and the corner of the crystal. This loop grows stronger while the BWPC channel become weaker. After a time lapse however, the SPPC loop and the BWPC channel again takes precedence. In the geometry adopted, neither of the beams incident upon the crystal underwent self pumping by themselves. Therefore the presence of the BWPC channel somehow provided the required gain which brought the fanned light above threshold, hence forming the SPPC loop.

A phenomenological model has been developed to describe the oscillation cycle observed. The model is developed from the previous work of Smout and Eason [8.11], and uses the beam nomenclature of Figure 8.4. We consider the BWPC to be a two interaction region configuration where refractive index gratings at region A and B control the reflectivity of the conjugator. A TBC interaction between the light circulating in the BWPC and residual fanned light takes place at region C and it is this interaction that is thought to bring the SPPC above threshold. As a result, the grating at region C diffracts light to region A, which reduces the modulation ratio m_A i.e., partially erases the grating. Therefore the power in the beam travelling towards region B in the BWPC channel is decreased, increasing the modulation ratio, m_B. This reduces m_A further, due to the increasing level of light diffracted towards

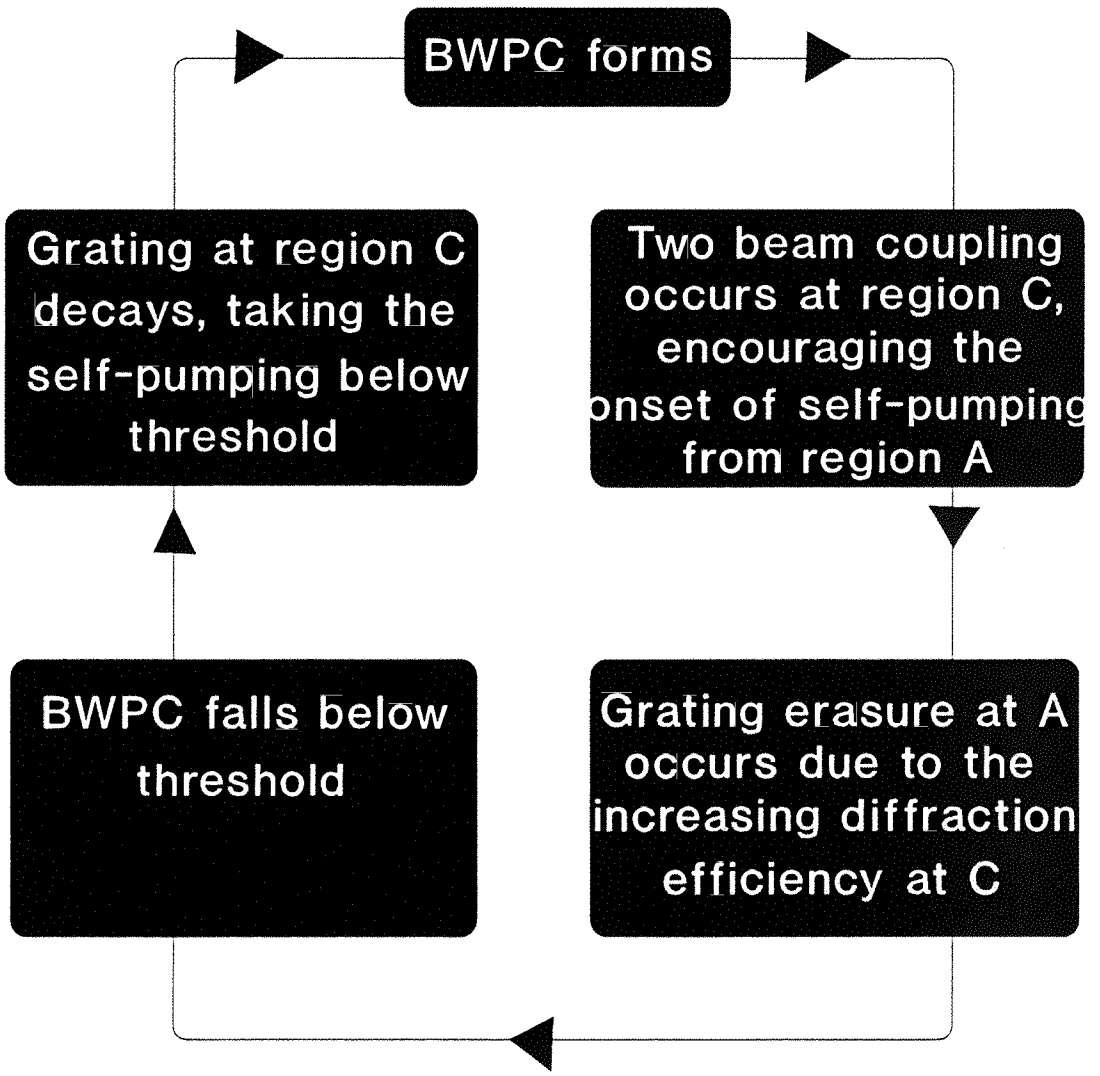

Figure 8.3 Illustrates typical oscillation cycle.

region A. This feedback process leads to the BWPC interaction going below threshold, which results in the subsequent decay of the induced SPPC process. The cycle is then repeated, apparently indefinitely

8.4 The Model

The beam nomenclature to be used in this section is illustrated in Figure 8.4. If the diffraction efficiency of the refractive index grating at region A is denoted by η_A, and beam powers I_3 and I_7, the diffracted and un-diffracted portions of beam 1, leaving region A will be given by

$$I_3 = \eta_A I_1 \qquad (8.1)$$

$$I_7 = I_1 (1 - \eta_A) - I_5 \qquad (8.2)$$

where I_5 is the power in the self-pumping beam, and η_A, in the limit $m_A << 1$, is given by

$$\eta_A = A m_A^2 \qquad (8.3)$$

where

$$m_A^2 = \frac{4 I_3 I_7}{(I_3 + I_7 + I_6 + I_{13})^2} \qquad (8.4)$$

is the modulation ratio of the interference pattern at region A. Beams 6 and 13 act to erase the grating at region A. From experimental observations of the beam geometries within the crystal the self-pumped loop appears to originate from a point on beam 7 beyond region A, and thus beam 5 does not figure in Equation 8.4. A is a parameter which describes the depth of modulation of the refractive index grating. Similarly at region B

$$I_4 = \eta_B I_2 \qquad (8.5)$$

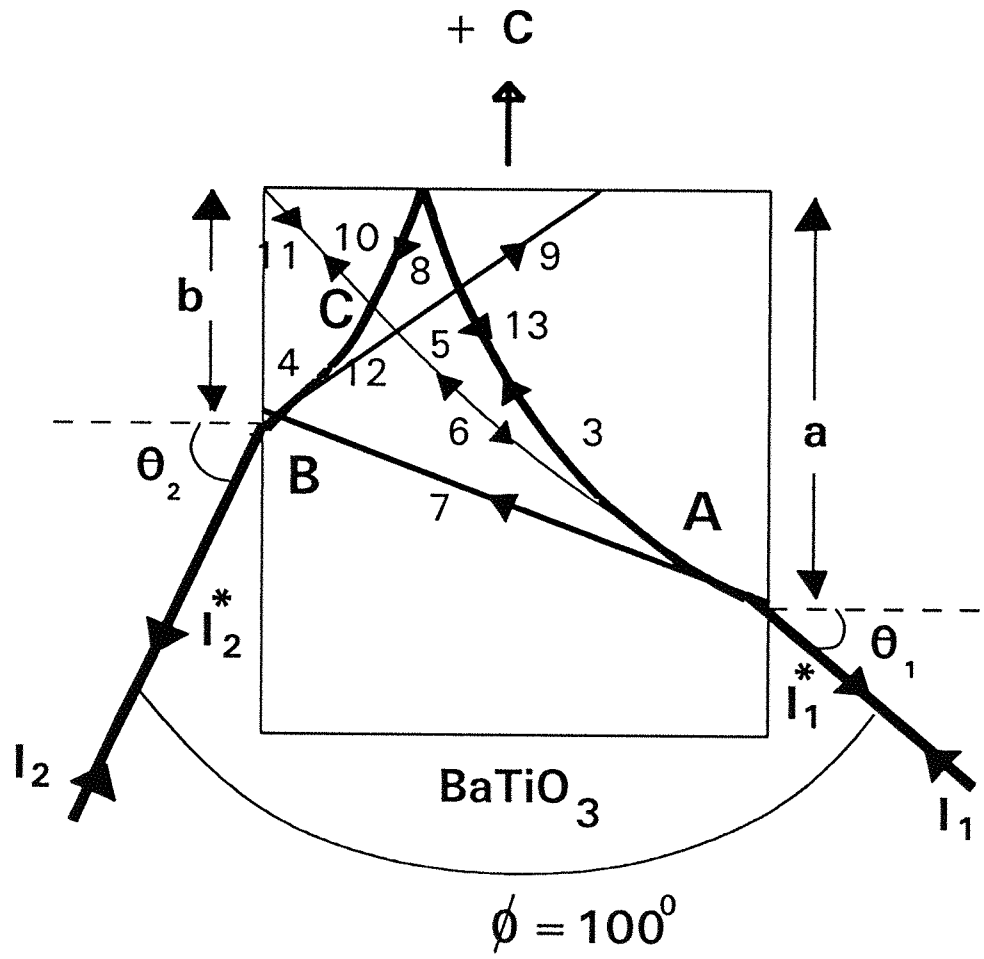

Figure 8.4 Schematic diagram of beam geometry with principle interaction regions and beam nomenclature.

$$I_9 = (1-\eta_B)\, I_2 \qquad (8.6)$$

where

$$\eta_B = B m_B^2 \qquad (8.7)$$

and

$$m_B^2 = \frac{4 I_4 I_9}{(I_4 + I_9 + I_{12})^2} \qquad (8.8)$$

The parameters A and B are used to allow the gratings to evolve exponentially in time according to

$$A = A_o\left[1-\exp\left[\frac{t'_A}{\tau_A}\right]\right] \qquad (8.9)$$

and

$$B = B_o\left[1-\exp\left[\frac{t'_B}{\tau_B}\right]\right] \qquad (8.10)$$

where τ_A and τ_B are the response times of the gratings written at regions A and B.

To allow the effects of erasure of the gratings to be included, t_A' and t_B' are the **effective grating times**, calculated as follows:

Consider the graph of Figure 8.5, which shows an exponentially increasing function. At time **t** an erase beam is turned on, reducing the value of m. The grating is continually trying to grow to its maximum efficiency (i.e., the efficiency in the absence of the erase beam), but is being prevented from doing so by the erase beam.

On each time step the effect of the erasing beams has to be considered both in terms of the reduction of the modulation ratio, and hence of the diffraction efficiency of each region, and also as a reversal of the effective time for which the grating has been growing, as though the grating were starting to grow again from time t-Δt, where

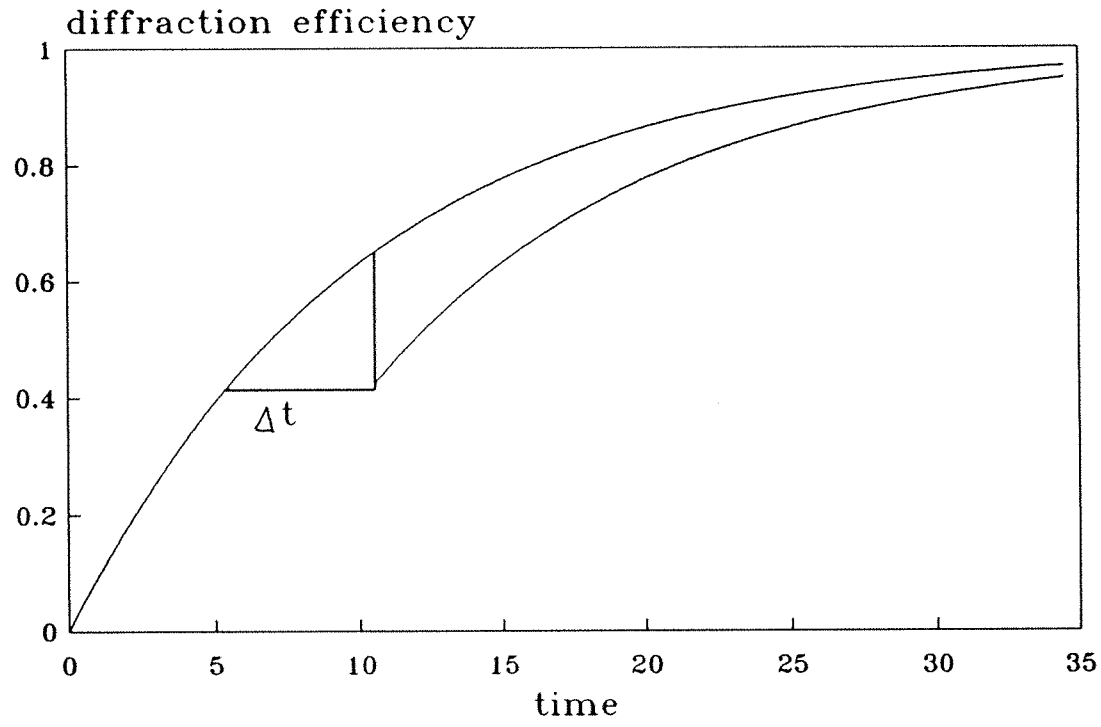

Figure 8.5 Shows the effect of erase beams on the diffraction efficiency of the photorefractive gratings.

$$t-\Delta t=t_A'=-\tau_A\left[\ln\left[1-\frac{m_A^2(t)}{m_A^2{}_{opt}}\right]\right] \qquad (8.11)$$

$$t-\Delta t=t_B'=-\tau_B\left[\ln\left[1-\frac{m_B^2(t)}{m_B^2{}_{opt}}\right]\right] \qquad (8.12)$$

where $m_{A\,opt}^2$, $m_{B\,opt}^2$ are the modulation ratios at regions A and B in the absence of the erasing beams

$$m_A^2{}_{opt}=\frac{4I_3I_7}{(I_3+I_7)^2} \qquad (8.13)$$

and

$$m_B^2{}_{opt}=\frac{4I_4I_9}{(I_4+I_9)^2} \qquad (8.14)$$

these calculations are carried out at the beginning of each time step.

Once the BWPC gratings at regions A and B have reached an arbitrarily set threshold diffraction efficiency, given by η_A or η_B = 0.4, the self-pumping beam I_5 builds exponentially according to

$$I_5=kI_1\left[1-\exp\left[\frac{t-t_{sp}}{\tau_{sp}}\right]\right] \qquad (8.15)$$

where k is a constant which defines the proportion of the input beam available to undergo self-pumping which, based loosely upon typical PC reflectivities obtained in SPPC configurations, is set at the value 0.4. t_{sp} is the time at which SPPC was initiated and τ_{sp} is the response time for SPPC.

At region C beams 5 and 8 undergo two beam coupling, with I_{10}, the beam travelling towards the corner of the crystal in the SPPC loop, being given by

$$I_{10}=\frac{I_8+I_5}{1+\frac{I_8}{I_5}\exp(-\Gamma L)}\left[1-\exp\frac{-(t-t_{sp})}{\tau_{sp}}\right] \qquad (8.16)$$

and I_{12}, travelling toward region B, by

$$I_{12}=\frac{I_8+I_5}{1+\frac{I_5}{I_8}\exp-\Gamma L}\left[1-\exp\frac{-(t-t_{sp})}{\tau_{tbc}}\right] \qquad ((8.17)$$

Considering the effects of diffraction from the grating at region C, I_6, the returning SPPC beam, is given by

$$I_6=(1-\eta_C)\,I_{10}+\eta_C\eta_B I_2 \qquad (8.18)$$

and I_{13}, the beam travelling toward region A, is given by

$$I_{13}=\eta_C I_{10}+(1-\eta_C)\,I_4 \qquad (8.19)$$

where η_C, the diffraction efficiency of the grating at region C, is given by

$$\eta_C=Cm_C^2 \qquad (8.20)$$

where

$$m_C^2=\frac{4I_8I_5}{(I_4+I_5+I_8+I_{10})^2} \qquad (8.21)$$

and

$$C=C_o\exp\left[\frac{t-t_{sp}}{\tau_{tbc}}\right] \qquad (8.22)$$

The system of Equations 8.1-8.22, was solved numerically for η_A and η_B using a fixed point interaction algorithm programmed into an IBM PC. at the beginning of each **time step**, i.e., incremented values of the time **t** in the program, the diffraction efficiencies are given a starting value from which the beam powers are calculated and hence used to recalculate η_A and η_B. These new values of η_A and η_B are then used to calculate the beam powers, and this process is repeated until η_A and η_B converge to a solution. The output beam powers $I_1^*(t)$, $I_2^*(t)$ are then calculated from

$$I_1^*(t)=\eta_A I_{13}+I_6 \qquad (8.23)$$

and

$$I_2^* = \eta_B I_{12} \qquad (8.24)$$

The condition for SPPC to occur is checked, i.e., whether or not η_A or η_B has exceeded the threshold value previously discussed, and once this condition is satisfied then the effects of the growth of the self-pumping beam, and the grating at region C, are included in the next time step.

Once the diffraction efficiencies η_A and η_B fall below an arbitrarily set threshold the system is returned to its initial state (i.e., the state at t=0) and the cycle repeated. In the absence of competition between BWPC and SPPC, the simulation produced the output shown in Figure 8.6, where the PC output is plotted as a function of time, using the parameter set $I_1 = I_2 = 1$, $\tau_A = \tau_B = 10$, $\tau_C = \tau_{sp} = 10^3$, $A_o = B_o = C_o = 0.8$.

The output grows exponentially to a steady state value, the symmetry in the parameters allowing the output powers to be equal. The introduction of an asymmetry in the input parameters, here by way of the beam powers, $I_2/I_1 = 0.5$, imposes an asymmetry on the output, (beam I_1 provides the light for I_2), as is shown in Figure 8.7. The introduction of competition between BWPC and SPPC produced periodic oscillations in the output from the simulation,as is illustrated in Figure 8.8, obtained using the input parameters $I_1 = I_2 = 1$, $\tau_A = \tau_B = \tau_C = 10$, $\tau_{sp} = 10$, $A_o = B_o = C_o = 0.8$.

Initially both beams show an exponential increase in output power. When I_1^* reaches ≈ 0.07 SPPC occurs for this beam. The onset of SPPC and the growth of the grating at region C results in the decrease of power travelling in the BWPC loop to region B, and hence the decay of the output from beam I_2^*. This decrease in the output is however accompanied by a decrease in the erasure of the grating at region B, (via the decrease of I_{12} in the denominator of Equation 8.8), and hence an increase in η_B, resulting in an increase in the power travelling to region A, increasing the erasure at region A, with a corresponding decrease in diffraction efficiency. The output from I_1^* continues to increase as the SPPC loop grows, but the depletion of the power in the BWPC loop results in a decrease in the light coupled into the SPPC loop at region C and the output begins to fall. The diffraction efficiency then fall

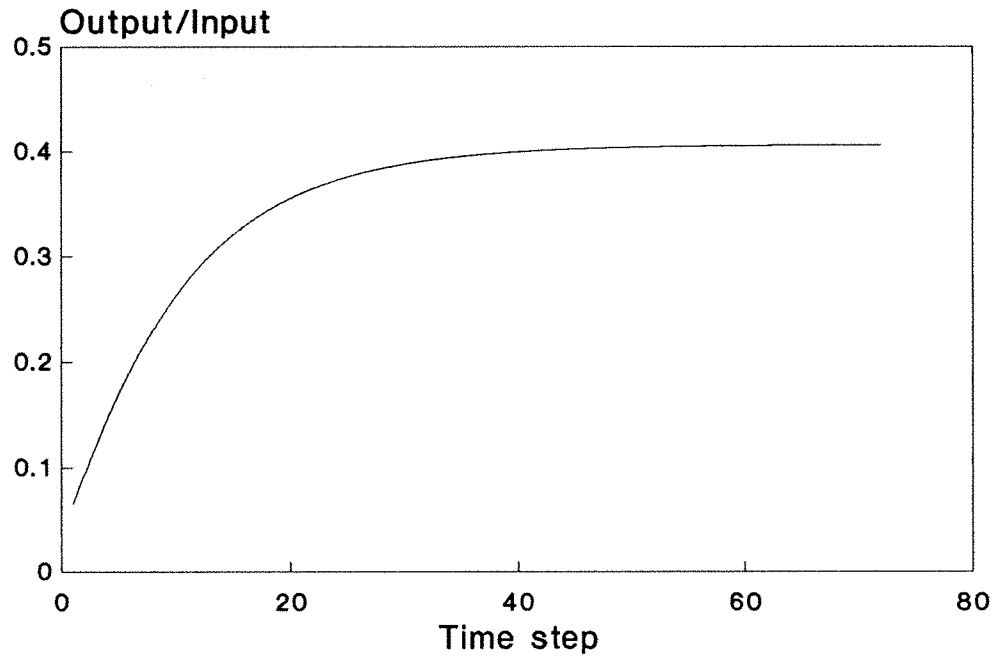

Figure 8.6 Simulation output in the absence of competition between BWPC and SPPC.

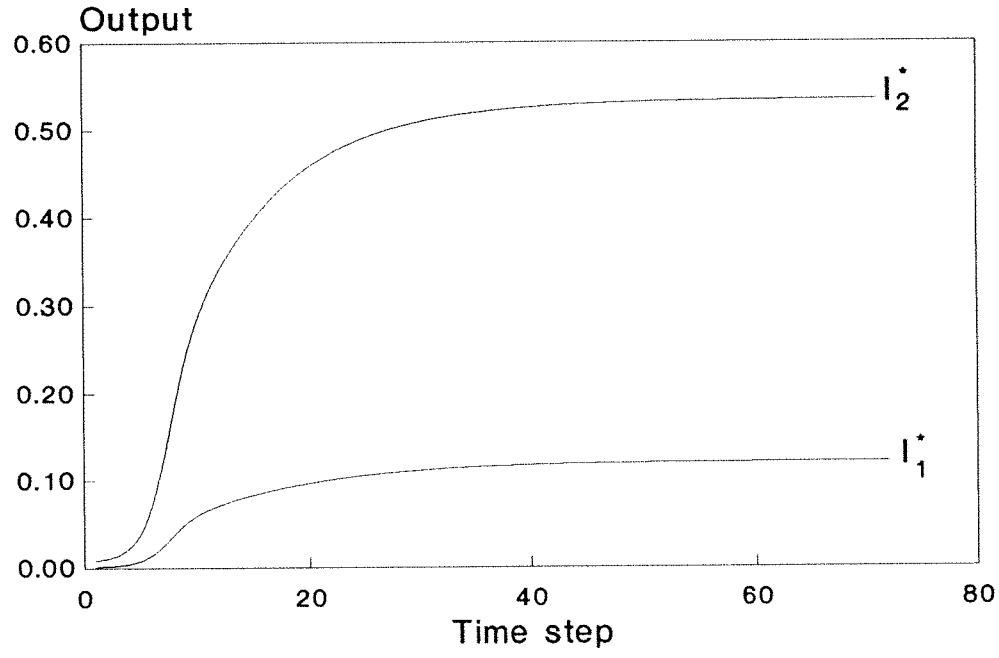

Figure 8.7 Simulation results shows output in the absence of competition between BWPC and SPPC.

below threshold, and the program is restarted. It should be noted that there is a phase shift between the peaks of the oscillations for the two outputs, since the onset of SPPC depletes the output from beam I_2^*, but increases the output from I_1^*.

An experimental parameter which seemed to play a significant role in determining the behaviour of the output was the position of the un-diffracted portion of I_1, i.e., I_7, relative to region B. A parameter was introduced to the simulation which modified the contribution of I_7 to the total power incident on region B, thus controlling its erasing effect at this region. It was found that, in the absence of competition between BWPC and SPPC, this did not result in oscillations in the output. It was observed experimentally that the frequency of oscillation was dependent upon the input intensity. This might be expected as the grating response time scales approximately inversely with the intensity. In this simulation there was no intensity dependence of the response time, and thus this property of the oscillation was not predicted.

The model shows qualitative agreement with the experimental observations in that oscillations were obtained in the output from the simulation, and that there is a phase shift between the output, although this is different from the experimentally observed 180°. However variation of the input beam intensity ratio in the model showed no effect upon the frequency of the oscillations, an effect which was observed experimentally.

The simulation described was based upon the observation of beam patterns within the crystal during a typical oscillation cycle. Both the BWPC and SPPC interaction have been shown to possess well defined gain-interaction length products, and thus the inclusion of threshold diffraction efficiencies at the interaction regions is a valid step. The simulation while neglecting absorption and the effect of intensity dependent response times, does demonstrate that the presence of competing processes and gratings may result in fluctuations in the PC output from a two interaction region conjugator, such as the BWPC.

While the model does show qualitative agreement with the experimental results, it clearly has its limitations. These stem mainly from the assumption that the grating

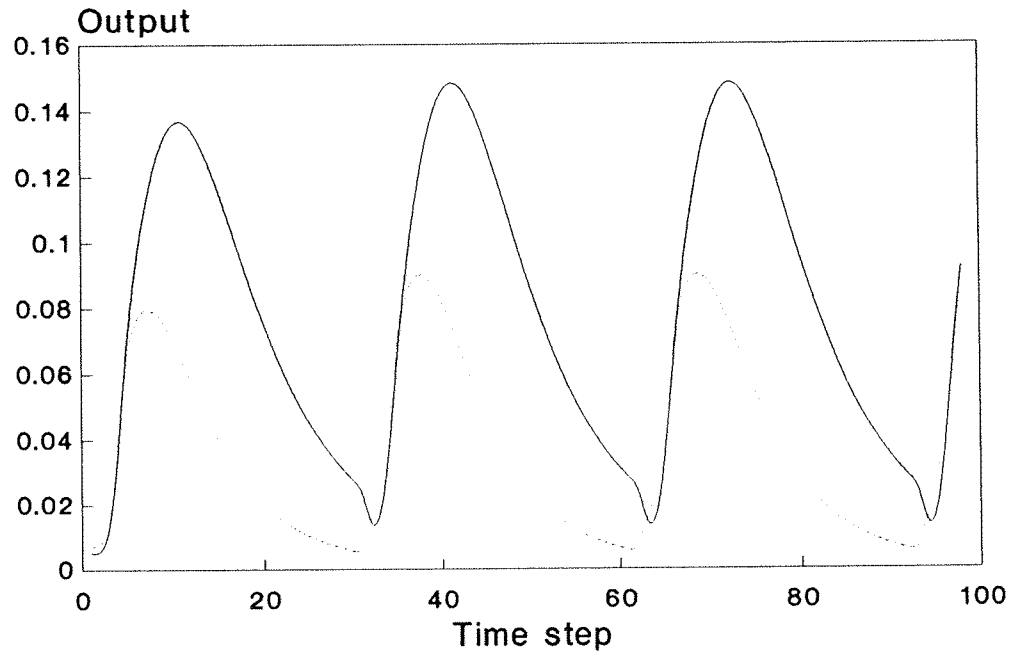

Figure 8.8 Simulation results illustrate in the presence of competition between BWPC and SPPC. Solid line: I_1^*, dashed line: I_2^*.

response times are independent of the intensity. The method used here for modelling this complex system was chosen in preference to solving the differential equations which govern the system since it offers greater insight into the mechanisms responsible for the oscillations via comparison with the experimental observation of beam configurations during an oscillation cycle.

8.5 Experimental Results

Figure 8.9, shows the experimental arrangement, which used an Ar^+ laser operating in multi-longitudinal mode at λ = 514.5 nm and a single-domain crystal of $BaTiO_3$ of dimensions 6 x 6 x 6 mm^3. The laser output was spatially filtered and divided by beam splitter BS_1 into two beams of similar intensities. These beams, reflected and transmitted by BS_1, were incident upon opposite faces of the $BaTiO_3$ crystal to form a BWPC loop. The path length between the two beams I_1 and I_2 was arranged to be $\approx$ 1.5 m to ensure mutual incoherence. Beam splitters BS_2 and BS_3 were used to monitor the simultaneous phase conjugate outputs, I_1^* and I_2^*. The input angles were $\theta_1 = 25°$ and $\theta_2 = 55°$ (measured outside the crystal). Both input beams were *e* polarised to ensure maximum coupling strength.

Figure 8.10, shows a typical trace obtained when the parameters (as defined in Figure 8.4) were set at a = 3.8 mm, b = 3.5 mm, I_1 = 4.5 mW, I_2 = 1.5 mW, i.e., a beam intensity ratio of $r = I_1/I_2 = 3$. It can be seen from the inset photograph that beam I_7 was directed at region B and hence strongly erased the fanning grating at that region. This prevented the BWPC loop formation. However, SPPM configurations from beam I_1 did occur, although the output was highly unstable. This may be explained as follows: The SPPM grating that formed resulted in reduced power in beam I_7. This permitted beam I_4 to grow, promoting erasure of the SPPCM grating at region C, thus leading to a minimum in the monitored output. This in turn led to increased power in I_7, and the cycle repeated. The maximum reflectivity in this case was low, $\approx$1%, and the fluctuations were not particularly regular (the average period was 13 $\pm$ 4 sec).

Figure 8.11 shows the traces obtained when parameter **a** was reduced to 3.6 mm, with **b** and r as before. It was observed here that the BWPC loop developed first in

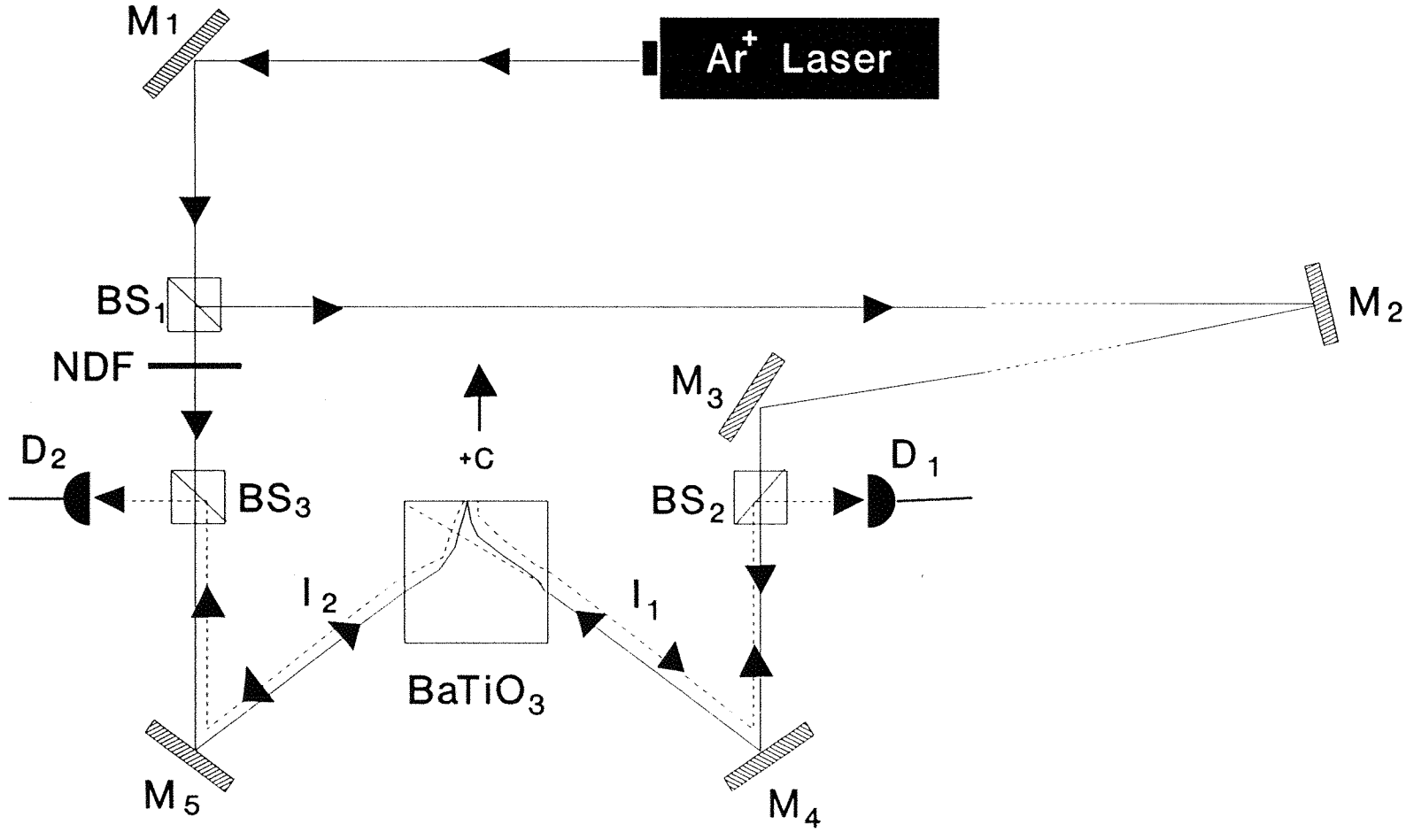

Figure 8.9 Experimental arrangement used to observe dynamic instabilities in the mutually pumped BWPC. M_1 - M_5 are mirrors; SF, spatial filters; ND, variable neutral-density filter; D_1, D_2, photodiodes.

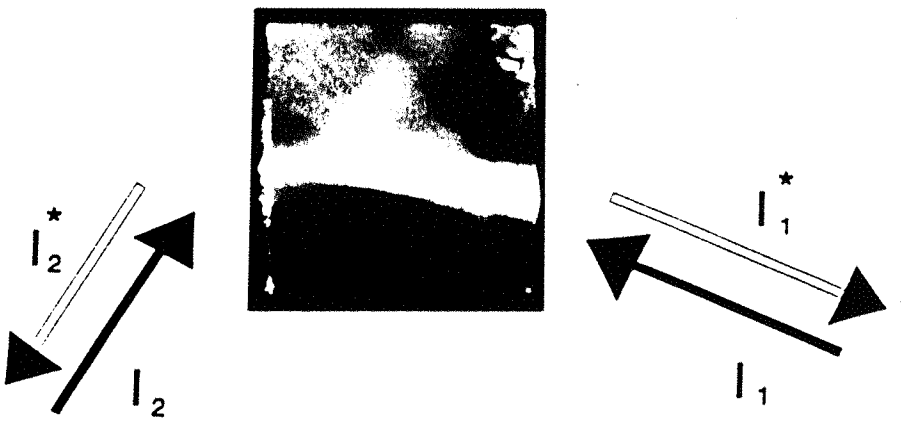

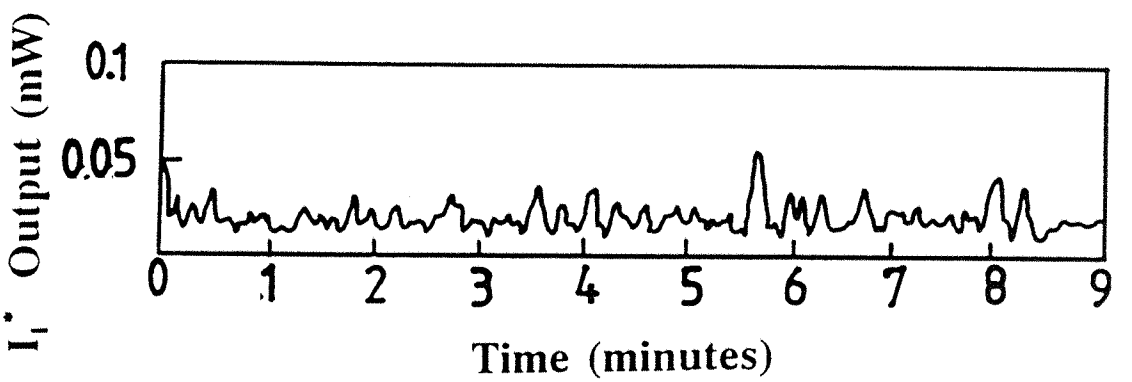

Figure 8.10 Phase conjugate output obtained with parameters a = 3.8 mm, b = 3.5 mm, I_1 = 4.5 mW, I_2 = 1.5 mW.

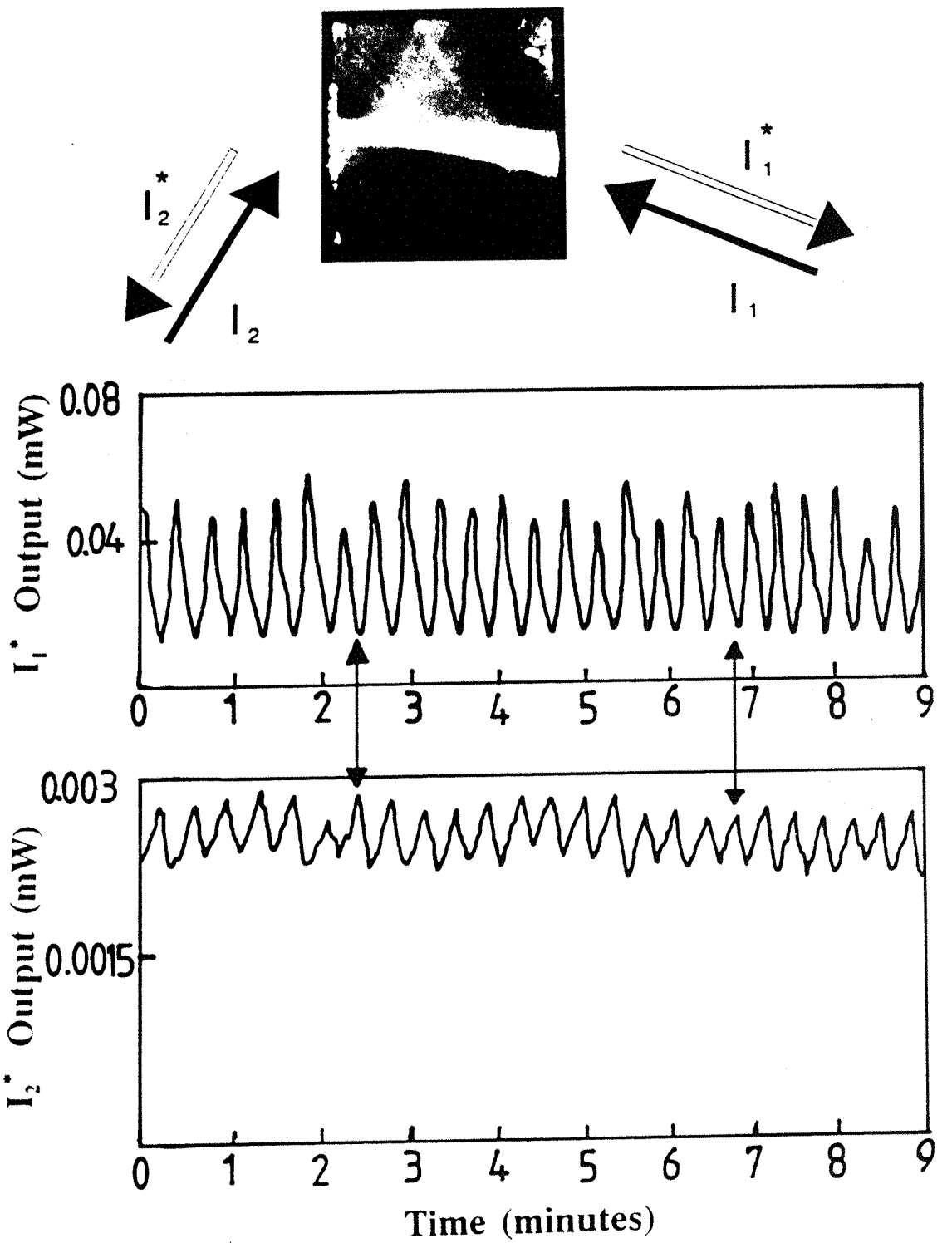

Figure 8.11 Periodic oscillations obtained with a = 3.6 mm, b = 3.5 mm, I_1 = 4.5 mW, I_2 = 1.5 mW.

this case. Subsequently energy transfer between fanned light and light circulating within the BWPC loop occurred as a result of TBC in region C. When the SPPCM loop reached its highest level, beams I_3 and I_7 were at their lowest; consequently m_B was at its maximum. This resulted in more light being incident upon region A, reducing m_A, thus causing erasure at C and the subsequent decay of SPPCM. The cycle then repeated.

With this particular parameter set, the oscillation cycle resulted in stable periodic pulsations. The average period of the oscillation of I_1^* was 21 ± 0.7 sec. The maximum reflectivity measured from the highest peak was again low, ≈1%. Beams I_1^* and I^*_2 are almost 180° out of phase. This is the result of the nature of the sequential formation of BWPC and SPPCM processes.

Figure 8.12 show the situation in which parameter *a* is reduced further to 3.2 mm (all other parameters remaining unchanged), causing region B to be shifted upward. In this arrangement we observed an overall increase in reflectivity from the BWPC loop. SPPCM configurations were not observed here, which may be because of the dominant presence of the BWPC loop, causing less fanned light to be available for SPPCM formation.

Finally, Figure 8.13, shows the output traces with the same beam configuration as that used in Figure 6 but with the beam intensities I_1 = 5.0 mW, I_2 = 3.4 mW, and r = 1.5. With this intensity ratio, beam I_2 formed stronger fanning gratings, and therefore a strong BWPC was observed. However, self-pumping never became significant, and therefore we did not observe any competition between the two processes. It is observable in Figure 8.13, that small perturbations may be present because of SPPCM competition, but these do not lead to oscillations as in Figure 8.11.

8.6 Conclusion

In this chapter we have discussed experimental observations and suggested the origins of oscillations in the BWPC. A phenomenological model, which is based upon the observation of beam patterns for an oscillation cycle, has been developed to

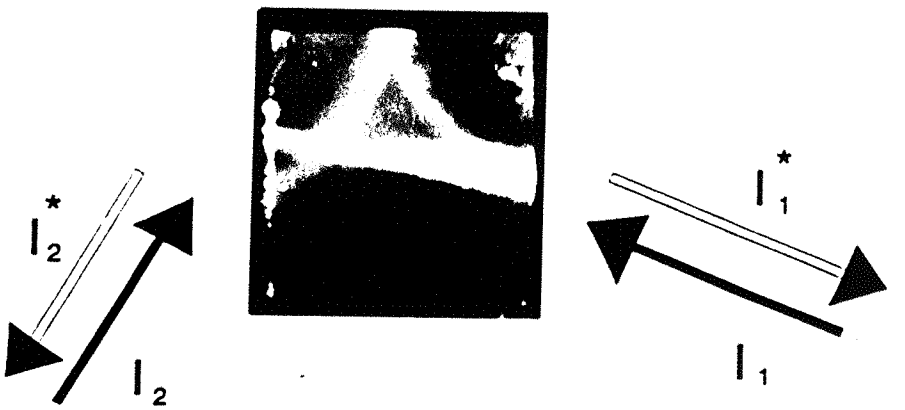

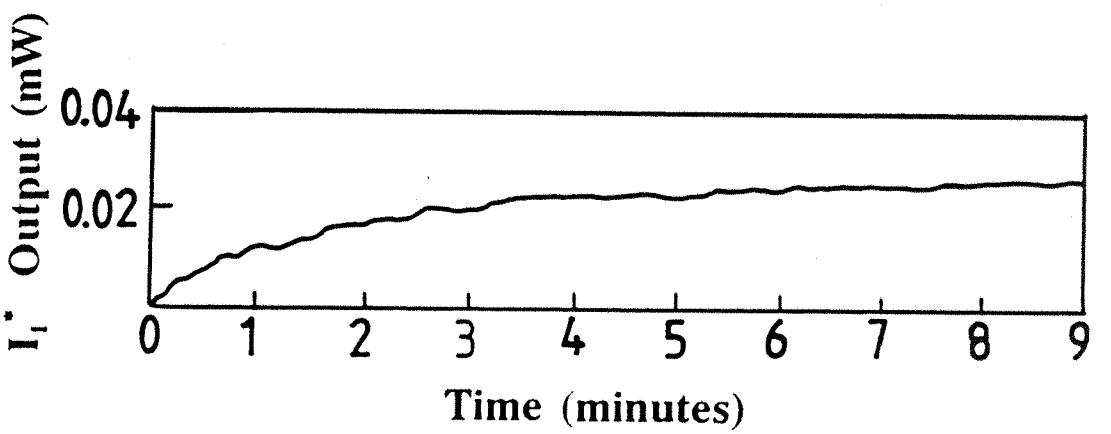

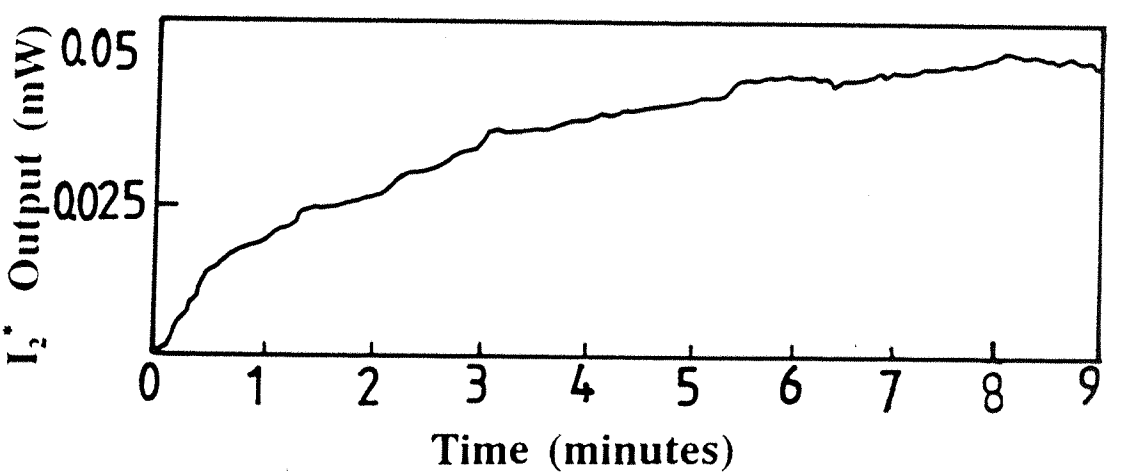

Figure 8.12 Outputs obtained with a = 3.2 mm and other parameters same as in Figure 8.11.

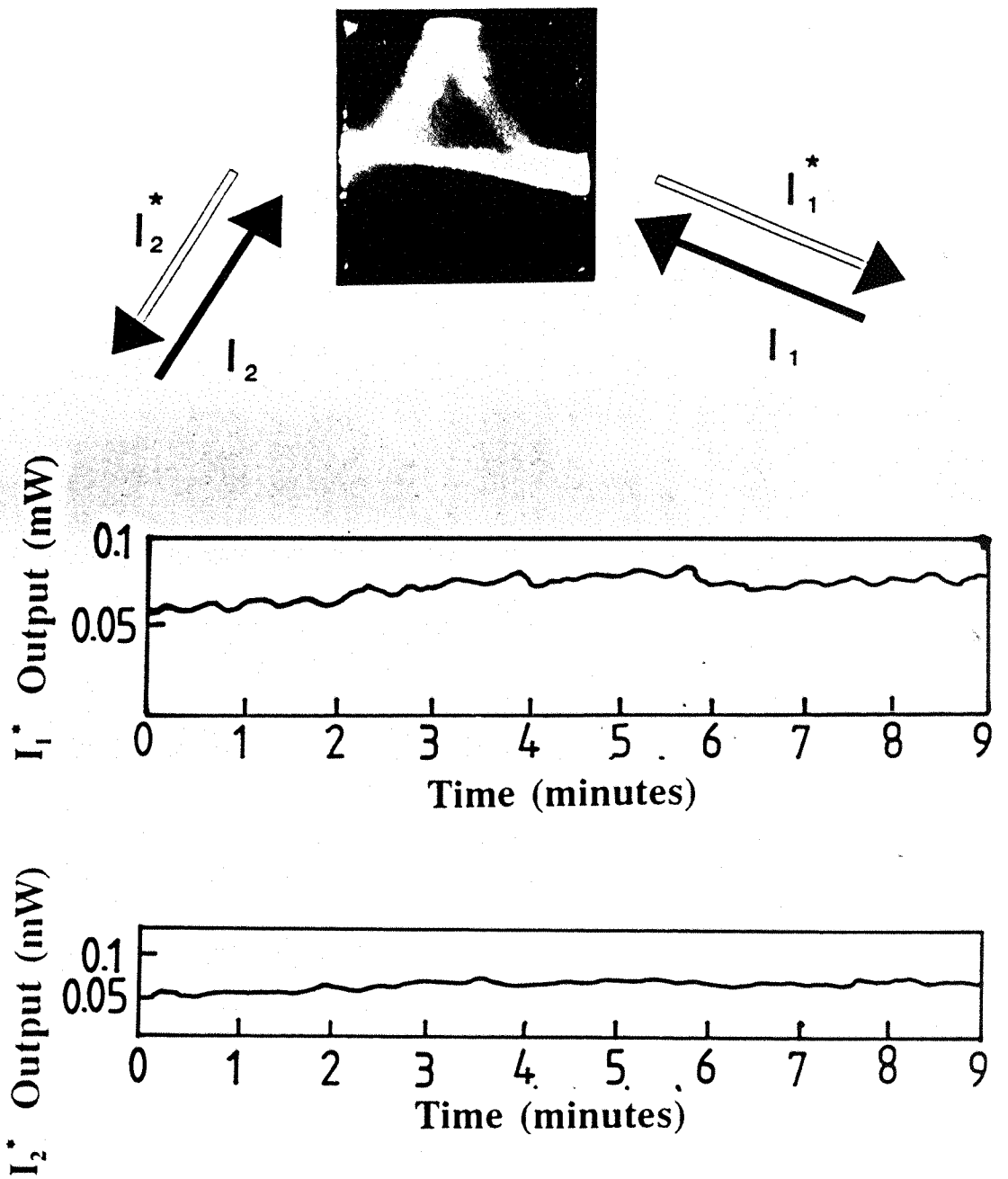

Figure 8.13 Output traces at beam intensity ratio $r = I_1/I_2 = 1.5$ and other parameters as in Figure 8.11.

explain the oscillations in the output from the BWPC. The model predicts the presence of competition between the SPPC and BWPC which gives rise to fluctuations in the PC outputs. The model does predict a phase shift, but not the 180^0 phase shift that exists between the oscillations in the two PC outputs, as have been observed experimentally.

Experimental results showed a dependence of the frequency of oscillation upon r. However this is not reflected by the model which showed no dependence upon **r.** This is because the grating response times in the model had no dependence upon intensity. The other experimental observation is that the position of the un-diffracted portion of beam I_1, on the interaction region B, has a significant effect upon the form of the observed fluctuations. The model does not result in oscillatory output if this parameter is included in the absence of competition. Despite all these deficiencies in the model, it is successful in predicting that the presence of competition between the BWPC and SPPC results in oscillations in the PC outputs.

REFERENCES

8.1 P. Gunter, E. Voit and M. Z. Zha, "Self-pulsation and optical chaos in self-pumped photorefractive $BaTiO_3$", Opt.Commun. **55**, 210 (1985).

8.2 A. M. C. Smout, R. W. Eason and M. C. Gower, "Regular oscillations and self-pulsating in self-pumped $BaTiO_3$" Opt. Commun. **59**, 77 (1986).

8.3 S. Sternklar, S. Weiss, M. Segev and B. Fischer, "Beam coupling and locking of lasers using photorefractive four-wave mixing", Opt. Lett. **11**, 528 (1986).

8.4 S. Weiss, S. Sternklar and B. Fischer, "Double phase-conjugate mirror: analysis, demonstration, and applications", Opt. Lett. **12**, 114 (1987).

8.5 B. Fischer, S. Weiss and S. Sternklar, "Spatial light modulation and filtering effects in photorefractive wave mixing", Appl. Phys. Lett. **50**, 483 (1987).

8.6 S. Weiss, O. Werner and B. Fischer, "Analysis of coupled photorefractive wave mixing junctions", Opt. Lett. **14**, 186 (1989).

8.7 M. D. Ewbank, "Mechanism for photorefractive phase conjugation using incoherent beams", Opt. Lett. **13**, 47 (1988).

8.8 M. D. Ewbank, R. A. Vazquez, R. R. Neurgaonkar, "Mutually pumped phase conjugation in photorefractive Strontium Barium Niobate: theory and experiment", J. Opt. Soc. Am. B, **7**, 2306 (1990).

8.9 P. Ye, D. Wang, Z. Zhang, "Self-pulsating and moving fringe-patterns in the outputs of a mutually-pumped $BaTiO_3$", Topical meeting on Photorefractive materials, Effects and Devices, Jan. 17-19, Aussois, France (1990).

8.10 D. Wang, Z. Zhang, Y. Zhu, S. Zang and P. Ye, " Observations on the coupling channel of two mutually incoherent beams without internal reflection in $BaTiO_3$", Opt. Commun. **73**, 495 (1989).

8.11 A. M. C. Smout and R. W. Eason, "Analysis of mutually incoherent beam coupling in $BaTiO_3$", Opt. Lett. **12**, 498 (1987).

8.12 G. Hussain, Stephen W. James, R. W. Eason, "Observation and modelling of dynamic instabilities in the mutually pumped bird-wing phase conjugator in $BaTiO_3$", J. Opt. Soc. Am. B **7**, 2294 (1990).

Conclusion

In this thesis I have presented various techniques for optical signal processing using photorefractive BSO and $BaTiO_3$, for contrast manipulation of optical images, optical motion detection and parallel optical logic operations. I also present the results for dynamic instabilities in photorefractive $BaTiO_3$.

Chapter 1 has briefly reviewed the various relevant aspects of the photorefractive effect, optical phase conjugation, and its applications.

In Chapter 2 we demonstrated two techniques of contrast manipulation which exploit the DFWM configuration in a BSO crystal. The first technique exploits the diffraction efficiency characteristics of volume phase holograms for contrast manipulation. Real time Fourier transform holograms have been recorded in the photorefractive crystal, whose diffraction efficiency is controlled by varying the beam intensity ratio by moving the spatial position of the Fourier transform (outside the crystal). Experimental results that we have achieved were not optimum due to the edge enhancement which caused a reduction in the overall illumination.

The problem of reduced background illumination was overcome in the second technique which is based upon a multiplexed DFWM arrangement. This technique mainly records and reads two gratings, one for the DC and the other for all the higher Fourier orders. The control of the diffraction efficiency of the two gratings gives higher background illumination as well as higher contrast of the spatial features. Therefore this technique may be easily implemented to improve the contrast. Experimental results for a binary object, a resolution test chart, have been reported which demonstrate that this principle can be applied for contrast manipulation of grey level objects.

Contrast manipulation via two beam coupling in $BaTiO_3$ was reported in Chapter 3, to achieve contrast enhancement, feature extraction, defect enhancement and contrast reversal. Using gain manipulation, various orders experience controllable gain. However the resolution of the output image may be is reduced, due to the limited spatial band width product, and Gaussian nature of the intensity profile of

the interfering beams.

The contrast manipulation techniques described in Chapter 4 are flexible and versatile due to their Fourier transform polarization encoding character which make these techniques unique from other reported contrast manipulation techniques. The techniques described in Section 4.3 of that chapter has applications in the field of phase contrast imaging, study of wind tunnel aerodynamics and possibly several others. The other two Sections 4.2.2 and 4.2.3 deals with contrast manipulation techniques in combination with DFWM and TBC. These two techniques may lead to some useful applications in the field of contrast manipulation of amplitude as well as phase objects.

In Chapter 5 motion detection via multiplexed DFWM has been demonstrated which exploits the differential response time of grating formation in the two arms of a PCMI. This feature allows tunability in the velocity filtering and can also process amplitude as well as phase objects.

The other technique of motion detection which has the characteristic of velocity filtering has been presented in Chapter 6. This technique exploits the recording of complementary gratings which in static case gives no output image. In the case of motion, one of the gratings may be stronger than the other and therefore gives a net output in the form of a moving object of a particular dimension among the different dimensional features. A comparison between the experimental and simulated results is presented which shows good qualitative agreement. Therefore this technique may be used for feature extraction applications.

Chapter 7 described a technique of optical logic on two variables using one or two PCMI in cascaded form. Multiple signal beams with a single reference beam here used to record multiplexed gratings in a single crystal of BSO. The reference beam from a self-pumped $BaTiO_3$ crystal simultaneously reads these gratings. Logic output is achieved via changing the polarizations of the two phase conjugate beams with specific phase shifts between them.

Complete subtraction was achieved when the PCMI was working in polarization

preserving mode. Varying degrees of interference were obtained when the (relative) polarization of the phase conjugate beams were rotated. Various improvements have also been proposed to improve this technique. We think that these optical logic gate techniques can provide the possibility to implement a large number of gates in parallel and may be further improved with the development of nonlinear crystal materials with higher gain and shorter response times.

In Chapter 8 experimental observations of oscillations in the BWPC have been discussed and a phenomenological model used, which is based upon the observation of beam patterns for an oscillation cycle. The model predicts the presence of competitions between the SPPC and BWPC. However the model does not predict all of detailed features of the experimental phase conjugate output, such as the phase shift behaviour observed.

Appendix A: Fourier Transforming Properties of Lens

The lens is one of the important components in any optical data processing system. When a plane wave incident normally on the front surface of a lens it will be transformed behind the lens into*,

$$U_L(x,y) = \exp[jkn\Delta_o] \exp\left[\frac{-jk}{2f}(x^2+y^2)\right] \qquad (1)$$

Where Δ_o is maximum thickness of the lens and **n** is the index of refraction of the lens. The first term is a constant path delay while the next term is a quadratic approximation to a spherical wave. If the focal length **f** is positive then the spherical wave will converge.

A converging lens is capable of transforming an input image into its two dimensional Fourier transform and therefore it can be considered as an optical processor. Consider an object which is placed at a distance d_o in front of the lens and is uniformly illuminated by a normally incident monochromatic plane wave of amplitude A. The field distribution at the back focal plane of the lens is given by

$$U_f(x_f,y_f) = \frac{A\exp\left[j\frac{k}{2f}\left(1-\frac{d_o}{f}\right)(x_f^2+y_f^2)\right]}{j\lambda f} \times$$

$$\int_{-\infty}^{\infty}\int t_o(x_o,y_o) \exp\left[-j\frac{2\pi}{\lambda} f(x_o x_f + y_o y_f)\right] dx_o dy_o \qquad (2)$$

where $t_o(x_o, y_o)$ is the amplitude transmittance of the object. In the above expression the phase factor will vanish if the object is placed in the front focal plane of the lens i.e., $d_o = f$ and expression (2) is simplified to give Fourier transform of the input light distribution.

Appendix B: THE COUPLED WAVE ANALYSIS FOR A DYNAMIC MEDIUM

Consider an electric field E, which is composed of the fields of incident reference and signal waves,

$$E = [R(x)\exp[i(wt - \varrho.r + \phi_R(x))] + S(x)\exp[i(wt - \sigma.s + \phi_s(x))]]\hat{e} \quad \text{(B.1)}$$

where ϱ and σ are reference beam and signal beam wavevectors respectively, and $\hat{e}$ is the polarization unit vector. We wish to solve the wave equation for a dynamic medium

$$\nabla^2 E - \frac{1}{c^2}\frac{\partial^2 (n^2 E)}{\partial t^2} - \mu\mu_o\sigma_e\frac{\partial E}{\partial t} = 0 \quad \text{(B.2)}$$

where c is velocity of light, μ is relative permeability and μ_o and is permeability of free space.

If we consider the amplitude and phase terms to be time independent i.e, R(x), S(x), $\phi_R(x)$ and $\phi_s(x)$ and the refractive index profile within the dynamic medium approximated by

$$n = n_o + n_{DC}(x) + n_c(x)\cos\boldsymbol{k}.\boldsymbol{r} + n_s(x)\sin\boldsymbol{k}.\boldsymbol{r} \quad \text{(B.3)}$$

where n_o is bulk ordinary refractive index, n_{DC}, n_c and n_s are the DC and fundamental components of the refractive index change respectively and we are also considering these to be time independent. Only the fundamental Fourier components have been considered and rearranged to give

$$n = n_o(1+\delta) + \Delta n(x)\cos(\boldsymbol{k}.\boldsymbol{r} + \phi(x)) \quad \text{(B.4)}$$

where δ is the ratio of n_{DC} to n_o. An approximate expression for n^2 can be derived as follows

$$\begin{aligned} n^2 &= n^2{}_o(1+\delta)^2 + 2n_o(1+\delta)\Delta n(x)\cos(\boldsymbol{k}.\boldsymbol{r} + \phi(x)) \\ &\quad + \delta^2\cos(\boldsymbol{k}.\boldsymbol{r} + \phi(x)) \\ &\approx n^2{}_o(1+2\delta) + 2n_o\,\Delta n\cos(\boldsymbol{k}.\boldsymbol{r} + \phi(x)) \end{aligned} \quad \text{(B.5)}$$

Taking the first and second derivatives of E with respect to time for Equation (B.2), gives

$$\frac{\partial E}{\partial t} = i\omega E \qquad)$$

$$\frac{\partial^2(n^2E)}{\partial t^2} = n^2\frac{\partial^2 E}{\partial t^2} = -\omega^2 n^2 E \qquad \textbf{(B.7)}$$

Further

$$\nabla^2 E = \frac{\partial^2 E}{\partial x^2} + \frac{\partial^2 E}{\partial Y^2} + \frac{\partial E^2}{\partial z^2} \qquad \textbf{(B.8)}$$

$$= \frac{\partial}{\partial x}\{[\frac{\partial R}{\partial x} + iR(-\rho_x + \frac{\partial \phi_R}{\partial x})]\exp[i(wt - \rho.r + \phi_R)]\} \qquad \textbf{(B.9)}$$
$$-(\rho^2{}_y + \rho^2{}_z)R\exp[i(wt - \rho.r + \Phi_R)] + F(s)$$

$$\begin{aligned} &= \frac{\partial^2 R}{\partial x^2} + i\frac{\partial R}{\partial x}(-\rho_x + \frac{\partial \phi_R}{\partial x}) \\ &- i\rho_x[\frac{\partial R}{\partial x} + iR(-\rho_x + \frac{\partial \phi_R}{\partial x})] \\ &+ i[(\frac{\partial R}{\partial x}\frac{\partial \phi_R}{\partial x} + R\frac{\partial^2 \phi_R}{\partial x^2}) + iR\frac{\partial \phi_R}{\partial x}(-\rho_x + \frac{\partial \phi_R}{\partial x})] \\ &.\exp[i(\omega t - \rho.r + \phi_R)] \\ &-(\rho^2{}_y + \rho^2{}_z)R\exp[i(wt - \rho.r + \phi_R)] + F(s) \end{aligned} \qquad \textbf{(B.10)}$$

However for the limiting case of the slowly varying amplitude approximation and phase we can approximates as follows

$$\frac{\partial^2 R}{\partial x^2} \sim 0, \frac{\partial^2 \phi_R}{\partial x^2} \sim 0, (\frac{\partial \phi_R}{\partial x})^2 \sim 0, \frac{\partial R}{\partial X}\frac{\partial \phi_R}{\partial x} \sim 0 \qquad \textbf{(B.11)}$$

This enable us to simplify Equation (B.10), as follows
Now the wave equation becomes of the form
where α is absorption coefficient and r is beam intensity ratio. Here we neglect the terms which violate the Bragg condition i.e., exp [-i((2ρ - σ).r)] and exp [i((ρ - 2σ.r], which violate the Bragg condition, have been neglected.

Appendix B:

$$\nabla^2 E = \{-i2\rho_x \frac{\partial R}{\partial x} - |\rho|^2 R + 2\rho_x R \frac{\partial \phi_R}{\partial x}\} \exp[i(\omega t - \rho.r + \phi_R)] + \{-i2\sigma_z \frac{\partial S}{\partial x} - |\sigma|^2 S + 2\sigma_x S \frac{\partial \phi_S}{\partial x}\} \exp[i(\omega t - \sigma.r + \phi_S)] \quad \textbf{(B.12)}$$

$$\begin{aligned}
&\{-i2\rho_x \frac{\partial R}{\partial x} - |\rho|^2 R + 2\rho_x R \frac{\partial \phi_R}{\partial x}\} \exp[i(\omega t - \rho.r + \phi_R)] \\
&+\{-i2\sigma_x \frac{\partial S}{\partial x} - |\sigma|^2 S + 2\sigma_x R \frac{\partial \phi_S}{\partial x}\} \exp[i(\omega t - \sigma.r + \phi_S)] \\
&+\{\frac{\omega^2}{c^2} n_o^2 (1 + 2\delta) - i\mu\mu_o\sigma_e\omega\}.(R\exp[i(\omega t - \rho.r + \phi_R)] + S\exp[i(\omega t - \sigma.r + \phi_S)]) \\
&+\frac{\omega^2}{c^2} n_o^2 (1 + \delta)\Delta n \\
&.(\exp[i((\rho - \sigma).r + \phi)] + \exp[-i((\rho - \sigma).r + \phi)]) \\
&.(R\exp[i(\omega t - \sigma.r + \phi_R)] + S\exp[i(wt - \sigma.r + \phi_S)]) \\
&= 0
\end{aligned} \quad \textbf{(B.13)}$$

$$\begin{aligned}
&\{-i2\rho_x \frac{\partial R}{\partial x} - |\rho|^2 R + 2\rho_x R \frac{\partial \phi_R}{\partial x}\} \exp[i(-\rho.r + \phi_R)] \\
&+\{-i2\sigma_x \frac{\partial S}{\partial x} - |\sigma|^2 S + 2\sigma_x R \frac{\partial \phi_S}{\partial x}\} \exp[i(-\sigma.r + \phi_S)] \\
&+(r^2 + r^2 2\delta - i\alpha r) \\
&.(R\exp[i(-\rho.r + \phi_R)] S\exp[i(-\sigma.r + \phi_S)]) \\
&+r\frac{2\pi}{\lambda}(1 + \delta)\Delta n \\
&.(R\exp[i(-\sigma.r + \phi + \phi_R)] S\exp[i(-\sigma.r - \phi + \phi_S)]) \\
&= o
\end{aligned} \quad \textbf{(B.14)}$$

Equating the coefficients of exp [i(-ρ.r)] and exp [i(-σ.r)] yields

$$\begin{aligned}
&\{-i2\rho_x \frac{\partial R}{\partial x} - |\rho|^2 R + 2\rho_x R \frac{\partial \phi_R}{\partial x}\} \exp(i\phi_R) \\
&+(r^2 + r^2 2\delta - i\alpha r) R\exp(i\phi_R) \\
&+r\frac{2\pi}{\lambda}(1 + \delta)\Delta n S\exp[i(\phi_S - \phi)] \\
&= 0
\end{aligned} \quad \textbf{(B.15)}$$

Rearrangement of Equation (B.15), gives

$$\begin{aligned}&\{-i2\sigma_x\frac{\partial S}{\partial x}-|\sigma|^2R+2\,\sigma_x S\frac{\partial\phi_S}{\partial x}\}\exp[i\phi_S]\\&+(r^2+r^2 2\delta-i\alpha r)S\exp[i\phi_s]\\&+r\frac{2\pi}{\lambda}(1+\delta)\Delta n\,R\exp[i(\phi_R+\phi)]\\&=0\end{aligned}\tag{B.16}$$

$$\begin{aligned}&-i2\rho_x\frac{\partial R}{\partial x}+2\rho_x R\frac{\partial\phi_R}{\partial x}\\&+(r^2 2\delta-i\alpha r)R\\&+r\frac{2\pi}{\lambda}(1+\delta)\Delta n\,S\exp[i(\phi_S-\phi-\phi_R)]\\&=0\end{aligned}\tag{B.17}$$

$$\begin{aligned}&-i\cos\theta\frac{\partial R}{\partial x}+\cos\theta\,R\frac{\partial\phi_R}{\partial x}+(r\delta-i\frac{\alpha}{2})R\\&+\frac{\pi}{\lambda}\Delta n\,S\exp[-i(\phi_R-\phi_S+\phi)]\\&=0\end{aligned}\tag{B.18}$$

$$\begin{aligned}&\cos\theta\frac{\partial R}{\partial x}+iR\cos\theta\,R\frac{\partial\phi_R}{\partial x}+(\frac{\alpha}{2}+ir\delta)R\\&+\frac{\pi}{\lambda}\Delta n\,S\exp[-i(\phi_R-\phi_S+\phi)]\\&=0\end{aligned}\tag{B.19}$$

$$\begin{aligned}&\frac{\partial R}{\partial x}+iR\frac{\partial\phi_R}{\partial x}+(\frac{\alpha}{2\cos\theta}+i\frac{\delta}{\cos\theta})R\\&+i\frac{\pi}{\lambda\cos\theta}\Delta n\,S\exp[-i(\phi_R-\phi_S+\phi)]\\&=0\end{aligned}\tag{B.20}$$

Similarly we can achieve for S

The amplitudes R and S are not complex as the intrinsic phase terms ϕ_R and ϕ_S have been expressed explicitly. Thus we have coupled wave equations containing both real

Appendix B:

$$\frac{\partial S}{\partial x} + iS\frac{\partial \phi_S}{\partial x} + \left(\frac{\alpha}{2\cos\theta} + i\frac{r\delta}{\cos\theta}\right)S + i\frac{\pi}{\lambda\cos\theta}\Delta n\, R\exp[+i(\phi_R - \phi_s + \phi)] = 0 \qquad \textbf{(B.21)}$$

and imaginary terms. Therefore equating real and imaginary terms yields

Real

$$\frac{\partial R}{\partial x} + \frac{\alpha}{2\cos\theta}R + \frac{\pi}{\lambda\cos\theta}\Delta n\, S\sin\Phi = 0 \qquad \textbf{(B.22)}$$

$$\frac{\partial S}{\partial x} + \frac{\alpha}{2\cos\theta}S + \frac{\pi}{\lambda\cos\theta}\Delta n\, R\sin\Phi = 0 \qquad \textbf{(B.23)}$$

Imaginary

$$R\frac{\partial \phi_R}{\partial x} + \frac{r\delta}{\cos\theta}R + \frac{\pi}{\lambda\cos\theta}\Delta n\, S\cos\Phi = 0 \qquad \textbf{(B.24)}$$

$$S\frac{\partial \phi_S}{\partial x} + \frac{r\delta}{\cos\theta}S + \frac{\pi}{\lambda\cos\theta}\Delta n\, R\cos\Phi = 0 \qquad \textbf{(B.25)}$$

where $\Phi = \phi_R - \phi_S + \phi$

To express in terms of intensities recall the following

$$I_R = R^2$$

Differentiating the above expression we achieved

$$\frac{dI_R}{dx} = 2R\frac{dR}{dx}$$

Therefore

Using the relation

Appendix B:

$$2R\frac{dR}{dx}+\frac{\alpha}{\cos\theta}R^2=-\frac{2\pi}{\lambda\cos\theta}\Delta n\,R\,S\,\sin\Phi$$

$$2S\frac{dS}{dx}+\frac{\alpha}{\cos\theta}S^2=\frac{2\pi}{\lambda\cos\theta}\Delta n\,R\,S\sin\Phi$$

$$I=I_o[1+M\cos(\boldsymbol{k}.\boldsymbol{r}-\phi)]$$

The product of amplitudes R and S becomes

$$RS=\frac{1}{2}MI_o$$

For the real terms;

$$\frac{dI_R}{dx}+\frac{\alpha}{\cos\theta}I_R=-\frac{2\pi}{\lambda\cos\theta}(-\frac{1}{2}n_o{}^3r_{eff}E'_{sc})2\frac{I_RI_S}{MI_o}\sin\Phi$$
$$=-\frac{\Gamma}{\cos\theta}\frac{I_RI_S}{I_o} \qquad \textbf{(B.26)}$$

where Γ is given by

$$\Gamma=2\delta\frac{E'_{sc}}{M}\sin\Phi$$

$$\delta=-\frac{\pi}{\lambda}n_o{}^3r_{eff}$$

similarly for signal

$$\frac{dI_S}{dx}+\frac{\alpha}{\cos\theta}I_S=\frac{\Gamma}{\cos\theta}\frac{I_RI_S}{I_o} \qquad \textbf{(B.27)}$$

For the imaginary terms

$$R\frac{\partial\phi_R}{\partial x}+\frac{r\delta}{\cos\theta}R+\frac{\pi}{\lambda\cos\theta}\Delta n\,S\cos\Phi=0 \qquad \textbf{(B.24)}$$

$$S\frac{\partial\phi_S}{\partial x}+\frac{r\delta}{\cos\theta}S+\frac{\pi}{\lambda\cos\theta}\Delta n\,R\cos\Phi=0 \qquad \textbf{(B.25)}$$

$$\frac{\partial\phi}{\partial X}=\frac{\partial\phi_R}{\partial x}-\frac{\partial\phi_S}{\partial X} \qquad \textbf{(B.28)}$$

Taking $\delta \sim$ o, in Equations (B. 24) and (B. 25) and then substituting the values of $\partial\phi_R$ / ∂x and $\partial\phi_S$ / ∂x in Equation (B.28), we get

$$\frac{\partial\phi_R}{\partial x}+\frac{\pi\,\Delta n}{\lambda\cos\theta}\frac{S}{R}\cos\Phi=0 \qquad \textbf{(B.29)}$$

$$\frac{\partial\phi_S}{\partial x}+\frac{\pi\,\Delta n}{\lambda\cos\theta}\frac{R}{S}\cos\Phi=0 \qquad \textbf{(B.30)}$$

$$\frac{\partial\phi_R}{\partial x}-\frac{\partial\phi_S}{\partial x}=\frac{\phi\,\Delta n}{\lambda\cos\theta}\left(\frac{R}{S}-\frac{S}{R}\right)\cos\Phi \qquad \textbf{(B.31)}$$

$$\begin{aligned}\frac{d\Phi}{dx}&=\frac{\pi}{\lambda\cos\theta}\left(-\frac{1}{2}n^3{}_o\,r_{eff}E'_{sc}\right)\frac{R^2-S^2}{SR}\cos\Phi\\&=\frac{\pi}{\lambda\cos\theta}\left(-n^3{}_o r_{eff}E'_{sc}\right)\frac{I_R-I_S}{MI_o}\cos\Phi\\&=\frac{\gamma}{\cos\theta}\frac{I_R-I_S}{I_o}\end{aligned} \qquad \textbf{(B.34)}$$

where

$$\gamma=\delta\frac{E'_{sc}}{M}\cos\Phi$$

The coupled first order differential equations (B.26), (B.27) and (B.34) can be solved

Appendix B:

as follows

$$\frac{dI}{dx} = -\frac{dI_S}{dx}$$

$$I_R = I_S + constant$$

$$I_R + I_S = I_o$$

$$\frac{dI_R}{dx} = -\frac{\Gamma}{I_o} I_R I_S$$

$$= \frac{\Gamma}{I_o} I_R (I_R - I_o)$$

$$\frac{I_o}{I_R (I_R - I_o)} dI_R = \Gamma dx$$

$$\int [\frac{1}{(I_R - I_o)} - \frac{1}{I_R}] dI_R = \int \Gamma dx$$

$$\ln (I_R - I_o) - \ln I_R + \ln C = \Gamma x$$

$$\ln \frac{(I_R - I_o) C}{I_R} = \Gamma x$$

Now applying boundary condition $I_S(0)/I_R(0) = r$ we get

$$\ln(-rC) = 0$$

$$C = -\frac{1}{r}$$

Appendix B:

$$\ln[-\frac{(I_R - I_o)}{I_R}\frac{1}{r}] = \Gamma x$$

$$\frac{(I_o - I_R)}{I_R} = r\exp(\Gamma x)$$

$$I_o = I_R[1 + r\exp(\Gamma x)]$$

$$I_R = \frac{I_o}{[1 + r\exp(\Gamma x)]}$$

$$I_S = \frac{I_o r\exp(\Gamma x)}{[1 + r\exp(\Gamma x)]} \qquad \textbf{(B.35)}$$

The gain is defined as the ratio of the output signal beam in the presence of pump beam to that in the absence of a pump beam. Therefore gain G can be expressed as

$$G = \frac{I_S}{I_S(0)} = \frac{\frac{I_o r\exp(\Gamma x)}{1 + r\exp(\Gamma x)}}{I_S(0)} \qquad \textbf{(B.36)}$$

where I_o can be expressed as

$$I_o = I_S(0) + I_R(0) \qquad \textbf{(B.37)}$$

Substituting the value of I_o in Equation (B.36), and simplifying, we achieve the gain G as

$$G = \frac{(1 + r)\exp(\Gamma x)}{1 + r\exp(\Gamma x)} \qquad \textbf{(B.38)}$$

Publications and Patent

Refereed Journal

1. J. A. Khoury, G. Hussain, R. W. Eason, "Contrast manipulation and controllable spatial filtering via photorefractive two-beam coupling", Opt. Common, **70**, 272, (1989).

2. J. A. Khoury, G. Hussain, R. W. Eason, "Optical tracking and motion detection using photorefractive $Bi_{12}SiO_{20}$", Opt. Common, **71**, 138, (1989).

3. G. Hussain, Stephen W James, R. W. Eason, "Observation and modelling of dynamic instabilities in the mutually pumped bird-wing phase conjugator in $BaTiO_3$", J. Opt. Soc. Am. B **7**, 2294, (1990).

4. G. Hussain and R. W. Eason, "Velocity filtering using complementary gratings in photorefractive BSO", Opt. Common, **86**, 106, (1991).

5. G. Hussain and R.W. Eason, "Optical logic operations via polarization encoding in a phase conjugate Michelson interferometer", International journal of "Optical Computing and Processing", Vol. **2(2), in press**, (1992).

8. Conference Presentations

1. G. Hussain, R. W. Eason, J. A. Khoury, "Fourier Manipulation Techniques in $Bi_{12}SiO_{20}/BaTiO_3$ for Contrast Enhancement and Motion Detection", **Mini-Symposium on Non-Linear Optical Phase Conjugation,** 4th-7th September, 1989, Broadway, Worcestershire, England. **(Invited Paper)**

2. G. Hussain, R. W. Eason, J. A. Khoury, "Optical tracking and motion detection using photorefractive $Bi_{12}SiO_{20}$", **The Ninth National Quantum Electronics Conference,** 18th-22th September, 1989, University Of Oxford, Oxford, England.

3. S. W. James, G. Hussain and R. W. Eason, "Dynamic Instabilities in the Photorefractive mutually pumped bird-wing phase conjugator", **The Ninth National Quantum Electronics Conference,** 18th-22th September, 1989, University Of Oxford, Oxford, England.

4. G. Hussain, R. W. Eason and J. A. Khoury, "Contrast manipulation and controllable spatial filtering via four-wave mixing and two-beam coupling in photorefractives", **The Ninth National**

Quantum Electronics Conference, 18th-22th September, 1989, University Of Oxford, Oxford, England.

5. S. W. James, G. Hussain, R. W. Eason, "Dynamic instabilities in the mutually pumped bird-wing phase conjugator", **Topical Meeting on Photorefractive Materials, Effects, and Devices II,** 17th-19th January, 1990, Aussois, France.

6. G. Hussain, R. W. Eason and J. A. Khoury, "Contrast manipulation and controllable spatial filtering via photorefractive four wave mixing and two-beam coupling", **Topical Meeting on Photorefractive Materials, Effects, and Devices II,** 17th-19th January, 1990, Aussois, France.

7. G. Hussain, R. W. Eason and J. A. Khoury, "Optical tracking and motion detection using Photorefractive $Bi_{12}SiO_{20}$", **Topical Meeting on Photorefractive Materials, Effects, and Devices II,** 17th-19th January, 1990, Aussois, France.

8. G. Hussain and Robert W. Eason, "Velocity Filtering using Complementary Gratings in Photorefractive BSO", **Topical Meeting on Photorefractive Materials, Effects, and Devices,** 29th-31th July 1991, Beverly, Massachusetts, USA.

9. G. Hussain and R.W. Eason, "Velocity Filtering using complementary gratings in Photorefractive BSO", **European Quantum Electronics Conference and Tenth National Quantum Electronics Conference,** 27th-30th August, 1991, Heriot-Watt University, Edinburgh, UK.

Patent

A patent has been filed on a Contrast Manipulation Technique of Optical Images and its applications in phase contrast microscopy and study of aerodynamics in wind tunnels. Ref. No. GP2/90 A, University of Southampton.

The following published papers were included in the bound thesis. These have not been digitised due to copyright restrictions, but the links are provided.

https://doi.org/10.1016/0030-4018(89)90318-0

https://doi.org/10.1016/0030-4018(89)90415-X

https://doi.org/10.1364/josab.7.002294

https://doi.org/10.1016/0030-4018(91)90543-M

AJR/33507

UNITED KINGDOM
PATENT SPECIFICATION

Application No. 9211166.5

Application Date 26th May 1992

Priority Date

Applicant University of Southampton

REDDIE & GROSE
Chartered Patent Agents
European Patent Attorneys
16 Theobalds Road
London WC1X 8PL

Telephone: 071-242-0901
Telex: 25445 Reddie G
LDE No. 280

Contrast Manipulation of Images

Background of the Invention

This invention relates to contrast manipulation of images and in particular to phase contrast imaging.

Light diffraction occurs when a portion of a wave front in an image is modulated in phase or amplitude. When a wave passes through a phase object such as a filter it is divided into two parts; one is phase modulated while the other is almost unmodulated. For a phase change e.g. less than a radian as is the usual case, a phase shift of 90° is introduced in the un-diffracted part by inserting a phase filter in the transform plane (of the phase object). The filter may be in the form of a small circular phase-lag or phase-lead thickness variation in a transparent plate. Ideally only the direct light passes through this thickness step. Therefore interference takes place between the modulated and unmodulated components and introduces greater contrast into the image. The character of this interference depends on both the amplitude of and the relative phase between these two components. Complete destructive interference takes place between the two components when their amplitudes are equal and have a relative phase shift of 180°. However this will not be the case for an arbitrary (irregular) phase object. Therefore not all the features of a phase object can be seen with optimum (maximum) contrast because in the existing technique there is no option to vary the relative phase and amplitudes of the two components wtihout changing the thickness and attenuation continuously.

To achieve variable relative phase and amplitude, different thickness phase filters and amplitude filters are required which therefore do not permit continuously variable contrast operation. Also positive and negative contrast require relative phase shifts of 0° and 180°, again needing different phase filters.

Summary of the Invention

This invention will provides a new method for phase contrast imaging, that overcomes the requirement of different phase filters to positive and negative contrast, and also for fixed values of these filters formerly required for different levels of contrast. Therefore the single device described herein can replace all these pre-determined phase filters for manipulation of continuous levels of contrast, from minimum to maximum for both positive and negative contrast.

Detailed Description of Preferred Embodiments

The invention will now be described in detail with reference to the accompanying figures which:

Figure 1. Different arrangements for polarization encoding using half-wave plates;

Figure 2. Shows polarization states of DC and higher orders in a plane after the polarization encoding in a contrast manipulation arrangement;

Figure 3(a) Theorectical plot of output amplitude at image plane for equal amplitudes of DC and higher orders versus angular position of transmission axis of the analyzer;

Figure 3(b) Plot of the output amplitude at the image plane when higher orders have the one-fourth amplitude as compared to DC versus angular position of the transmission axis of the analyzer;

Figure 4. Shows the illumination schemes of an object and subsequent polarization encoding of the diffracted and non-diffracted light for variable phase contrast microscope;

Figure 5. Schematic diagram of variable phase contrast microscope showing its basic features i.e., annular diaphragm, condenser, an eye piece, a combination of polarizer, polarization rotation mask, a compensator and an analyzer inside the dotted Boxes 1 and 2;

Figure 6. Schematic diagram shows a comparison between a conventional phase contrast microscope and variable phase contrast microscope. (a) and (b) shows arrangement for the conventional positive and negative phase contrast microscope while (c) is a variable contrast phase microscope; and

Figure 7. Schematic diagram shows the arrangement for ballistics and ultrasonic wind tunnel studies.

The embodiment of invention described here is based on polarization encoding of the Fourier transform i.e., Fraunhofer diffraction pattern of the input light distribution in the object plane. Figure 1, shows the three possible configurations of polarization encoding of Fourier transforms. While our technique relates to all three possible configurations, we shall restrict the detailed discussion here to Figure 1(a) only. This figure shows a lens (system) L_1 which makes the optical Fourier transform of the object distribution function in its back focal plane. In this Fourier plane the central DC order (which represents Direct Component or steady state value), contains the background image information while higher orders have the phase information. Instead of introducing a fixed 90° phase shift in the DC order via a fixed phase filter as used in former conventional techniques, we have placed a half-wave plate and their polarization direction is

rotated through 90° from their initial position for a specified initial HWP orientation.

The polarization encoded Fourier transform is re-transformed by a second lens (system) L_2 as shown in the Figure 1. Due to the orthogonal polarizations of the background and higher order illumination, no interference takes place at the image plane between these two components. However, placing an analyzer before the image plane allows the DC and higher orders to be resolved along and perpendicular to its allowed transmission axis. Therefore the transmitted components will interfere at the output plane. Using existing techniques, objects which introduce smaller phase shifts as is the usual case, show poor contrast. This is because of the 90° phase shift introduced by the phase filter in addition to the small phase shift introduced by the object. However this invention here provides the maximum positive and negative contrasts for any phase object which may introduce arbitrary small phase shifts, because of the characteristic 0° and 180° phase shifts and amplitude control between the DC and high orders that are achieved by this invention.

Figure [2], illustrates a sequence of polarization states for this device. Such an arrangement, in terms of polarization aspect, may also be expressed by

$$\mathrm{Re}[A_{DC}e^{i(\Theta-psi)} + A_{HO}\, e^{i(\Theta+\phi-psi)}] = \text{Output} \qquad (1)$$

Where Θ is the polarization angle from a reference e.g. horizontal axis ϕ is the relative polarization angle between the direct light and the diffracted light (we take here $\phi = 90°$), while psi is the angle between the reference axis and the transmission axis of the analyzer. A_{DC} and A_{HO} are the maximum amplitudes of DC and higher orders which can be achieved when psi = Θ and psi = $(\Theta+\phi)$ respectively. Contrast of the phase object can be manipulated by varying any one two or all of the three angles described above.

Figure 3(a), shows the representation of Equation (1) in the form of a graph, for equal amplitudes of DC and higher orders. this graph shows complete subtraction is achieved at psi = 0°, 180° and 360°, at these positions amplitudes of DC and higher orders are equal and out of phase while at all other positions a net output is always achieved. The contrast of the less visible features in the object may be improved if some of the DC is attenuated to equate the light amplitudes of DC and any particular higher orders. In our technique it is quite easy to attenuate the DC or higher orders to any specified level, from 0 i.e., minimum, to a maximum value. This is achieved by rotating the transmission axis of the analyzer to attenuate the DC component while increasing the relative transmission of the higher orders.

Unlike previous techniques of phase contrast imaging, where special attenuation masks of particular values or steps are fabricated our technique does not require any such fabrication, yet can arbitrarily adjust the desired proportion of DC and higher orders. Therefore when the amplitudes of DC and higher orders are not equal, for example when higher orders have amplitudes one fourth of that of the DC amplitude, the total subtraction is achieved at a different angular positions of transmission axis of the analyzer. This is illustrated graphically in Figure 3 (b), it is clear that our new technique is easy, versatile and flexible, and represents a great improvement on previous art of phase contrast imaging.

The invention can also be extended to any other types of illumination schemes of the object such as light illumination in the form of a ring which is focused onto the object in the form of a hollow cone of light and is illustrated for three types of polarization encoding schemes in Figure 4. We discuss here arrangement of Figure 4(a) for its application in variable phase contrast microscope only however, the other schemes can also be implemented similarly.

Figure 5 shows a schematic diagram of our phase contrast microscope

where the required illumination is achieved by using an annular diaphragm below the condenser. A hollow cone of light is directed to the transparent object as shown. The objective collects this light and directs it towards a ring shaped and circular half-wave plate combination as shown in the figure. To make the light polarized before it travels through the polarization rotation mask a polarizer is placed in any convenient plane before the mask as shown in the dotted Box 1 in the figure. The light which is diffracted from the object is rotated through 90° while the direct (un-diffracted), light remains of the same polarization (or vice versa by placing a HWP mask in the un-diffracted light to rotate it through 90°). Therefore the two components of light are orthogonally polarized to each other and do not interfere with each other. An analyzer is placed in any convenient plane to analyze these two components of light. Therefore contrast manipulation can be achieved using same mechanism as described in the above explanation.

We can also place a compensator, for example a Soleil compensator to introduce a variable relative phase change between orthogonally polarised DC and higher orders which are to be analyzed in the next stage by an analyzer. For best results orthogonal optical axes of the uniform slab and pair of wedges of the compensator be used. Using such an arrangement polarizations of DC and higher orders will remain unchanged while a variable relative phase change can be introduced between the two orthogonally polarized lights by controlling the total thickness of the two wedges in the compensator.

A comparison of conventional phase contrast microscope and our variable phase contrast microscope is illustrated by the schematic diagram of Figure 6. The basic set up is same for both the techniques. However positive and negative step phase filters and amplitude filter are replaced by a single polarization rotation filter, a polarizer and an analyzer. Similarly a compensator can

also be introduced in the microscope shown in (c) as discussed above.

Apart from Zernike's technique * for observing phase objects there is another technique to see phase object which is known as the dark field technique. In this technique the DC order is removed completely by an opaque disk. Therefore the phase object is seen in the image plane as bright due to the localized diffraction of light on the otherwise dark background. This operation is also achieved using our new technique by rotating the analyzer only to a position where its axis of tranmission is parallel to the polarization direction of all higher orders, while simultaneously being perpendicular to that of the DC component. This results in complete attenuation of the DC term and maximum transmission of higher orders. Therefore our technique not only improves on the previous technique of phase contrast imaging but also simultaneously combines the two techniques in one new device.

Our technique can also replace Schlieren methods of observing phase variations in fluid dynamics. Schlieren methods of observing phase variations has a wide range of applications such as observing shock waves that are developed around bullets in ballistics and airfoils in jet aircraft when the flight of these objects is for example at supersonic speeds. Figure 7, shows a schematic diagram to achieve Schlieren method via our arrangment with further improvements to control the amplitude and phase of the two portions of Fourier transform. In conventional techniques a knife edge is used usually to block out half of the Fourier spectrum of the (phase) object. Our technique can also perform this operation using the above mentioned polarization encoding schemes. However this time we can use HWP in the form of a knife edge and attenuating the required portion of the Fourier transform by analyzing the polarization encoded light at the output as shown in Figure 7. However a similar HWP mask as shown in the Figure 1, can also be used to manipulate the contrast of the phase variations by analyzing the output light.

* Zernike, F Das, "Phasenkontrastverfahren bei der Midroskopischen Bcobachtung", Z. Tech. Phys. 16,454 (1935).

Further Explanations

(a)
Different illumination schemes may be used for contrast manipulation of objects such as critical, kolner illumination etc. Therefore illumination schemes, light wavelength, and polarization directions are not specific.

(b) The polarization rotation filter may be of different shapes depending on the illumination schemes and applications.

(c) Polarization rotation components are not specific and use of a particular type of component or components and their geometry i.e., single pass, double pass, or many pass, of light through these components via reflection, transmission or their combinations may depend on the convenience to achieve the requried operation. Similarly linearly polarized lights give better results.

(d) Designs of condenser, objective, eyepiece and of other optical systems described above are not specific and may vary on the bases of individual applications etc. For example, in Schlieren method shown in Figure 7, instead of lens L_1 one may use parabolic mirror.

(e) Use of polarization selection components such as polarizers, polarizing beam-splitters etc are not specific therefore different types of such components may be used to achieve the required operation which may depend on the convenience to perform that operation.

(f) The schemes shown in Figure 1 and Figure 4 may not even require analayzer to perform the contrast manipulation of objects in situation such as when un-diffracted (DC), light and diffracted (higher orders), light have relative rotation of 180° which make the two types of light components out of phase (or in-phase depending on the phase introduced by the object) and they will interfere correspondingly at the image plane. However when the polarization of the diffracted and un-diffracted lights are in different planes optimum results will not be achieved without analyzer.

(g) The positions of half-wave plates for scheme shown in Figure 1, and Figure 4, are such that HWP_1 is placed before HWP_2 in any convenient plane. Similarly polarizer is placed in a convenient plane before the HWP which is used for polarization encoding of Fourier transform of the object.

(h) Only Higher orders (diffracted light), or DC (un-diffracted light) need to be rotated in Fourier Transform plane, however both of these light components can also be rotated by placing two half-wave plates in Fourier plane.

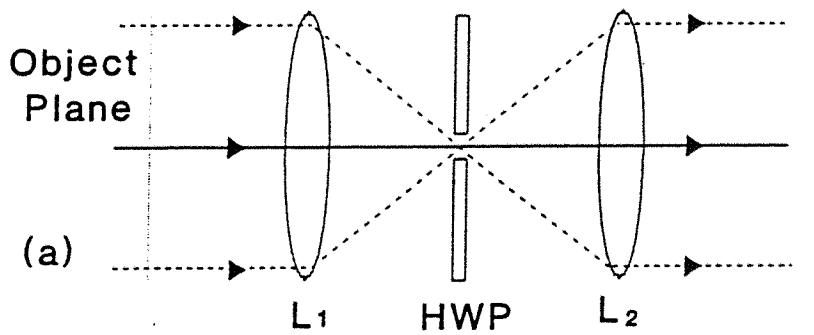
Object
Plane
(a)
L1
HWP
L2

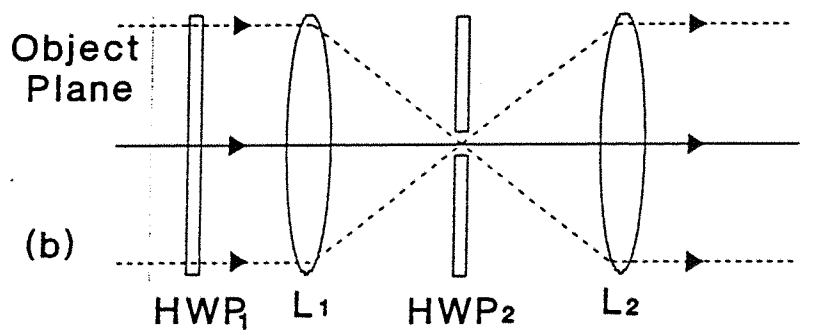
Object
Plane
(b)
HWP1
L1
HWP2
L2

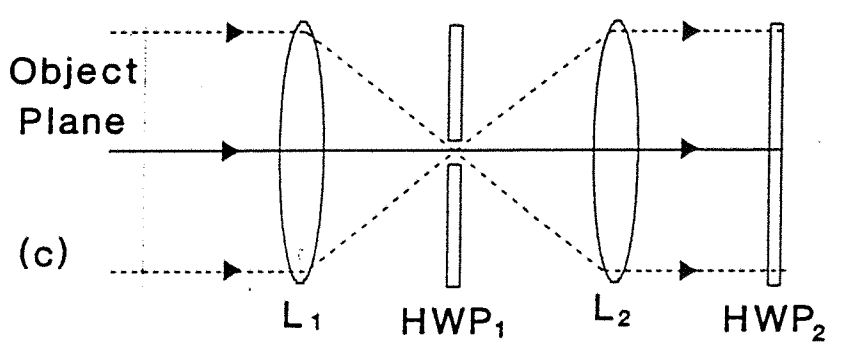
Object
Plane
(c)
L1
HWP1
L2
HWP2

Figure 1

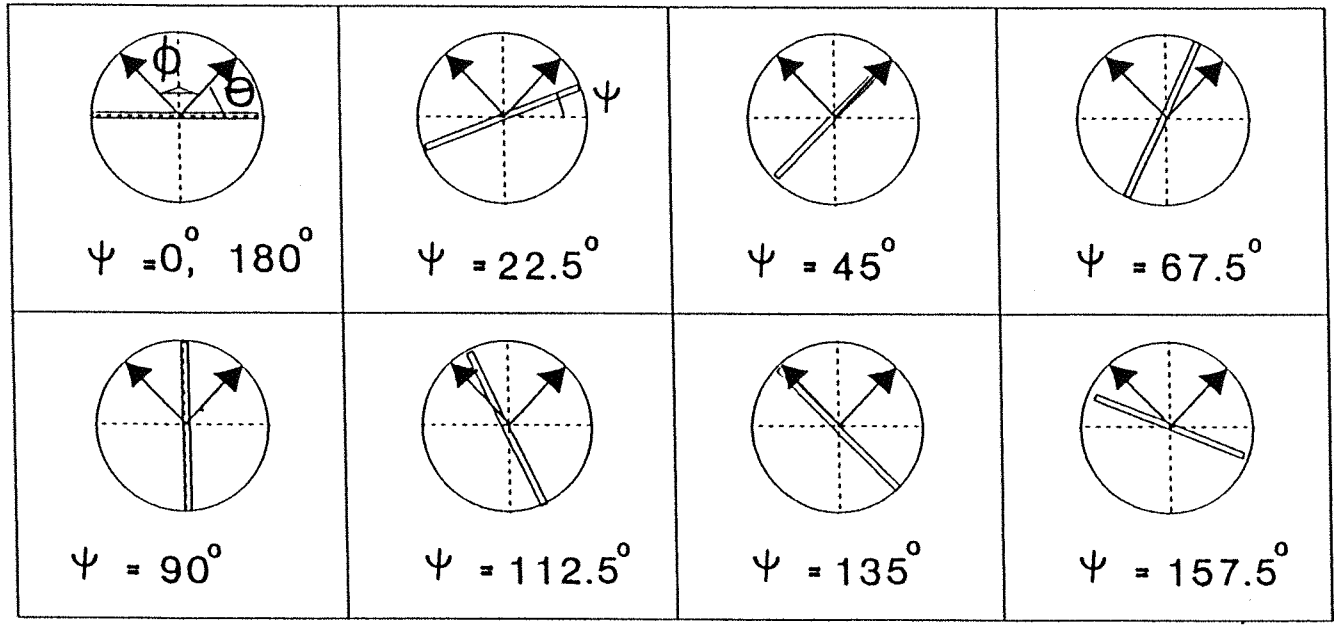
ϕ
θ
Ψ
Ψ =0, 180°
Ψ = 22.5°
Ψ = 45°
Ψ = 67.5°
Ψ = 90°
Ψ = 112.5°
Ψ = 135°
Ψ = 157.5°
Reference Axes
Transmission Axis of Analyzer

Figure.2

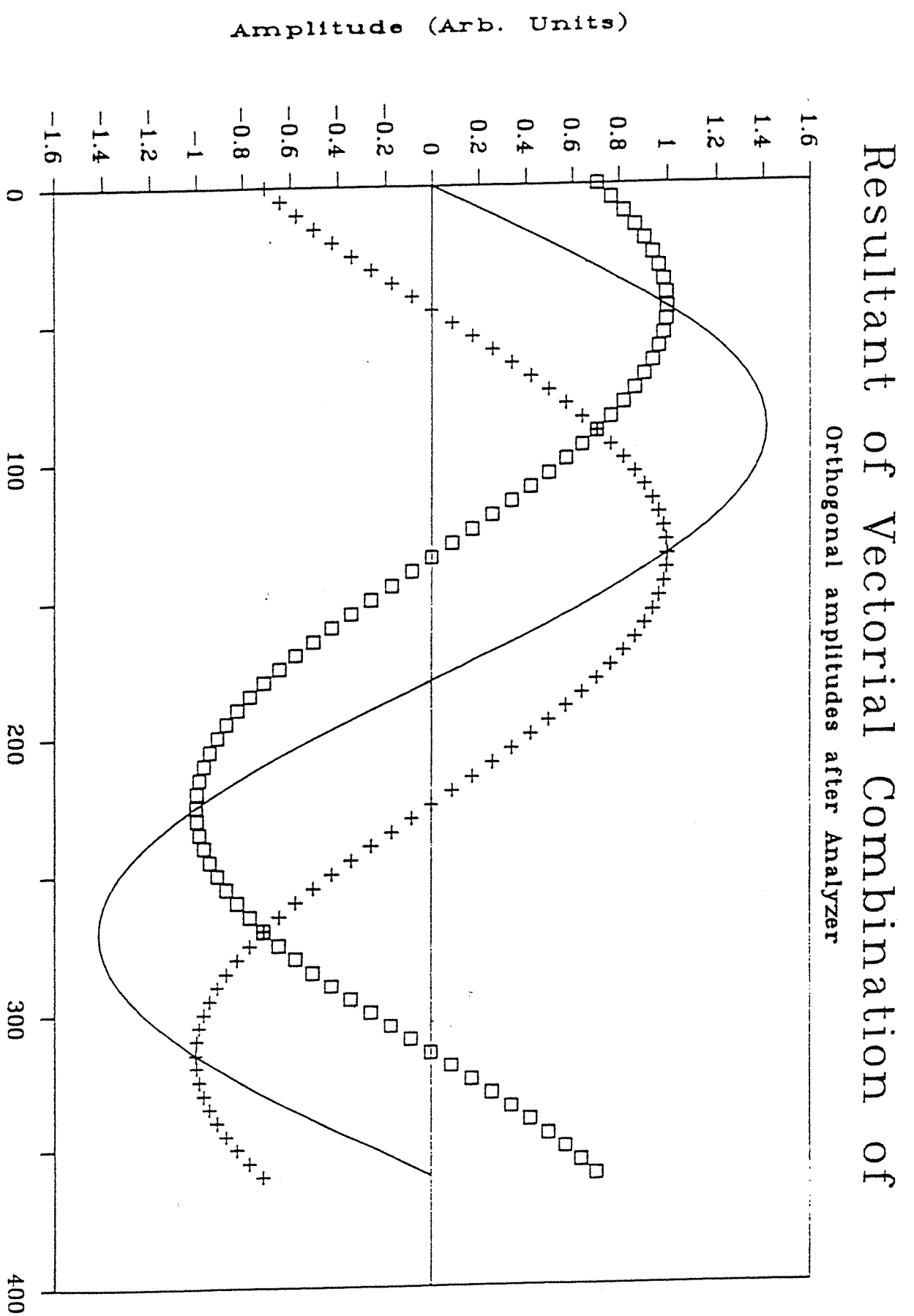
Resultant of Vectorial Combination of
Orthogonal amplitudes after Analyzer
Amplitude (Arb. Units)
1.6
1.4
1.2
1
0.8
0.6
0.4
0.2
0
−0.2
−0.4
−0.6
−0.8
−1
−1.2
−1.4
−1.6
0
100
200
300
400

Figure 3(a)

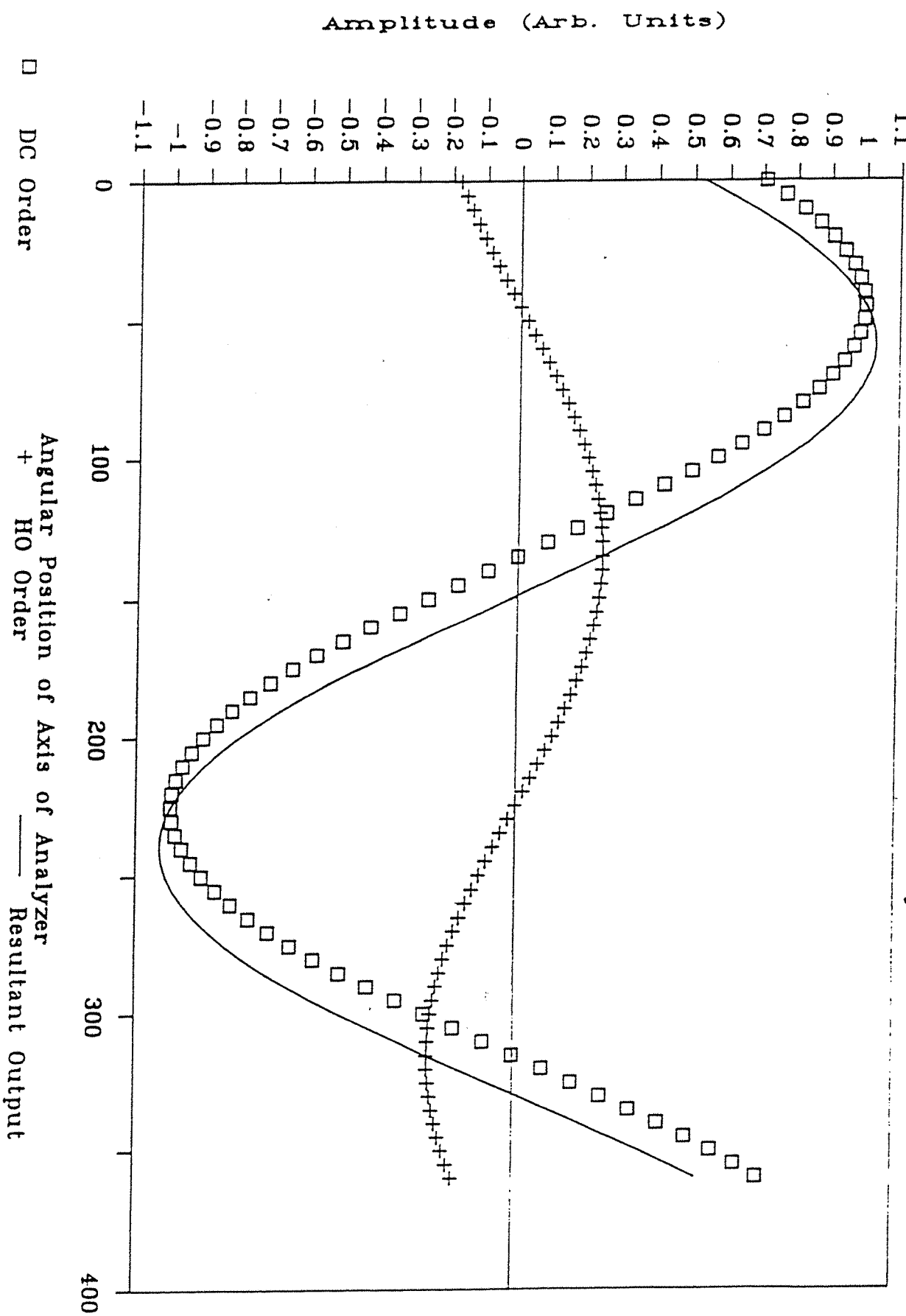
Resultant of Vectorial Combination of
Orthogonal amplitudes after Analyzer
Amplitude (Arb. Units)
1.1
1
0.9
0.8
0.7
0.6
0.5
0.4
0.3
0.2
0.1
0
−0.1
−0.2
−0.3
−0.4
−0.5
−0.6
−0.7
−0.8
−0.9
−1
−1.1
0
100
200
300
400
Angular Position of Axis of Analyzer
□ DC Order
+ HO Order
—— Resultant Output

Figure 3(b)

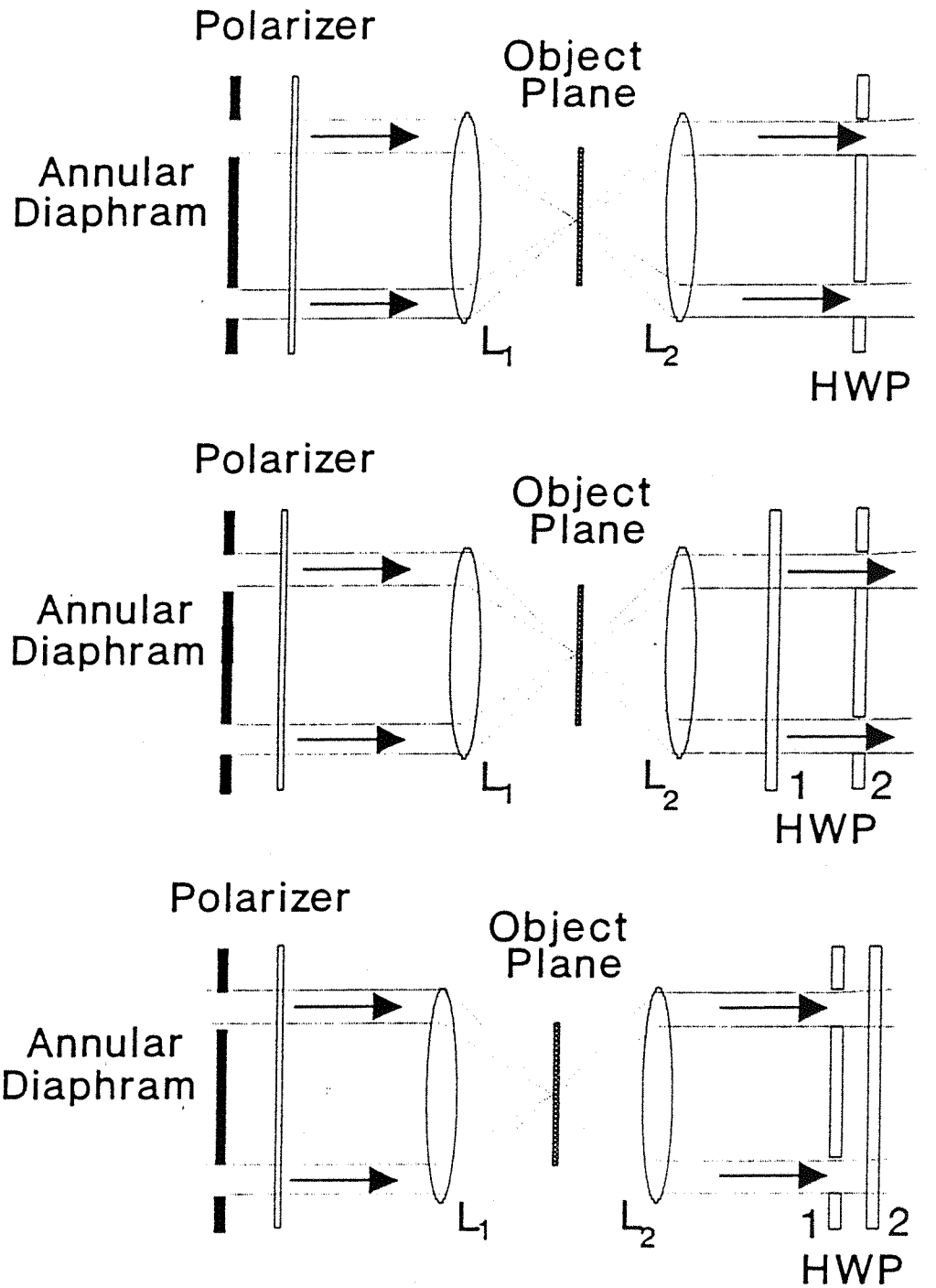
Polarizer
Object Plane
Annular Diaphram
L1
L2
HWP
(a)
Polarizer
Object Plane
Annular Diaphram
L1
L2
1
2
HWP
(b)
Polarizer
Object Plane
Annular Diaphram
L1
L2
1
2
HWP
(c)

Figure .4

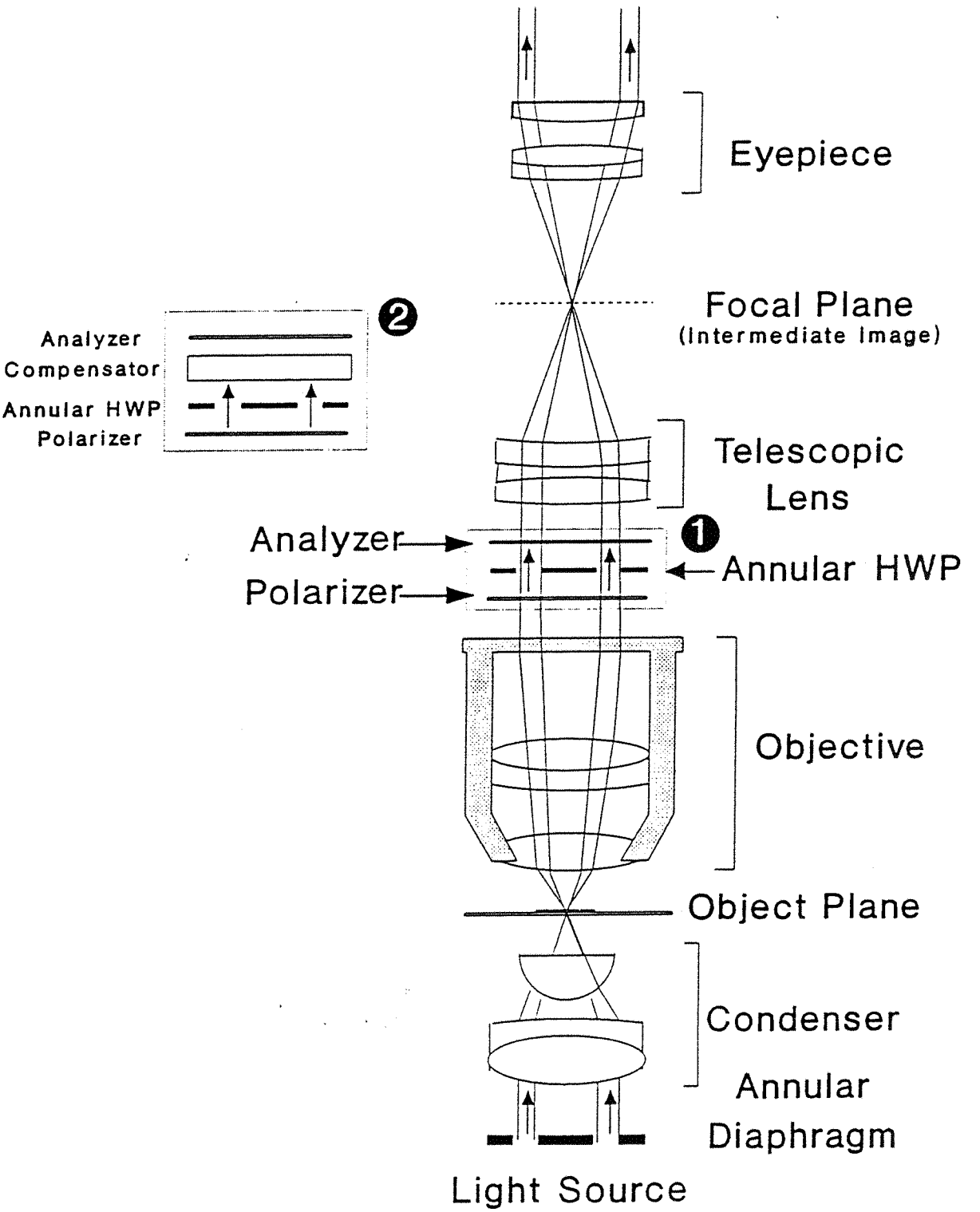
Eyepiece
Focal Plane
(Intermediate Image)
Telescopic
Lens
Analyzer
Polarizer
Annular HWP
Objective
Object Plane
Condenser
Annular
Diaphragm
Light Source
Analyzer
Compensator
Annular HWP
Polarizer
1
2

Figure 5

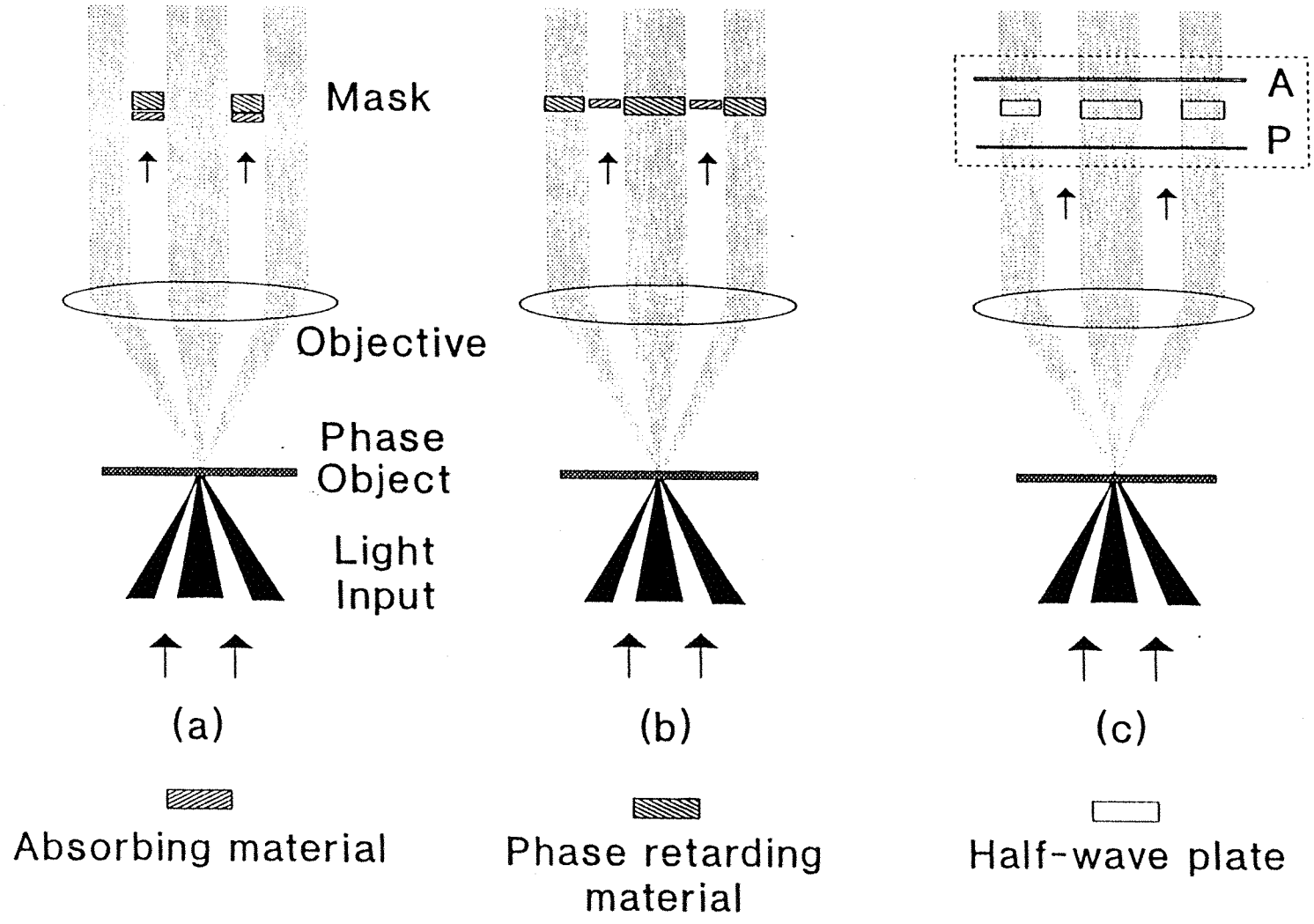
Mask
Objective
Phase
Object
Light
Input
(a)
(b)
(c)
A
P
Absorbing material
Phase retarding
material
Half-wave plate

Figure. 6

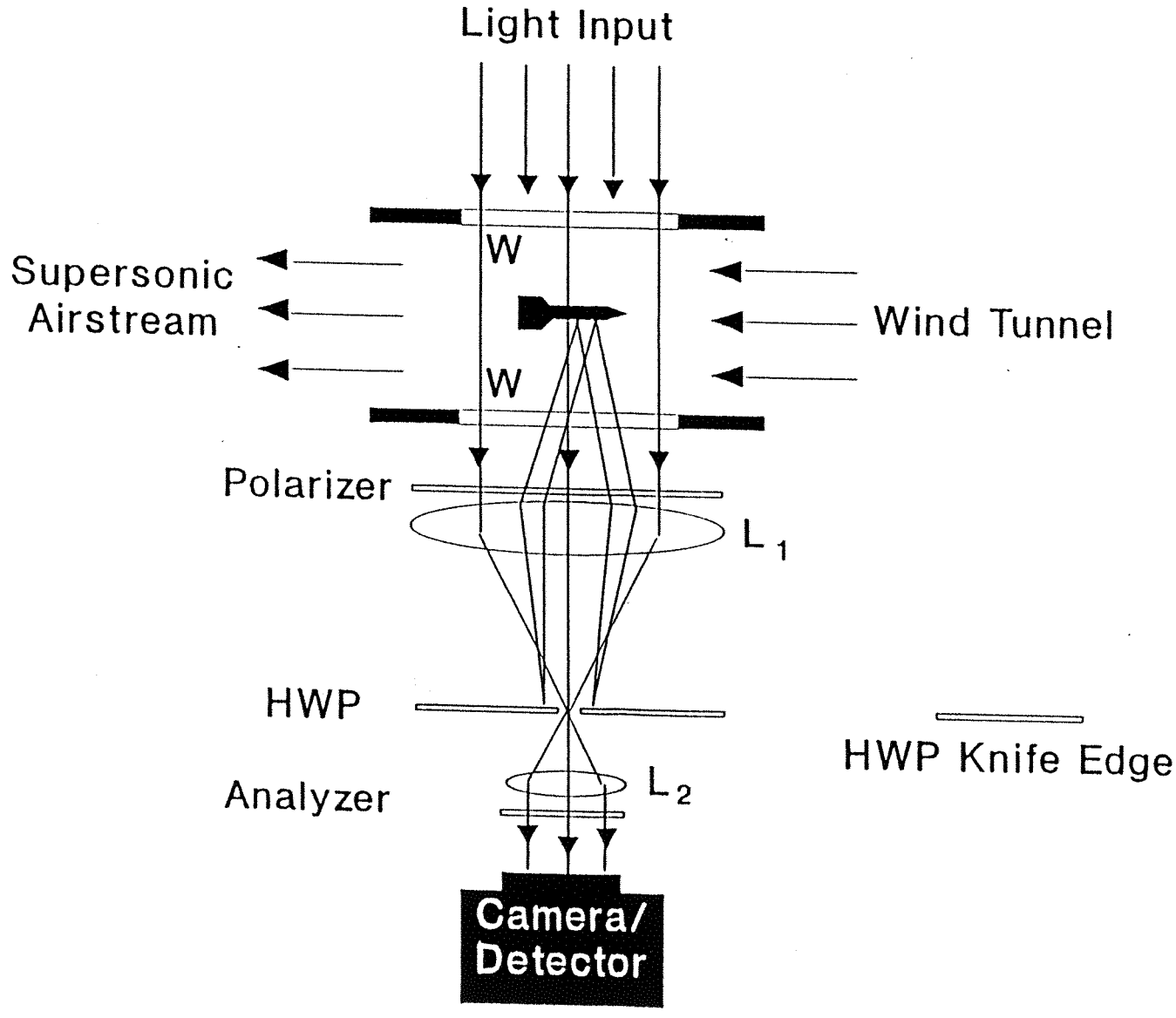
Light Input
W
Supersonic
Airstream
Wind Tunnel
W
Polarizer
L_1
HWP
HWP Knife Edge
Analyzer
L_2
Camera/
Detector

Figure 7